Final Technical Report

CRRP2017-02MY-SENTIAN

Climate Change, Biomass Burning and Biogenic Emissions Impact on Surface Ozone and Particulate Matter in Southeast Asia

APN

ASIA-PACIFIC NETWORK FOR
GLOBAL CHANGE RESEARCH

The following collaborators worked on this project:

- Assoc. Prof. Dr. Justin Sentian, Universiti Malaysia Sabah, Malaysia, jsentian@ums.edu.my
- Assco. Prof. Dr. Carolyn Melissa Payus, Universiti Malaysia Sabah, Malaysia, melpayus@ums.edu.my
- Assoc. Prof. Dr. Mohd. Shahrul Mohd Nazir, Universiti Kebangsaan Malaysia, shahrulnadzir@ukm.edu.my
- Dr. Steven Kong Soon Kai, National Central University, Taiwan, skong@gmail.com
- Dr. Narisara Thongboonchoo, King Mongkut's Institute of Technology Thailand, nthongbo@gmail.com
- Dr. Ronald C. Macatangay, NARIT, Thailand, ronmcdo@gmail.com
- Prof. Ir Puji Lestari, Institut Teknology Bandung, Indonesia, pujilest@indo.net.id
- Assoc. Prof. Dr. Nina Yulianti, University of Palangkaraya, Indonesia, nyulianti@agr.upr.ac.id
- Assoc. Prof. Dr. Mylene G. Cayetano, University of The Phillipines Diliman, mbgonzaga@gmail.com

Table of Contents

Project Overview

Project Duration	**:**	3 Years (Aug 2017-July 2020) + 1-year extension (Aug 2020 – Aug 2021)
Funding Awarded	**:**	US$ 104,000 for Year 1, Year 2, Year 3
Key organisations involved	**:**	Universiti Malaysia Sabah (UMS) (Malaysia) Universiti Kebangsaan Malaysia (UKM) (Malaysia) University of Philippines Diliman (The Philippines) National Astronomical Research Institute of Thailand (Thailand) Universitas Palangka Raya (Indonesia) Institute Teknologi Bandung (Indonesia) King Mongkut's Institute of Technology Ladkrabang (Thailand) National Central University of Taiwan (Taiwan) Department of Environment Malaysia (Mdm Marshitah Darus)

Project Summary

The first main task of this project is to investigate climate change in Southeast Asia using WRF Model at a higher resolution project, with aim of developing climate change scenarios (RCP4.5, 6.0, and 8.5) for the region. The output would help to identify which areas in the region that potentially important in assessing climate vulnerability for adaptation purposes. The second task is to develop biomass burning emission inventory for the whole of Southeast Asia. This region is prone to forest fire especially the tropical forest over Borneo Island, Sumatera Island as well as savannah forest over continental Southeast Asia (Indochina). For this investigation the year 2013 was selected as it was considered a neutral year. The inventory of biomass emission is important as an input for the air quality model of the region. The third task is developing the biogenic emission inventory for Southeast Asia. The main compound in the investigation was isoprene as it is very reactive and important in atmospheric chemistry, particularly on ozone chemistry and secondary aerosol formation. The last task was to investigate the regional air quality (ozone and other pollutants) under climate change scenarios. Four workshops and research meetings were organised as part of the commitment to disseminate information on the research focus to the collaborating countries.

Keywords*: Biogenic Emission, Biomass Burning, Climate Change, Southeast Asia, Surface Ozone*

Project outputs and outcomes

Project outputs:

Output A: Completion of climate change scenarios for Southeast Asia.

Output B: Identification of vulnerable areas due to climate change in Southeast Asia

Output C: Completion of biomass burning emission and inventory for Southeast Asia

Output D & E: Completion of biogenic emissions and inventory for Southeast Asia

Output F: Completion of air quality simulation for Southeast Asia.

Output G: Identification of air quality hot spot areas in Southeast Asia

Output H: Project outcomes archive, communication, and dissemination through centralised data management storage, and organised meetings and workshops

Project Outcomes:

Outcome A: Completion of climate change scenarios for Southeast Asia.

Outcome B: Identification of vulnerable areas due to climate change in Southeast Asia

Outcome C: Completion of biomass burning emission and inventory for Southeast Asia

Outcome D & E: Completion of biogenic emissions and inventory for Southeast Asia

Outcome F: Completion of air quality simulation for Southeast Asia.

Outcome G: Identification of air quality hot spot areas in Southeast Asia

Outcome H: Project outcomes archive, communication, and dissemination through centralised data management storage, and organised meetings and workshops

Key facts/figures

- Developed climate change scenarios (RCP4.5, RCP6.0, and RCP8.5) for Southeast Asia – warming the atmosphere over Southeast Asia in the future especially towards the end of the century
- Biomass emissions were found to be higher in Southeast Asia particularly particulate matter from biomass burning
- Biogenic Emissions (isoprene) in Southeast Asia are influenced greatly by climate change. High emission of biogenic over Borneo Island, Papua New Guinea, and Sumatera Island.
- Great variability of surface ozone and other air pollutants parameter under climate change scenarios over part of Southeast Asia region (Malaysia)

Potential for further work

Over the Southeast Asia domain, the current works focused on the development of climate change scenarios, biomass emission inventory, biogenic emission inventory, and regional air quality. How climate change affects regional biogenic emissions and air quality were also explored. Due to the wides scope of the study, coupled with the limited access to the computing system during the pandemic period in 2020 and 2021, a few work details warrant further investigation to understand the intricate relationship between climate-biomass emission-biogenic emissions-air quality. Relevant to the current scope of investigations, potential works for future investigation are:

a) We have a reasonably good understanding of regional climate change over Southeast Asia. Future works on the enhancement of the spatial resolution and the investigation of inter-model comparison and higher spatial resolution using the latest climate scenarios could further enhance the understanding of the regional climate change variability. Consideration under extreme climate for the impacts, vulnerability, and adaptations investigation will enhance the understanding of future climate scenarios and their impacts on various issues.

b) With a limited understanding of the future ozone response to future climate change scenarios, further investigation could be expanded on how climate change, biomass, and biogenic emissions affect the regional oxidising capacity. The unexpected role of biomass burning in terms of tropospheric ozone formation potential (OFP) when including the large contributions of VOCs of biomass burning such as aldehydes, biomass burning could significantly enhance the regional atmospheric oxidizing capacity, in addition to the well-recognised contributions of primary pollutants, which should be seriously considered in the future works that will employ atmospheric chemistry models.

c) A large scale of biomass burning over the tropics generates large amounts of atmospheric pollutants yearly. The development of an emissions inventory of biomass burning is very challenging, especially when performing modelling of regional air quality. This study has employed remote sensing techniques in developing regional biomass inventory. However further evaluation on the generated datasets needs to be performed by comparing them with other available techniques. In this case, the Sparse Matrix Operator Kernel Emissions (SMOKE) could be considered to produce a spatial distribution of the forest fire emissions in the region. Future air quality modelling at a local level could apply the results and the methodology of this study. The biomass burning emissions could add a better performance of the results and more knowledge on the effect of this source.

d) Current investigation on the future biogenic emissions is based on the current landcover, To improve the future biogenic emission inventory, apart from the future climate forcing, the assumption on possible future landcover forcing can be explored to investigate the combined effects of climate and landcover forcing on future biogenic emissions. This is particularly true for areas that are considered biogenic emission hot-spot areas such as Borneo Island, Papua New Guinea, and Sumatera Island, where large tropical rainforests are still to be found.

e) Biomass emissions in the Southeast Asia region may not only on the long-range transport of pollutants issue but may resulting effects on atmospheric chemistry along with determining the potential effects of these changes on atmospheric processes and the resulting impacts on society. The analysis of satellite and other measurement datasets and use of the higher resolution of regional models such as WRF-CHEM and CMAQ or an ultra-high-resolution, fully-particle-resolve aerosol model (PartMC) can be explored.

Publications

1. Sentian, J., Payus., C.M., Herman, F., Kong, V. & Mohd Nadzir, M.S. (2021). Biomass Burning Scenarios in Malaysia: Associated Sources and Its Impacts. In Vadrevu, K.P., Ohara, T. & Justice, C. (Eds.), *Biomass Burning in South and Southeast Asia: Mapping and Monitoring* (pp. 159-182). CRC Press.

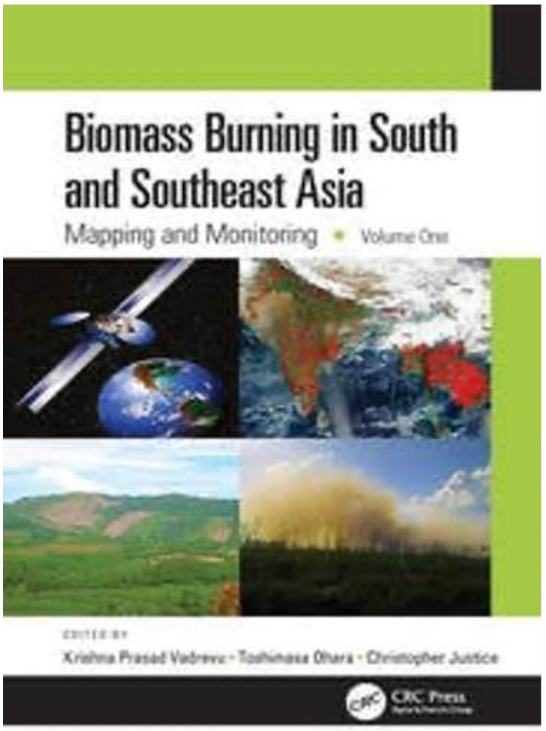

2. Perez J. G, J.C. Comiso & M. G. Cayetano. (2021). Swidden Agriculture and Biomass Burning in the Philippi. In Vadrevu, K.P., Ohara, T. & Justice, C. (Eds.), *Biomass Burning in South and Southeast Asia: Mapping and Monitoring* (pp. 183-198). CRC Press.

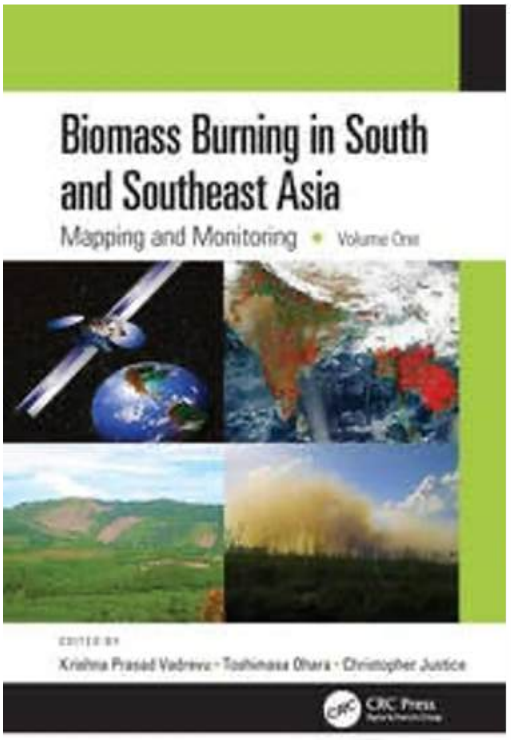

11 Swidden Agriculture and Biomass Burning in the Philippines

Gay J Perez
University of the Philippines Diliman, Philippines

Jaserino C. Comiso
University of the Philippines Diliman, Philippines
NASA Goddard Space Flight Center, USA

Mylene G. Cayetano
University of the Philippines Diliman, Philippines

CONTENTS

INTRODUCTION

Swidden agriculture started about 12,000 years ago when humans stopped hunting and gathering and decided to stay put where they are and began to grow crops and domesticate animals. Among the motivations is the hesitance to leave an ideal location that, at the same time, is endowed with a perfect climate. By swidden agriculture, we mean the conversion of forest and grassland to open land suitable for farming. It is sometimes referred to as "slash-and-burns agriculture," and it is called the *kaingin* system in the Philippines. The strategy is to clean up an area by cutting down the vegetation, allowing it to dry, and then setting it on fire to produce

3. Sentian, J., Yih, C.Y., Herman, F. & Wui, J.C.H. (2019). Long-term Air Pollution Trends Analysis in Malaysia. International Journal of Environmental Impacts. *International Journal of Environmental Impacts*. 2(**4**):309-324.

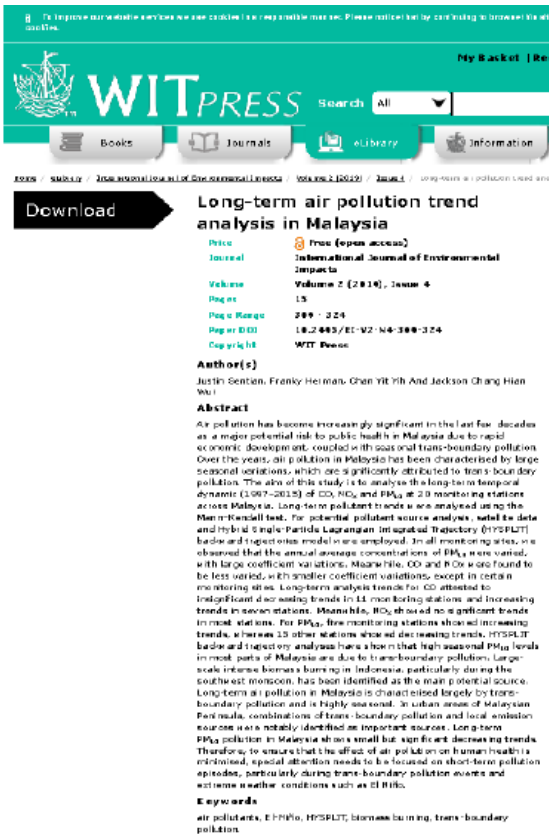

Awards and honours

During the project period, the following research collaborators were promoted to Associates Professors. Congratulations!

1. Assoc. Prof. Carolyn Melissa Payus (Universiti Malaysia Sabah, Malaysia)
2. Assoc. Prof. Dr Mohd Shahrul Mohd Nadzir (Universiti Kebangsaan Malaysia, Malaysia)
3. Assoc. Prof. Dr. Mylene G. Cayetano (University of the Philippines Diliman, Philippines)
4. Assoc. Prof. Nina Yulianti (University of Palangka Raya, Indonesia)

Pull Quote

"The main key issues have been raised and brought out in this research for Southeast Asia on Biomass Burning and Biogenic Emission that could be one of the important platforms to move forward for the next steps, especially cooperation from both sides of the Governments to tackle the climate change. It is time for all relevant parties to talk to each other and understand what is happening to their communities, understand the problem, and make a difference in the climate crisis for the future of our young generation"

Assoc. Prof. Carolyn Melissa Payus, Universiti Malaysia Sabah, Malaysia

"The APN has opened a wider networking opportunity for me, with my fellow young scientist in southeast Asia. Because of the APN Project, I was able to interact with SEA scientists, and understand that their air pollution situation is both unique and ubiquitous to our region. Unique because the sources of emissions are of particular fingerprint based on the type of biogenic emissions in each country. Ubiquitous because the biogenic emissions, once in the atmosphere, has a potential of being transported and shared within the Southeast Asian region. I was also able to share these learnings to our local students, who have gained interest in long-range transported emissions. Aside from the recently published works, we are writing a book chapter on characterizing long-range transported emissions during a SEA Haze event in 2019. This would not be possible if not through the help of this APN Project"

Assoc. Prof. Mylene G. Cayetano, University of the Philippines Diliman

Acknowledgments

I would like to take this opportunity to express my profound gratitude and deep regard to Asian Pacific Network (APN) for the funding support for this important collaboration research work in Southeast Asia *(CRRP2017-02MY-SENTIAN)*. Valuable contributions from all collaborating universities and institutes in Southeast Asia, namely Universiti Malaysia Sabah (UMS), National Universiti of Malaysia (UKM), University of Philippines Diliman (The Philippines), National Astronomical Research Institute of Thailand (Thailand), Universitas Palangka Raya (Indonesia), Institute Teknologi Bandung (Indonesia), King Mongkut's Institute of Technology Ladkrabang (Thailand), National Central University of Taiwan (Taiwan) throughout the project are highly appreciated. Positive suggestions and perceptive criticism have kept this project in a much better way and more meaningful. As a project leader, working under different times, spaces and situations was an extremely knowledgeable experience. I would also like to give my

sincere gratitude to the APN staff dealing with this project, and Universiti Malaysia Sabah for providing me to lead this project till the end of this project.

1 Introduction

The Southeast Asian region was identified by IPCC (2007) as one of the most vulnerable regions due to climate change and its already posing a physical risk to the people, as it only getting worse. Without proper adaptation and commitment for mitigation for further decarbonization, the society and economies of SEA people will become increasingly vulnerable to climate change impact. What's more, this region has also one of the highest rates of landcover changes through deforestation and conversion into large oil palm plantations. Recent studies have shown that by magnitude, oil palm trees have the potential to emit biogenic emission larger than the tropical evergreen forest, particularly isoprene, which is playing important role in atmospheric chemistry that eventually affect ozone formation since it is a greenhouse gas as well as a secondary pollutant.

Climate change and air pollution are like "two sides of the same coin". Climate change and air pollution issues converge in the increasing background concentrations of ozone, which the ozone itself is the third most important greenhouse gas (IPCC, 2013) and a pollutant that brings adverse effects on human health, crop, and natural ecosystem (Leung and Gutherson, 2005). Other atmospheric pollutants such as atmospheric aerosols have received increasing attention in the region, simply because of their role not only as a pollutant but also significantly affect the radiation balance of the atmosphere. Climate change on the other hand may cause feedback in terms of changes in emission (increase biogenic emission, which is greatly dependent on temperature) and emissions patterns (affect the frequency and intensity of forest fires).

Several studies have shown that climate change has a significant impact on future air quality notably surface ozone and secondary aerosol (Sentian et al, 2015; Forkel and Knoche, 2006; Murazaki and Hess, 2006). Using the previous SRES A2 emission scenario of the IPCC into the high resolution (45 km) regional climate model PRECIS, and employing a simple box model (CiTTyCAT) for the air quality simulation, the increase of surface temperature is responsible for the increase of surface ozone in Malaysian urban areas and the decrease in rural areas both during the wet season (winter monsoon) and dry season (summer monsoon) (Sentian et al., 2015). On a global scale, several recent investigations have found large variability of ozone responses to climate change. The surface ozone simulation by GCM-CTM coupled model using the new RCPs scenarios has shown that the global surface ozone concentration would increase under the RCP 8.5 scenario, and decrease under RCP 2.6, RCP 4.5, and RCP 6.0 scenarios at the end of this century (Lamarque et al., 2011; Cionni et al., 2011; Kawase et al., 2011; Gao et al., 2013; Young et al., 2013; Kim et al., 2015).

Increased surface temperature due to climate change also was responsible for the increase of biogenic emissions (i.e isoprene and monoterpene) (He et al., 2016). Sentian et al. (2011) has observed an

increase in isoprene emission due to climate change in Southeast Asia. Similar responses were also observed in other investigations (see Chatani et al., 2015; Zare et al., 2014; Pyle et al., 2011; Zhang et al., 2008). Ozone and secondary aerosol formation in the atmosphere are sensitive to biogenically emitted volatile organic compounds (BVOC emissions) which are strongly dependent on weather and land cover changes (see more in; Geddes et al., 2016; Kim et al., 2014; Jacob & Winner, 2009; Guenther et al., 2006). An increase in future surface temperature was found to be responsible for the increase of isoprene and monoterpene emissions, thus causing the average surface ozone to increase (Penrod et al., 2014; Dawson et al., 2009).

In the northern hemisphere, the biogenic emission can contribute to the increment of surface ozone between 4-30 ppbv (Zara et al., 2014). The increase of biogenic emission was also observed to cause the particulate matter to increase by up to 15% over the United States and suggested that about 90% of particulate (PM2.5) reduction in the future was contributed by the biogenic emission reduction, and the climate penalty only caused around 10% (Lam et al., 2011). A combined effect of climate change and biogenic emission on the increase of atmospheric secondary aerosol formation was also observed in several investigations (see Chatani et al., 2015; Lam et al., 2011). Thus, BVOCs emissions inventories are a very important database when exploring surface ozone and particulate matter as pollutants and at the same time support the establishment of appropriate regulatory control strategies for air pollution (e.g., Chatani et al., 2015). However, BVOC emissions inventories were poorly developed in Southeast Asia (Woo & Kim, 2015).

The multifaceted impact of climate change on biogenic emissions as well as the combined impact of climate forcing and biogenic forcing on the regional air quality, particularly surface ozone and secondary aerosol is relatively unexplored in the Southeast Asia region. This region is one of the most vulnerable regions in the world due to climate change (IPCC, 2007) and also one of the largest contributors to the biogenic emission mainly from the rainforest and huge area of oil palm plantation (Mitszal et al., 2010). A rapid change in landcover mainly due to agricultural expansion such as oil palm plantation is equally important as this will affect the spatial distribution of biogenic emission, which is important in ozone chemistry. An increase in biogenic emissions from sources that are associated with the conversion of forest into oil palm and other land uses was found to be significant over Southeast Asia (Pyle et al., 2011; Skiba et al., 2012; Sentian et al., 2011). Therefore, the future status of regional air quality will not be only associated with the increase of surface temperature due to climate change, increase in biogenic emissions, and increase kinetic reaction in the atmospheric chemistry reaction but also affected by emissions from biomass burning and other anthropogenic sources.

In USA, the surface concentration of particulates (PM2.5) decreased over most of the domain area by up to 40% due to surface warming (Zhang et al., 2008). Other factors that contributed to this observation were the decrease in gaseous precursors, primary particulate emission, and an increase in

precipitation in winter (Penrod et al., 2014). Biomass burning and anthropogenic emissions from transportation activities are the main sources of ozone precursors in atmospheric chemistry reactions in the region, which are relatively stronger effects than the climate change on ozone-aerosol production (Wang et al., 2013). High aerosols region of Southeast Asia that is triggered by biomass burning results in low UV radiation, the low photochemical activity causing low ozone production (Deng et al. 2008). Lin et al. (2013) and Cristofanelli et al. (2013). suggested that biomass burning could enhance ozone production, which is probably due to the local meteorological condition and photochemistry.

The quest for much higher resolution of climate change, improved biomass, and biogenic emission inventories, and high temporal and spatial resolution of air quality model is crucial and a necessity for the improvement of understanding on the individual and combined impact of climate change, biomass, and biogenic emissions to the regional air quality. Therefore, the objectives of this project are:

1. To develop and assess climate change for Southeast Asia based on multi-climate RCPs scenarios
2. To develop biomass burning emission inventory for Southeast Asia
3. To develop and assess biogenic emission for Southeast Asia under multi-climate RCPs scenarios
4. To simulate and assess the regional air quality (surface ozone and other pollutants) under the influence of climate change, biomass burning emission, and biogenic emission

Understanding the future climate impacts on air quality and its feedbacks on exposure and vulnerability of future human health is crucial particularly in the Southeast Asia region, where its economic activities are highly dependent on natural resources utilisation, large conversion of forest into other agriculture and frequently experiencing extreme trans-boundary air pollution. The development of multi-climate change scenarios for Southeast Asia provides a platform to employ high resolutions climate change output as a driver for the projection of future regional biogenic emissions and air quality. The outcomes of this project will provide a better insight for the policymakers in reviewing, strengthening, and formulating relevant policy on a wide range of issues that link to a climate-air quality relationship. The most notable one would be related to greenhouse gases emissions and climate change; biogenic emissions and landcover changes; biomass burning emissions and forests; and air quality and health.

A policy that jointly addresses climate change and sustainability in the region is highly sought and more effective when consistently embedded within broader designed strategies for sustainable development. This is particularly true as the impact of climate variability and change made complicated by the socio-economic development in the region affects the ability of countries to achieve sustainable goals. The consequence outcome policies from this project that encompass various issues can be translated into strategy and action plans, and eventually on specific programmes and activities. To support the country's sustainable goals, formulated strategies and action plans need to be implemented and

monitored efficiently, alongside actions in mainstreaming mitigations and adaptations of climate change impacts into their local planning and policy development process.

Apart from the respective country's policy, this project undoubtedly contributes significantly to the national and regional scientific capacity development in the areas of developing regional high-resolution climate scenarios; developing and improving regional biomass burning and biogenic emissions inventories; and simulating regional air quality under climate and biogenic emissions scenarios. Active participation of each collaborative country at various levels of planning, execution, analysis, and interpretation will provide direct opportunities for enhancing national/regional scientific capacity development. In addition, there are opportunities for other young scientists from the collaborative countries to be involved in the project implementation and discussion of the project outcomes through a series of workshops and a conference. This project is in line with the IPCC programme, which is emphasising communicating information to the global community and supporting the implementation of the WCRP Strategic Framework. The outcome of this project will be eventually shared with WRCP global secretariat via WCRP's Earth System Grid Federation (ESGF) and other initiatives such as PROVIA (Programme of Research on Climate Change Vulnerability, Impacts, and Adaptation).

2 Methodology

2.1 Regional Climate Modelling

2.1.1 Climate Model Description: Weather Research and Forecasting (WRF) Model

The Weather Research Forecast (WRF) is a specific computer program that can be used in either in weather forecast or climatic research purpose. The model is developed under collaborative effort including National Centre of Environmental Prediction (NOAA/NCEP), the NOAA earth Systems Research Laboratory Global Systems Division (NOAA/ESRL/GSD), National Center for Atmospheric Research (NCAR), Mesoscale Microscale Meteorology Division (MMM), the Department of Defense's Air Force Weather Agency (AFWA), the Federal Aviation Administration (FAA), and also a number of institute and university in United States (Dodla et al., 2011). The WRF model is the state-of-science mesoscale model framework.

There are two types of WRF which divided according to the two different dynamics cores such as Non-hydrostatic Mesoscale Model (NMM) and Advanced Research Model (ARW) (NCAR, 2006; NOAA, 2007). NMM is developed under support of NCEP while ARW is developed by NCAR (Skamarock et al., 2008). In this project, ARW was used as it is created to be flexible and state of art atmospheric model. The WRF-ARW with scales ranging from meters to thousands of kilometres can be used in several applications such as idealized simulations, regional and global applications, parameterization research, data assimilation research, real-time NWP, forecast research, coupled-model

applications, hurricane research and teaching purpose (WRF-ARW, 2012). The WRF-ARW was developed based on few components as shown in Figure 2.1.1. The modelling system component including Advanced Research WRF (ARW) dynamic solver, WRF Pre-processing System (WPS) and also WRF Data Assimilation (WRF-DA) system.

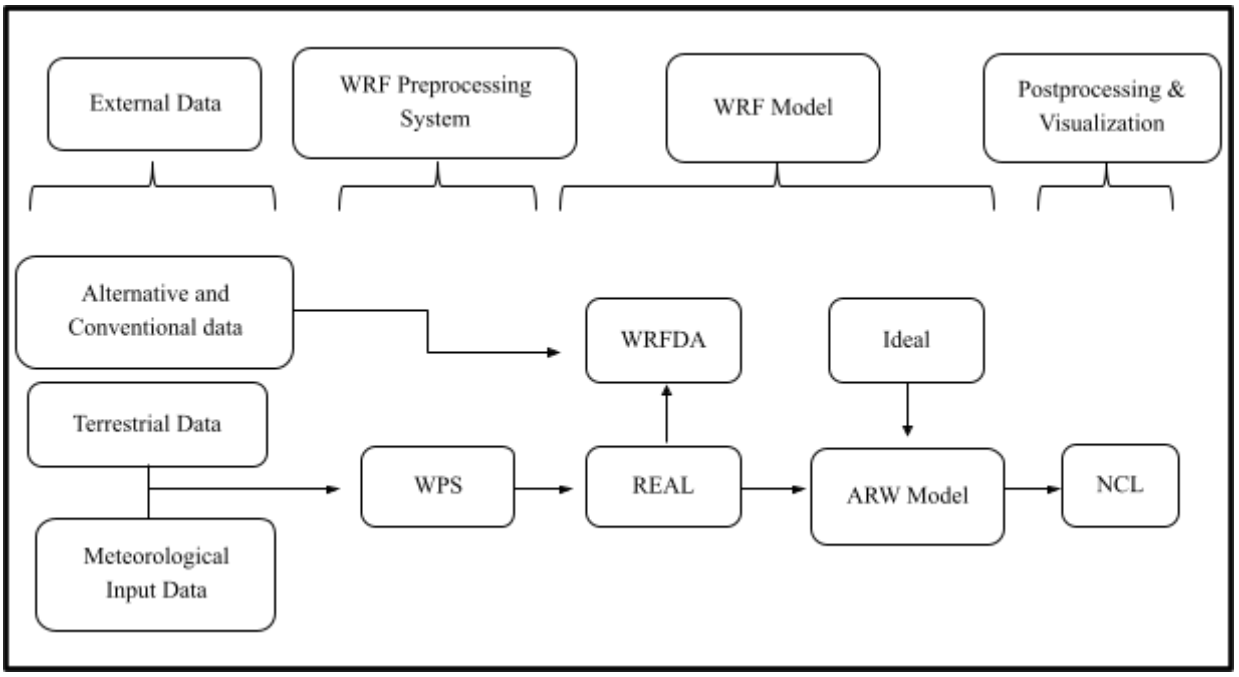

Figure 2.1.1: Framework of the WRF-ARW modelling system. ARW consists of four major programs such as WPS, WRF-DA, ARW solver and post-processing and visualization.

2.1.2 Data Input

There are two types of input data: static terrestrial data database and time dependent meteorological fields. Both data can be downloaded in WRF Official Website and it is stored in grid binary format GRIB. The model required initial, lateral and boundary conditions data as input data. WRF Pre-processing System contain geogrid program which function as defining model domains and interpolates static geographical data to grids (Figure 2.1.2). Besides, the GRIB files that contain meteorological data which read by a program called “ungrid” to identify the variables and level in GRIB files. Then, the intermediate data file of meteorology field is interpolated onto simulation domain produced by geogrid program. The metgrid output then becomes real program for WRF model and it is converted into NetCDF format.

2.1.3 Model Setup and Experimental Design

One-way nesting WRF model was used in this study, where the simulations were carried out in one nested horizontal domain (Figure 2.1.3). The domain covered the whole Southeast Asia region with 30 km

resolution. Table 2.1.1 shows the summary of model setup and all the selected option features. The year of 2013 was selected as the base year of the present-day simulation, and the future projections are in the year of 2030, 2050, 2070 and 2100. The projection for January (to represent winter monsoon) was selected between 0000 UTC 31 December and ended at 0000 UTC 01 February for both present-day and future projections (2013, 2030, 2050, 2070, 2100). Meanwhile, the simulations for July (to represent summer monsoon) were run from 0000 UTC 31 June and ended at 0000 UTC 01 August for both present-day and future projection.

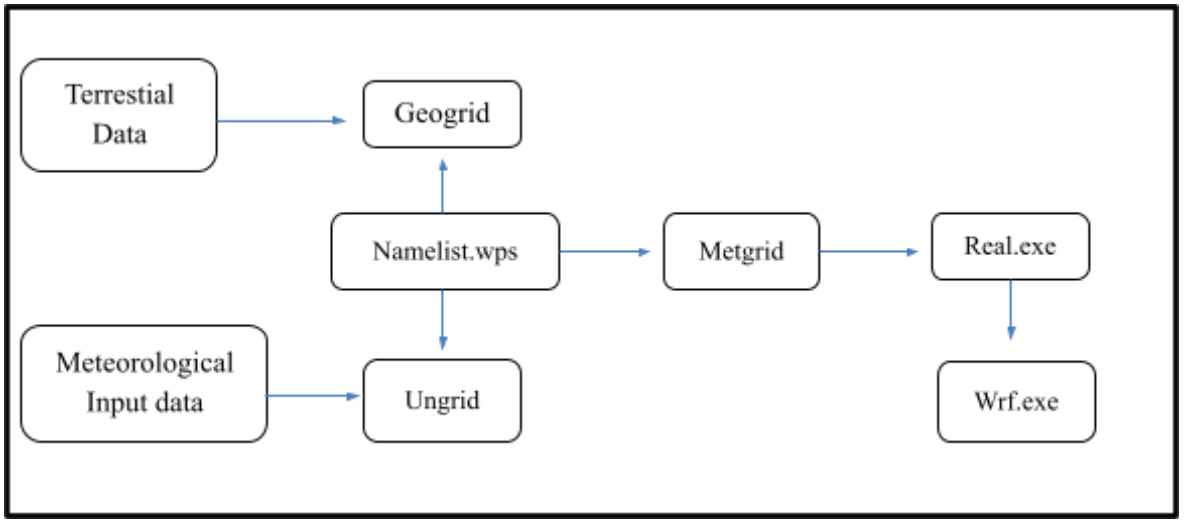

Figure 2.1.2: Framework of WRF Pre-processing System (WPS), which consists of three major programs such as geogrid, ungird and metgrid.

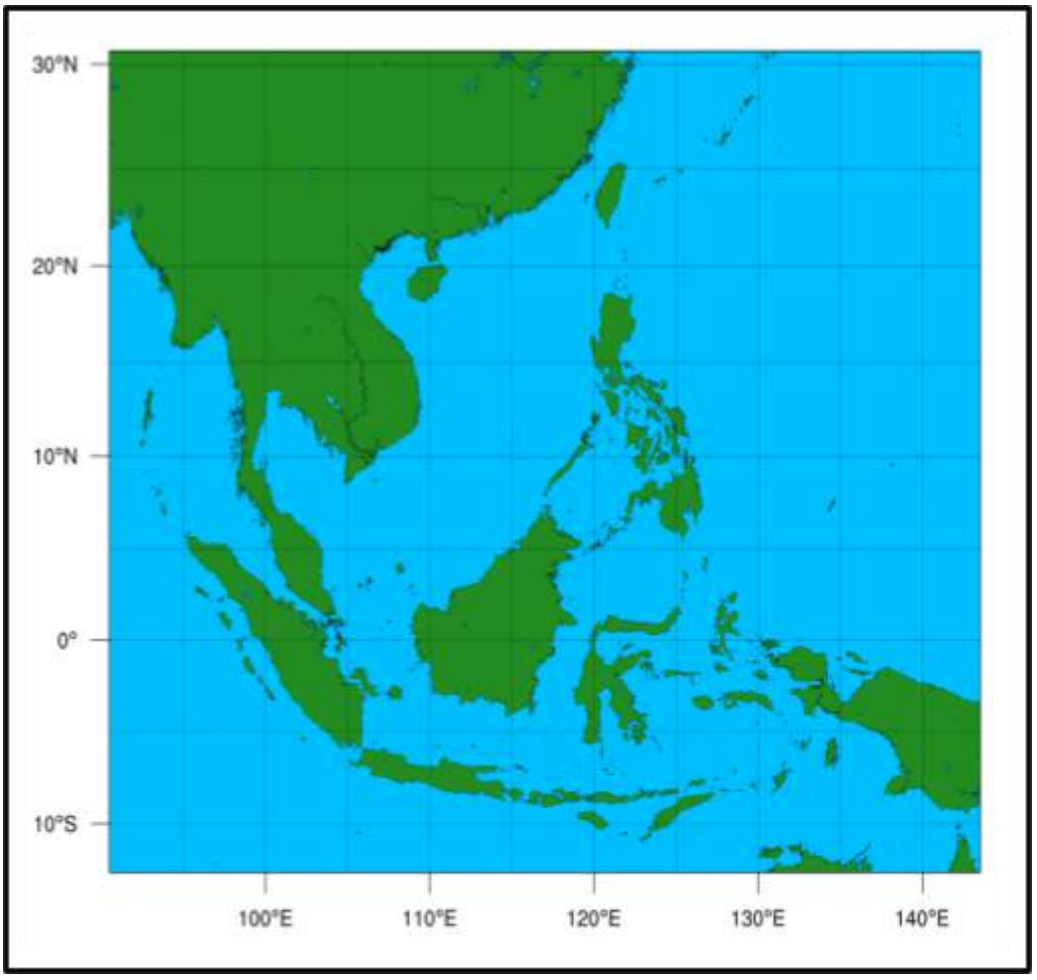

Figure 2.1.3: Research domain (Southeast Asia) for the climate change modelling

Table 2.1.1: Summary of the model setup and features used in the model.

Model Setup	**Option**
Map projection	Lambert
Temporal resolution	1 hours
Spatial resolution	30 km
Vertical levels	27
Dynamic core	ARW
Surface layer scheme	Revised MM5 Monin-Obukhov Scheme
Land surface scheme	Noah Land Surface Model (LSM)
Microphysics parameterizations	Thompson Aerosol-Aware Scheme (initialized by 2001-2007 GOCART Climatology)
Long wave radiation physics	Rapid Radiative Transfer Model (RRTM)
Short wave radiation physics	Dudhia Shortwave Scheme
Boundary layer	Mellor-Yamada-Janjic Scheme
Urban surface	3-category Urban Canopy Model (roofs, walls and streets)

2.1.4 Climate Scenarios

Previous regional climate model research used A1, A2, B1and B2 scenarios (IPCC, 2007). Nowadays, the Intergovernmental on Climate Change Fifth Assessment (IPCC, 2013) has developed new scenarios, the Representative Concentration Pathways (RCP) scenarios is in the support of Coupled Model Intercomparison Experiment Phase 5 (CIMP5) (Taylor et al., 2012). The new developed scenarios provided a more comprehensive of external forcing, more types of scenarios and higher resolution compared to CMIP3 from IPCC AR4 (Knutti and Sedlacek, 2013).

The Representative Concentration Pathways (RCPs) database aims at documenting the emissions, concentrations, and land-cover change projections. It is based on the selected scenarios which are from four modelling teams/models (NIES/AIM, IIASA/MESSAGE, PNNL/MiniCAM, and PBL/IMAGE) (Van vuuren et al., 2011a). The RCPs are meant to serve as input for climate and atmospheric chemistry modelling as part of the preparatory phase for the development of new scenarios for the IPCC's Fifth Assessment Report and beyond. The four RCPs reflect the range of year 2100 greenhouse gas radiative

forcing values from 2.6 to 8.5 W m22 (Nazarenko et al., 2015) (Table 2.2). The lowest forcing level scenario RCP2.6 (Van Vuuren et al., 2011b), two median range or stabilization scenarios RCP4.5 (Thomson et al., 2011) and RCP6.0 (Masui et al., 2011), and the high-end or business as-usual scenario RCP8.5 (Riahi et al., 2011).

For the climate change assessment, the present day (2013) and future (2030, 2050, 2070, 2100) simulation scenarios are analysed, and present based on Representative Concentration Pathways (RCPs) emission scenarios of RCP4.5, RCP6.0 and RCP8.5. The future scenario of RCP4.5 is a low-to-moderate emission scenario, where the greenhouse gases (GHGs) radioactive forcing will reach 4.5 Wm^{-2} by the year 2100 (Thomson et al., 2011). It represents a scenario where variety of adaptive policy has applied to limit the radiative forcing. Besides, medium range RCP6.0 will be stabilizing without overshoot pathway to 6 W/m2 at stabilization after 2100 (Hijioka et al., 2008). While RCP8.5 indicates a high emission scenario with GHGs radiative forcing that will reach 8.5 Wm by year 2100 (Riahi et al., 2011).

Table 2.1.2 Representative Concentration Pathway Descriptions (Source: IPCC, 2017)

RCP	Description	IA Model	Publication (IA Model)
RCP2.6	Peak in radiative forcing at ~ 3 W/m2 before 2100 and decline	IMAGE	• van Vuuren et al. (2006; 2007)
RCP4.5	Stabilization without overshoot pathway to 4.5 W/m2 at stabilization after 2100	GCAM (MiniCAM)	• Smith and Wigley (2006) • Clarke et al. (2007) • Wise et al. (2009)
RCP6.0	Stabilization without overshoot pathway to 6 W/m2 at stabilization after 2100	AIM	• Fujino et al. (2006) • Hijioka et al. (2008)
RCP8.5	Rising radiative forcing pathway leading to 8.5 W/m2 in 2100.	MESSAGE	• Riahi et al. (2007) • Rao and Riahi (2006)

2.1.5 Climate Model Input Dataset

The present study applied two types of time dependent meteorological fields as initial and boundary condition for WRF model, namely NCEP FNL (Final) Operational Global Analysis data and NCAR's Community Earth System Model. Both datasets used the same model setup and design to isolate the effect physical scheme of the model itself. The time series and domain setup were also remaining the same for both simulations. Meanwhile, one type of observation dataset was applied for the purpose of model evaluation and assessment.

NCEP FNL (Final) Operational Global Analysis data which obtained from the Global Data Assimilation System (GDAS) was one of the lateral boundary conditions that used in this study. Global

Telecommunications System (GTS) and few sources continuously provides observational data to GDAS. The dataset is in gridded format with 1-degree resolution grids and updated every six hours. The NCEP data consists of surface information with 26 mandatory levels (1000 millibars – 10 millibars) of surface boundary level. The meteorological parameters included temperature, sea surface temperature, sea level pressure, geopotential height, relative humidity, ice cover, vertical motion, vorticity, ozone, u and v winds. The continuous time series is updated and extended to a close-present date (NCEP, 2015).

The operational analyses from global bias corrected climate model output files (version 1) of NCAR's Community Earth System Model (CESM) (Hurrell et al., 2013) were used as initial and boundary conditions for WRF model simulation. The spatial resolution of the data was 1 degree resolution grid. Meanwhile, the temporal resolution was 6 hours of time-step, with the sequence of 00, 06,12, 18 UTC. The simulation of meteorological parameters was generated using Bias-corrected Community Earth System Model (CESM) version 1 as initial and boundary conditions (Gent et al., 2011; Hurrell et al., 2013). CESM is the coupled global climate model that constructed by four component model such as atmosphere, land use, sea-ice and ocean. In the support of Coupled Model Intercomparison Experiment Phase 5 (CMIP5) (Taylor et al., 2012) and the Intergovernmental on Climate Change Fifth Assessment Report (IPCC, 2013), the CESM simulations were utilized to produce present-day dataset.

2.1.6 Climate Model Evaluation and Assessment

Dynamical downscaling by RCMs from GCMs is being apply by most of the climate change research. This is due to the inconsistency that embedded within the GCMs (IPCC, 2001). Moreover, the error of GCMs with large scale resolution can be transmitted to the RCM (Noguer et al., 1998). As a result, the validation or evaluation process is necessary for RCM, downscaled from GCMs before using it for the climate projection. The model evaluation was statistically performed between WRF climate model and Reanalysis datasets (WRF_NCEP). This project used statistical measures of FB (Fractional Bias), NMSE (Normalised Mean Square Error), and Fa2 (Factor of 2) (Ojha and Kumar, 2010), and NMB (Normalised Mean Bias) (Penrod et al., 2011; Chung et al., 2011) for the model evaluation.

When the value of bias less than zero, the model is underestimated the mean, while if the bias more than zero, the model is overestimated the mean. The Fa2 statistical analysis method lies between +2 and -2 and has a value of zero for and ideal model. Mean Square Error (MSE) was used to estimate the typical difference between observations and the model predictions. The value of zero gives a perfect forecast. Root Mean Square Error (RMSE) is the variant of MSE. It means the expected error of simulations. While Normalised Mean Square Error (NMSE) is another variance. It is used to compare the relative efficiency between on observations and simulation. The Factor of two (Fa2) is a method presented in percentage and the predictions with a factor of two of the observed values.

$$\text{Normalized Mean Bias (NMB)} = \sum_{1}^{N}(Sim - Obs)/\sum_{1}^{N}(Obs)\times 100\% \quad \text{(Eq 2.1.1)}$$

$$\text{Fractional Bias (FB)} = 2\times\left(\frac{\sum_{1}^{N}(Sim-Obs)}{\sum_{1}^{N}(Sim+Obs)}\right) \quad \text{(Eq 2.1.2)}$$

$$\text{Normalised Mean Square Error (NMSE)} = \frac{\sum_{i=1}^{n}\left(O_i-P_i\right)^2}{\sum_{i=1}^{n}(O_iP_i)} \quad \text{(Eq 2.1.3)}$$

Factor of Two (Fa2) = Fraction of data which $0.5 \leq P/O \leq +2.0$

(Eq 2.1.4)

2.2 Biomass Burning Emission Inventory in Southeast Asia

2.2.1 Study Areas

For the investigation of biomass burning emission in Southeast Asia, due to distinctive landcover type, as well as the climatological conditions, the region was divided into two sub-regions namely north ASEAN (Mynamar, Thailand, Cambodia, Laos and Vietnam) and south ASEAN (Malaysia, Indonesia, Brunei and Timor Leste). The physical geography of mainland northern ASEAN spreads interchangeably, which includes forests, mountains, valleys, rivers, deltas and coastlines, but is mainly mountainous. Stretching from Tibetan plateau, Himalayan foothills give very distinct geography to northern ASEAN from the rest of the places in continental Asia (Frederick and Leinbach, 2018). Southeast Asia is influenced by two tropical monsoons namely southwest monsoon (May-September) and northeast monsoon (October-March). In general, vegetation in Southeast Asia is classified into tropical rainforest or tropical evergreen rainforest, which can be grouped into wet evergreen forest, semi-evergreen forest, freshwater swamp forest and evergreen montane forests. However, though under the same classification, there are forests with very distinctive characteristics between these two sub-regions.

2.2.2 Research Framework and Approach

The general flow for the research on biomass burning emission for SEA is illustrated in Figure 2.2.1. Remote sensing and Geographical Information System (GIS) were mainly applied in this research to generate maps and to collect relevant data on burned mass of biomass and land cover type. The data was discussed by each country. Pollutants included in this study are CO_2, CO, CH_4, NO_x, PM, NMVOC, SO_2, NH_3 and carbonaceous aerosols which are major precursors of air pollution from biomass burning. A map of land cover across Southeast Asia (two sub-regions) was first produced using GIS system and was digitized using ArcGIS into raster data for overlaying of maps later.

Moderate Resolution Image Spectroradiometer (MODIS) was then used to obtain land cover data (MCD12Q1) and burned area (MCD64A1). MODIS provides twice-daily image frequency and has surface reflectance correction applied to land (Mccullough et al., 2013), which is sufficient to provide data needed for this study, in accordance with the performance of available processing tools. The processes involved in producing inventory are processing activity data and related parameters, determination of emission factors (EF), decision on spatial and temporal distribution and speciation of $PM_{2.5}$ and NMVOCs. In this study, only open burning of biomass was included, involving both anthropogenic and natural sources, but not domestic burning.

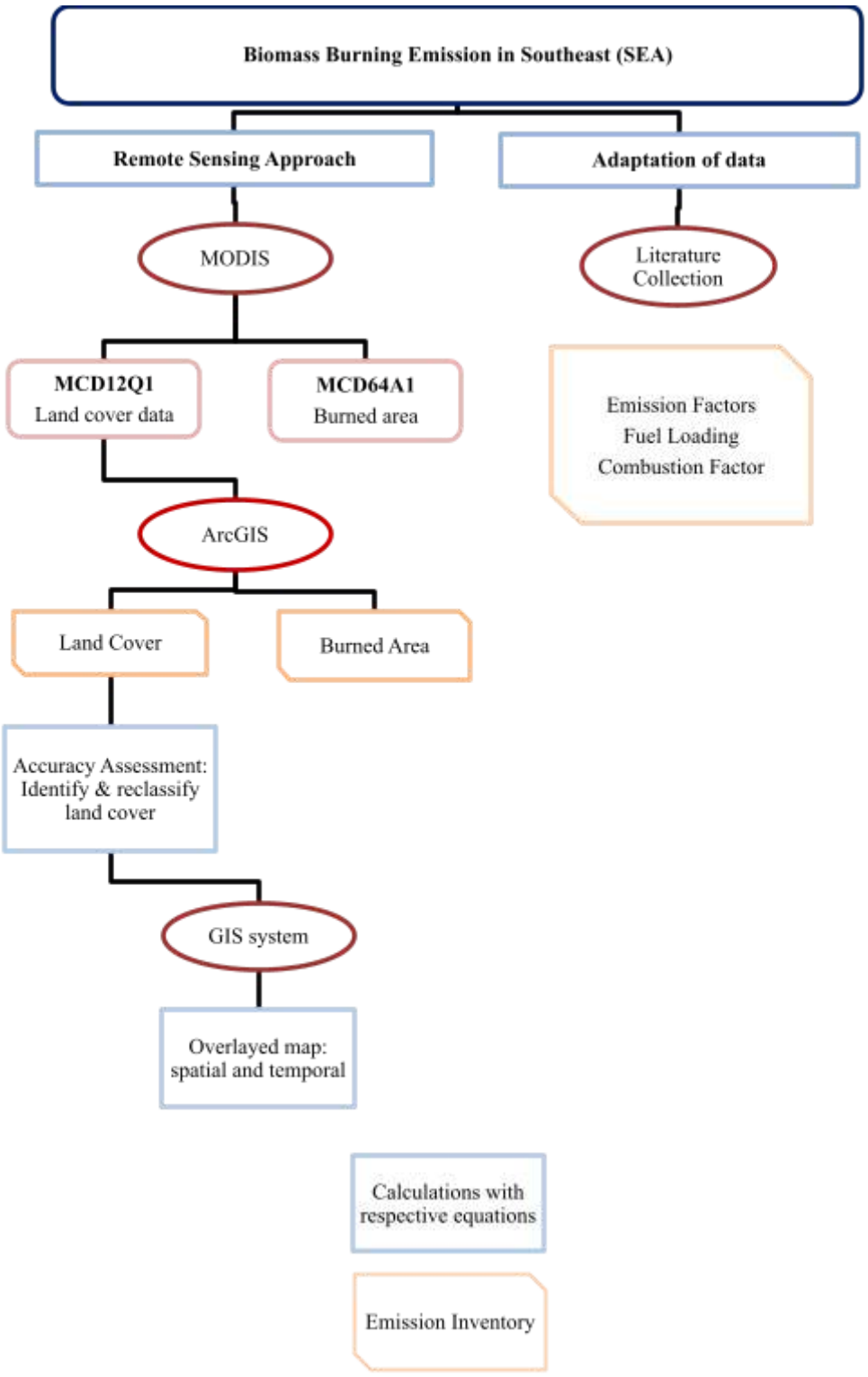

Figure 2.2.1: Framework of Biomass Burning Emission Inventory in SEA

2.2.3 Land Cover of SEA

Land cover data is important in this study in order to detect and determine burned area sources. The process of data collection is based on the procedure by (Sulla-Menashe and Friedl, 2018). Data in MCD12Q1 are of spatial resolution of 500m x 500m, which were then digitized into raster data of 25m x 25m using ArcGIS. Meanwhile, land cover classification is essential to identify the bio-physical characteristics of land cover, which vegetation index and biomass are useful in this study (Lam, 2008). In this study, IGBP was used as it provides highest quality of remote-sensing data as compared to other primary global land cover databases (Thenkabail, 2018). MCD12Q1, which is a product of MODIS, combines the Aqua and Terra supervised classification data providing a high-quality global land data (Friedl and Sulla-Menashe, 2019). In MCD12Q1 legacy classification of IGBP, there are 17 types of land cover, however, since different regions have different land cover type, therefore reclassification of land cover is required, adapting from the actual 17 classes, while considering the eligibility in describing the land cover to prevent misclassification of land. The reclassification of IGBP land classes for the suitability of SEA is shown in Table 2.2.1.

2.2.4 Accuracy Assessment

Classification of land cover is an important part in emission inventory, and although ground truthing can be done in field, it will be very time consuming and less cost efficient. Therefore, ground truth data is often obtained from interpretation of existing high-resolution data. However, thematic mapping often contain difference, and which affects the accuracy and precision of map, causing them less reliable (Foody, 2002). Accuracy assessment is an important part in classification studies, which compares data of classified image with another source which is believed to be ground truth data to determine the classification errors as well as to ensure the reliability of data. In this study, considering the two sub-regions of SEA, a few hundred points were randomly selected using stratified random sampling method which can be done using ArcGIS tools. The accuracy assessment flow for this study is shown in Figure 2.2.2. There are three types of sampling methods, which are random, stratified random and equalized stratified random (Table 2.2.2).

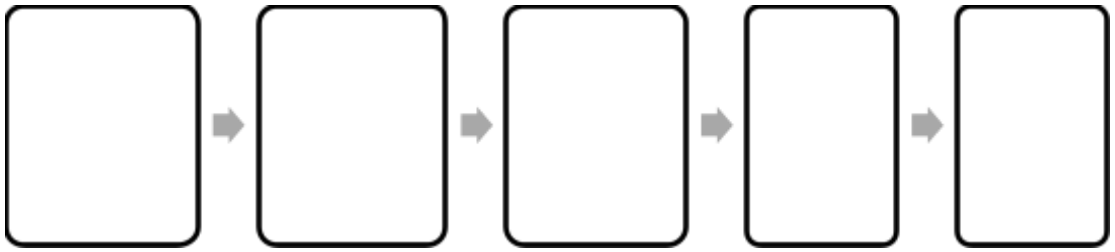

Figure 2.2.2 Accuracy Assessment Flow

Table 2.2.1 Reclassification of IGBP Legends and Land Classes

Class	Land Cover	Value	Description
Evergreen Forests	Evergreen Needleleaf Forests	1	Dominated by evergreen conifer trees (canopy >2m). Tree cover >60%.
	Evergreen Broadleaf Forests	2	Dominated by evergreen broadleaf and palmate trees (canopy >2m). Tree cover >60%.
Deciduous Forests	Deciduous Needleleaf Forests	3	Dominated by deciduous needleleaf (larch) trees (canopy >2m). Tree cover >60%.
	Deciduous Broadleaf Forests	4	Dominated by deciduous broadleaf trees (canopy >2m). Tree cover >60%.
Mixed Forests	-	5	Dominated by neither deciduous nor evergreen (40-60% of each) tree type (canopy >2m). Tree cover >60%
Shrublands	Closed Shrublands	6	Dominated by woody perennials (1-2m height) >60% cover
	Open Shrublands	7	Dominated by woody perennials (1-2m height) 10-60% cover.
	Woody Savannas	8	Tree cover 30-60% (canopy >2m).
Savannas	Savannas	9	Tree cover 10-30% (canopy >2m).
	Grasslands	10	Dominated by herbaceous annuals (<2m).
Wetlands	Permanent Wetlands	11	Permanently inundated lands with 30-60% water cover and >10% vegetated cover.
Croplands	Croplands	12	At least 60% of area is cultivated cropland.
	Cropland/Natural Vegetation Mosaics	14	Mosaics of small-scale cultivation 40-60% with natural tree, shrub, or herbaceous vegetation.
Others	Urban/Built-up Lands	13	At least 30% impervious surface area including building materials, asphalt, and vehicles.
	Barren	16	At least 60% of area is non-vegetated barren (sand, rock, soil) areas with less than 10% vegetation.
	Water Bodies	17	At least 60% of area is covered by permanent water bodies.
	Unclassified	255	Has not received a map label because of missing inputs.

Source: (Sulla-Menashe and Friedl, 2018)

Table 2.2.2 Accuracy Assessment Points with Different Sampling Methods

Sampling Methods	Accuracy Assessment Points
Random	Points are distributed randomly across whole input dataset.
Stratified random	Number of points selected are proportional to the area of each class.
Equalized stratified random	Number of points selected are equal in each land class.

Source: (Esri, 2019)

In selection of accuracy assessment points however, due to coarse spatial resolution and large number of mixed pixels, selection of pixels can be challenging (Lin et al., 2019). The process of determining accuracy level of classified and misclassified land cover, classification of land cover was done by per pixel approach. For the process of accuracy assessment, 408 points (for each sub-region region) were chosen using stratified random method from user's classified data and was compared with ground truth data. Stratified random sampling points created in ArcGIS were imported into Google Earth Pro, and the land cover type can be observed point by point in Google Earth Pro. An attribute table with

user's classified data and ground truth data of land cover types was produced, and a confusion matrix was created from the accuracy assessment table.

Confusion matrix is a table which shows true classes of land in column and classified land in row (Congalton, 2008; Esri, 2019). The accuracy was determined from this matrix, which shows proportions of true and error classifications. The diagonal matrix shows correctly classified pixels, and the remaining matrix shows the wrongly classified pixels. The overall accuracy of land classification was then calculated with Kappa coefficient, which is the result of accuracy assessment. The misclassified pixels were then validated using Google Earth Pro which has high resolution data as ground truthing reference. Kappa analysis was first brought into remote sensing accuracy assessment in 1981, and has then become a standard (Congalton, 2008). The proportions are shown in Kappa's coefficient, which will then imply the reliability of land data (Table 2.2.3).

Table 2.2.3 Interpretation of Kappa's Value

Kappa's value	Reliability of Land Cover
0.0	None
0.01-0.20	Minimal
0.21-0.40	Weak
0.41-0.60	Moderate
0.61-0.80	Strong
0.8-1.0	Almost perfect

Source: (McHugh, 2012)

2.2.5 Biomass Burning Emission Inventory Calculation

In this study of biomass burning emission inventory, only open burning from both natural and anthropogenic sources were taken into consideration, domestic burning was not included. To produce emission inventory, MODIS MCD64A1 was utilized in mapping the burned area as it was improved to be able to detect small fires of all regions better, which has been used in various research and is a main source of datasets in Global Fire Emissions Database (Giglio et al., 2018). MCD64A1 provides data in 500 x 500m^2 grids that has burned area in per pixel data (Yin et al., 2019). Temporal resolution chosen is throughout year 2013, and spatial resolution is 500m x 500m. A bottom-up approach was used to develop the emission inventory which processes data from smaller information, progressing upwards, as this method is able to provide more accurate reflection of the local conditions (Nicholls et al., 2015). For the calculation of concentration of pollutants emitted, annual amount of dry biomass burned (A) and Emission factor (EF) were determined beforehand (Zhou et al., 2017). The calculation of biomass burning emission (E_i) was then calculated with Eq. 2.2.1 extracted from (Zhou et al., 2017).

$$E_i = \Sigma (A_j \times EF_{i,j})/1000 \quad \text{(Eq 2.2.1)}$$

Where,

E: annual typical pollutant emission (Mg/year)

i: type of pollutant

j: biomass burning source

A: annual amount of dry biomass burned (Mg/year)

EF: Emission factor (g/kg)

2.2.5.1 Annual amount of dry biomass burned (A)

To calculate the estimated biomass burning emission, the activity data (magnitude of anthropogenic activities affecting burned area and biomass burned) has to be determined. In this study, the main activity data was focused on forest and grassland. The annual amount of biomass burned (A) is affected by burned area, fuel loading, combustion factor and land cover type. The equation for calculation of (A) was done using Eq. 2.2.2 retrieved from (Zhou et al, 2017).

$$A = [\Sigma (BA_{x,j} \times FL_{x,j} \times CF_j)] \times 10^{-6} \quad \text{(Eq.2.2.2)}$$

Where,

j: land cover type

x: location

$BA_{x,j}$: burned area (m^2 /year) of land cover type j at x

$FL_{x,j}$: fuel loading of land cover type j at x (g/m^2)

CF_j: combustion factor of land cover type j

There are two methods in obtaining estimation of burned area (BA), which are burn scar approach and active fire method. Burn scar area approach was used in this study as it is more efficient in estimating total emission from biomass burning but it is less detail in terms of temporal data (Yue, 2016). Burn scar approach estimates burned area by comparing the before and after changes of land surface caused by fire, which was done by comparing data obtained from MODIS, specifically MCD64A1 which was retrieved from (MCD64A1: https://earthdata.nasa.gov). For fuel loading (FL), the value of each land class was extracted as follow (Table 2.2.4)

Table 2.2.4 Fuel Loading (FL) of Respective Land Cover

Land Cover	**Fuel Loading (g/m^2)**
Forests	7184.80[a]
Shrublands	2196.16[a]
Savannas	133.87[a]
Wetlands	1100[b]
Croplands	60[b]

Source: [a](Michel, 2005); [b](Song et al., 2009)

On the other hand, combustion factor (CF), or burning efficiency is the ratio of available fuel which is exposed to the fire and the part where the fuel is burned (Table 2.2.5). The CF obtained for each land cover are forests 0.25, closed shrublands 0.50, open shrublands 0.85, woody savannas 0.40, savannas 0.95, wetlands 0.30, and croplands 0.6 (Michel, 2005; Song et al., 2009). Since closed shrublands, open shrublands and woody savanna are classified under one land class, the mean of the CF was derived through calculation $\bar{x} = \frac{\Sigma fx}{n}$, where $\bar{x}$ is the mean CF, f is the number of pixels of each class and x is the CF obtained from literature collection.

Table 2.2.5 Combustion Factor (CF) of Respective Land Cover

Land Cover	Combustion Factor
Forests	0.25[a]
Shrublands	0.40[a]
Savannas	0.95[a]
Wetlands	0.30[b]
Croplands	0.60[b]

Source: [a](Michel, 2005); [b](Song et al., 2009)

2.2.5.2 Emission Factor (EF)

Emission factor represents the amount of pollutant released per kilogram of biomass burning (Akagi et al., 2011). EF is expressed in g/kg, which comes from the mass of pollutant divided by the mass of biomass burned. According to Amaral et al. (2016), the value of EF was obtained from the average of all adequate data. The value of EF varies with types of land cover or biomass sources as well as species of pollutant. Therefore, to ensure accuracy of estimated emission, appropriate EF for respective pollutants is essential. Selection of EF considered of the types and sources of biomass, which values were obtained from literature and was averaged. In this study, EF values as shown in Table 2.2.6 are derived from several literature collections.

Table 2.2.6 Emission Factors (g/kg) from Different Biomass Sources

Land Cover	CO_2	CO	CH_4	NO_x	NH_3	SO_2	PM_{10}	$PM_{2.5}$	EC	OC	NMVOC
Evergreen Forests	1643[a]	92[a]	5.1[a]	2.6[a]	0.76[a]	0.45[a]	12.8[c]	10.2[c]	0.5[a]	4.7[a]	24[a]
Deciduous Forests	1630[a]	102[a]	5[a]	1.3[a]	1.5[a]	1[b]	12.8[c]	12.3[c]	0.6[a]	9.2[a]	11[a]
Mixed Forests	1630[a]	102[a]	5[a]	1.3[a]	1.5[a]	1[b]	12.8[c]	12.3[c]	0.6[a]	9.2[a]	14[a]
Shrublands	1716[a]	68[a]	2.6[a]	3.9[a]	1.2[a]	0.68[a]	8.5[c]	7.9[c]	0.5[d]	6.6[d]	4.8[a]

Savannas	1692[a]	59[a]	1.5[a]	2.8[a]	0.5[a]	0.68[a]	9.9[c]	6.3[c]	0.4[a]	2.6[a]	9.3[a]
Wetlands	1765.5[c]	94[c]	1.5[c]	2.1[c]	0.6[c]	0.8[c]	12.5[c]	11.2[c]	0.52[c]	6.3[c]	6.8[c]
Croplands	1353.5[c]	76.1[c]	2.8[c]	2.9[c]	1.4[c]	0.4[c]	6.3[c]	5[c]	0.63[c]	2[c]	9.8[c]

Sources: [a](Akagi et al., 2011); [b](Andreae & Merlet, 2001); [c](Song et al., 2009); [d](McMeeking, 2008)

2.2.5.3 Burned Area of SEA

In biomass burning emission inventory, land cover type and amount of biomass burned significantly affect the types of pollutants emitted. Burn scar approach was used in this study to estimate the total emission of biomass burning, therefore burned area in MSEA was an important element for calculation and evaluation of biomass burning emission. There are two products of MODIS providing global fire data, but MCD64A1(C6) was used in this study as the improved algorithm has reduced error due to data gap, and is able to detect small fires better, and new improvement of MCD45A1 will no longer be done. The detection and measurements of burned area was done by retrieving data from MCD64A1 collection 6, which uses daily surface reflectance and active fire input data to generate detection. MCD64A1 is in Hierarchical Data Format (HDF) format, which allows it to store and organize large amount of data. MCD64A1 has five layers of raster data as shown in Table 2.2.7 and are stored in Scientific Data Set (SDS) (Giglio et al., 2016; Giglio et al., 2018).

2.2.6 Spatial Distribution

The spatial distribution has a spatial resolution of 500m x 500m. Remote sensing approach was used to produce land data, using MODIS product MCD12Q1, and the allocation of data into grid cells was done by using GIS system, and ArcGIS software was also used to produce spatial distribution of burned area. The burned areas were expressed in the form of polygons on the map, which helped to classify the characteristics of land cover type and burned area.

Table 2.2.7 Data Layers of MCD64A1

Data Layer	Information stored	Unit	Data Type
Burn Date	Day of burning	Day	16-bit signed integer
Burn Date Uncertainty	Estimated uncertainty in day of burning	Day	8-bit unsigned integer
QA	Quality Assurance Indicator	Bit field	8-bit unsigned integer
First Day	First day of year of reliable change detection	Day	16-bit signed integer
Last Day	Last day of year of reliable change detection	Day	16-bit signed integer

Source: (Giglio et al., 2016)

2.2.7 Temporal Distribution

The temporal distribution of this study is a year throughout 2013, with a temporal resolution of monthly emission of biomass burning (Zhou et al., 2017). The specific fire points of biomass burning were observed using Julian days. Unlike solar day which considers the position of the sun, Julian day is a uniform count of days in a year, 365.25 days, and does not have a leap year. Julian day starts from noon instead of midnight (Curtis, 2020). The annual emission data is allocated into monthly resolution, which data was collected at daily resolution to detect more subtle changes of land cover and emission from the annual data. The year 2013 was chosen as it was a neutral year with no weather extremes, and there was Southeast Asian haze crisis in 2013, which had created large-scale air pollution due to transboundary pollution.

2.3 Biogenic Emission in Southeast Asia

2.3.1 Model Description: Model of Emission Gases and Aerosols from Nature (MEGAN)

MEGAN is built to model the net emission of gases and aerosols from terrestrial ecosystems into the atmosphere (Guenter et al., 2006). It is designed for both global and regional emissions modelling with lowest spatial resolution of 1 km^2 or less. MEGAN is a semi-mechanistic model that accounts for the major known processes controlling biogenic emissions. MEGAN estimates only emissions of known compounds and includes additional compounds whenever they are identified as being of interest for the atmosphere. The emissions of 150 chemical species are included in the MEGAN2.1 and the model can output individual compounds or categories associated with various atmospheric chemistry schemes. These 150 compounds are lumped into 20 categories based on how emissions vary in response to changes in environmental conditions. Emission variations are first estimated for the 20 categories and then speciated into the 150 compounds or output in chemical categories associated with common atmospheric chemistry schemes (e.g. CB4, CB5, CB6, SAPRC99, and MOZART). Also, the driving variables are including land cover, weather, and atmospheric chemical composition. Overall model components and driving variables are summarised in Figure 2.3.1.

In order to quantify the net emission rate (mg compound m^{-2} earth surface h^{-1}) of biogenic emission between the atmosphere and terrestrial ecosystem at a specific location and time, parameterization has considered the impact of temperature, radiation, leaf age, soil moisture and canopy loss as (Eq 2.3.1):

$$\text{Emission} = [\varepsilon][\gamma][\rho] \quad \text{(Eq 2.3.1)}$$

where ε ($mgm^{-2}\ h^{-1}$) is an emission factor which represents the emission of a compound into the canopy at standard conditions, γ (normalized ratio) is an emission activity factor that accounts for emission changes due to deviations from standard conditions and ρ (normalized ratio) is a factor that accounts for production and loss within plant canopies. The emission factor incorporated in the model was developed

for the canopy-scale model, though it was extrapolated from the leaf and branch-scale environment model. Table 2.3.1 shows the standard conditions for MEGAN canopy-scale emission factor.

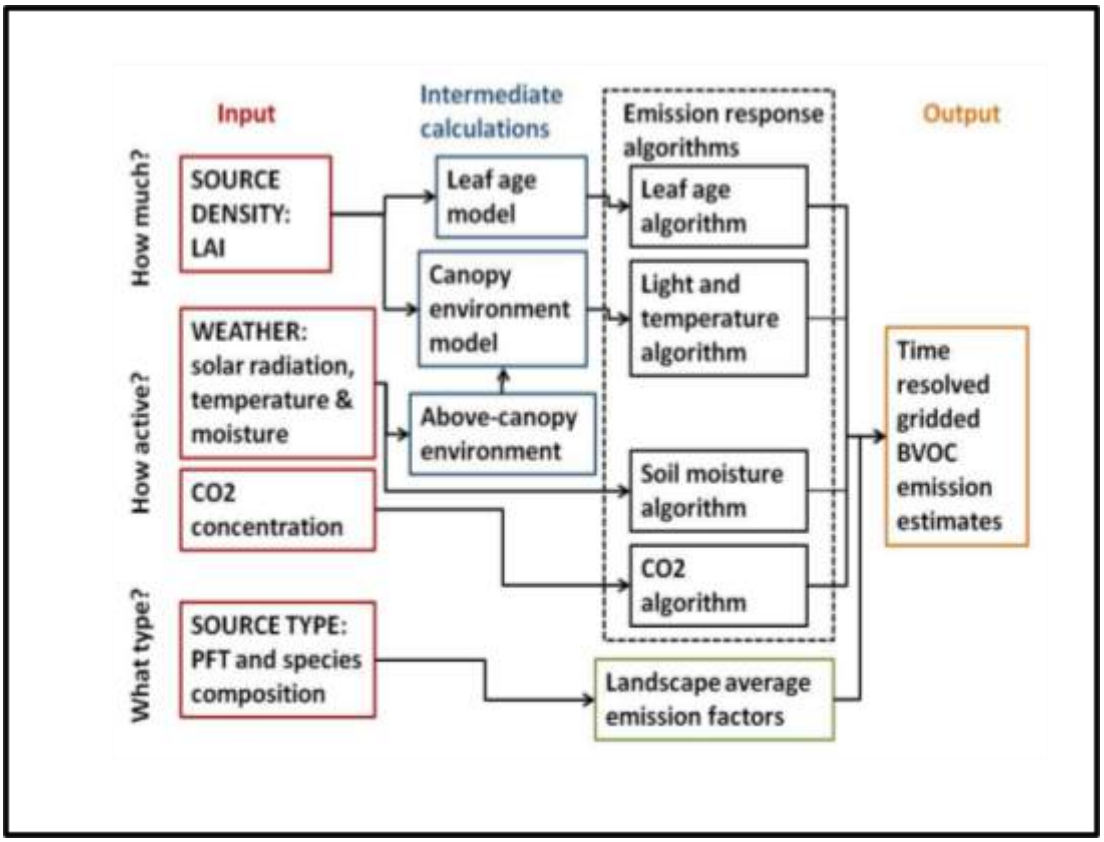

Figure 2.3.1: Schematic of MEGAN2.1 model components and driving variables (Guenther et al., 2012).

Table 2.3.1: Standard condition for MEGAN emission factors at the canopy-scale

Model's Parameter	Standard Conditions
Leaf Area Index (LAI)	5
Canopy	- 80% mature - 10% Growing - 10% foliage
Solar angle	60 degrees
Photosynthetic photon flux density transmission (PPFD)	0.6
Air temperature	303 K
Humidity	14 g kg-1
Wind speed	3 ms-1
Soil moisture	0.3 m3m-3
Average canopy environmental condition of the past 24 to 240 hour: ● Leaf temperature	- 297 K

• PPFD (sun leaves) • PPFD (shade leaves)	- 200μmol $m^{-2}s^{-1}$ - 50μmol $m^{-2}s^{-1}$

(Source: Guenther et al., 2006; Sentian et al., 2011).

2.3.1.1 Emission Factor at the Canopy-Scale (ε)

Land cover changes due to either natural or anthropogenic activities could affect the ecosystem in terms of vegetation composition, distribution, and the canopy structure, which are important factor for biogenic emission. Woody type of vegetation, particularly the board leaf trees are known to generally emit higher isoprene levels that non-woody plants. Board leaf trees isoprene emission factors were found to be closer to the global average of 12.6 mg m^{-2} h^{-1} in most regions. However, needle deciduous tree emission was observed to be even lower, for example grasslands in Austria (~0.004 mg m^{-2} h^{-1}) (Kirstine et al., 1998) and grasslands in China (~0.004 mg m^{-2} h^{-1}) (Bai et al., 2004). In some regions, crops are known to be a major source of isoprenes emissions, for example the emission factors were found in the range from 3 to 28 mgC g^{-2} h^{-1} for oil palm and from 25 to 130 mgC g^{-2} h^{-1} for mango (Mangifera indica) (Geron et al., 2006).

In MEGAN, PFTs are classified into a number of schemes, whose applications are dependent on the purpose of simulation. For the global simulation, MEGAN use the standard PFT-5 for version 2.1 which includes five general PFTs namely: broadleaf trees, needle leaf trees, grass, crops and shrubs. Meanwhile, for the regional simulation, the PFT-REG scheme is normally used, which includes the details of the plant genera in the region of interest.

2.3.1.2 Emission Activity Factor at the Canopy-Scale (γ)

The emission activity factor describes variations due to the physiological and phonological processes that drive the biogenic emissions rate changes. In BVOC, the total of the emission factor die to these processes is estimated based on the product of a set of non-dimensional emission activity factors that are each equal to 1 in standard conditions, as described by Guenther et al. (2006) in the following equation.

$$\gamma = \gamma_{CE} \times \gamma_{age} \times \gamma_{SM} \quad \text{(Eq 2.3.2)}$$

Where γ_{CE} describes variation due to Leaf Area Index (LAI) and light, temperature, humidity and wind conditions within the canopy environment, γ_{age} makes adjustments for effects of leaf age, and γ_{SM} accounts for direct change in γ due to changes in soil moisture. The calculation of each of these factors is described in the study of Guenther et al. (2006). Local climatic conditions, which affect the incident PPFD and leaf temperature, are known to control the biogenic emission such as isoprene from short periods (seconds to minutes) to longer periods (hours to weeks) of time scales (Guenther et al., 1993; Monson et al., 1994; Geron et al., 2000; Petron et al., 2001; Sharkey et al., 2001).

Studies have also shown that a lead's ability to emit isoprene is influence by leaf phenology. The young leaves of isoprene-emitting species do not emit isoprene, while the mature leaves emit at the highest capacity and the old leaves lose their ability to photosynthesize and produce isoprene (Guenther et al., 1991; 2006). Thus, the model will take account for leaf age in the BVOC model, the parameterization for the leaf age factor as described by Guenther et al. (1991), Monson et al. (1994), Golstein et al. (1998), Petron et al. (2001) and Karl et al. (2004) and was adopted from Guenther et al. (2006).

In addition, soil moisture was also observed to play an important role in biogenic emissions through an indirect effect on stomatal conductance, which influences the leaf temperature. Studies by Pegoraro et al. (2004;2005) have found thar at low levels of soil moisture the isoprene emissions began to drop and eventually became negligible when plants are exposed to extended severe drought. The emission activity factor that is dependent on soil moisture has been also included in the model parametrization (see more on; Guenther et al., 2006 and Pegoraro et al. 2004). The emission of soil moisture for any soil depth to be used to drive the PFT dependent approach (Zeng, 2001) in order to determine the fraction of roots within each soil layer and applies the weighted average of emission activity factor for each soil layer (Guenther et al., 2006). Other factor such as the availability of soil nutrients, ambient carbon dioxide concentration (Possell et al., 2004; 2005), CO2 (Buckley, 2001; Rosenstiel et al., 2003), ozone (Velikova et al., 2005), nitrogen availability (Harley et al., 1994), and physical stress (Alessio et al., 2004) are also known to affect the biogenic emissions particularly isoprene from the plants.

2.3.1.3 Production and Loss within Canopy (ρ)

At the canopy level, the production of biogenic chemicals is emitted into the atmosphere above the canopy and at the same time there are losses through the involvement of biological, chemical and physical processes within the canopy atmosphere, vegetation surfaces and on soil. The canopy production and loss factor of these chemicals (ρ) has been taken into account in the MEGAN as net canopy emission (Guenther et al., 2006), which is important in model simulation of the impact of biogenic emission such as isoprene on atmospheric chemistry. The net canopy emission is parameterized as function of canopy depth, friction velocity and chemical lifetime, which is based on measure isoprene emission profiles and turbulence profiles in recent studies in the tropical forest (Karl et al., 2004) and temperate forest (Stround et al., 2005).

2.3.2 Model Set-up

2.3.2.1 Compiler and Resources

In this study, the MEGAN2.1 was installed from UCA BAI official website (https://bai.ess.uci.edu/megan). The PGI compiler was used to compile the model. This biogenic model is developed under 64bit Linux Operation System (Ubuntu version 18.04). There are few programming

libraries are required in the system, such as I/O API, NetCDF library, MCIP and HDF in order to run the MEGAN model. The MEGAN input files are available with no cost. MEGAN ver. 2.1 accepts Plant Functional Type (PFT), Leaf Area Index (LAI) and Emission Factor (EF) map data in ASII format and meteorological data in NetCDF or I/O API format. Hence, the native outputs are in NetCDF format.

2.3.2.2. Dataset Input

There are two types of input data: climate data and land cover data. In this study, the climate data are obtained from WRF Model for present and future simulation (Section 3.1) under the same climate scenarios. While the global land cover data used in this study is adopted from the study of Ooi, et al., (2020).

2.3.2.3 Meteorology-Chemistry Interface Processor (MCIP)

Meteorology – Chemistry Interface Processor (MCIP) is used to ingests the output from the WRF model to prepare meteorology files that are used within other modelling system (Otte and Pleim, 2010). In this study, MCIP version 4.3 is used as a conversion of NetCDF format into I/O API format for MEGAN model. Hence, MCIP extract and conversion of the meteorological information that are required for MEGAN. Since the domain for MEGAN is smaller than WRF model, MCIP will extracts the domain by removing the boundary or part of the WRF domain.

2.3.2.4 I/O API

The Models-3/EDSS Input/Output Applications Programming Interface (I/O API) provides the environmental model developer with programming library for data storage and access, available from both Fortran and C. In this research, I/O API version 3.2 was downloaded to convert text files to I/O API format (.ncf). The raw dataset of land use, including leaf area index (LAI), plant functional types (PFTs), and emission factors (EFs) are in text file format. These datasets then converted into I/O API format which compatible with MEGAN model.

2.3.2.5 Developing Isoprene Emission

There are 3 major steps in developing isoprene emissions in MEGAN model, namely MET2MGN, EMPROC and MGN2MECH. The final output will be in NetCDF format and can be view using post-processing – visualization tool such as NCL. The first process is MET2MGN, which involves the process of converting meteorological data into format that readable by MEGAN. Meteorological data provided from the climate change simulation and using the same three scenario mentioned. During this process, the output each of WRF RCPs simulations are converted, and from MCIP, it will be used as input

data for MET2MGN. Second process is EMPROC, which is the process of calculating emissions using the climate information and PFT distribution. MGN2MECH is the final step where it covert the gas species result into common chemical reaction schemes used in atmospheric modelling. The final isoprene emission therefore will consist of three different emission scenario (following climate change simulation of RCPs) of the year of 2013, 2030, 2050, 2070, and 2100 for both period of January and July respectively.

2.4 Climate Change Impact on Regional Air Quality

2.4.1 Air Quality Modelling System

Community Multiscale Air Quality (CMAQ) System is a third-generation air quality model. The model was developed by US Environmental Protection Agency (EPA) since 1990s. According to Forley et al. (2010), the system continues to evolve and enhance. CMAQ is designed for applications ranging from regulatory and policy analysis to understanding the complex interactions of atmospheric chemistry and physics. It is a 3D Eulerian (i.e., gridded) atmospheric chemistry and transport modelling system that simulates ozone, particulate matter (PM), toxic airborne pollutants, visibility, and acidic and nutrient pollutant species throughout the troposphere. The CMAQ is a "one-atmosphere" model that addresses the complex couplings among several air quality issues simultaneously across spatial scales ranging from local to hemispheric. The meteorological information and emission rates from sources of emissions that affect air quality act as two primary inputs for CMAQ as a framework for simulating the interactions of multiple complex atmospheric processes.

Generally, meteorological models cannot be utilised for air quality simulation purpose. This is because meteorological models do not have same map projection, coordinate system, and grid format, and layer structure as air quality model. Hence, Meteorology-Chemistry Interface Processor or MCIP is developed to overcome this problem. MCIP acts as bridge to fill the gap by providing meteorology input data for CMAQ. The conversions involve are unit conversion, format conversion, vertical grid resolution related interpolation. The calculation conversion also includes creating additional diagnostic variables that are required by CMAQ but not available in meteorology model.

The WRF-ARW model has been employed to generate meteorological fields for EPA Community Multiscale Air Quality (CMAQ) because the WRF-ARW meteorological model is comparable with CMAQ like MM5 before (Yu et al., 2012). The emission model, Sparse Matrix Operator Kernel Emissions (SMOKE) model (IE, 2008) are available for computing emissions inputs to CMAQ from annual, county-level emissions inventories. These emissions inputs must be on the same horizontal and vertical spatial scales and cover the same period as are used in the air quality model simulation.

2.4.2 Chemistry-Transport Model Conceptual Formulation

The chemistry-transport model (CTM) is the final program to be run in the CMAQ modelling sequence. The four main programs: ICON, BCON, JPROC, and MCIP prepared input data for CMAQ CTM. A conceptual formulation of CMAQ and Eulerian air quality modelling is presented in form of framework. The coupled ordinary differential equations (ODEs) are applied to predict changes in pollutant concentrations throughout a three-dimensional grid that is fixed in space. The changes in the predicted concentrations in each grid cell can be affected by the several processes including emissions sources, horizontal and vertical advection, horizontal and vertical diffusion, chemical transformations, and deposition. The continuity equation is used to relate the processes with the concentration change in each grid cell over time ($\partial C/\partial t$) as shown below in Eq 2.4.1:

$$\partial C/\partial t = Adv + Diff + Rc + Ec - Sc \quad \text{(Eq 2.4.1)}$$

where

Adv = advection
Diff = diffusion
Rc = chemical transformation of species c
Ec = emissions of species c
Sc = loss processes for species c

The advection and emissions terms are calculated based on input files generated by the meteorology and emissions models in CMAQ. Besides that, the diffusion, chemical transformation, and deposition terms are calculated within CCTM. The Eulerian represent the area to be modelled, which is a series of contiguous grid cells that form a limited-area modelling domain on a subset of the globe. The boundary conditions should be established within limited-area domain. This is important to account for advection of pollutants and other chemical species into the modelling domain from areas outside it. Currently, CMAQ accounts for advection into the domain only from the horizontal such as lateral boundaries. It is assumed that there is no exchange through the top boundary of the domain such as vertical exchange.

The boundary conditions processor, BCON is used to estimate the spatial lateral boundary conditions. The initial conditions processor, ICON establishes temporal boundary condition that estimates the chemical conditions in the first-time step of a CMAQ model simulation. The program JPROC calculates clear-sky photolysis rates at various latitude bands and hours based on solar hour angles too model incoming solar radiation, which provides the energy source for photolysis reactions. At the end, the required input data for running CCTM is obtained from output of the three CMAQ programs, the emissions, and meteorological models and other CMAQ pre-processors (CMAQ version 5.0, 2012).

2.4.3 CMAQ Set-up

The Fortran 90 program is needed to operate CMAQ system. There are five main components: initial conditions processor (ICON), boundary conditions processor (BCON), The clear-sky photolysis rate calculator (JPROC), Meteorology-Chemistry Interface Processor (MCIP) and CMAQ Chemistry-Transport Model (CCTM) . In addition, there are also a few ancillary support programs with CMAQ such as the code builder/manager (Bldmake), the chemical mechanism compiler (CHEMMECH) and the process analysis preprocessor (PROCAN) (Refer CMAQ version 5.0, 2012).

2.4.3.1 Initial Conditions Processor (ICON)

For the first hour of a simulation, ICON generates a gridded binary netCDF file of the chemical conditions in the modelling domain. An ASCII file of vertically resolved concentration profiles (distributed with CMAQ) or existing CCTM output file is responsible in producing these initial conditions. ICON will interpolate the data to a vertical structure consistent with CCTM's if the profiles in an ASCII file do not have the same vertical structure as the CCTM configuration. The existing CCTM output file may be able to generate initial conditions when extrapolating initial conditions from a coarse to a fine grid simulation. The situation may occur when setting up nested simulations. The nested simulations refer to simulations with finer-resolution grids that cover part of coarser-resolution grids. The configuration options for ICON include selecting the chemical mechanism to model, defining the horizontal and vertical grids, and choosing whether the initial conditions are generated from an ASCII profile or from an existing CCTM output file (CMAQ version 5.0, 2012).

2.4.3.2 Boundary Conditions Processor (BCON)

The function of BCON is to generate a gridded binary netCDF file of the chemical conditions along the horizontal boundaries of the modelling domain. Same as ICON, an ASCII file of vertically resolved concentration profiles or from an existing CCTM output file to generate boundary conditions. In addition, BCON will interpolate the data in ASCII profiles into a vertical resolution which consistent with the CCTM configuration. BCON generates time-varying dynamic boundary conditions which extracted either from CCTM outputs from or from a CCTM simulation using a global-scale model. The ASCII input profiles also used to create dynamic boundary conditions (static data only). This options for BCON include selecting the chemical mechanism to model, defining the horizontal and vertical grids, and choosing whether the boundary conditions are generated from an ASCII profile or from an existing CCTM output file.

2.4.3.3 Meteorology-Chemistry Interface Processor (MCIP)

Modelling Output files from the MM5 or WRF meteorological models are used by MCIP to create netCDF as input meteorology data that are used by SMOKE (the emissions processor that computes

emissions inputs to CMAQ) and by CMAQ. All the meteorological fields that are required for SMOKE and CCTM are prepared and diagnoses by MCIP and to uniformly trim cells off the horizontal boundary of the domain defined by the meteorological model. The vertical resolution of the meteorological data can be decreased by "layer collapsing,". The configuration options for MCIP include horizontal and vertical grid definitions, the time periods over which to extract data from the meteorological model output files, and selections for calculating dry deposition velocities and integrating satellite cloud observations into MCIP output.

2.4.3.4 CMAQ Chemistry-Transport Model (CCTM)

CCTM integrates the output from the pre-processing programs such as JPROC, BCON, ICON, MCIP and CMAQ-ready emissions inputs which are output from SMOKE. As result, the continuous atmospheric chemical conditions are simulated. The output files of CCTM are all binary netCDF files of gridded and temporally resolved air pollutant information, such as gas- and aerosol-phase species mixing ratios, hourly wet and dry deposition values, visibility metrics, and integral-averaged concentrations. The input meteorology information dictated the spatial and temporal coverage of CCTM. The science configuration is specific to each application of the model and can be adjusted to optimize model performance both computationally and in the numerical reproduction of observed air quality trends.

2.4.3.5 Photolysis Rate Processor (JPROC)

The chemical-mechanism-specific clear-sky photolysis rates at fixed altitudes, solar hour angles, and latitude bands from tabulated absorption cross section and quantum yield (CSQY) data calculated by JPROC. These will support the default chemical mechanisms, updating or adding new CSQY data is straightforward. The selection of the chemical mechanism to use in the modelling is the only configuration option. The JPROC output is an ASCII look-up table of photolysis rates.

2.4.4 CMAQ Chemistry-Transport Model Science Modules

CMAQ modelling system used the meteorological model, emissions model, and analysis package (Byun and Ching, 1999) to simulate air quality. CCTM simulates each of the atmospheric processes by using state-of-the-science techniques that affect the transport, transformation, and removal of ozone, particulate matter, and other pollutants by using this information.

2.4.4.1 Gas-Phase Chemistry Solvers

In CMAQ version 5.0, gas-phase chemistry can be simulated with the CB05, SAPRC-07, or SAPRC-99 photochemical mechanisms. Difference equations governing chemical reaction kinetics and species

conservation used to solve and to compute time-varying species concentrations (including their rate of formation or depletion) but only CB05 considered in this project. Currently, CCTM contains three options for solving gas-phase chemical transformations: the Rosenbrock (ROS3) solver (Sandu et al., 1997), the Euler Backward Iterative (EBI) solver (Hertel et al., 1993), and the Sparse Matrix Vectorized GEAR (SMVGEAR) solver (Jacobson and Turco, 1994). The simulation of the chemistry of chlorine, mercury, and other toxic compounds in a multipollutant (mp) version of the CB05 also included within CMAQ version 5.0, 2012.

2.4.4.2 Photolysis

Most of the chemical reactions in the atmosphere are initiated by photolysis or photo dissociation of trace gases by using the energy from sunlight. Photolysis is involved in the formation of smog, an air pollution problem that affects human, animal, and plant health. The performance of air quality model is strongly influences by simulating photochemical reactions. State-of-the-science techniques are used within CMAQ to simulate photolytic reactions is the PHOT module which determines the photolysis reactions and their rates of reaction thus quantify how much reactant is produced from a photolytic reaction within a period.

The rate of photolysis is a function as the amount of solar radiation or actinic flux. It varies based on the time of day, season, latitude, and terrestrial features. The total amount of cloudiness and by aerosol absorption and scattering in the atmosphere determined the amount of solar radiation. Besides that, the photolysis rate also depends on species-specific molecular properties such as absorption cross section. An absorption cross section is the effective molecular area of a particular species when absorbing solar radiation, which results in a shadow region behind the particle. Another property is called quantum yield or the number of molecules that dissociate for each light photon incident on the atmosphere. The estimation of photolysis rate is complicated by these temperature and wavelength dependencies.

An advanced photolysis model (JPROC) is included within the CMAQ modeling system. The function is to calculate temporally varying photolysis rates for use in simulating photolysis in CCTM. The CMAQ contains an in-line photolysis module (Binkowski et al., 2007) start with version 4.7. The in-line photolysis calculations account for the presence of ambient PM and ozone predicted by CMAQ and uses these estimates to adjust the actinic flux (CMAQ version 5.0, 2012). It should be noted that the in-line photolysis method does not need to be run if JPROC module is used. The photolysis rates are calculated internally by CCTM. Hence, there is no need for the clear-sky look-up tables produced by JPROC by in-line configuration.

2.4.4.3 Advection and Diffusion

The advection and sub-grid-scale diffusion define pollutant transport model. Advection is related to mean wind fields which, the plume can travel a long distance without changes in concentration pollutants. On

the other hand, diffusion is related to sub-grid-scale turbulent mixing of pollutants. By diffusion process, the pollutants will mix more quickly and nearer to the source. This will then result in substantial changes to pollutant concentrations. Both advection and diffusion can be divided into horizontal advection, vertical advection, horizontal diffusion, and vertical diffusion.

2.4.4.4 Particulate Matter (PM)

The CCTM uses three lognormal sub-distributuins or modes to represent PM. $PM_{2.5}$ can be representing by Aitken and accumulation mode. Then, PM_{10} is the sum of the $PM_{2.5}$ and coarse-mode PM. The coarse-mode PM represents the PM with diameter greater than 2.5 micron and equal or less than 10 microns. Besides that, CMAQ also model the wet and dry deposition. The wet deposition transfer PM by rainfall and is calculated within CMAQ's cloud module. The turbulent air motion and direct gravitational sedimentation of larger particles are the two processes in dry deposition. The aerosol size distribution, meteorological and land use information can be used to calculate the deposition velocity for particles. The size distribution can be calculated from the mass and number concentration for each of the three modes. The velocity of dry deposition is then calculated (CMAQ version 5.0, 2012).

2.4.4.5 Clouds and Aqueous-phase Chemistry

Clouds play an important role in aqueous chemical reactions, vertical mixing of pollutants and removal of pollutants by wet deposition. Clouds can alter the solar radiation and indirectly affect pollutant concentrations like ozone and the flux of biogenic emissions. There are three types of clouds modelled in CMAQ: sub-grid convective precipitating clouds, sub-grid non-precipitating clouds, and grid-resolved clouds.

2.4.5 Experimental Design

The focus of this project is to simulate surface ozone and the corresponding precursors using CMAQ version 5.0 under climate change scenario. The model was ran based on one-way nesting technique where the input meteorological element and emission inventory was insert into the modelling system. The Simulation for the first domain with 45km horizontal grid resolution covered the entire East Asia, while the second domain with 15km resolution covered the Malaysia domain that utilized the initial and boundary condition from the first domain. Simulations of CMAQ were performed in 15 vertical layers from surface to 10mb. However, the analysis was focus on the surface layer of the earth. Moreover, a spin-up for 5 days was also performed to reduce the effect of initial condition on the model results. Gas phase chemistry is represented as Carbon Bond V (CB05) chemical mechanism with the aerosol module (AERO5).

In order to reflect the relationship between climate change scenario and tropospheric chemistry scenarios, the critical concentrations is determined by using WRF-RCM meteorological output datasets from a number of climate scenarios. This step is to answer one of the objectives studies, which is to investigate the impacts of climate change on regional surface O_3 and its precursors. Both climate and air quality model contain two modes: off-line mode and on-line mode. Since there are a few disadvantages of off-line mode, off-line mode is utilized within this study. The on-line mode coupling can be difficult to achieve because the configuration of both climate model and air-quality model are very complex. A longer simulation times are needed for the interactions. In addition, online-mode only use very simplified representations of chemistry and aerosols for climate- change simulations (Giorgi and Meleux, 2007).

In this study, the hourly (or finer temporal resolution) gridded meteorological data from WRF model and hourly gridded emission inventory from MISC-Asia used as input to CMAQ. As in line with the simulations in climate change modelling investigation, the tropospheric chemistry baseline scenario or present day tropospheric ozone is run following the same simulations though only RCP4.5 and RCP8.5 will be the prime investigation. As coherent with the time variables of emission inventory, the year of 2013 was selected as the base year of the simulation.

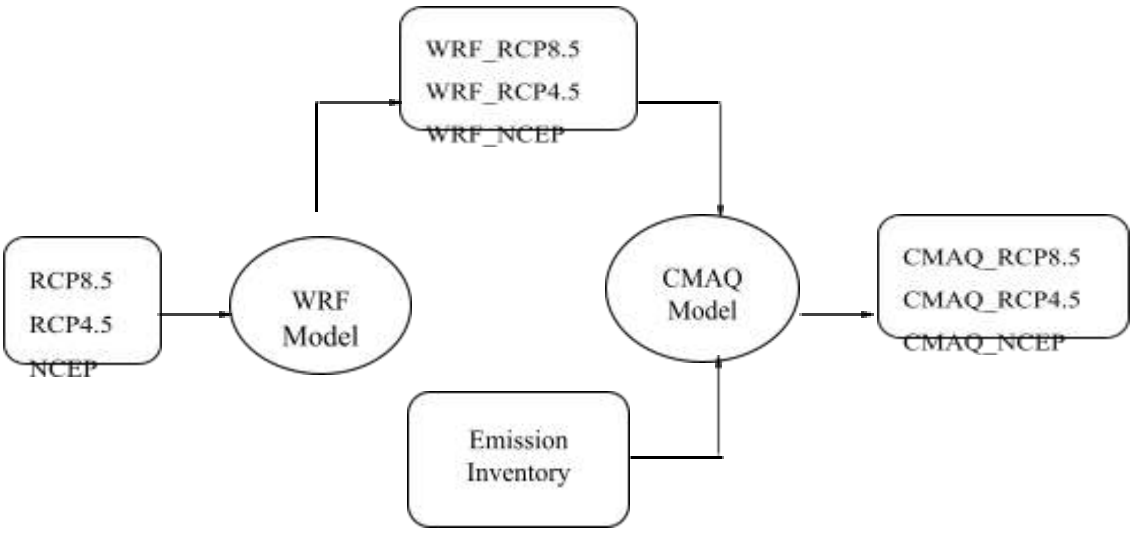

Figure 2.4.1: Experimental design for simulation climate change impact on air quality

2.4.6 Air Quality Observation Dataset

Using the meteorological input data simulated from WRF model (see Chapter 3 in detail), a present year (2013) as well as January and July for ozone and the precursors mixing ratios were simulated by applying CMAQ modelling system with also the emission inventory prepared by Model Inter-Comparison Study for Asia (MICS-Asia) Phase III. The modelling evaluation was performed by comparing the modelling output with the measurement dataset provided by Department of Environment (DOE Malaysia). This section utilised several statistical formulae to evaluate the model results which include normalized mean

bias (NMB), fractional bias (FB), normalized mean square error (NMSE) and factor of two (Fa2) to evaluate the model's behaviour.

2.4.6.1 Model Inter-Comparison Study for Asia (MICS-Asia) Phase III

MICS-Asia III is an anthropogenic inventory Asia developed for the year 2010 in-cooperated of Task Force on Hemispheric Transport of Air Pollution (TF HTAP) projects which developed based on a mosaic of the latest regional emission inventories (Li et al., 2015). The mosaic inventory is incorporated by five emission inventories selected including REAS inventory version 2.1 covering whole Asia (Kurokawa et al., 2013), the Multi-resolution Emission Inventory for China (MEIC) constructed by Tsinghua University (http://www.meicmodel.org), a NH_3 emission inventory created by Peking University (Huang *et al*., 2012), an Indian emission inventory developed by Ar-gonne National Laboratory (Lu et al., 2011; Lu and Streets, 2012) and the official Korean emission inventory from the Clean Air Policy Support System (Lee et al., 2011).

Emission inventory provided anthropogenic pollutants covers 30 countries and regions with greenhouse gas emissions data such as sulphur dioxides (SO_2), nitrogen oxides (NO_x), carbon monoxide (CO), ammonia (NH_3), NMVOC (volatile organic compounds), particulate matter with diameter less than or equal to 10 μm (PM_{10}), particulate matter with diameter less than or equal to 2.5 μm ($PM_{2.5}$), black carbon (BC), organic carbon (OC), and carbon dioxide (CO_2). Two chemical mechanisms such as CB05 (the Carbon Bond mechanism, Yarwood et al., 2005) and SAPRC-99 (the State Air Pollution Research Centre 1999 version, Carter, 2000) were inserted with NMVOC emissions. The inventory consists of five emission sectors: agriculture, industry, power, residential and transportation, and developed at 0.25×0.25 resolution (Li et al., 2015).

2.4.6.2 Air Quality Measurement Dataset

The observed air concentrations, available since 1996 until 2011 were obtained from Department of Environment (DOE) in Malaysia. There are 94 air quality monitoring stations distributed across the region. The selection of observation sites was in random way as the evaluation of model output with the observation data is to provide as a context or idea about the level of agreements between the projected and observed quantities (Zhang et al., 2008). The comparison between both datasets is to clarify the downscaling skill of air quality projection, and not to study the air quality variation. Therefore, a qualitative evaluation of CMAQ air concentration predictions for current climate in January and July was conducted to assess the model in representing the observed air quality. Five observation stations in urban areas were obtained from DOE for the evaluation purpose. Three stations were selected from Malaysian Peninsula (Kuala Lumpur - representing central area; Ipoh – representing northern part; and Seremban –

representing Southern area. Meanwhile in Malaysian Borneo, Kuching in Sarawak State, and Kota Kinabalu in Sabah State.

3 Results & Discussion

This section will present the four main research subjects of the project. The research subject will be presented in sequence using the following subsections and headings:

3.1 Climate Change in Southeast Asia

3.2 Biomass Emission Inventory in Southeast Asia

3.3 Biogenic Emission Inventory in Southeast Asia

3.3 Air Quality in Southeast Asia Under Climate Change Scenarios

3.1 Climate Change in Southeast Asia

3.1.1 Climate Change Evaluation

Table 3.1.1 shows the evaluation and assessment of WRF modelling system under all RCPs scenarios as relative to NCEP reanalysis dataset. These NCEP FNL (Final) Operational Global Analysis dataset is from the Global Data Assimilation System (GDAS), which collects observational data from the Global Telecommunications System (GTS) and other sources on a continuous basis to allow for the utilisation from climate observational dataset (Rife *et al*., 2014). The evaluation result of all RCPs simulation is almost similar with DOE dataset evaluation during January period, but a slight lower bias is observed during July period.

Table 3.1.1: Comparison of surface temperature in January and July under RCP4.5, RCP6.0 and RCP8.5 as relative to NCEP for normalized mean bias (NMB), fractional bias (FB), normalized mean square error (NMSE), and factor of two (Fa2).

Variable	**Temperature (°C)**		**NMB**	**FB**	**NMSE**	**Fa2**
Scenario	**Model**	**NCEP**				
January						
RCP 4.5	25.81	26.80	-3.69	-0.04	0.0010	0.96
RCP 6.0	25.04	26.80	-6.57	-0.07	0.0050	0.93
RCP 8.5	25.56	26.80	-4.63	-0.05	0.0020	0.95
July						
RCP 4.5	27.41	26.88	1.97	0.02	0.0004	1.02
RCP 6.0	27.22	26.88	1.26	0.01	0.0002	1.01
RCP 8.5	27.55	26.88	2.49	0.02	0.0006	1.02

Similarly, for RCP6.0 scenario, the model under has underestimated the NCEP reanalysis data with slightly higher cold bias of 6.57% during January but overestimated the reanalysis with a warm bias of 1.26% during July period. That being said, the model simulated surface temperature with 25.04°C during January and 27.22°C compared to 26.80°C and 26.88 under NCEP reanalysis for both periods accordingly. It can be observed that both FB and NMSE has value of insignificancy difference from zero while Fa2 equal to 1 thus leaving an impression of paralleling observational surface temperature dataset.

For RCP8.5, the model also has underestimated the NCEP reanalysis dataset with cold bias of 4.63% during January and despite overestimated the NCEP dataset with warm bias of 2.49%. Not the less, the model has simulated surface temperature of 25.56°C during January and 27.55°C for July while NCEP giving a value of 26.80°C and 26.88°C correlatively. In agreement with RCP4.5 and RCP6.0, both FB and NMSE has value of insignificancy difference from zero while Fa2 equal to ranging from 0.96 – 1.02 thus indicating an exceptional homogenous surface temperature data from climate simulation output.

3.1.1 Surface Temperature

3.1.2.1 RCP4.5 Scenario

Under RCP4.5 the simulated mean surface temperature in SEA region for January of 2013, 2030, 2050, 2070 and 2100 are 22.88℃, 22.51℃, 23.48℃, 23.25℃ and 23.70℃ respectively. Whereas in July, the mean surface temperature for the same time slice is 26.66℃, 26.88℃, 27.43℃, 27.18℃ and 27.59℃ respectively (Table 3.1.2). Though the mean surface temperature is simulated to be cooler during January 2030 period (with reduction of 0.37℃), warmer climate is expected from the result of the rest simulation period. It is also worthy to highlight that the mean surface temperature for both January and July of 2070 are lower than what been observed in 2050 and 2100.

Table 3.1.2**:** Mean surface temperature of SEA under RCP4.5

Year	Month	Surface Temperature (℃)	Changes (℃)	Percentage of Increment (%)
2013	**January**	22.88	-	-
	July	26.66	-	-
2030	**January**	22.51	-0.37	-1.62
	July	26.88	0.22	0.83
2050	**January**	23.48	0.60	2.62
	July	27.43	0.77	2.89
2070	**January**	23.25	0.37	1.62
	July	27.18	0.52	1.95
2100	**January**	23.70	0.82	3.58

	July	27.59	0.93	3.49

As RCP4.5 is based on a progressive stabilization of GHG emissions after the middle of the 21st century, this finding carries the expectation that there is a decrease in energy demand during winter season and progressive stabilization of greenhouse gases over that period (Thomson et al., 2011; IPCC, 2014). The cumulative function of simulated mean surface temperature under RCP4.5 over SEA region for the period of 2013, 2030, 2050, 2070 and 2100 of January and July was shown in the figure 3.1.1 and 3.1.2 respectively. The result from figures 3.1.1 and 3.1.2 also suggest that there is overall a less significant increase of surface temperature at about 2 ℃ from the period of 2050 until end of century especially in the maritime continent of SEA.

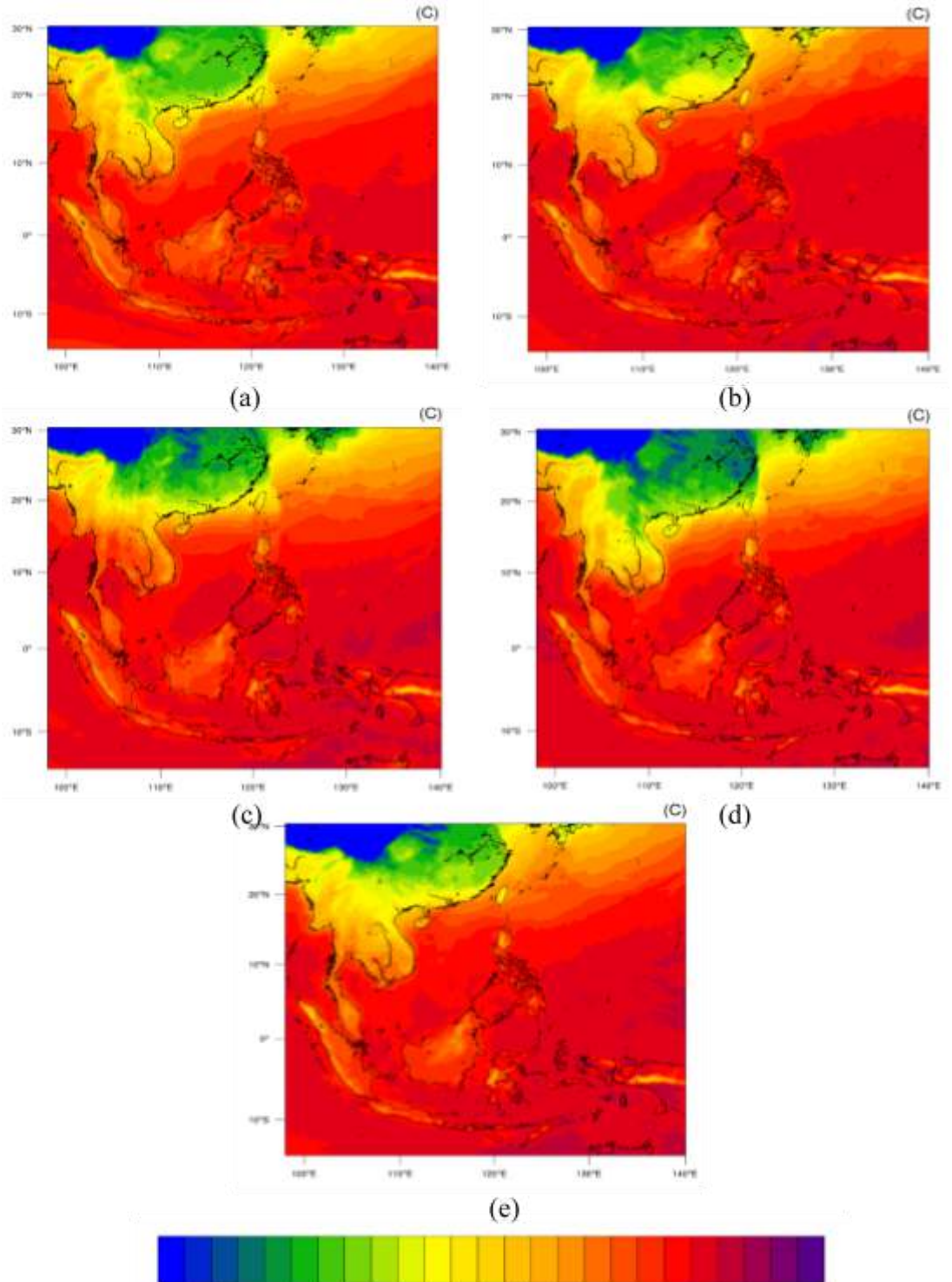

Figure 3.1.1: Mean surface temperature for SEA region under RCP4.5 during January of 2013 (a), 2030 (b), 2050 (c), 2070 (d) and 2100 (e).

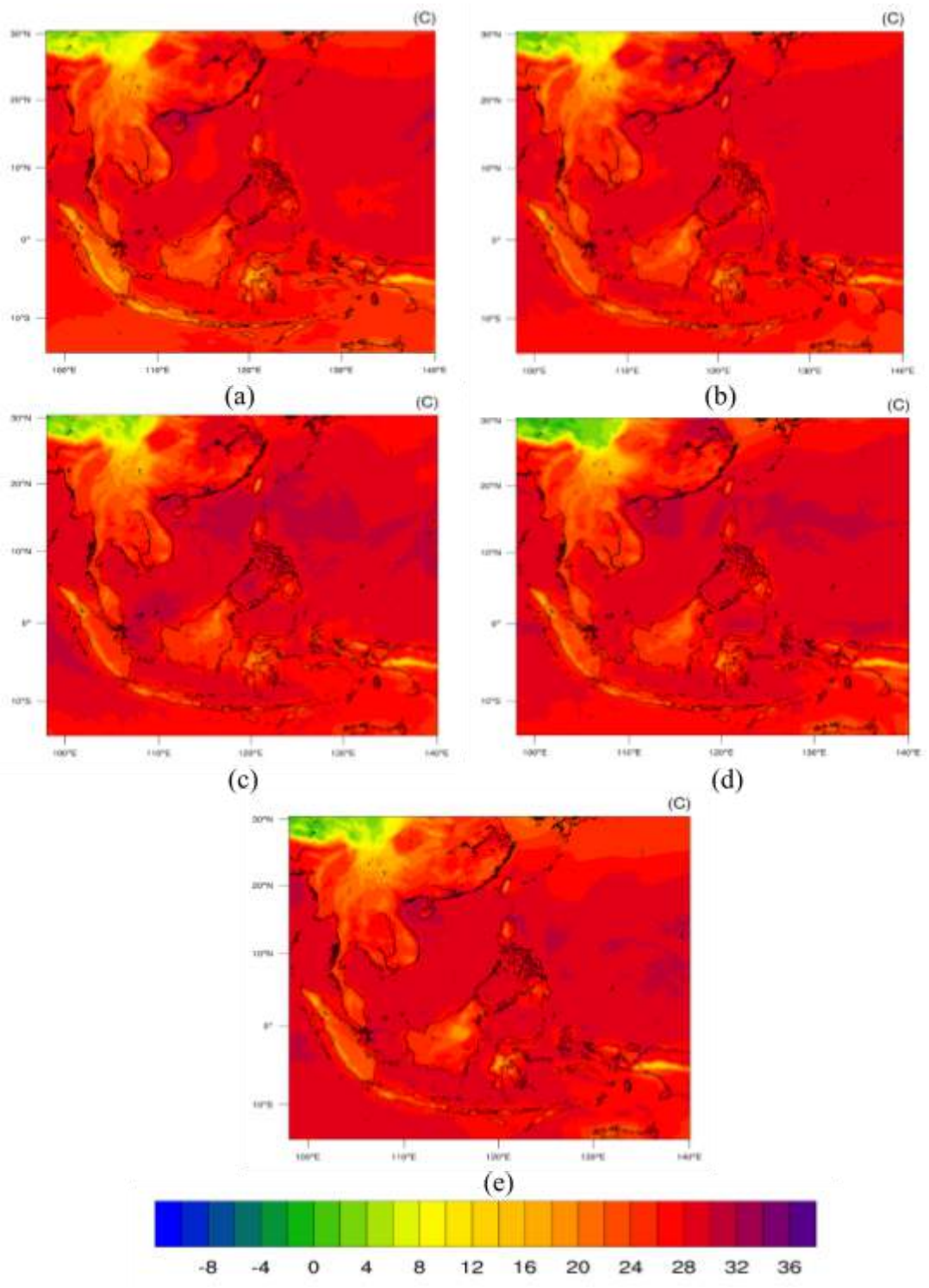

Figure 3.1.2: Mean surface temperature for SEA region under RCP4.5 during July of 2013 (a), 2030 (b), 2050 (c), 2070 (d) and 2100 (e).

For January of mid-century, Cambodia and Thailand set the highest temperature increment with 4.6℃ (from 28.24℃ to 32.96℃) and 4.7℃ (from 22.08℃ to 26.29℃) respectively. Both Myanmar and Laos experience less significant warming of 0.89℃ (from 16.24℃ to 17.14) and 2.86 ℃ (from 22.83℃ to 26.84℃) during the mid-century, before expected to become colder at the end of century with reduction temperature anomaly of -5.17℃ and -5.14℃ respectively. The mean average surface temperature anomaly toward the end of century are less pronounced at other countries of SEA except Thailand which expected to become cooler by 4.49℃.

Additionally, the result from RCP4.5 also suggest that the surface temperature in mainland SEA is more variable during January compared to July for the entire simulation period. The climate of mainland SEA has a tropical maritime forcing thus there is not much surface temperature difference during dry season (Nguyen et al., 2019). The maritime continent of in SEA particularly Borneo Island, Sulawesi and the Philippines relatively has higher temperature, high relative humidity and higher precipitation rate due to the effect of tropical rain belt, and the seasonal shifting (Christensen et al., 2013). More details on regional surface temperature projection under RCP4.5 scenario can be found on Appendix 3.1.1A.

3.1.2.2 RCP 6.0 Scenario

Under RCP6.0 the average mean surface temperature over SEA for January of 2013, 2030, 2050, 2070, and 2100 are 22.41℃, 23.18℃, 24.05℃, 23.45℃ and 24.06℃ respectively. Whereas in July, the mean surface temperature are 26.46℃, 26.76℃, 27.40℃, 27.73℃ and 28.20℃ (Table. 3.1.3). The increase in projected average surface temperature anomalies for the future period indicates a level of steady increase in emissions by the year 2030, 2050, 2070 and 2100 under RCP6.0 and similar in the findings of Gupta et al., (2021). Overall, the future mean surface temperature in SEA region is projected to increase two times higher than RCP4.5 of about 0.77 ℃ to 1.66 ℃ for January period and 0.31 ℃ to 1.74 ℃ (Table 3.1.3).

That being said, the mainland of SEA (from figure 3.1.3) particularly Laos, Thailand, Cambodia, Vietnam and Myanmar will experience warmer climate during the mid-century with increment of 12.68℃ (from 14.64℃ to 27.33℃), 12.27℃ (from 14.64℃ to 26.87℃), 10.43℃ (from 22.54℃ to 30.28℃), 8.8℃ (from 16.66℃ to 23.02℃) and 5.43℃ (from 11.72℃ to 17.16℃) respectively compared to the baseline period (refer to Appendix 3.1.1B). Toward the end of century, the simulated mean surface temperature over Laos, Cambodia, Thailand, and Vietnam is most pronounced compared to other regions where it increases by 10.90℃ (from 14.64℃ to 25.55℃), 10.17℃ (from 22.54℃ to 32.71℃), 9.26℃ (from 14.60℃ to 23.87℃), and 9.25℃ (from 16.66℃ to 25.92℃) respectively.

Simulated surface temperature increment for July (figure 3.1.4) comparatively lower than January for SEA countries with the highest increment of 4.35℃ for Myanmar (from 21.41℃ to 25.77℃) and the lowest of 0.83℃ (from 28.76℃ to 29.58℃) for Malaysia. The projected surface temperature increment also pronounced in Thailand with 3.03℃ (from 25.96℃ to 28.99℃) temperature increment during mid of century while 2.69℃ (from 26.98℃ to 29.67℃) and 2.29℃ (from 27.83℃ to 30.13℃) for Laos and Vietnam. Towards the end of century, the whole region except Thailand and Laos will experienced surface temperature increment ranging from 1.93 to 3.69 which is less pronounced during in the mid-century.

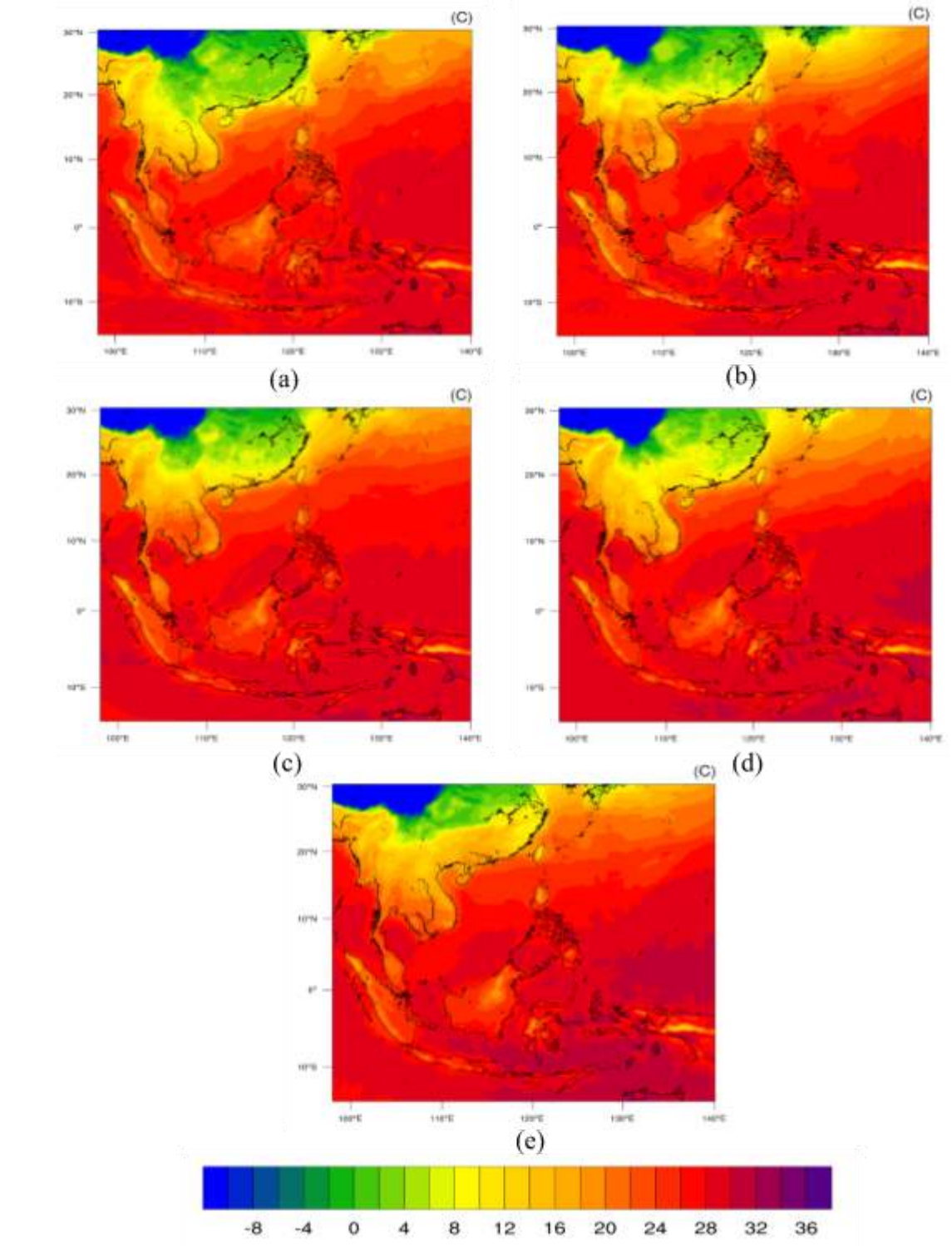

Figure 3.1.3: Mean surface temperature for SEA region under RCP6.0 during January of 2013 (a), 2030 (b), 2050 (c), 2070 (d) and 2100 (e).

As RCP6.0 has higher CO_2 concentrations in 2050 than RCP4.5 which the energy consumption reaches the peak during 2080 and start to decline afterward (IPCC, 2013). Therefore, higher surface temperature associated with higher forcing scenario during the mid- century. Moreover, RCP6.0 is a scenario of long-term, global emissions of GHGs, land-use and land-cover change which stabilizes radiative forcing at 6.0 Wm^{-2} in the year 2100 (Masui et al., 2011). This corresponding well with the result in which higher surface temperature change during mid-century in the mainland might be due to the increase of agricultural activities and land cover conversion has been observed in China previously (Dong et al., 2019).

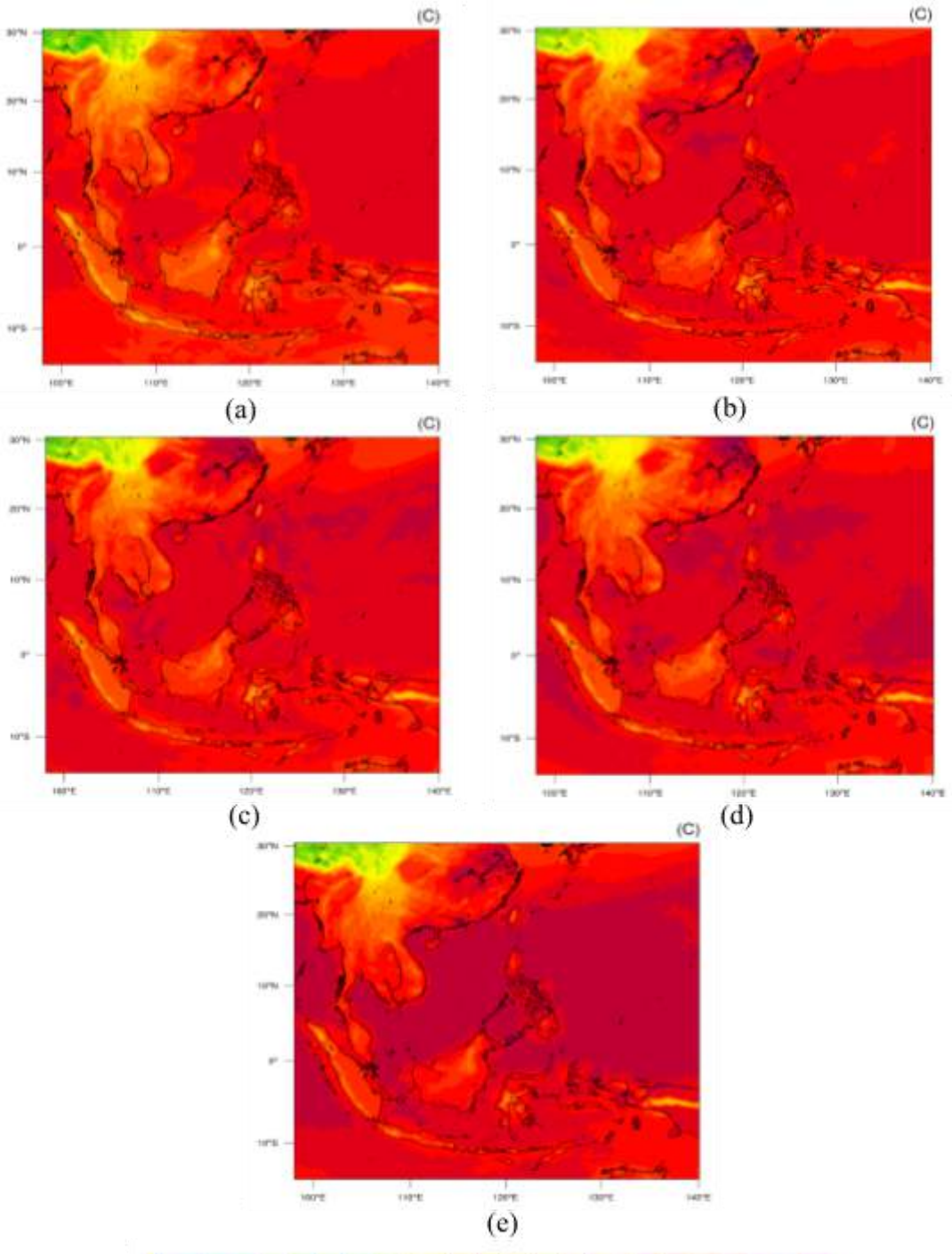

Figure 3.1.4: Mean surface temperature for SEA region under RCP6.0 during July of 2013 (a), 2030 (b), 2050 (c), 2070 (d) and 2100 (e).

Table 3.1.3: Mean surface temperature of SEA under RCP6.0

Year	Month	Surface Temperature (℃)	Changes (℃)	Percentage of Increment (%)
2013	**January**	22.41	-	-
	July	26.46	-	-
2030	**January**	23.18	0.77	3.45
	July	26.76	0.31	1.15
2050	**January**	24.05	1.64	7.33
	July	27.40	0.94	3.55
2070	**January**	23.45	1.05	4.67
	July	27.73	1.27	4.80
2100	**January**	24.06	1.66	7.40
	July	28.20	1.74	6.58

3.1.2.3 RCP 8.5 Scenario

The mean surface temperature in both January and July for SEA under RCP 8.5 scenario were found to be the highest compared to RCP4.5 and RCP6.0 scenarios. The average mean surface temperature for January of year 2013, 2030, 2050, 2070 and 2100 are 23.29°C, 22.95°C, 23.09°C, 24.65°C, 25.40°C respectively. While in July the mean surface temperature for the respective same year are 26.63°C, 27.39°C, 27.62°C, 28.51°C and 29.13°C respectively (Table 3.1.4). Similar to RCP4.5 and RCP6.0 scenarios, surface temperature projection under RCP8.5 shows a drop in temperature during January period with decrement of -0.34℃ in 2030 and -0.20℃ in 2050.

Table 3.1.4: Mean surface temperature of SEA under RCP8.5

Year	Month	Surface Temperature (℃)	Changes (℃)	Percentage of Increment (%)
2013	**January**	23.29	-	-
	July	26.63	-	-

2030	**January**	22.95	-0.34	-1.45
	July	27.39	0.76	2.85
2050	**January**	23.09	-0.20	-0.86
	July	27.62	0.99	3.72
2070	**January**	24.65	1.36	5.83
	July	28.51	1.87	7.03
2100	**January**	25.40	2.11	9.05
	July	29.13	2.50	9.37

The spatial distribution of surface temperature simulation under RCP8.5 are shown in figure 3.1.5 for January and figure 3.1.6 for July respectively. The results depict that during January an increment of surface temperature concentrate over SEA mainland region during mid-century. Laos recorded highest temperature increment with 5.74°C (from 21.84°C – 27.60°C) followed by Vietnam with 4.29°C (from 22.87°C – 27.16°C), Thailand 4.18°C (from 25.46°C – 21.28°C) and Cambodia 3.25°C (from 28.27 – 31.52°C). However, toward the end of century, the mainland of SEA become more colder while the maritime continent become warmer. More information on RCP8.5 regional surface temperature projection is shown on Appendix 3.1.1C

On the other hand, the maritime continent of SEA is simulated to have higher temperature increment over the end of century with 2.45 °C over Indonesia, 2.16°C in Singapore, 1.98°C over Philippines and 1.63 over Malaysia during January period (figure 3.1.5). This temperature anomaly during mid-century and end of century can be contributed by seasonal monsoon changed which has been discussed in the study of Loo et al., (2014). The ocean-atmosphere interaction can be a source of climate variability and shaping the dynamic of regional monsoon system therefore influence changes in atmosphere temperature (Zhou et al., 2009).

Whereas in July (figure 3.1.6), there is no notable increase of mean surface temperature in SEA countries but the result of RCP8.5 simulation expected that it will be colder in mid-century with temperature anomalies of -3.50°C in Thailand (from 28.90 – 25.40), -3.32°C in Laos (from 30.97°C – 27.65°C), and -2.15°C over Vietnam (from 31.36°C – 29.21°C). Towards the end of century, the result of RCP8.5 simulations projected that Malaysia, Philippines, Thailand and Myanmar will experience warmer temperature ranging from 1.75°C to 2.28°C (from 29.72°C – 31.47 over Malaysia, 29.01°C – 30.83°C over Philippines, 28.90°C – 30.88°C over Thailand, and 24.65°C – 26.93°C in Myanmar respectively).

The southeast Asian countries especially Myanmar, Thailand, Vietnam, Laos, Philippines and Thailand influenced by the large-scale seasonal reversals of wind regime (Serreze and Barry, 2010). The two regimes of monsoon are the Southeast Asian summer monsoon (10°–20°N) and the western North Pacific summer monsoon (10°–20°N, 130°–150°E), which separated by the South China Sea (Kripalani and Kulkarni, 1997*)*. During winter, the tilting of the Earth allows less solar radiation at the northern

hemisphere. This results in rapid cooling followed by pressure decrease in the atmosphere (Loo et al., 2015). Anti-cyclones develop over Siberia and the cold north-easterly air reaches the coastal waters of China before heading towards Southeast Asia (MMD, 2012*)*.

RCP8.5 climate scenario also referred as baseline scenario which does not include any specific mitigation target (Riahi et al., 2011). Higher temperature is expected at the end of century as the region has undergone rapid economic development and GHG emission considerably high over time leading to a forcing of 8.5 W/m^2 (IPCC, 2013). Thus, temperature changes might be as well induced by land use changes under RCP8.5 which suggesting larger land-cover conversion (Dong et al., 2019) over Malaysia, Philippines, Thailand and Myanmar. Difference between landcover background would contribute difference between temperature as GHG emission warms the whole atmospheric temperature while evaporations from vegetation promote colling effect (Zeng et al., 2017).

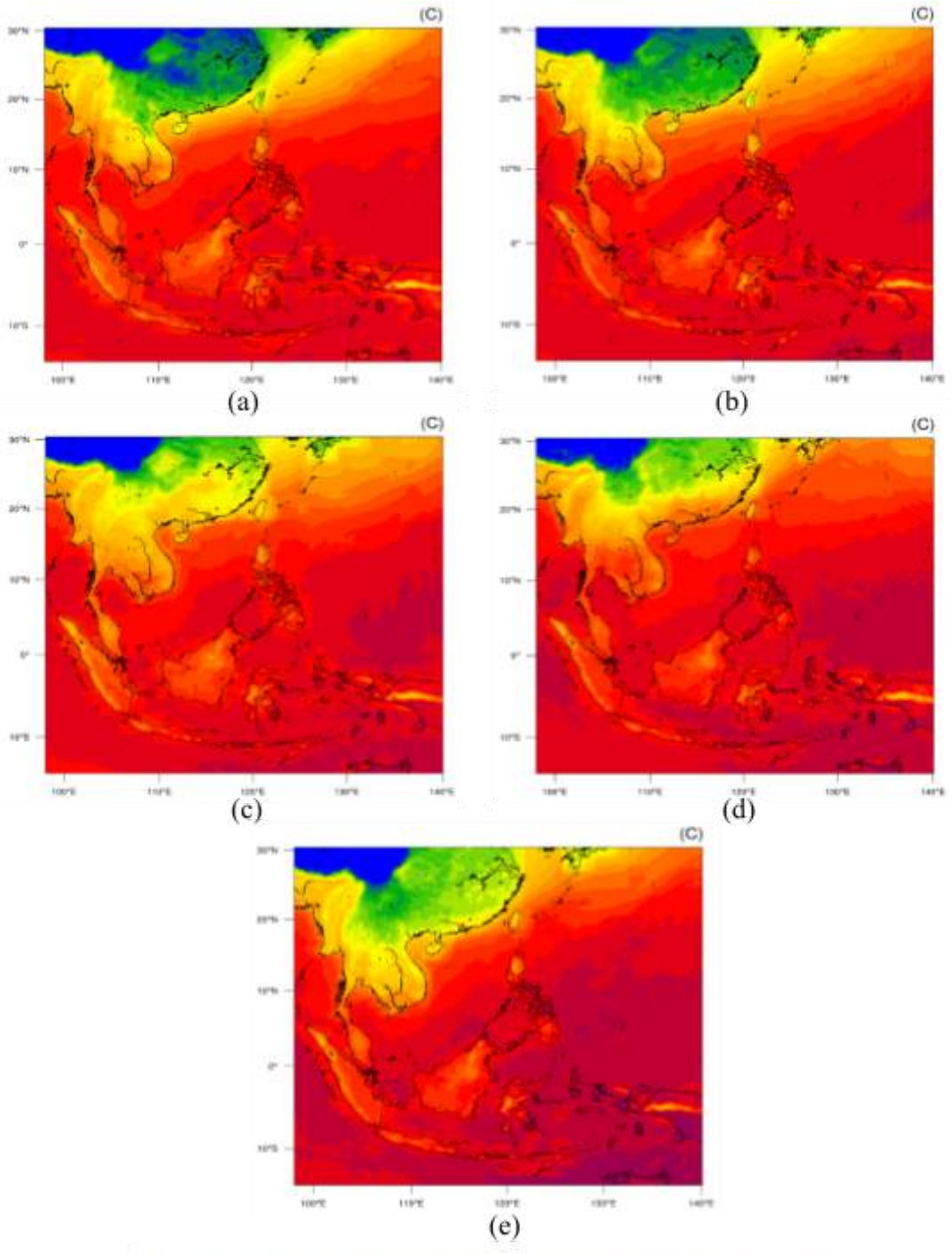

Figure 3.1.5: Mean surface temperature for SEA region under RCP8.5 during January of 2013 (a), 2030 (b), 2050 (c), 2070 (d) and 2100 (e).

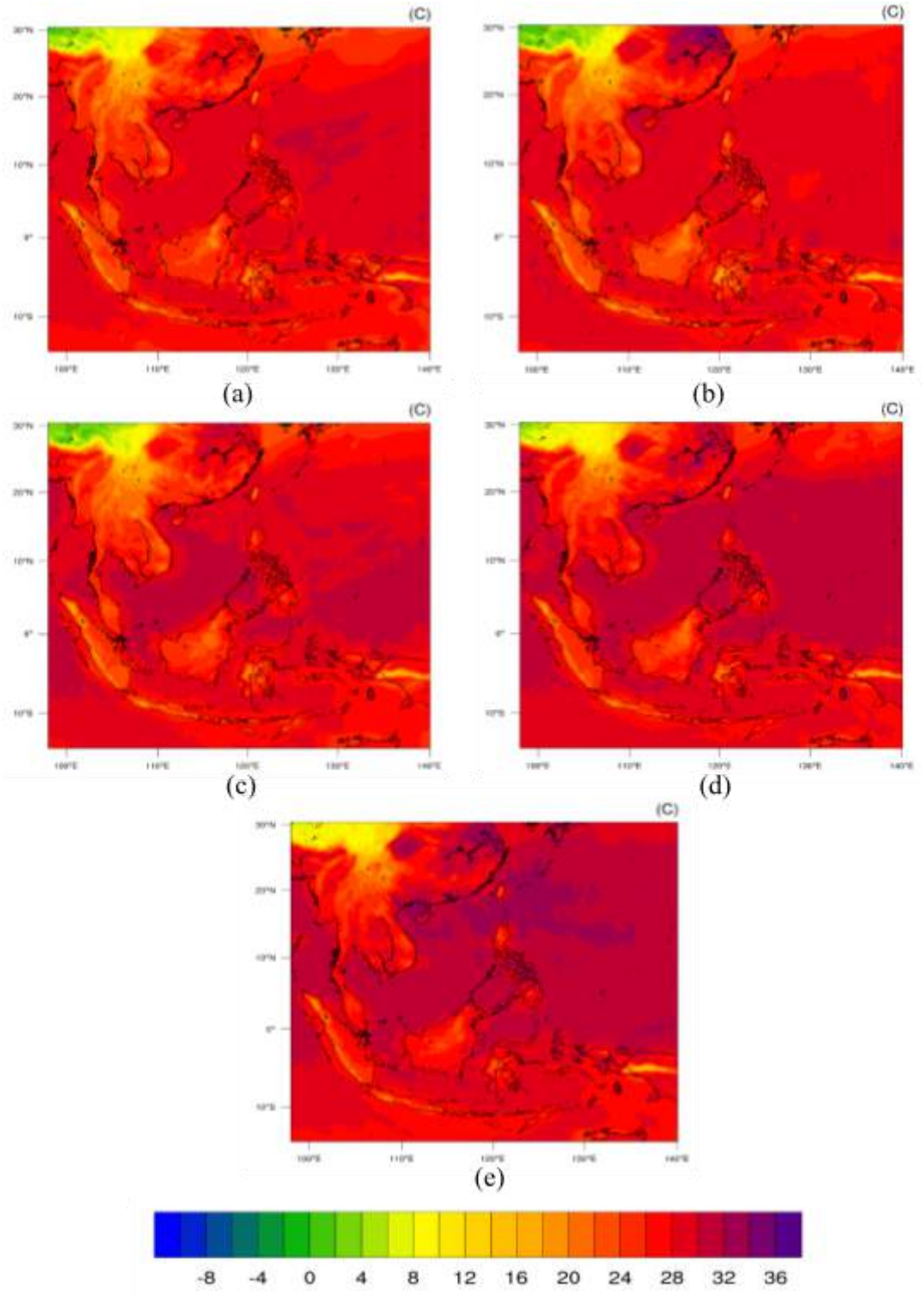

Figure 3.1.6: Mean surface temperature for SEA region under RCP8.5 during July of 2013 (a), 2030 (b), 2050 (c), 2070 (d) and 2100 (e).

3.1.3 Total Precipitation

3.1.3.1 RCP4.5

The total mean precipitation projected in WRF model under RCP4.5 scenario in the year of 2013, 2030, 2050, 2070 and 2100 are 0.92, 96.76, 5.61, 9.61 and 90.02 inches/day during January (Table 3.1.5). The mean of total precipitation was highest in 2030 (with 95.84 inches/day), followed 2100 (89.10 inches/day), 2070 (8.69 inches/day) and 2050 (5.61 inches/day) as relative to baseline scenario (2013), which represent an increment of total precipitation between 5.09% to 96.86%. The increase of rainfall over this region might be caused by increase of overall temperature. As highlighted in the study of Ge et al. (2021), the tropical region was also projected with an increase of precipitation and the changes is caused by their sensitivity of global warming drives by the GHGs emission.

Table 3.1.5: Total Precipitation of SEA under RCP4.5

Year	Month	Total Precipitation (inches/day)	Changes (Inches)	Changes rate (x 100%)
2013	**January**	0.92	-	-
	July	8.80	-	-
2030	**January**	96.76	95.84	104.17
	July	5.42	- 3.37	- 0.38
2050	**January**	5.61	4.69	5.09
	July	15.27	6.48	1.73
2070	**January**	9.61	8.69	9.44
	July	134.88	126.09	14.32
2100	**January**	90.02	89.10	96.84
	July	105.72	96.93	11.01

The future distribution of total precipitation during January can be observed with a higher rate of rainfall in Malaysia and Indonesia over the rest of SEA countries (figure 3.1.7). The highest total precipitation increment during January was projected in Indonesia with a range of 1.93 to 205.74

inches/day (with 105.60% increment on January 2030 period) within the projection time slice. Then, continued by Malaysia with a range of 0.27 to 164.95 inches/day (over 600% rate of increment) inches during the same period. Besides, the increment of total precipitation from 1.43 to 59.16 inches/day (of 40.37%) over Philippines under the same period is worthy to be highlighted. While the mainland SEA countries such as Myanmar, Thailand, Cambodia, Laos and Vietnam revealed a lower total precipitation change with a range from 0 to 10.32 inches. More details on total precipitation projection under this RCP is shown on Appendix 3.1.1D.

Simulated total mean precipitation increment for July (figure 3.1.8) comparatively less pronounced than January for SEA countries with the highest increment of 1.73% and 11.01% on the mid-century and end of century respectively. The projected temperature increment is most pronounced in Indonesia with 23.06 increment (from 0.30 inches/day to 7.22 inches/day) for mid of century. Towards the end of century, the maritime continental of Malaysia and Indonesia experiencing significant increment amount of rainfall with over 52.59% in Malaysia and 100.46% in Indonesia compared to the baseline period. The result is not in parallel with the finding of Tangang et al., (2020) which suggest that the changes are the significant and robust mean rainfall reductions of 10–30% over Indonesia and Malaysia.

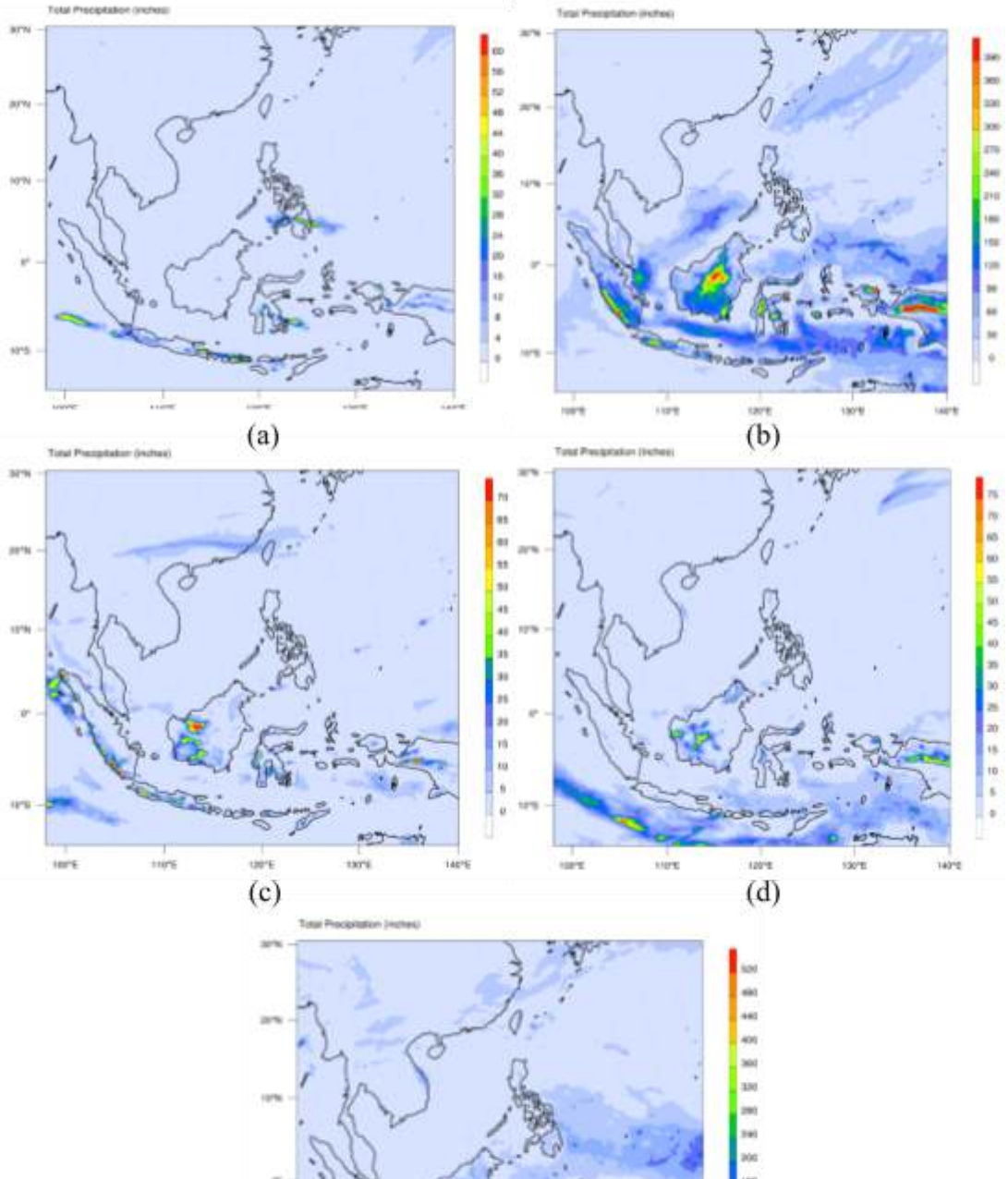

Figure 3.1.7: Total precipitation for SEA region under RCP4.5 during January of 2013 (a), 2030 (b), 2050 (c), 2070 (d) and 2100 (e).

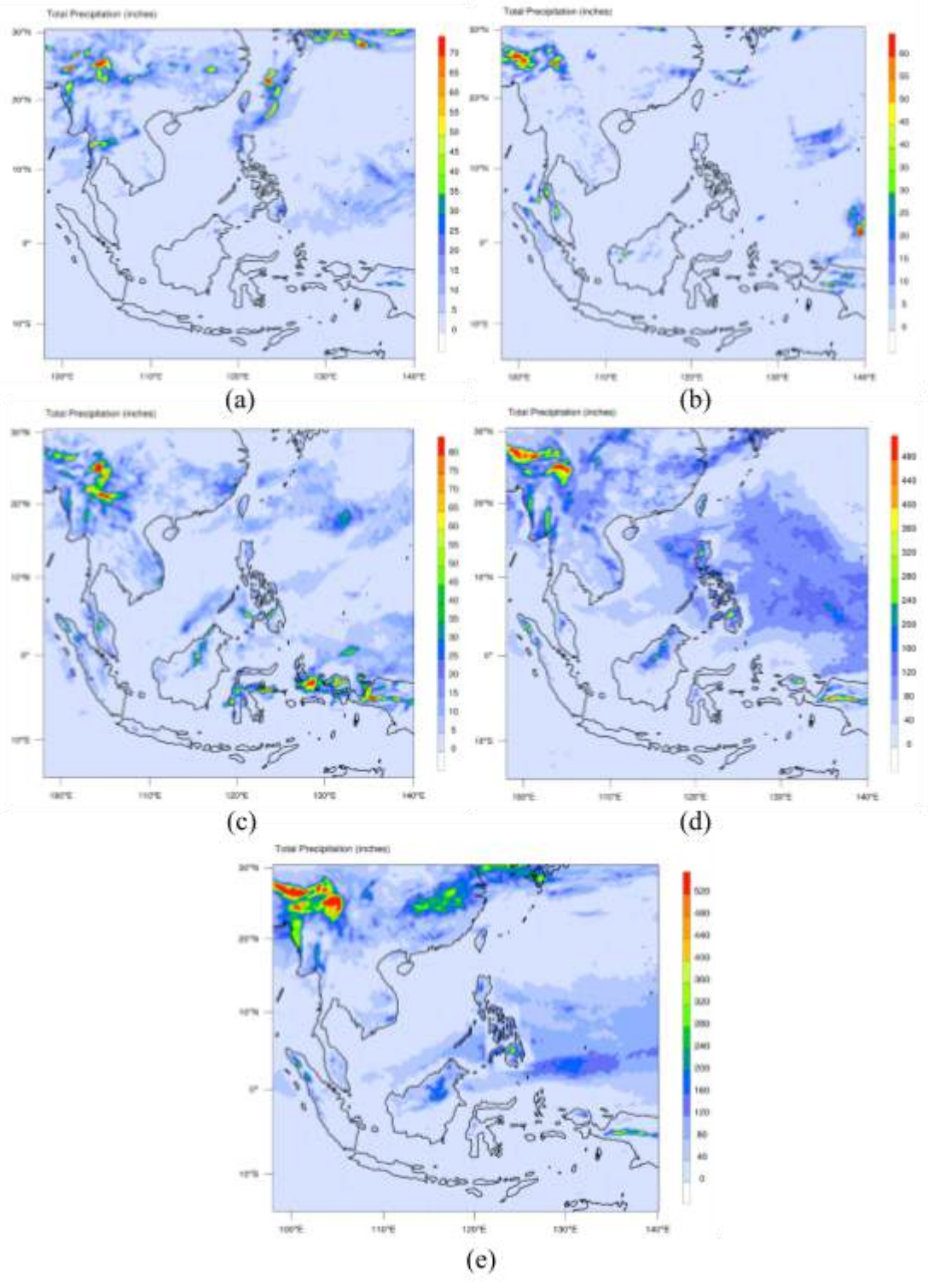

Figure 3.1.8: Total precipitation for SEA region under RCP4.5 during July of 2013 (a), 2030 (b), 2050 (c), 2070 (d) and 2100 (e).

The high projected total precipitation during July most notably distributed over Myanmar with total precipitation of 18.86 inches/day during the baseline period increase to 30.60 (0.62%) and 196.61 (9.42%) inches/day for the mid-century and end of century respectively. While the projected total precipitation for the rest of MSEA shows a value ranging from 6.32 – 11.92 inches/day on baseline period, 20.72 – 31.47 inches/day during mid-century and 86.09 to 145.69 inches/day over the end of century. This projected total precipitation over MSEA however only consistent in Myanmar with the finding of Tangang et al., (2020) who also suggesting an increment between 4-8 % over the same region. The inconsistency and uncertainty in the simulations are difficult to reduce and can be attributed to the shortcomings in the parameterization and boundary condition of WRF model.

3.1.3.2 RCP6.0

The total mean precipitation over SEA region under RCP6.0 during January and July is shown on Table 3.1.6 and it was projected the overall mean total precipitation for January over the whole region is 3.14 inches/day for baseline period (2013) and increase up to 61.32 inches/day in 2030, decrease to 4.72 and 6.96 inches/day during mid-century and 2070 before increase again to 52.72 inches/day over the end of century. This result indicates that there will be a shift in seasonal precipitation over the SEA region during 2030 and 2100. Whereas in July, the projected total mean precipitation increases and consistently high over the future period as relative to baseline period, and the projected total precipitation recorder are 8.50, 112.26, 126.53, 103.64, and 131.79 inches/day for all respective time slices.

Table 3.1.6: Total Precipitation of SEA under RCP6.0

Year	Month	Total Precipitation (inches/day)	Changes (Inches)	Changes rate (x 100%)
2013	**January**	3.14	-	-
	July	8.50	-	-
2030	**January**	61.32	58.17	18.52
	July	112.26	103.77	12.20
2050	**January**	4.72	1.58	0.50
	July	126.53	118.04	13.88
2070	**January**	6.96	3.82	1.21

	July	103.64	95.14	11.19
2100	**January**	52.72	49.57	15.78
	July	131.79	123.29	14.50

Figure 3.1.9 shows that the insular region of SEA has a higher rate of total precipitation in January period, especially in 2030 and 2100. Similar to RCP4.5 scenario, January period shows a lower rate of total precipitation in mainland SEA which has the range between 0 to 8.76 inches/day under this scenario. While in the year of 2030, Indonesia, Philippines, and Malaysia were found at the highest rate of total precipitation at 92.87, 41.19 and 31.66 inches/day. During the end of the century, the insular region of SEA shows the highest rate of 108.75 inches/day in Indonesia, and 70.74 inches/day in Malaysia, except for Philippines as it has a moderate rate in 2100 (with 27.58 inches/day) but the highest rate was in 2030 (with 41.19 inches/day). Details on this total precipitation under RCP6.0 are shown in Appendix 3.1.1E.

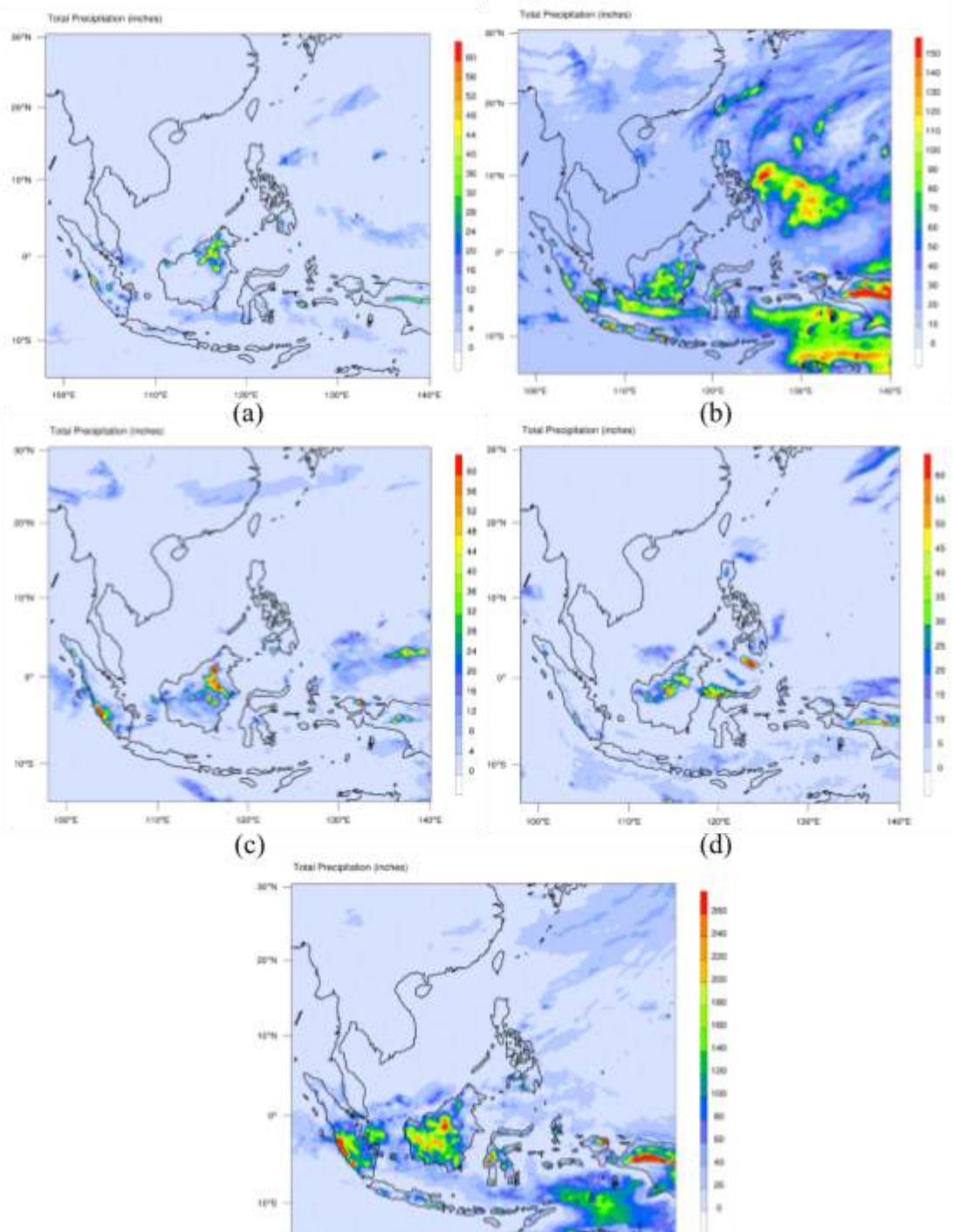

Figure 3.1.9: Total precipitation for SEA region under RCP6.0 during January of 2013 (a), 2030 (b), 2050 (c), 2070 (d) and 2100 (e).

Nevertheless, the projected total precipitation over SEA shows a higher value in July compared to January as shown in figure 3.1.10. During the end of the century, RCP6.0 scenario projected higher rate of total precipitation in all SEA countries by comparing to RCP4.5 scenario, with a range between 40.26 to 406.66 inches/day in July period. The higher precipitation rate is distributed on the upper domain area and

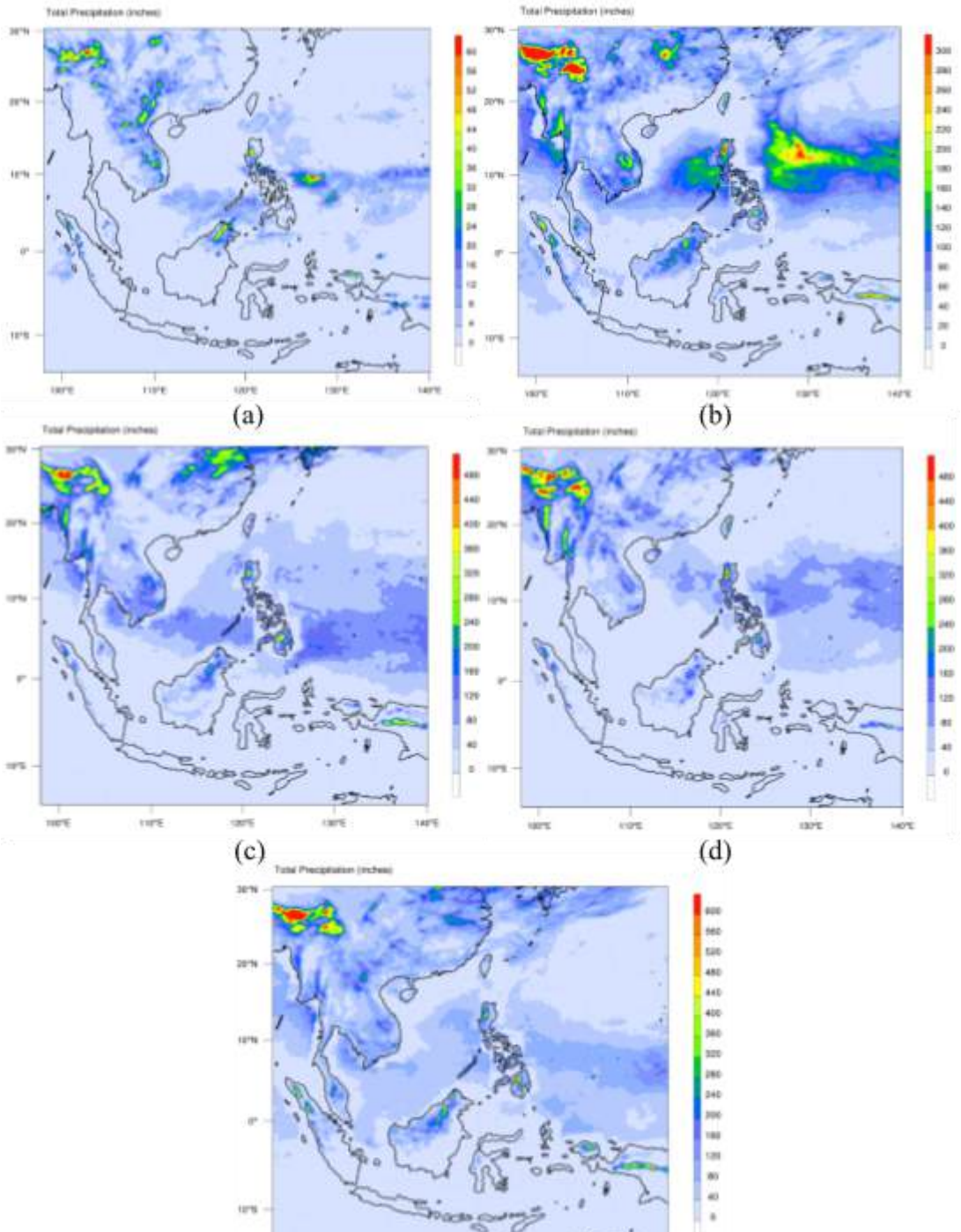

Figure 3.1.10: Total precipitation for SEA region under RCP6.0 during July of 2013 (a), 2030 (b)2050 (c), 2070 (d) and 2100 (e).

scattered over the ocean. More rainfall over sea area as compared to the land area can be associated with warm surface water, and eventually trigger the local process such as convection. Similar to RCP45, the highest projected total precipitation during July most notably distributed over Myanmar with total precipitation of 7.04 inches/day during the baseline period, before increase to 197.37 (27.01%) and 205.04 (28.10%) inches for the mid-century and end of century respectively.

A study by Serreze and Barry (2010) suggests that SEA region influenced by the monsoon which has a large-scale seasonal reversal of the wind regime. Also, the projected total precipitation in SEA projected in this study revealed a higher rate in July compared to January, which can be explained by the monsoon system in SEA as the monsoonal areas receive summer rainfall maximums (Serreze and Barry, 2010). In term of seasonal monsoon in SEA, it is largely characterized by the asymmetric seasonal march of maximum convection from the northern parts of the region during the summer monsoon to the southern parts of SEA during the winter monsoon (Chang et al. 2005; Robertson et al. 2011). Therefore, mainland SEA has the maximum rainfall summer monsoon (July) insular region of SEA experience maximum rainfall during winter monsoon (January) (Chang et al. 2005)

3.1.3.3 RCP8.5

Under RCP8.5 scenario, the projected total precipitation in SEA was found at 5.49, 126.28, 108.02, 4.28 and 63.75 inches/day in 2013, 2030, 2050, 2070 and 2100 during January (Table 3.1.7). Relative to baseline period (2013), the mean total precipitation was increased by 18.67% and 10.61% during mid and end of century. The pattern of the total precipitation projected in SEA was not consistent with other climate scenario used in this study during the projected period and the high variability of total precipitation could also probably due to climate forcing used during simulation, ENSO phenomenon (Hidayat and Kizu 2010; van der Linden et al. 2016; Birch et al. 2016; Kim et al. 2017; Xavier et al. 2020) and distribution and also number of tropical cyclone (Chatomonsal et al., 2011) which are not resolved in the model.

In early (2030) to mid of century of January, the insular region of SEA will experienced high increase of rainfall (figure 3.1.11) with increment rate of 15.74% (from 8.04 to 134.77 inches/day) and

15.85% (to 135.67 inches/day) for Malaysia, while increment rate of 26.49% (from 9.75 to 268.24 inches/day) and 14.57% (to 160.70 inches/day) in Indonesia, and increment rate of 22.19% (from 3.35 to 77.75 inches/day) and 30.87% (to 106.84 inches/day) over Philippines for 2030 and 2050 respectively. However, toward the end of century these insular regions only experienced a slight increment amount of rainfall with 2.37% increment (from 8.04 to 27.20 inches/day) in Malaysia, 8.10% (from 9.75 to 88.86 inches/day over Indonesia and 9.12% (from 3.35 to 33.95 inches/day) over Philippines respectively.

Table 3.1.7: Total Precipitation of SEA under RCP8.5

Year	Month	Total Precipitation (inches/day)	Changes (Inches)	Changes rate (x 100%)
2013	**January**	5.49	-	-
	July	131.59	-	-
2030	**January**	126.28	120.79	22.01
	July	129.12	-2.47	- 0.01
2050	**January**	108.02	102.53	18.67
	July	138.79	7.20	0.05
2070	**January**	4.28	-1.21	- 0.22
	July	119.88	-11.72	- 0.08
2100	**January**	63.75	58.26	10.61
	July	49.66	-81.94	- 0.64

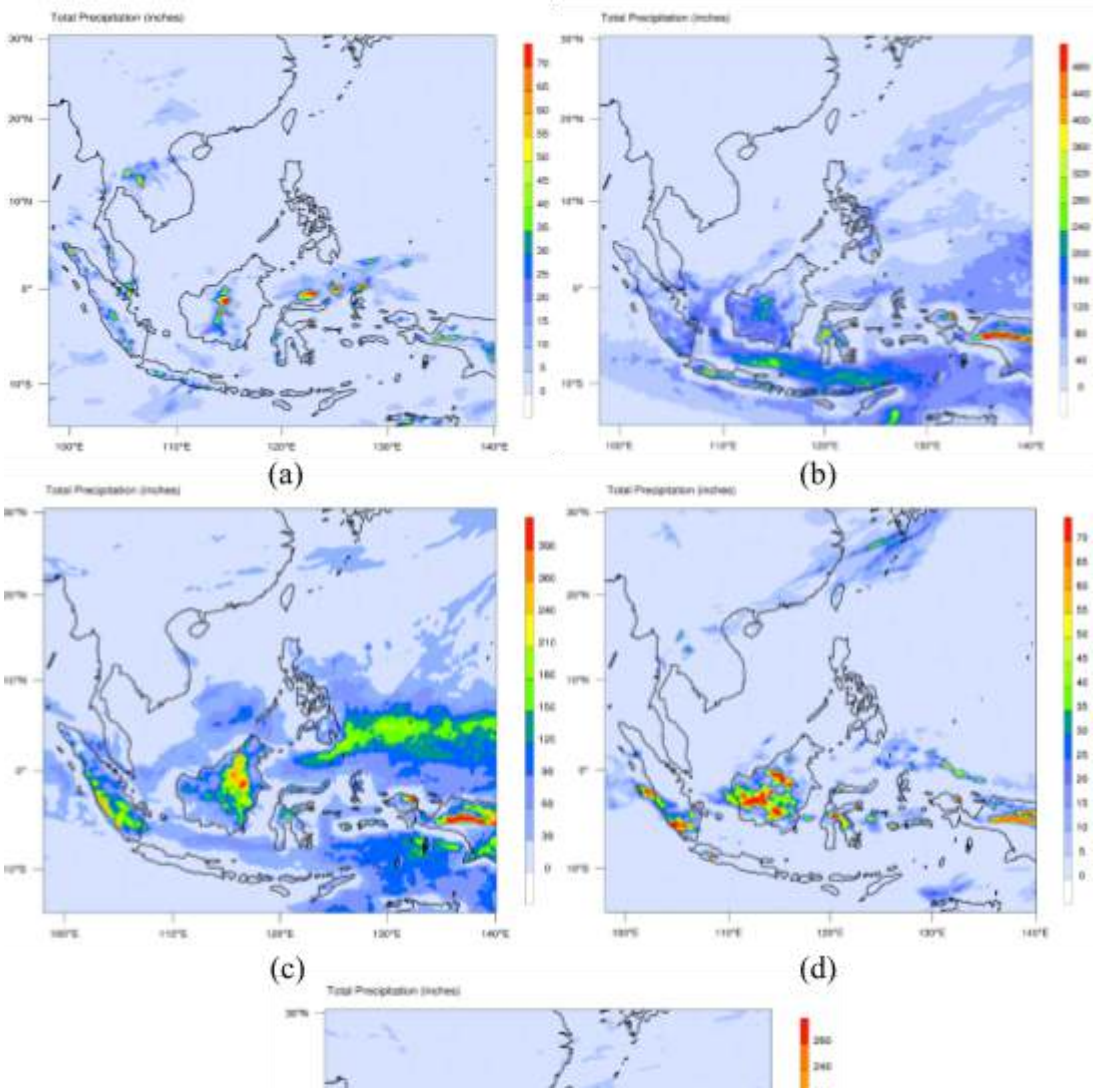

Figure 3.1.11: Total precipitation for SEA region under RCP8.5 during January of 2013 (a), 2030 (b), 2050 (c), 2070 (d) and 2100 (e).

Whereases in July (figure 3.1.12), the projected simulation of RCP8.5 estimated a higher consistently amount of total precipitation in SEA compared to January period, with total projected precipitation in 2013, 2030, 2050 and 2070 of 131.59, 129.12, 138.79, 119.88 inches/day respectively. Yet,

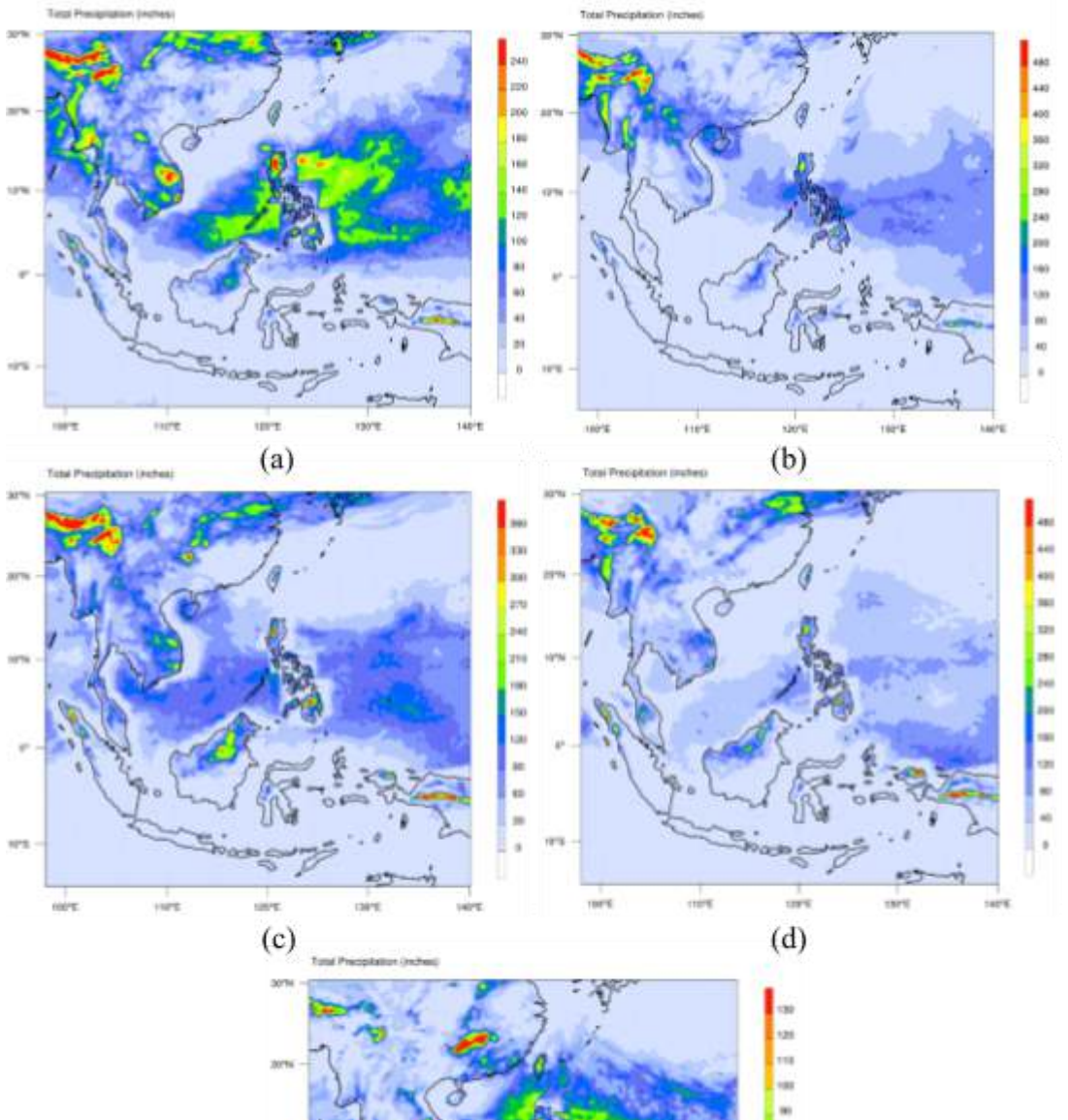

Figure 3.1.12: Total precipitation for SEA region under RCP8.5 during July of 2013 (a), 2030 (b), 2050 (c), 2070 (d) and 2100 (e).

at the end of century, the total mean precipitation reduced notably by -0.64% (from 131.59 to 49.66 inches/day). It is speculated that the reduced amount of rainfall in SEA during July might be due to the increased dry spell length which probably related back to the reduction of cloudiness (Marengo et al., 2009). The reduction of total projected precipitation during July under this RCP8.5 was consistent with the finding of Tangang et al., (2020) which also highlighted a reduction of mean precipitation by 10-30% over this region.

As shown in 3.1.12, the overall total high projected precipitation over SEA region in July period also distributed over mainland SEA and at the centre of the domain. Cambodia was expected to receive highest amount of rainfall with 299.06 inches/day during baseline period, 342.36 inches/day during mid-century (with increment rate of 0.14%) and reduced to 108.50 inches/day (reduction rate of - 0.63%) over the end of century. The trend was similar, but the change was smaller in other part of MSEA (see Appendix 3.1.1F for more details). The changes in total precipitation in Philippines was also to be highlighted with total projected precipitation of 295.67 inches/day on baseline period, to 223.13 inches/day (decrease by – 0.24%) in mid-century and 113.45 inches/day (decrease by – 0.61%) towards the end of century.

However, in Indonesia, though it was projected with the lowest rate of total precipitation among the SEA countries under RCP8.5 scenario with 19.95 inches/day on 2013, the mean total precipitation was expected to increase at 0.38% (to 27.61 inches/day) before decrease by – 0.81% (to 3.77 inches/day) toward the mid and end of century. Recent study of (Tangang et al., 2020) revealed that the decrement in total precipitation in Indonesia during this period was brought by the increasing drying condition. Thus, by the end of century, the projected total precipitation during July over SEA region were slightly lower

than previous period, which might be related to the reduction in thick cloud cover, soil moisture content, water availability and evaporation rate (Held and Soden, 2006; Donat et al., 2016;2019; Norris et al., 2019).

3.1.4 Climate Change Over Borneo Island

Borneo is one of the regions in Southeast Asia that vulnerable regions to climate change and contributing significantly to the world greenhouse gas emissions Generally long coastlines (the third largest island in the world) and heavily populated in low-lying areas make this island extremely vulnerable to weather extremes and rising sea levels associated with global warming. A global warming increase of 1.5 degrees Celsius will cause rising seas, dangerous flooding, and changing rain patterns leading to violent typhoons and drought (IPCC, 2018). The first major assessment from climate experts (IPCC, 2013) in nearly a decade predicts no end to rising temperatures before 2050 unless greenhouse gas emissions are slashed. Therefore, Borneo Island needs to mount stronger climate defences.

This Borneo Island could shift to a "new climate regime" by the end of the century, when the coolest months would be warmer than the hottest summer months (ADB, 2017). The island of Borneo is projected to be severely affected by climate change - increased risk of floods and forest fires activity (ADB, 2016). Between 1970 and 2013, Malaysian Borneo (Sabah and Sarawak) regions experienced surface mean temperature increase of 0.14°C–0.25°C per decade and expected to rise under future climate change scenarios. In this part, the climate change projections in term of surface temperature and total precipitation for Borneo Island are presented based on RCP 4.5 and RCP 8.5 climate scenarios. The climate change scenarios were analysed for the year of 2013 (baseline), 2050, and 2100.

The average monthly variations of surface temperatures and temperature changes projection over Borneo Island under climate change scenarios (RCP4.5 and RCP8.5) are shown in Table 3.1.8. While figure 3.1.13 shows the spatial distribution of monthly average of surface temperature over Borneo Island under RCP4.5 and RCP 8.5 scenarios, while Figure 3.1.14 shows the surface temperature changes (^{o}C) over the region. Spatially, higher means surface temperature over the coastal waters than over the land in both scenarios, with much higher changes under RCP8.5 and more pronounced at the end of the century. At the mid- and end of the century the temperature changes are in the range of -1.1 -2.1 ^{o}C and 0.2 – 4.17 ^{o}C, respectively.

Table 3.1.8 Average monthly variation of surface temperature (^{o}C) and changes projections over Borneo Island under RCP 4.5 and RCP8.5 for the year 2050 and 2100

Year	RCP4.5	Changes	RCP8.5	Changes

2013	25.14 – 27.74	Baseline	25.94 – 27.76	Baseline
2050	25.88 – 28.82	-0.5 – 1.6	25.80 – 28.92	-1.1 – 2.1
2100	25.94 – 29.59	-0.8 – 2.3	26.47 – 30.47	0.2 – 4.17

In term of precipitation, the average monthly variation of total precipitation (mm/day) and precipitation changes (mm/day) projection over Borneo Island under climate change scenarios (RCP4.5 and RCP8.5) are shown in Table 3.1.9. Meanwhile, the figure 3.1.15 depicts the spatial distribution of total precipitation over Borneo Island under RCP4.5 and RCP 8.5 scenarios, and the figure 3.1.16 shows the total precipitation changes (mm/day) over the region as relative to the baseline. Spatially, higher variability of total precipitation over the region was observed and comparatively more pronounced at the end of the century under RCP8.5.

Spatially, both RCP4.5 and RCP8.5 projection show that the total projected precipitation will decrease over time. The reduction is noticeable during the mid of century in RCP8.5 projection and as much as 55% of total precipitation reduction was simulated during the mid-century while 67% during the end of century respectively. The reduction of total projected precipitation over Borneo region however is less pronounced under RCP4.5 scenario with simulated of 7% reduction during mid of century and 50% at the end of century respectively. The reduction of total precipitation is parallel with the increase of overall surface temperature over this region.

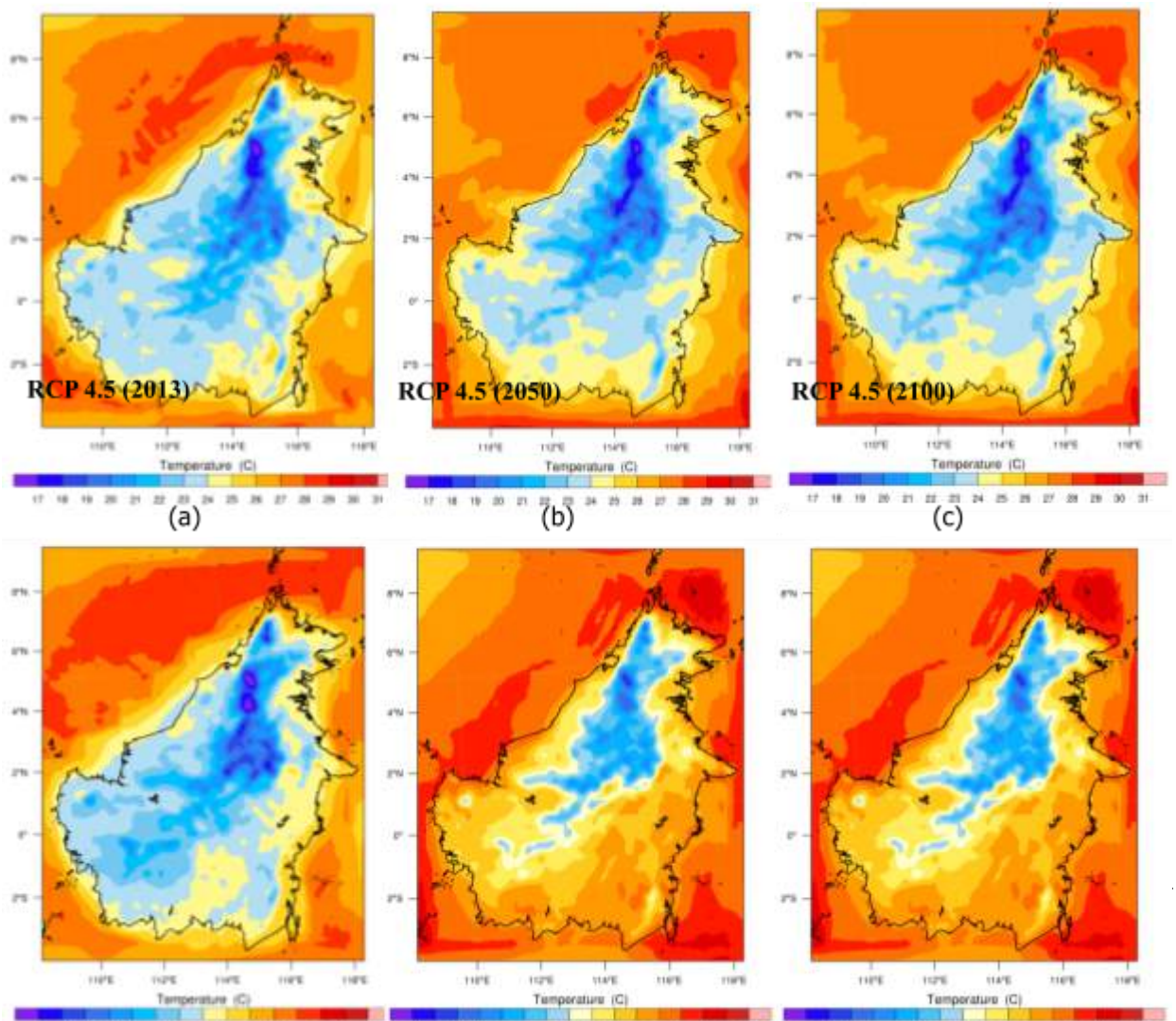

(d) (e) (f)

Figure 3.1.13 The spatial distribution of monthly average of surface temperature (°C) over Borneo Island under RCP 4.5; (a) 2013, (b) 2050, (c) 2100 and RCP8.5; (d) 2013, (e) 2050, (f) 2100.

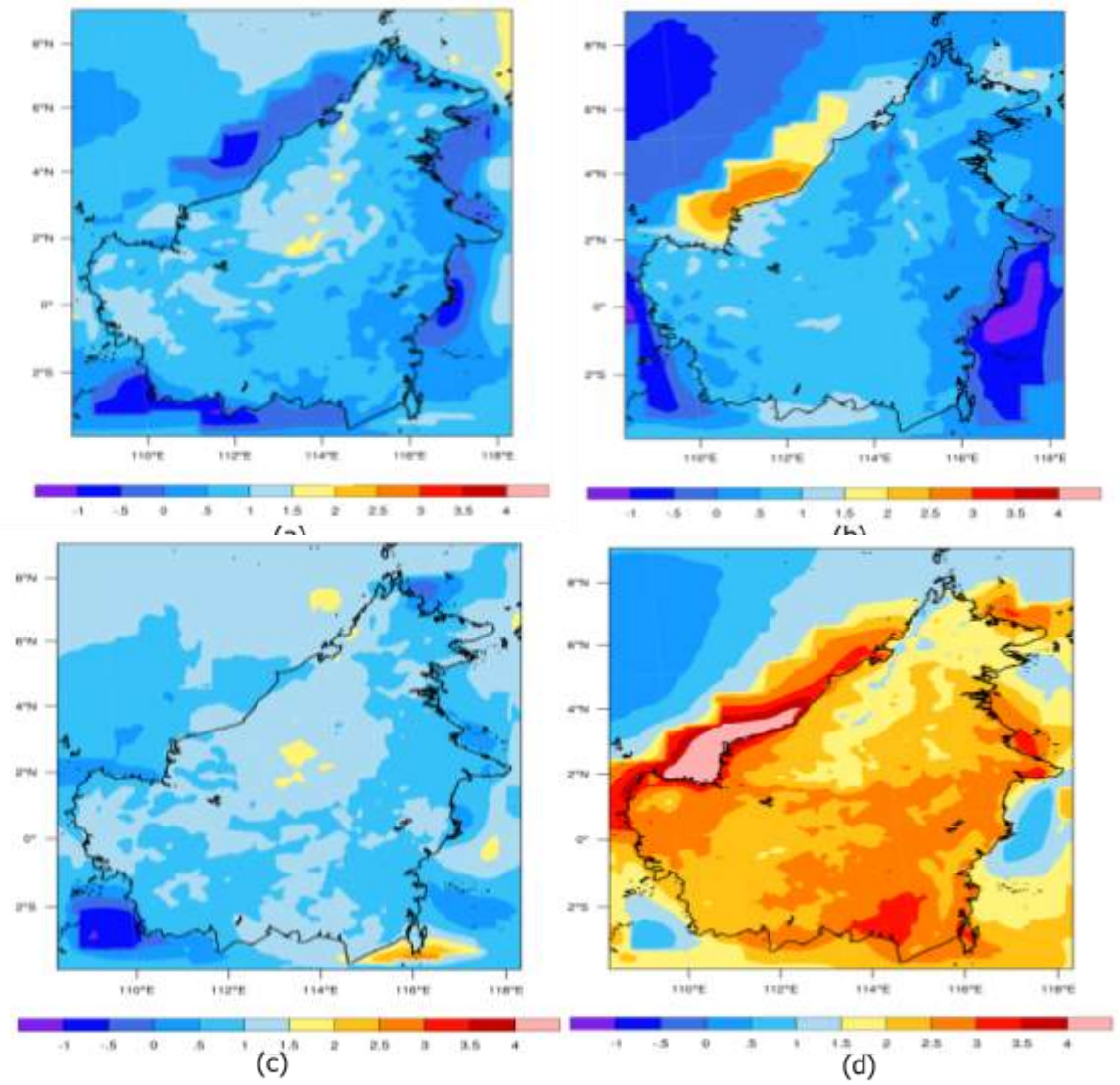

Figure 3.1.14 Spatial distribution of monthly average of surface temperature changes (°C) over Borneo Island under RCP 4.5 and RCP8.5; (a) and (b) for the year 2050, (c) and (d) for the year of 2100

Table 3.1.9 Average monthly variation of total precipitation (mm/day) and changes projections over Borneo Island under RCP 4.5 and RCP8.5 for the year 2050 and 2100

Year	RCP4.5	Changes	RCP8.5	Changes
2013	2.39 – 33.46	Baseline	3.79 – 35.67	Baseline
2050	2.58 – 65.87	0.19 – 32.41	1.70 – 40.70	-2.09 – 5.03
2100	1.11 – 42.40	-1.28 – 8.94	1.25 – 70.95	-2.54 – 35.28

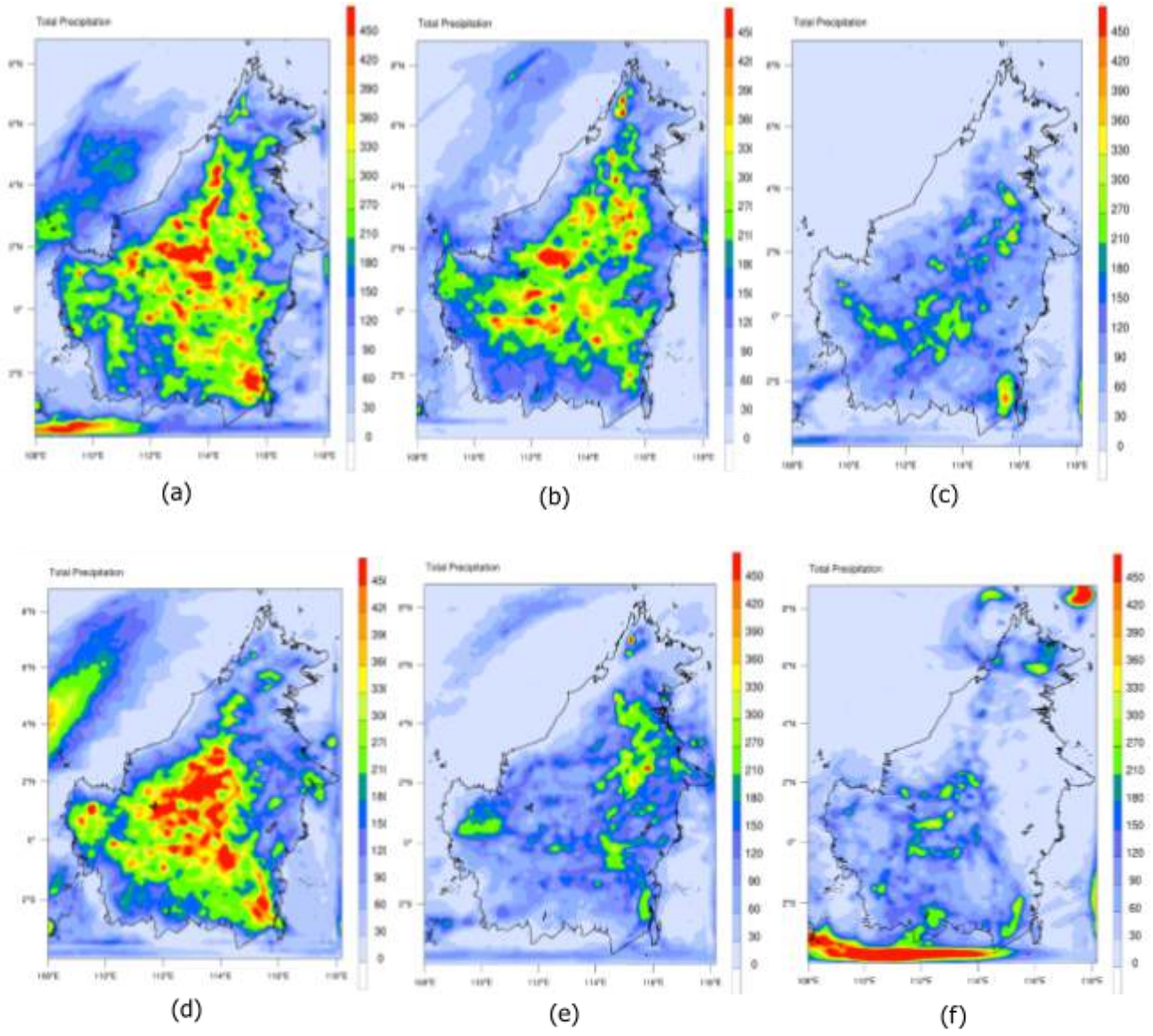

Figure 3.1.15 The spatial distribution of monthly average of total precipitation (mm/day) over Borneo Island under RCP 4.5; (a) 2013, (b) 2050, (c) 2100 and RCP8.5; (d) 2013, (e) 2050, (f) 2100.

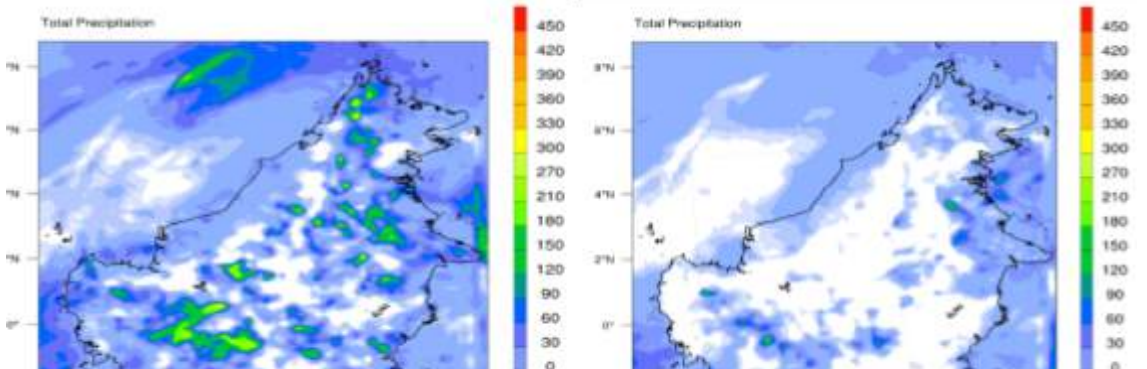

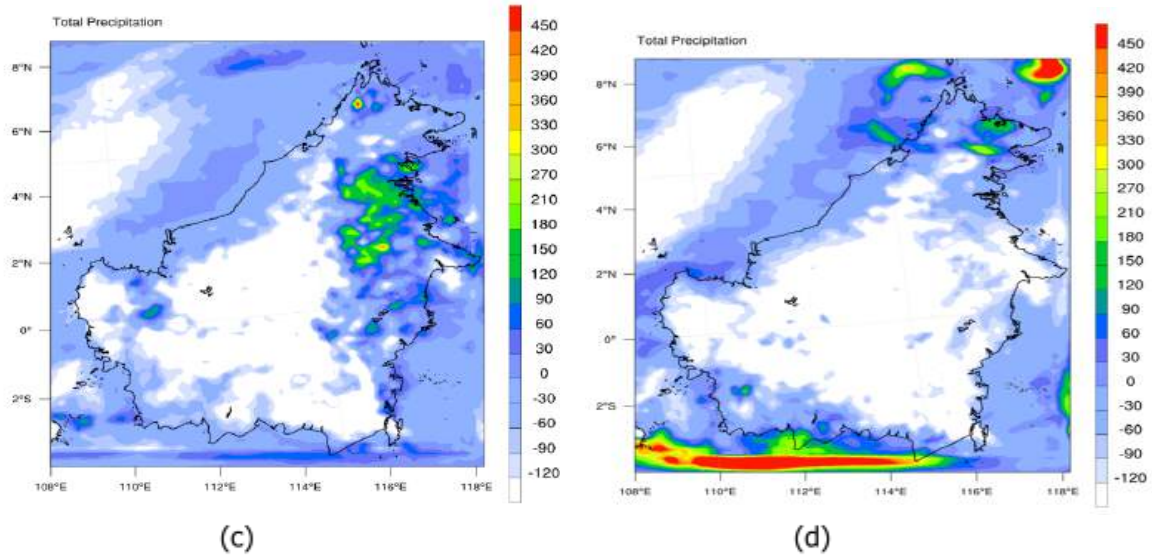

Figure 3.1.16 Spatial distribution of monthly average of total precipitation changes (mm/day)) over Borneo Island under RCP 4.5 and RCP8.5; (a) and (b) for the year 2050, (c) and (d) for the year of 2100.

3.2 Biomass Burning Emissions in Southeast Asia

3.2.1 Indochina (Mainland SEA-MSEA)

3.2.1.1 Land Cover Classification of MSEA

Land cover is the physical and biological characteristics of Earth's cover, which includes the distribution of vegetation, water, soil and some other physical components (Kaul and Sopan, 2012; Roy P. and Roy A., 2010). The land cover of MSEA in 2013 was obtained from MODIS Land Cover Satellite, MCD12Q1, classified under IGBP legends (Figure 3.2.1), which were then reclassified from the 17 land classes in IGBP into eight classes as shown in Table 3.2.1.

Table 3.2.1: Area of each land cover class in Indochina in 2013

Land cover	Division (km^2)					Total	Percentage (%)
	Cambodia	Laos	Myanmar	Thailand	Vietnam		
Evergreen Forests	40488.5	135190.45	218219.45	90089.91	84685.72	568674.03	29.51

Deciduous Forests	10177.5	2068.97	36302.34	16888.41	1520.52	66957.74	3.48
Mixed Forests	4007.98	2143.43	81729.37	4879.03	1597.16	94356.97	4.90
Shrublands	13596.1	53238.3	111294.31	85537.29	65696.81	329362.81	17.09
Savannas	58870.9	32721.62	71258.00	92710.17	87489.36	343050.05	17.80
Wetlands	1942.44	442.5	7508.88	5621.01	12011.89	27526.72	1.43
Croplands	48718.7	3739.74	137252.47	211513.3	67872.86	469097.07	24.35
Others	4173.64	1034.33	6394.96	8195.06	7999.35	27797.34	1.44
Total	181975.76	230579.34	669959.79	515434.17	328873.67	1926822.7	100

Indochina is mainly covered by evergreen forests, croplands, savannas and shrublands. 568 674 km^2 of land is covered by evergreen forests, which is 29.5% of the MSEA land. Croplands made up 24.35% of MSEA land cover, followed by savannas 17.8%, and shrublands 17.09%. Evergreen forests are forests with green leaves all year long, in contrast with deciduous forests which change leaves colour or falling leaves (Dreiss & Volin, 2014). Cropland is a major land cover in MSEA, as agricultural production is the main contributor to economic growth in Southeast Asia, and extensive growth of agricultural sector had happened especially in 1900s to 2010, corresponding to increase of food demand associated to population growth (Booth, 2018). Croplands cover 41.04% of land in Thailand, which is the largest land cover class, 20.49% in Myanmar and 26.77% in Cambodia, which is third largest land class in these countries. In Vietnam, 20.64% of lands are croplands.

In Cambodia and Vietnam, savanna has the highest area of land cover, which in Cambodia covers 32.35% and Vietnam 26%, while in Thailand and Laos, savanna comes second and third respectively, dominating 17% of Thailand and 14% of Laos. Savannas are thought to be extensive grasslands with sporadic trees (Ratnam et al., 2016), but they can be ranging from grasslands with sporadic trees to thick open canopy forests with grassy forest floor (Hirota et al., 2011; Staver et al., 2011; Lehmann et al., 2014). Savannas are known to be formed due to forest degradation associated with human mismanagement (Veldman, 2016). Logging activities since 19th century and associated forest fires, shifting cultivation with short fallow time since thousands of years ago and anthropogenic fires for vegetations were the main activities contributing to forest degradation into savanna (Miettinen et al., 2014).

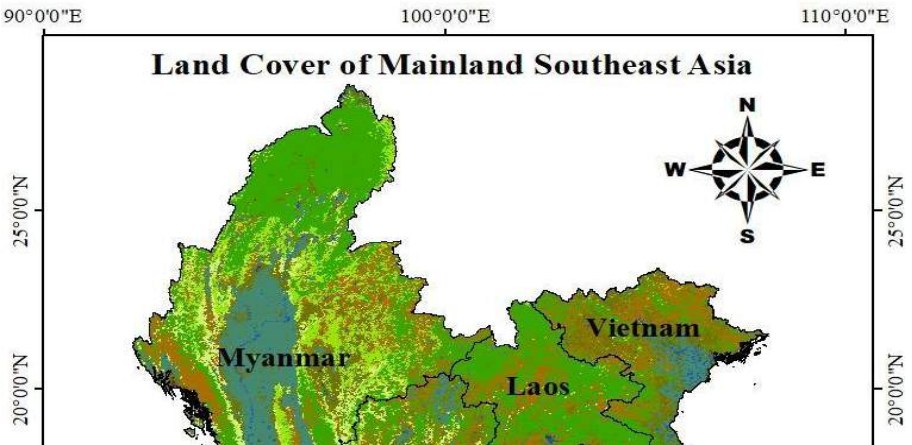

Figure 3.2.1: Land Cover of Indochina in 2013 from MODIS MCD12Q1

3.2.2.2 Accuracy Assessment

To determine the reliability of IGBP land cover classification data obtained from MCD12Q1, an accuracy assessment was conducted using confusion matrix to obtain an overall accuracy and Kappa's value through comparison of the 408 stratified random sampling points generated from ArcGIS with Google Earth Pro historical imagery of year 2013. The overall accuracy obtained is shown in Table 3.2.2, and the Kappa analysis is shown in Appendix 3.2.1A. The overall accuracy obtained is 86.55%, while Kappa coefficient obtained is 0.83, both showing strong reliability of data. From (Appendix 3.2.1A), the level of agreement b ough both values show high r cy is calculated directly fror count into other aspects, whi n matrix, taking into account iera and Garrett, 2005).

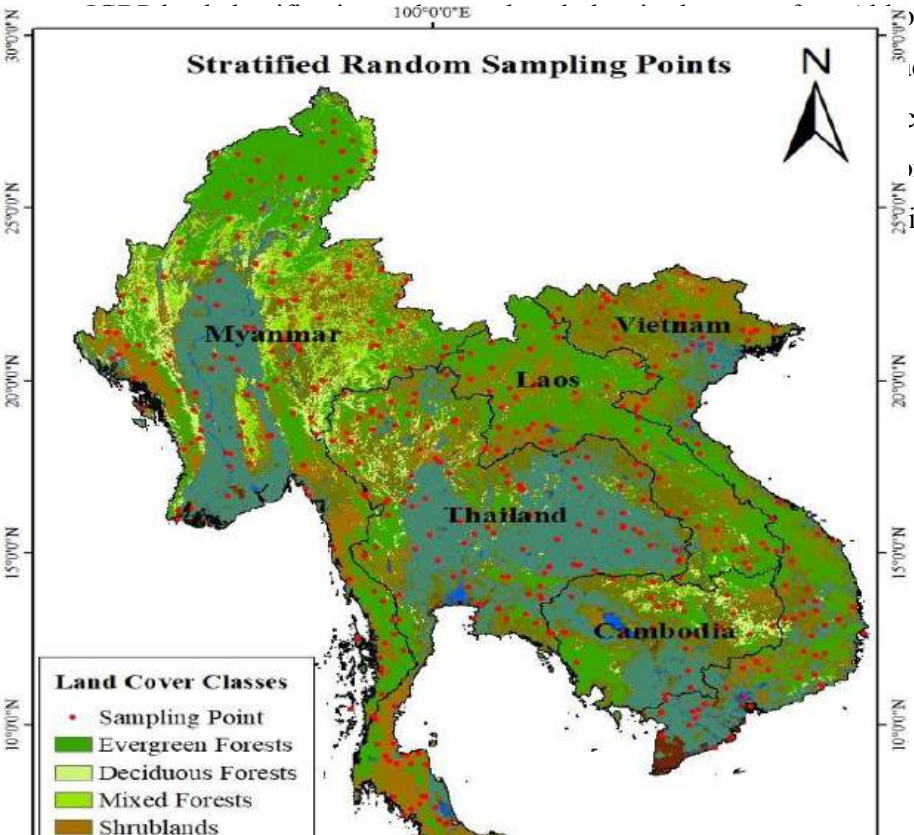

Figure 3.2.2: Stratified Random Sampling Points

Table 3.2.2: Overall Accuracy of Land Cover Classification of MSEA in 2013

Land Cover Type	User's Accuracy (%)	Producer's Accuracy (%)	Overall Accuracy (%)
Evergreen Forests	97.46	94.26	86.55
Deciduous Forests	100.00	100.00	
Mixed Forests	100.00	100.00	
Shrublands	82.61	77.03	
Savannas	70.42	92.59	
Wetlands	90.00	75.00	
Croplands	86.60	89.36	
Others	50.00	26.31	

From Google Earth Pro imagery, evergreen forests and deciduous forests can be identified by shifting the timeline, as evergreen forests are green and denser as compared to deciduous forests which is less dense and lose their leaves in cold and dry season (Givnish, 2002). A mix forest is a forest with two or more types of species, consisting of both coniferous and deciduous broadleaf forests (Bravo-Oviedo et al., 2013). Overall, there were no specific class consistently being misclassified. Land class 8 has the highest proportion of misclassified land, as most of the points were at the border of land class type. Some croplands were misclassified into wetlands, and some shrublands were found to be misclassified as savannas. Most of the wetlands were found to be located near the coastal lagoons and bays. On the other hand, shrublands have denser trees as compared to savannas. According to Afrin et al. (2019), land cover is an important tool in managing environmental issue, and although MODIS with unrestricted access and corrected with fine quality is one of the commonly applied satellite data, regional studies have lower accuracy due to its coarser resolution of 250m.

3.2.2.3 Total Emission in MSEA

a) Burned Area in MSEA

Biomass burning in Indochina for 2013 was derived from MODIS land cover type, MCD12Q1 version 6 product, which has temporal resolution of one-year, spatial resolution of 500m x 500m, and burned area product, MCD64A1 with temporal resolution of one month, and spatial resolution of 500m. MCD64A1 is produced from satellite through surface reflectance, daily fire detections as well as land cover in order to label burn cells with burn data to portray burned areas (Shi and Yamaguchi, 2014). Burned area with respective land cover type (Figure 3.2.3) was obtained from the estimation and calculation using ArcGIS, which is important in determining the annual dry biomass burned.

Annual dry biomass burned on the other hand, is the result from multiplication of burned area, combustion efficiency and fuel loading relevant for each land cover type. Figure 3.2.3 and Figure 3.2.4 provides a visual of burned area and land cover type. While, Table 3.2.3 shows the burned area and annual dry biomass burned for each land cover type for the whole MSEA. Savanna land has the largest area burned in 2013, followed by croplands and deciduous forests. However, deciduous forests have the highest mass burned in 2013 of about 22477.35 Gg/year followed by mixed forests with 8146.96 km^2, and evergreen forests. Although large area of savannas was burned, the annual dry mass burned was third lowest, and croplands with second highest area burned has second lowest dry mass burned. More details for each country can be referred in Appendix 3.2.2A-E and Appendix 3.2.5A.

Larger burned area does not depict more biomass burned, as mass of dry biomass burned is influenced by fuel loading and combustion factor or combustion efficiency. Fuel load is the accessible fuel during biomass burning, or the available biomass density above ground surface, while combustion factor is the fraction of burned fuel, or in this case, biomass above ground surface (Shi and Yamaguchi, 2014; Zhou et al., 2017). Although savannas have high combustion factor, the fuel loading is low as compared, which explains the low burned mass of savannas. Besides, although evergreen forests land type has second lowest burned area and has low combustion factor, it has very much higher fuel loading, therefore higher dry mass burned. Forests contains abundant amount of oxygen, especially evergreen forests which are denser can contribute to higher oxygen content. According to Hungerford et al. (1990), different typ and below ground surfa ecipitation can affect th s burned is shown in Ap

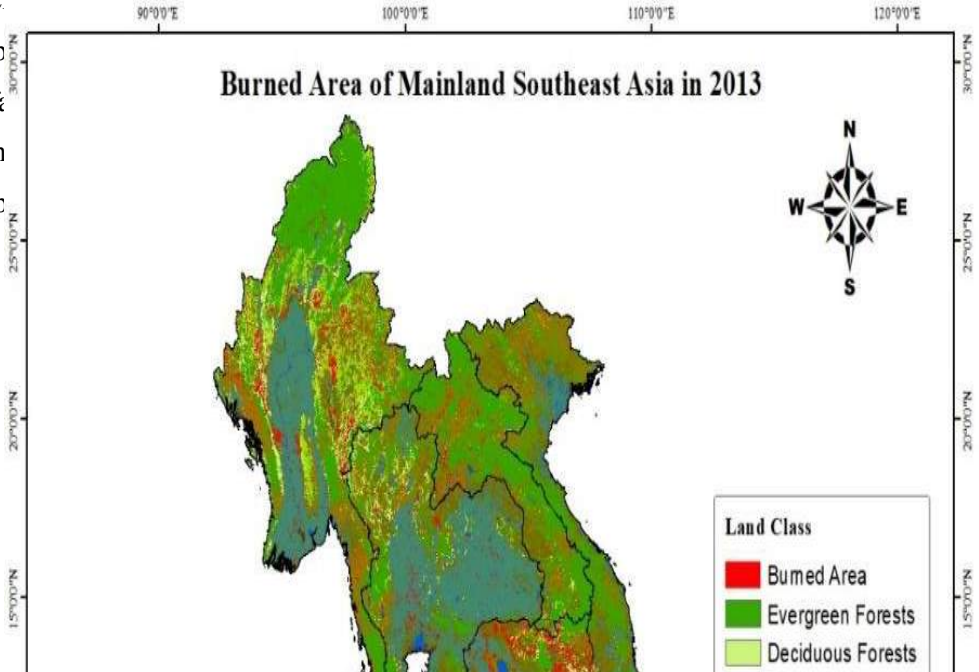

Figure 3.2.3: Burned Area and Land Cover Types of Continental SEA in 2013

Table 3.2.3: Annual Amount of Dry Biomass Burned of MSEA in 2013

Land Cover Types	Burned Area (km^2)	Annual Dry Biomass Burned (Gg/year)
Evergreen Forests	7682.20	13798.77
Deciduous Forests	12513.84	22477.35
Mixed Forests	8146.96	14633.58
Shrublands	11647.33	10231.76
Savannas	20659.72	2627.43
Wetlands	69.77	23.02
Croplands	16612.36	598.04
Total	77332.18	64389.95

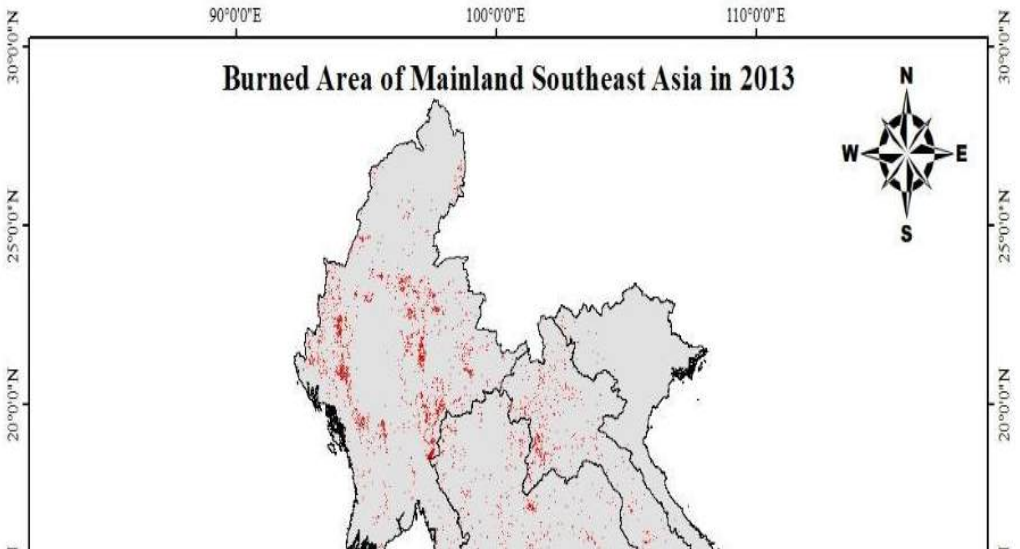

Figure 3.2.4: Total Burned Area of Continental SEA in 2013

b) Sources of Biomass Burning Emission

The emissions of biomass burning of continental SEA in 2013 are shown in Table 3.2.4, and the annual typical pollutant emission from different land cover sources in 2013 is shown in Figure 3.2.5, while the contribution of different land cover sources to annual biomass burning emissions are shown in Figure 3.2.6. The annual emission of CO_2, CO, CH_4, NO_x, NH_3, SO_2, PM_{10}, $PM_{2.5}$, EC, OC and NMVOC were 106067.53 Gg, 5952.61 Gg, 288.16 Gg, 133.14 Gg, 80.59 Gg, 52.34 Gg, 768.60 Gg, 697.78 Gg, 35.74 Gg, 481.95 Gg and 862.76 Gg respectively. The highest contribution of annual biomass burning emission in 2013 is from deciduous forests, followed by mixed forests, evergreen forests and shrublands.

Table 3.2.4 Annual biomass Burning Emission Inventory (Gg) by countries in MSEA for 2013

Country	CO_2	CO	CH_4	NO_x	NH_3	SO_2	PM_{10}	$PM_{2.5}$	EC	OC	NMVOC
Cambodia	27607.03	1565.46	74.58	31.10	21.47	14.54	202.91	184.84	9.37	129.52	209.39
Laos	13538.31	689.56	34.56	23.47	7.75	4.67	92.86	78.00	4.12	45.72	136.70
Myanmar	54059.80	3115.91	151.59	62.71	43.51	28.27	398.33	368.87	18.63	262.64	431.92
Thailand	8043.10	434.4	20.56	11.28	5.96	3.76	55.80	50.21	2.68	34.53	60.28
Vietnam	2819.29	147.28	6.87	4.59	1.89	1.10	18.70	15.86	0.93	9.54	24.48
Total	106067.53	5952.61	288.16	133.14	80.59	52.34	768.60	697.78	35.74	481.95	862.76

For all land cover types, CO_2 is the highest concentration of emitted pollutant, followed by CO. Carbon of biomass react with oxygen to produce CO_2 in a complete combustion, other than releasing a proportionate amount of sequestered CO_2 in biomass from photosynthesis (Cherubini et al., 2011). Besides, since biomass is an organic matter which contains high amount of C, and during an incomplete combustion, CO is produced. Figure 3.2.5 shows that deciduous forests is the largest contributor to most of the pollutants emitted (except for NO_x and NMVOC) of which is CO2 (35%), CO (38%), CH_4 (39%), NH_3 (42%), SO_2 (43%), PM_{10} (38%), $PM_{2.5}$ (40%), EC (38%) and OC (43%). Meanwhile, shrublands contribute to highest NO_x emission of 30%, and evergreen forests contribute to highest NMVOC of 38%.

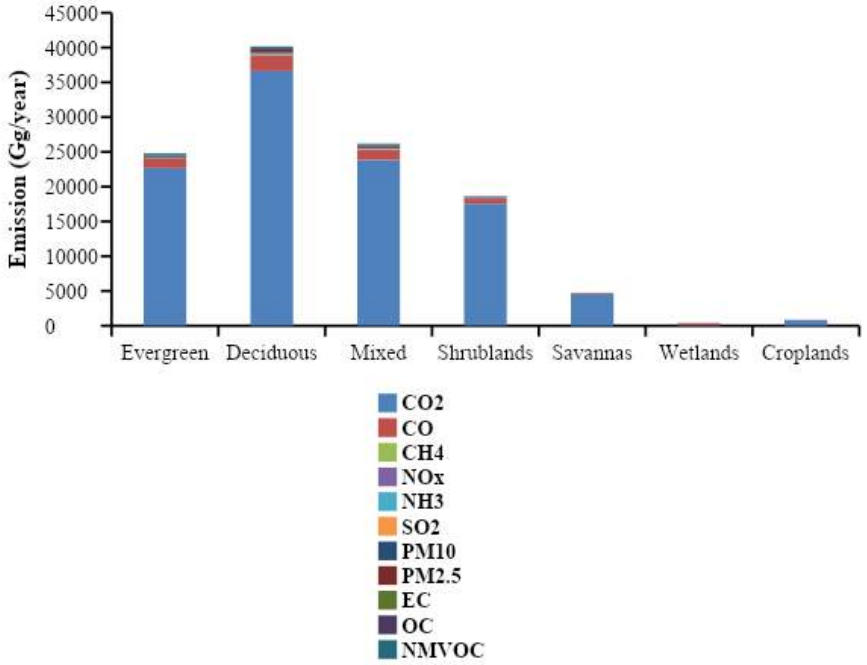

Figure 3.2.5: Annual Typical Pollutant Emission from Different Land Cover Sources in 2013

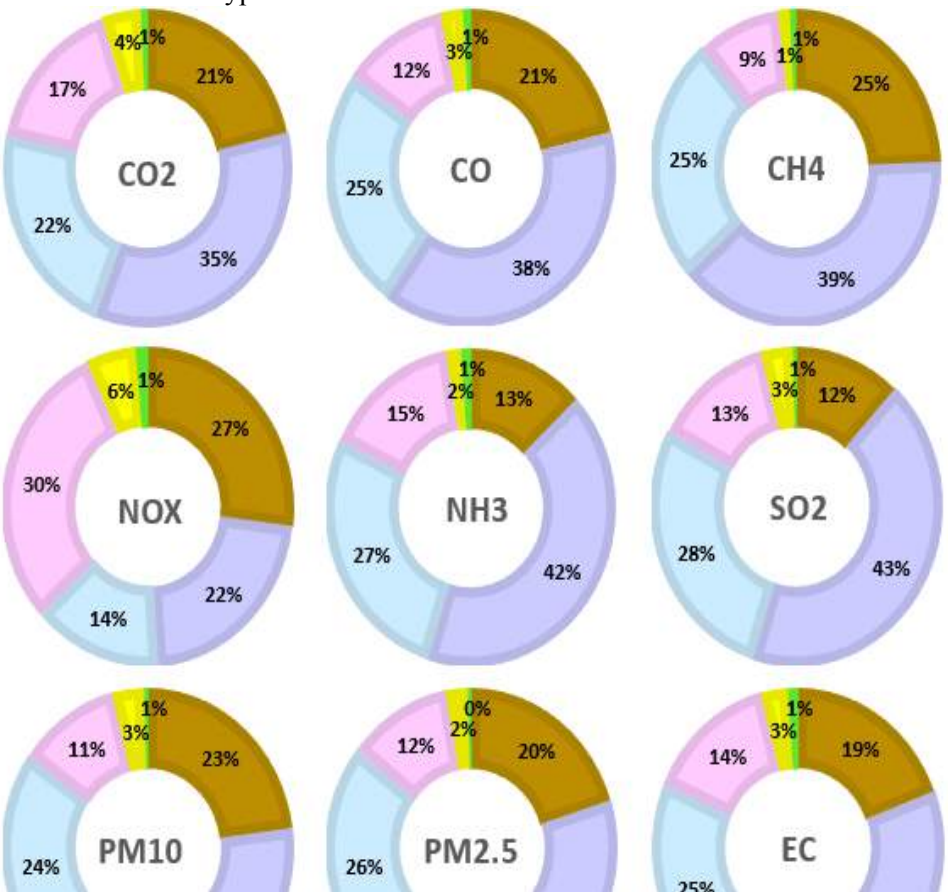

Figure 3.2.6: Contribution of Different Land Cover Type to Annual Biomass Burning Emissions in Indochina in 2013

c) Comparisons of Biomass Burning Emission of MSEA

The landscape in MSEA is characterized by mountainous areas, and swidden agriculture is a consistent threat to indigenous forests. Most BB in mainland SEA is attributed to slash-and-burn agriculture and land clearing, especially during the dry season. Though the distribution of BB in MSEA is inhomogeneous, Myanmar has the highest burned area of 27103.05 km^2, followed by Cambodia 23562.70 km^2, Thailand 9826.15 km^2, Vietnam 9551.57 km^2 and Laos 7283.34 km^2 (Table 3.2.6 – Table 3.2.10). Based on calculation of burned area with total land area of each country, Cambodia has the highest percentage of burned area, 12.95%, followed by Myanmar, 4.05%, Laos 3.15%, Vietnam 2.90% and Thailand 1.91%.

Table 3.2.5 – Table 3.2.9 below shows that forests are the main contributor of biomass burning emission in Cambodia, mainly deciduous forests although deciduous forests cover only 5.59% of the land. 4610.28 km^2 of deciduous forests were burned, covering 19.57% of total burned area. Savanna has the largest burned area in Cambodia, covering 12592.31 km^2 out of total 23562.70 km^2, which is 53.44% of burned area, but less significant contribution of emissions due to the remarkably lower FL of savannas. For Laos, the main sources of biomass burning emissions are evergreen forests and shrublands. Shrublands has the highest burned area of 2823.38 km^2, followed by

evergreen forests 2654.10 km^2 and savannas 1356.72 km^2. Similarly, contribution of savannas to emitted pollutants is less significant, due to low FL.

In Myanmar, forests contributed the highest emission of pollutants in Myanmar, where 56.60% of the 27103.05 km^2 of burned area are forests, followed by shrublands (19.87%), savannas (13.88%) and croplands 9.57%. Meanwhile, Thailand has only 1.91% of total burned area. Croplands have contributed 48.84% of total burned area followed by savannas (19%), and forests (18.88%). In term of emissions, shrublands have the highest emissions after forests although the burned area is less due to high FL and EF. Vietnam has the lowest biomass burning emissions as compared to all other countries in MSEA, although it has larger land area than Cambodia and Laos. Biomass burning emissions are dominated by forests, specifically evergreen and deciduous forests, with small portion by mixed forests, as well as shrublands, savannas and croplands. However, in term of burned area, croplands have the largest burned area of about 78.69% of the total burned area (7515.68 km^2) followed by forests (5.77%) and shrublands (4.08%).

d) Spatial Variations of Biomass Burning Emission

Gridded emission data is beneficial in presenting disaggregated emissions of each pollutant from their point sources in the region, which can better represent the situation of emissions (Oda et al., 2019). Since all the pollutants emissions show similar trend of gridded distribution, $PM_{2.5}$ is taken as example for discussion as $PM_{2.5}$ is a fundamental indicator for air pollution, and main contribution of atmospheric PM is anthropogenic sources, besides posing negative impacts to both human health as well as climate change (Sirignano et al., 2019). Details for other species emission sources are shown in Appendix 3.2.4A-L and Appendix 3.2.5A-B.

Table 3.2.5: Typical Pollutant Emission of Cambodia in 2013 (Gg/year)

Land Cover Types	CO_2	CO	CH_4	NO_x	NH_3	SO_2	PM_{10}	$PM_{2.5}$	EC	OC	NMVOC
Evergreen Forests	3540.31	198.24	10.99	5.60	1.64	0.97	27.58	21.98	1.08	10.13	51.72
Deciduous Forests	13498.0	844.66	41.40	10.77	12.42	8.28	106.0	101.86	4.97	76.19	91.09
Mixed Forests	5084.51	318.17	15.60	4.06	4.68	3.12	39.93	38.37	1.87	28.70	43.67
Shrublands	2645.91	104.85	4.01	6.01	1.85	1.051	13.11	12.18	0.77	10.18	7.40
Savannas	2748.08	94.49	2.40	4.48	0.80	1.09	15.85	10.09	0.64	4.16	14.89
Wetlands	9.73	150.54	2.40	3.36	0.96	1.28	20.02	17.94	0.83	10.09	10.89
Croplands	80.49	4.53	0.17	0.17	0.08	0.02	0.37	0.30	0.04	0.12	0.58
Total	27607.03	1715.48	76.97	34.45	22.43	15.811	222.86	202.72	10.20	139.57	220.24

Table 3.2.6: Typical Pollutant Emission of Laos in 2013 (Gg/year)

Land Cover Types	CO_2	CO	CH_4	NO_x	NH_3	SO_2	PM_{10}	$PM_{2.5}$	EC	OC	NMVOC
Evergreen Forests	7832.66	438.59	24.31	12.39	3.62	2.15	61.02	48.63	2.38	22.41	114.42
Deciduous Forests	614.67	38.46	1.89	0.49	0.57	0.377	4.83	4.64	0.23	3.47	4.15
Mixed Forests	533.91	33.41	1.64	0.43	0.49	0.33	4.19	4.03	0.20	3.01	4.59
Shrublands	4256.09	168.66	6.45	9.67	2.98	1.69	21.08	19.59	1.24	16.37	11.91
Savannas	296.08	10.18	0.26	0.48	0.09	0.12	1.71	1.09	0.07	0.45	1.60
Wetlands	2.33	16.22	0.26	0.36	0.10	0.14	2.16	1.93	0.09	1.09	1.17
Croplands	2.57	0.14	0.0053	0.0055	0.0027	0.00076	0.012	0.0095	0.0012	0.0038	0.019
Total	13538.31	705.66	34.82	23.3	7.85	4.81	95.00	79.92	4.21	46.80	137.86

Table 3.2.7: Typical Pollutant Emission of Myanmar in 2013 (Gg/year)

Land Cover Types	CO_2	CO	CH_4	NO_x	NH_3	SO_2	PM_{10}	$PM_{2.5}$	EC	OC	NMVOC
Evergreen Forests	8601.37	481.63	26.70	13.61	3.98	2.36	67.01	53.40	2.62	24.61	125.64
Deciduous Forests	18644.25	1166.70	57.19	14.87	17.16	11.44	146.41	140.69	6.86	105.23	125.82
Mixed Forests	17736.58	1109.90	54.41	14.15	16.32	10.88	139.28	133.84	6.53	100.11	152.34
Shrublands	8117.62	321.68	12.30	18.45	5.68	3.22	40.21	37.37	2.37	31.22	22.71
Savannas	821.26	28.24	0.72	1.34	0.24	0.33	4.74	3.02	0.19	1.24	4.45
Wetlands	12.37	44.99	0.72	1.01	0.29	0.38	5.98	5.36	0.25	3.02	3.25
Croplands	126.35	7.10	0.26	0.27	0.13	0.037	0.59	0.47	0.0599	0.19	0.91
Total	54059.80	3160.24	152.30	63.70	43.80	28.65	404.22	374.15	18.88	265.62	435.12

Table 3.2.8: Typical Pollutant Emission of Thailand in 2013 (Gg/year)

Land Cover Types	CO_2	CO	CH_4	NO_x	NH_3	SO_2	PM_{10}	$PM_{2.5}$	EC	OC	NMVOC
Evergreen Forests	1689.30	94.59	5.24	2.67	0.78	0.46	13.16	10.49	0.51	4.83	24.68
Deciduous Forests	3280.42	205.28	10.06	2.62	3.02	2.01	25.76	24.75	1.21	18.52	22.14
Mixed Forests	475.91	29.78	1.46	0.38	0.44	0.29	3.74	3.59	0.18	2.69	4.09
Shrublands	1950.04	77.27	2.95	4.43	1.36	0.77	9.66	8.98	0.57	7.50	5.45
Savannas	407.70	14.02	0.36	0.67	0.12	0.16	2.35	1.50	0.10	0.62	2.21
Wetlands	5.90	22.33	0.36	0.50	0.14	0.19	2.97	2.66	0.12	1.50	1.62
Croplands	233.83	13.15	0.48	0.50	0.24	0.069	1.09	0.86	0.11	0.35	1.69
Total	8043.10	456.42	20.91	11.77	6.10	3.95	58.73	52.83	2.80	36.01	61.88

Table 3.2.9: Typical Pollutant Emission of Vietnam in 2013 (Gg/year)

Land Cover Types	**CO_2**	**CO**	**CH_4**	**NO_x**	**NH_3**	**SO_2**	**PM_{10}**	**$PM_{2.5}$**	**EC**	**OC**	**NMVOC**
Evergreen Forests	1004.95	56.27	3.12	1.59	0.46	0.28	7.83	6.24	0.31	2.87	14.68
Deciduous Forests	597.51	37.39	1.83	0.48	0.55	0.37	4.69	4.51	0.22	3.37	4.03
Mixed Forests	18.40	1.15	0.056	0.015	0.017	0.011	0.14	0.14	0.0068	0.10	0.16
Shrublands	586.90	23.26	0.89	1.33	0.41	0.23	2.91	2.70	0.17	2.26	1.64
Savannas	235.40	8.09	0.21	0.38	0.069	0.093	1.36	0.86	0.055	0.36	1.28
Wetlands	9.92	12.89	0.21	0.29	0.082	0.11	1.71	1.54	0.071	0.86	0.93
Croplands	366.21	20.59	0.76	0.78	0.38	0.11	1.70	1.35	0.17	0.54	2.65
Total	2819.29	159.64	7.08	4.87	1.97	1.20	20.34	17.34	1.00	10.36	25.37

In Figure 3.2.7, most of the areas emitted $PM_{2.5}$ at concentration range of 0 to 30 Gg per year, except several areas in Cambodia and Myanmar which have moderately higher emissions, and some high emissions in Myanmar. Higher emissions of pollutant in Myanmar and Cambodia mainly occur in forested area. Emissions of pollutants are mainly distributed at areas with high agricultural activities, dense population with lower income, as well as high cultivation and forest resources (Zhou et al., 2017; Reddington et al., 2021). Although gridded emission can better present point source emissions of pollutants, several errors can occur due to uncertainties, spatial scale, bias in spatial disaggregation and model sensitivity (Oda et al., 2019; Dai et al., 2020; Ojha et al., 2021).

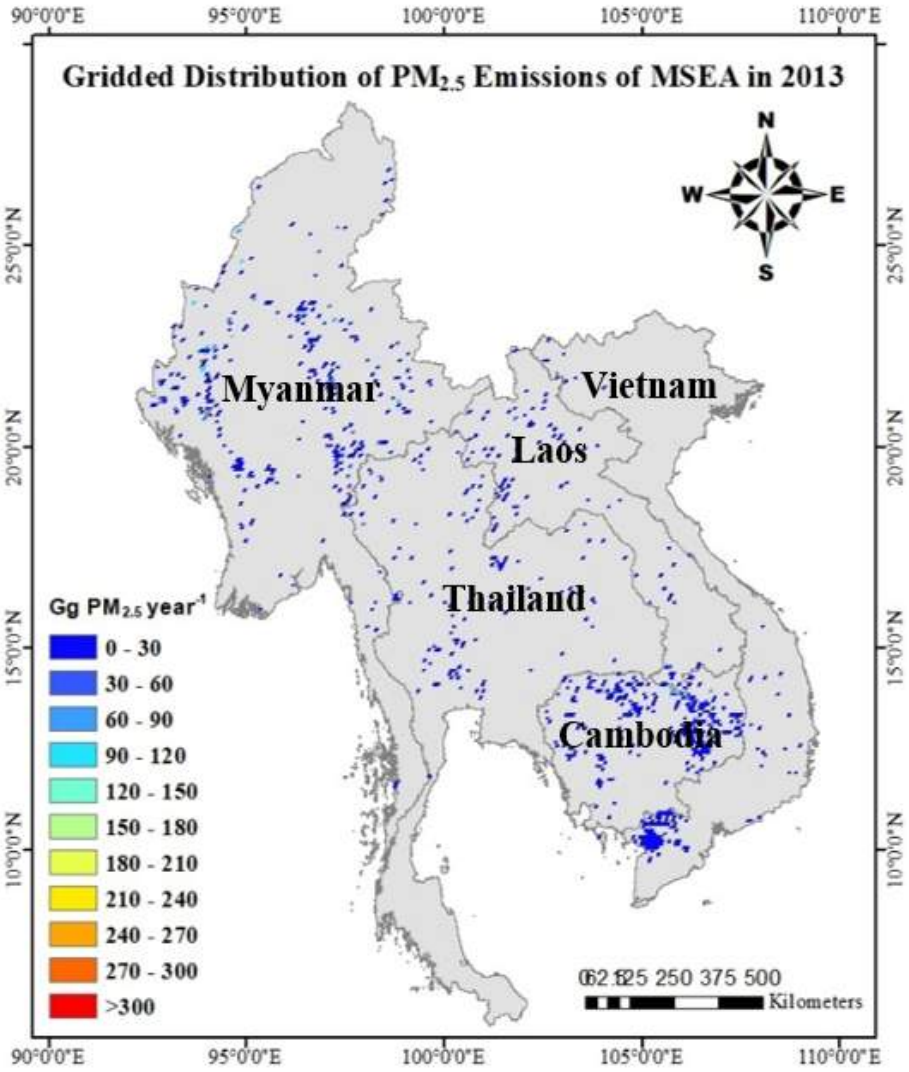

Figure 3.2.7: Gridded Distribution of $PM_{2.5}$ Emissions of MSEA in 2013

e) Temporal Variations of Biomass Burning Emission

Figure 3.2.8 shows the monthly burned area of MSEA in 2013, and Figure 3.2.9 shows the variations of 11 emitted pollutant species over 12 months in 2013. The main fire type observed is forest fire, while

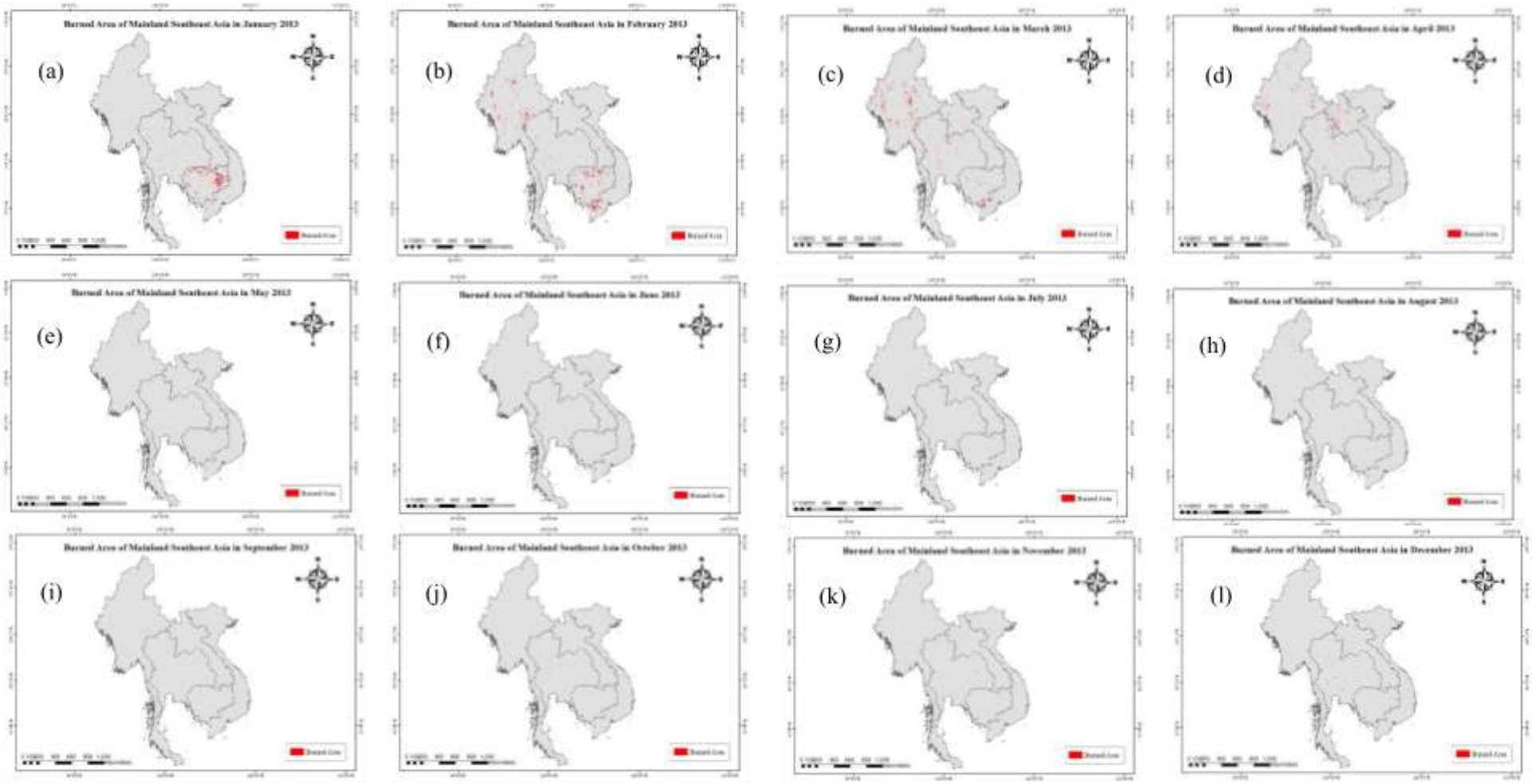

Figure 3.2.8: Monthly Variations of Biomass Burning Area of MSEA in 2013; (a) January (b) February (c) March (d) April (e) May (f) June(g) July (h) August (i) September (j) October (k) November (l) December

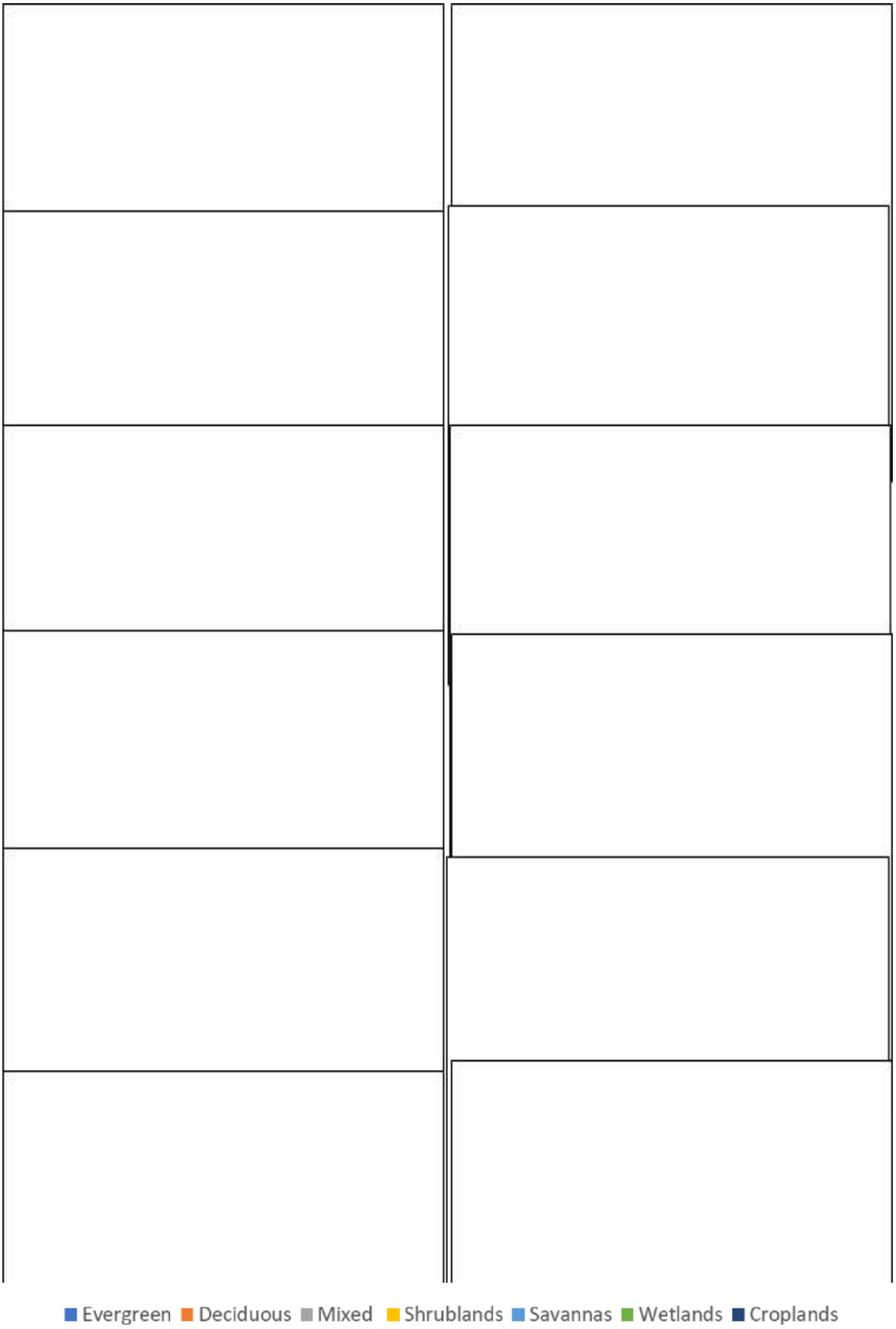

Figure 3.2.9: Monthly Variations of Biomass Burning Emission Species for 2013: (a) January (b) February (c) March (d) April (e) May (f) June(g) July (h) August (i) September (j) October (k) November (l) December

shrublands, savannas and croplands were found to contribute a smaller portion of the emissions. The biomass burning peaks in February and gradually decreases until April, with slight burning in the remaining months and start increasing again in December. Over 12 months (Figure 3.2.9), NO_x and NMVOC showed different trend from other pollutants, which have relatively higher emissions in April probably due to the dominated emissions from evergreen forests. Relatively, pollutants emitted from biomass burning showed large monthly variations. For all the emitted pollutants, forests are the main contributors, with exception to NO_x and NMVOC. More comprehensive information for temporal variation of BB emission in MSEA is shown in Appendix 3.2.4A – Appendix 3.2.4L.

Biomass burning activity in MSEA occurs mainly during pre-monsoonal season, after harvesting, to prepare for sowing season during summer monsoonal season which is more suitable for cultivation due to weather and precipitation (Huang et al., 2016). Clearing of plantation through biomass burning to enhance soil fertility, as well as replenish soil nutrient (Zhou et al., 2017). During biomass burning, the temperature of soil increases, increasing soil microbial activity, subsequently increasing nutrient circulation from decomposition of plant materials which are used as fertilizers (Shi & Yamaguchi, 2014; Winkler et al., 2019). During pre-monsoonal season, a winter monsoon starting from December to January, regional air becomes dry and stagnant, biomass burning in MSEA begins from south (Zhu et al., 2016), starting from Cambodia in December and January, and burning activities gradually propagate northwards, creating burning peaks from February to April, and at the end of April, summer monsoon onset bringing increased precipitation, reducing biomass burning until the next dry season (Huang et al., 2016; 2019; Reddington et al., 2021).

3.2.3 Biomass Burning Inventory in South ASEAN and Borneo

3.2.3.1 Land Cover Map of South ASEAN and Borneo in 2013

The land cover distribution of South ASEAN and Borneo in 2013 is shown in Figure 3.2.10 and Figure 3.2.11 respectively. Meanwhile the coverage area (in km^2) of each type of land cover for Borneo is shown in Table 3.2.10. Borneo Island was mainly covered with broadleaf forest followed by open forest/oil palm plantation in 2013; both, occupied up to 71.3% and 23% of total land cover as presented. Wetland and grassland are the second and third largest land cover, followed by cropland, which covered 2.2%, 2%, and 0.8% from total coverage, with area 15144.26 km^2, 16246.18 km^2, and 5897.228 km^2, respectively. Shrubland has the lowest coverage, which covered 0.03% in Borneo, with only 205.94 km^2.

Kalimantan showed that the broadleaf forest had the greatest coverage area, which accounted for 371055.75 km^2 from the total area. The central part of Borneo, where large areas were unexplored and thus covered with thick and dense forested areas (> 60% of tree cover). The rapid development of

the oil palm industry in Borneo, especially in Kalimantan, has led to a significant expansion of oil palm plantations over the years (Tarigan et al., 2016; Langston et al., 2017). Shrubland is one of the major land sources for new plantation areas, as reported by Gunarso et al., (2013) and Langston et al., (2017). Previous studies (Tarigan et al., 2016; Purnomo et al., 2020) also revealed that the rapid decline of shrubland was primarily attributed to the expansion of the oil palm industry as most of the oil palm concessions from 1988 to 2013 were developed in shrubland. Based on Gunarso et al. (2013), approximately 48% of shrublands in Kalimantan were cleared from 1990 to 2010 for palm oil cultivation, resulting in the highest proportion of oil palm plantation in Kalimantan, with an area 134736.71 km^2

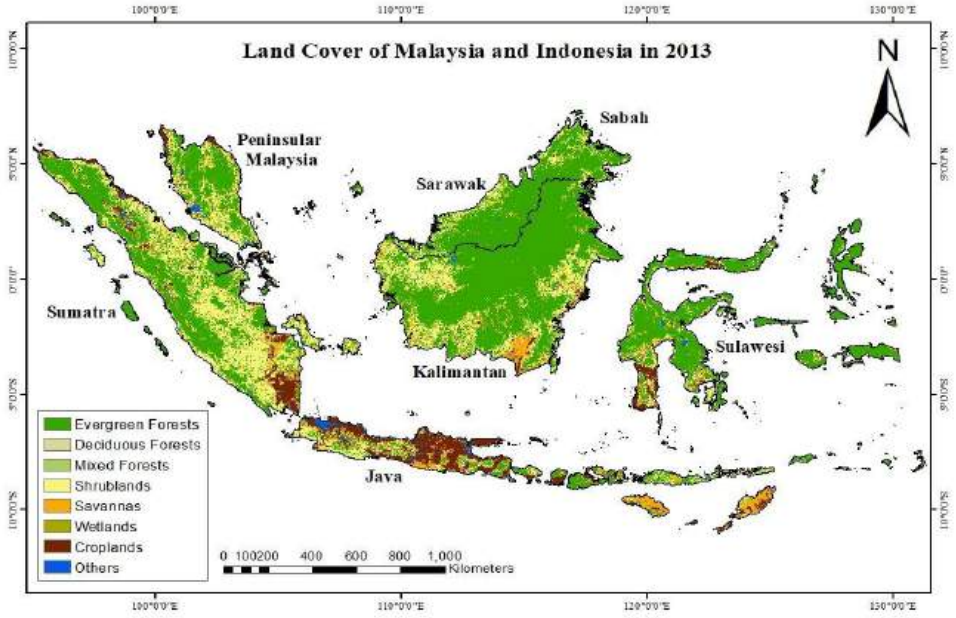

Figure 3.2.10: Land Cover of South ASEAN in 2013 from MODIS MCD12Q1

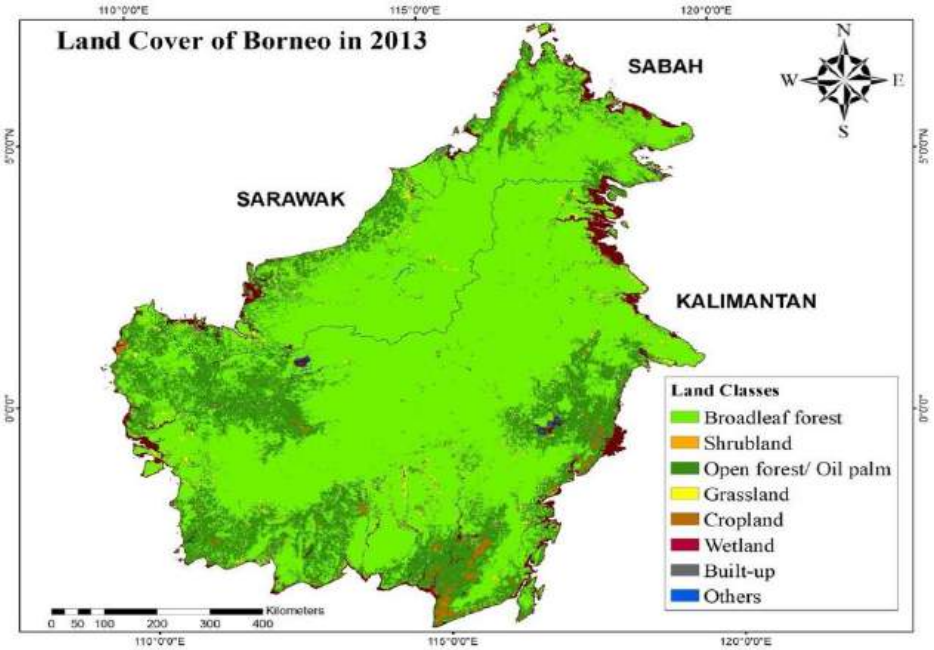

Figure 3.2.11: Land cover classification for Borneo in 2013 from MODIS MCD12Q1

These oil palm plantations in Borneo were mainly dominated in the western and southern parts of Kalimantan. Overall, the distribution of land cover helps assess the spatial variation of aboveground biomass distribution that serves as important variables for emission estimation. The insignificance of shrubland may also be attributed to confusion errors in which errors arose from the classification process by performing visualization algorithms (Tharwat, 2021). Thus, an accuracy assessment was carried out to evaluate the current land classification's confidence levels and were discussed in this following section.

Table 3.2.10: Land cover area of Borneo in 2013.

Land Cover Types	Division (km^2)			Total	Percentage (%)
	East Malaysia	Kalimantan Indonesia	Brunei		
Broadleaf Forest	152221.22	371055.75	4854.14	528131.1	71.3
Shrubland	14.37	191.57	0.00	205.9357	0.03
Open Forest/ Oil Palm	34984.32	134736.71	422.61	170143.6	23.0
Grassland	4671.09	10359.33	113.85	15144.26	2.0
Cropland	286.07	5611.15	0.00	5897.228	0.80
Wetland	4997.38	11077.84	170.96	16246.18	2.20
Built-up	656.67	871.31	223.90	1751.874	0.24
Others	526.77	2604.59	10.47	3141.836	0.42

3.2.3.2 Accuracy Assessment of Borneo Land Classification

The accuracy evaluation of each land class is shown in Table 3.2.11 below. In terms of user's and producer's accuracies, all land classes exceeded an accuracy level of 70%, except for Shrubland. Overall, the classification system used in this study was considered reliable for analysis. "Broadleaf Forest" showed the highest user's and producer's accuracies, followed by Wetland and Grassland. Ambiguous classes primarily exist between land covers with similar spectral and phenological characteristics (Lu et al., 2014) which cause lower accuracy for other types of land cover. Details analysis for accuracy assessment can be found in Appendix 3.2.1B.

Table 3.2.11: Accuracy assessment of Borneo land classification

Land Cover Types	User's Accuracy (%)	Producer's Accuracy (%)	Overall Accuracy (%)
Evergreen Forests	0.93	0.91	**85.0**
Deciduous Forests	0.90	0.69	
Mixed Forests	0.74	0.79	

Shrublands	0.82	0.81	
Savannas	0.75	0.75	
Wetlands	0.88	0.88	
Croplands	0.77	0.89	
Others	0.85	0.75	

3.2.3.3 Total Emission in South ASEAN and Borneo

a) Burned area in South ASEAN and Borneo

The spatial distribution of monthly burned area for South ASEAN is shown in Figure 3.2.12a, while the total burned area in 2013 is shown in Figure 3.2.12b respectively. The figure shows that the forest and shrubland fires predominately occurred in eastern Sumatra and peaked from June to August of 2013 with less significant total burned area (which accounted only less than 5%). Figure 3.2.12a and 3.2.12b also illustrates that there was hardly any detectable BB for the rest of period in 2013 over South ASEAN region expect for Borneo. The finding of this study was similar to what highlighted in the study of Yin (2020) which further pointed that the increase of shrubland fire rate over this region was likely related to the dramatic land cover change induced by the local swidden agriculture.

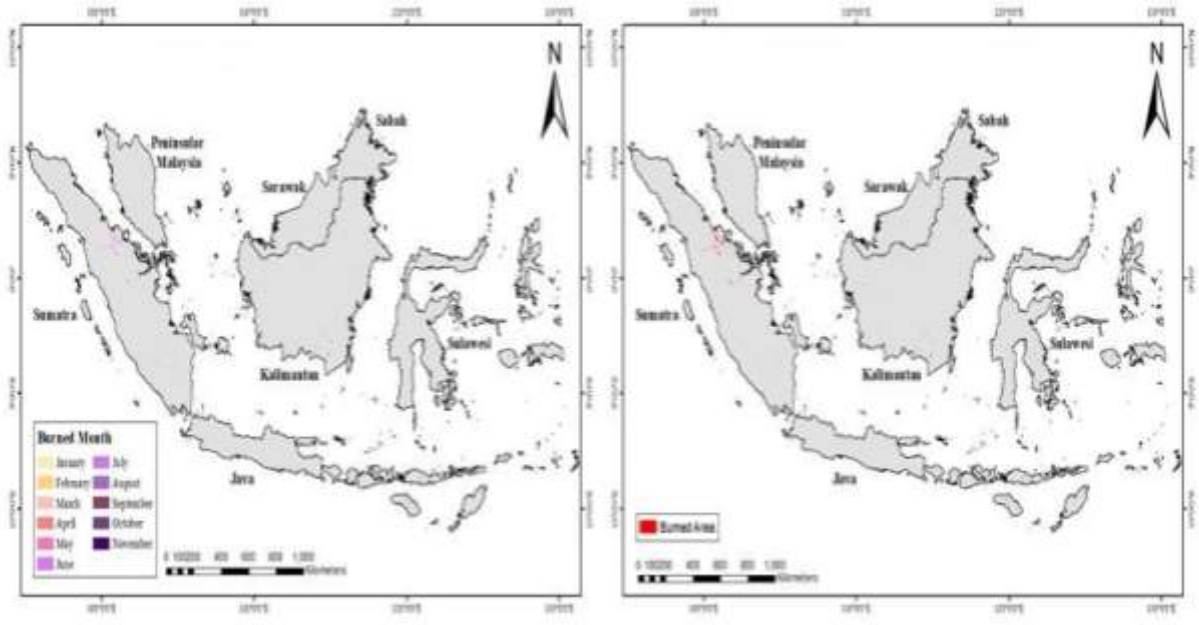

(a) (b)

Figure 3.2.12: Monthly Variations of Biomass Burning (a) and Total Burned Area of South ASEAN (b) in 2013.

Peatland fires in Indonesia are usually caused by humans in order to clear land and create ash for fertiliser (Moran et al., 2019; Vadrevu et al., 2019). The increased need for arable land, particularly for oil palm plantations, has accelerated deforestation and draining of Indonesia's peat swamp forests. The link between fire and deforestation has also been shown in other SEA regions including the

MSEA (Reddington et al., 2020) and Indonesia (Adrianto et al., 2019, 2020). Peatlands were thus more vulnerable to BB during the dry season, which ran from April to October. However, the annual BB for in South ASEAN are less than what been observed in MSEA (Huang et al., 2016). The annual BB are less scattered and only concentrated over eastern part of Sumatra and lower part of Borneo region. Moreover, the BB is hardly observed during wet season and almost none for sub-region other than Sumatra and Borneo.

For Borneo, the monthly variations of burned area in 2013 are shown Figure 3.2.13. The monthly spatial for Borneo burned area distributions were predominantly concentrated in Kalimantan, and no burning was detected in Brunei. According to Langner and Siengert (2009), forest fire activity in Kalimantan was much stronger than in Malaysia and Brunei, with only 0.3-0.4% of forest area affected in Malaysia and Brunei even during the El Niño year. The first burning in 2013 was detected in West Kalimantan in January. These fires continued to burn until March, as about the same region was seen in following months. In tropical areas, the peak fire season usually occurred later in the year during the August–October period (Yin, 2020). In Kalimantan, fires that recorded from January to May and November to December were comparatively rare. During the dry season, June to October, fires began to spread throughout the region of Kalimantan, resulting in a drastic increase of burning spots in Borneo. The tremendous increase of Kalimantan fire spots was mainly associated with prolonged dry season coupled with human activities (Jayachandran., 2009). whereby uncontrolled forest fires likely to occur from June to September every year in both Malaysia and Indonesia (Adrianto et al., 2020; Bruni Zani et al., 2020).

Dryer conditions associated with the southwest monsoon can be favourable for forest or any vegetation burning (Liu et al., 2018); thus, the risk of fire occurrence would be high (Yin, 2020). On the other hand, the most severe burning region in Borneo was detected in Kalimantan as several large burning spots were detected in Banjarmasin, South Kalimantan. Similar results were also obtained by Spessa et al. (2010), who reported burning across Borneo predominated in South Kalimantan, as most also the forest fires occurred overwhelmingly in South Kalimantan. While in Malaysian Borneo (Sarawak and Sabah), burning spots were scattered around the regions, one can observe that these fires were mainly concentrated in Sarawak from April to October. However, fire activity observed in Sarawak and Sabah, and central Borneo was less significant compared to Kalimantan in 2013.

The estimated burned areas (in km^2) by land classes in 2013 for Borneo are shown in Table 3.2.12. Over half of Borneo's biomass loss in Borneo was attributed to broadleaf forest burning, which accounted for 88% of total biomass burned in 2013. The results also revealed that 11% of biomass burned was made up by open forest/oil palm burning. Conversely, biomass loss from grassland, wetlands, and croplands, collectively, is negligible in which only occupying 0.5%, 0.15%, and 0.00007%, respectively, from total biomass burned. Broadleaf forest, open forest/oil palm,

grassland, cropland and wetland, were five out of eight land classes relatively susceptible to burning in Borneo.

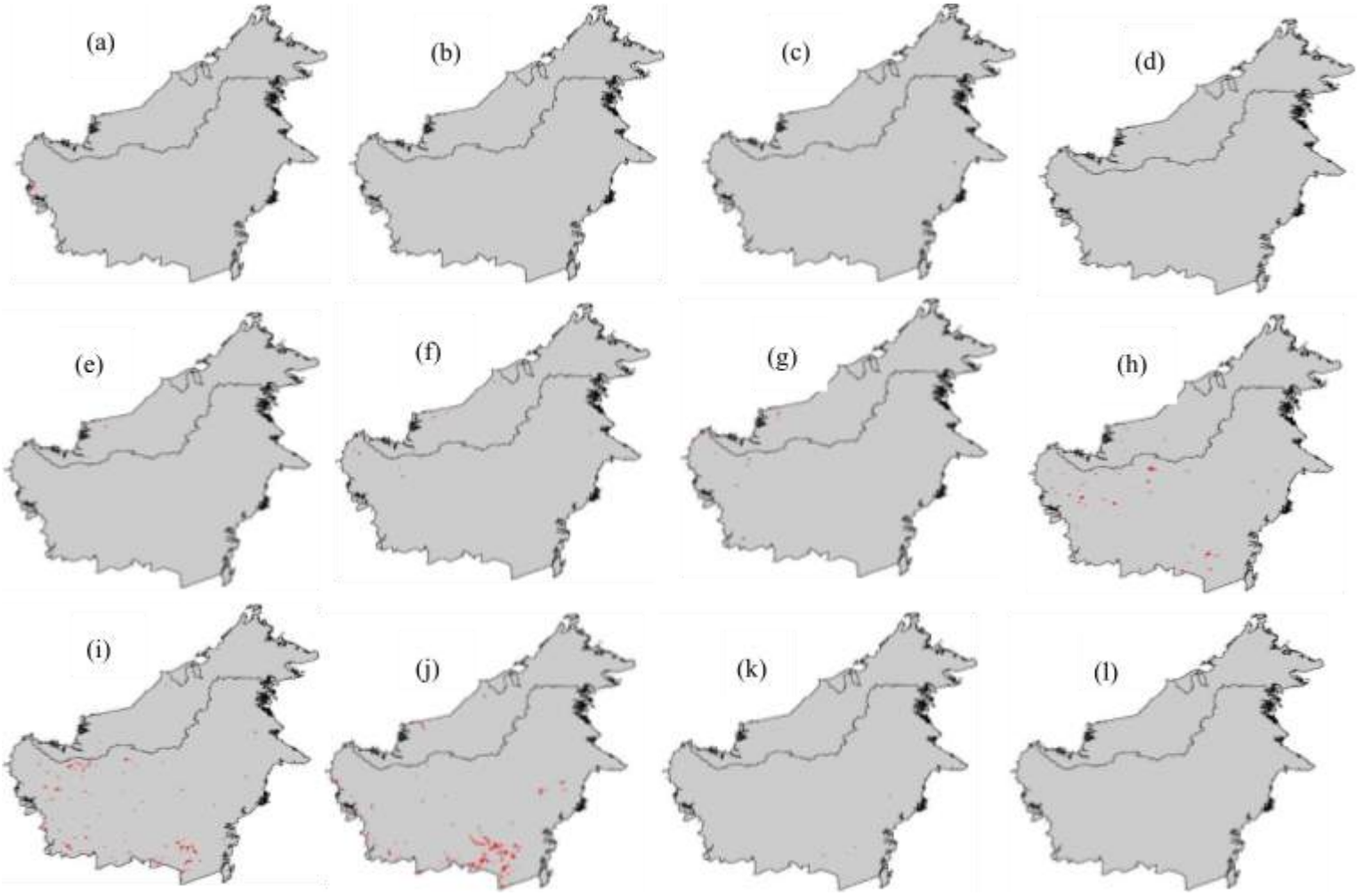

Figure 3.2.13: Monthly Variations of Biomass Burning Area of Borneo in 2013; (a) January (b) February (c) March (d) April (e) May (f) June(g) July August (i) September (j) October (k) November (l) December

Table 3.2.12: Annual Amount of Dry Biomass Burned in 2013

Land Cover Types	Burned area (km^2)	Annual Dry Biomass Burned (Mg/year)
Broadleaf Forest	344.35	618521.47
Open Forest/ Oil Palm	627.33	79781.63
Grassland	27.95	3554.58
Cropland	13.46	0.48
Wetland	3.26	1075.8

The MODIS algorithm estimated, approximately 1016.36 km^2 area were burned in 2013, 70.62 km^2 from Sabah and Sarawak, and 945.74 km^2 from Kalimantan (refer Appendix 3.2.5B). There was no burned area detected in Brunei. Fire incidence in Brunei can be challenging to detect due to insufficient radiation for satellite detection. Agriculture fire is the dominant biomass fire in Brunei as reported by Kim Oanh et al. (2018). These fires were usually small and did not emit sufficient radiation to penetrate dense canopies or cloud cover, making it difficult to distinguish from the non-fire background by using MODIS algorithms (Wang et al., 2014; Randerson et al., 2012). Based on the result, the most severely fire-damaged land cover in Borneo were open forest/oil palm, with 627.33 km^2 of the burned area, followed by broadleaf forest with 344.35 km^2 area burned, grassland and cropland come after with area 27.95 km^2 and 13.46 km^2 respectively.

Wetland showed the lowest severity with 3.26 km^2 of burned area was estimated. Overall, most of the Borneo's burning sports were detected in Kalimantan which made up over half of the burned area in 2013. Among the land classes, the burning of open forest/oil palm was the most prominent in Kalimantan, followed by broadleaf forest, with an estimated area of 599.29 km^2 and 312.17 km^2 were burned, respectively. The burning activity detected from other land classes (wetland, cropland, and grassland) was less significant and no burning was detected from shrubland in 2013. The burning spots detected in East Malaysia mainly from broadleaf forests with 32.18 km^2 of area burned (Appendix 3.2.2F). However, the total burned area in East Malaysia was comparatively insignificant as compared to Kalimantan.

The fire activity in Kalimantan mainly occurred in August, September, and October, and was dominated by open forest/oil palm burning mainly in October. On the other hand, fires observed in East Malaysia were more frequent, however with lower severity than Kalimantan. No fires were detected in January, February, November, and December in East Malaysia. The most severe burning was recorded in March and dominated by open forest/oil palm burning. Overall, the burning in Borneo reached its peak in October and declined in the following months.

b) Source of Emission of Biomass Burning in South ASEAN

The fire intensity and biomass consumed during the burning activity were significantly affected by the land covers characteristics (Ivanova et al., 2020; Yin, 2020). In this study, the biomass consumed (Gg/year) in 2013 was calculated as the burned area (km^2), fuel loads, and combustion factor. Both fuel loading and combustion factors for respective land covers were retrieved from Michel et al. (2005), Song et al. (2009), and Zhou et al. (2017). The emissions of biomass burning of South Asean in 2013 are shown in Table 3.2.13, and the annual typical pollutant emission from different land cover sources in 2013 is shown in Figure 3.2.13. The annual emission of CO_2, CO, CH_4, NO_x, NH_4, SO_2, PM_{10}, $PM_{2.5}$, EC, OC and NMVOC were 5201.98 Gg, 254.43 Gg, 11.48 Gg, 10.38 Gg, 3.11 Gg, 1.90 Gg, 33.94 Gg, 28.8 Gg, 1.60 Gg, 18.13 Gg and 42.26 Gg respectively.

Table 3.2.13: Annual biomass Burning Emission Inventory (Gg) in South ASEAN for 2013

Land Cover	**CO_2**	**CO**	**CH_4**	**NO_x**	**NH_3**	**SO_2**	**PM_{10}**	**$PM_{2.5}$**	**EC**	**OC**	**NMVOC**
Evergreen	2200.77	123.23	6.83	3.48	1.02	0.6	17.15	13.66	0.67	6.3	32.15
Deciduous	22.52	1.41	0.07	0.02	0.02	0.01	0.18	0.17	0.001	0.13	0.15
Mixed	1.58	0.1	0.01	0.001	0.001	0.001	0.01	0.01	0.001	0.01	0.01
Shrublands	2711.7	107.46	4.11	6.16	1.9	1.08	13.43	12.48	0.79	10.43	7.59
Savannas	236.16	8.12	0.21	0.39	0.07	0.09	1.36	0.87	0.06	0.36	1.28
Wetlands	9.35	12.94	0.21	0.29	0.08	0.11	1.72	1.54	0.07	0.87	0.94
Croplands	19.9	1.12	0.04	0.04	0.02	0.01	0.09	0.07	0.01	0.03	0.14
Total	5201.98	254.38	11.48	10.38	3.11	1.90	33.94	28.8	1.60	18.13	42.26

Similar to what has been observed over MSEA, CO2 is the highest concentration of emitted pollutant, followed by CO for all land cover types in South ASEAN region. Carbon of biomass react with oxygen to produce CO_2 in a complete combustion, other than releasing a proportionate amount of sequestered CO_2 in biomass from photosynthesis (Cherubini et al., 2011). The high CO_2 emission is contributed by Shrublands and Evergreen Forest and in agreement with the finding of Yin (2020), which highlighted that shrubland fire is dominant and increasing along the SEA region while forest fire is decreasing. Yin (2020), further added that Shrubland fire was principal form of BB emission in Equatorial SEA such in Malaysia Borneo and Sumatra, Indonesia.

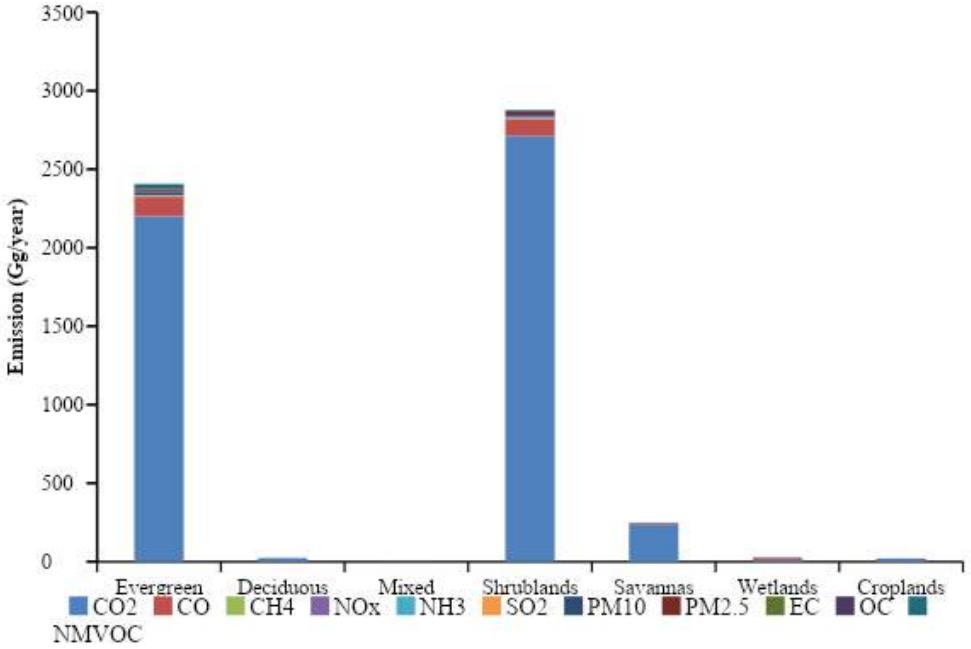

Figure 3.2.14: Contribution (%) of different land cover type to annual biomass burning emissions in South ASEAN for 2013

c) Source of Biomass Burning Emission of Borneo

Table 3.2.14 summarises the total BB emission (Gg/year) from various land covers. Lowland forests and plantations were burned annually, especially during the dry seasons (Engling et al., 2014). Biomass burning in Borneo was mainly dominated by forest fire (broadleaf forest and open forest/oil palm), contributing mostly half of the biomass burned in 2013. Based on the estimation, broadleaf forest contributed to 618521.47 Mg/year of biomass burned while open forest/ oil palm contributed to 79781.63 Mg/year (Table 3.2.13). By contrast, grassland, cropland, and wetland, collectively, showed a minor proportion of biomass burned in 2013. However, biomass loss from grassland and wetland were relatively higher compared to cropland, with an estimate of 3554.58 Mg/year and 1075.8 Mg/year, respectively. As Lasslop and Kloster (2015) studied, burned area is one of the measures to quantify the consumption of biomass fuel from vegetation fires.

The total emissions of 11 typical pollutants, namely CO_2, CO, CH_4, NO_x, NH_3, SO_2, PM_{10}, $PM_{2.5}$ EC, OC and NMVOC are 1160.102 Gg/yr, 62.900 Gg/yr, 3.306 Gg/yr, 1.857 Gg/yr, 0.983 Gg/yr, 0.305 Gg/yr, 8.751 Gg/yr, 6.229 Gg/yr, 0.360 Gg/yr, 3.296 Gg/yr, and 16.684 Gg/yr. Overall, CO_2 and CO were two of the dominant species recorded during biomass burning in 2013. A similar result was also obtained from other studies (Van der Werf et al., 2006; Carlson et al., 2012; Shi and Yamaguchi, 2014; Ponette-Gonzales et al., 2016). Over decades, high carbon emission was often recorded from forest burning (Huang et al., 2016; Adrianto et al., 2020), especially in SEA (Shi and

Yamaguchi, 2014; Reddington et al., 2020). This result was different from the finding of Shi and Yamaguchi (2014), who reported most of the CO_2 emission from East SEA was majorly from the burning of peatland.

Table 3.2.14: Annual biomass Burning Emission Inventory (Gg) in Borneo for 2013

Land Cover	CO_2	CO	CH_4	NO_x	NH3	SO_2	PM_{10}	$PM_{2.5}$	EC	OC	NMVOC
Broadleaf Forest	1016.236	57.523	3.136	1.577	0.823	0.247	7.917	5.629	0.322	2.913	16.082
Open Forest/ Oil Palm	135.949	5.066	0.164	0.267	0.068	0.054	0.790	0.566	0.036	0.367	0.562
Grassland	6.015	0.210	0.005	0.010	0.002	0.002	0.030	0.022	0.001	0.009	0.033
Cropland	0.001	0.000	0.000	0.000	0.000	0.000	0.000	0.000	0.000	0.000	0.000
Wetland	1.901	0.101	0.002	0.002	0.001	0.001	0.013	0.012	0.001	0.007	0.007
Total	1160.102	62.900	3.306	1.857	0.893	0.305	8.751	6.229	0.360	3.296	16.684

The emission of otCO_2 and CO species are less significant for other land cover types. Furthermore, CH_4, NO_x, NH_3, SO_2, EC and OC are relatively insignificant with total emission less than 4 Gg/yr. The insignificance can be associated with low associated species contents and emission factors, which consequently result in a low emission rate (Chang and Song, 2010). The emission of OC and EC were closely related and mostly came from the same source. However, as reported by several studies (Wu et al., 2019), the proportion of EC and OC vary significantly in different combustion sources. A high OC/EC ratio has been found in response to biomass burning. In most cases, the OC's emission factor is often higher than EC typically during the smouldering phase of fire burning, which explained the higher OC emission than EC from all sources in this study. While the emission of $PM_{2.5}$ and PM_{10} suggests that the PM emitted from burning activity mostly belonged to coarse particles.

In general, the result suggested broadleaf forest burning showed the most significant biomass emissions, while open forest/oil palm was the second largest contributor of biomass emission in Borneo for the period of 2013. By comparison, the emissions from the remaining land cover types were relatively small and nearly negligible from cropland and similar finding highlighted in the study of Vadrevu et al., (2019). Biomass burning from broadleaf forest contributed up to 80% of total

emission in 2013, with 81% of SO_2, 85% of NO_X, 88% of CO_2, 96% OF NMVOC, 94% of CH_4, 89% of EC, 88% of OC, 90% of $PM_{2.5}$, 91% of PM_{10}, 93% of NH_3 and 91% of CO (Figure 3.2.15). On the other hand, the burning of open forest/oil palm occupied a range of 5-14% of biomass emission. The emissions from others were less significant and almost negligible with less than 1% for all pollutants.

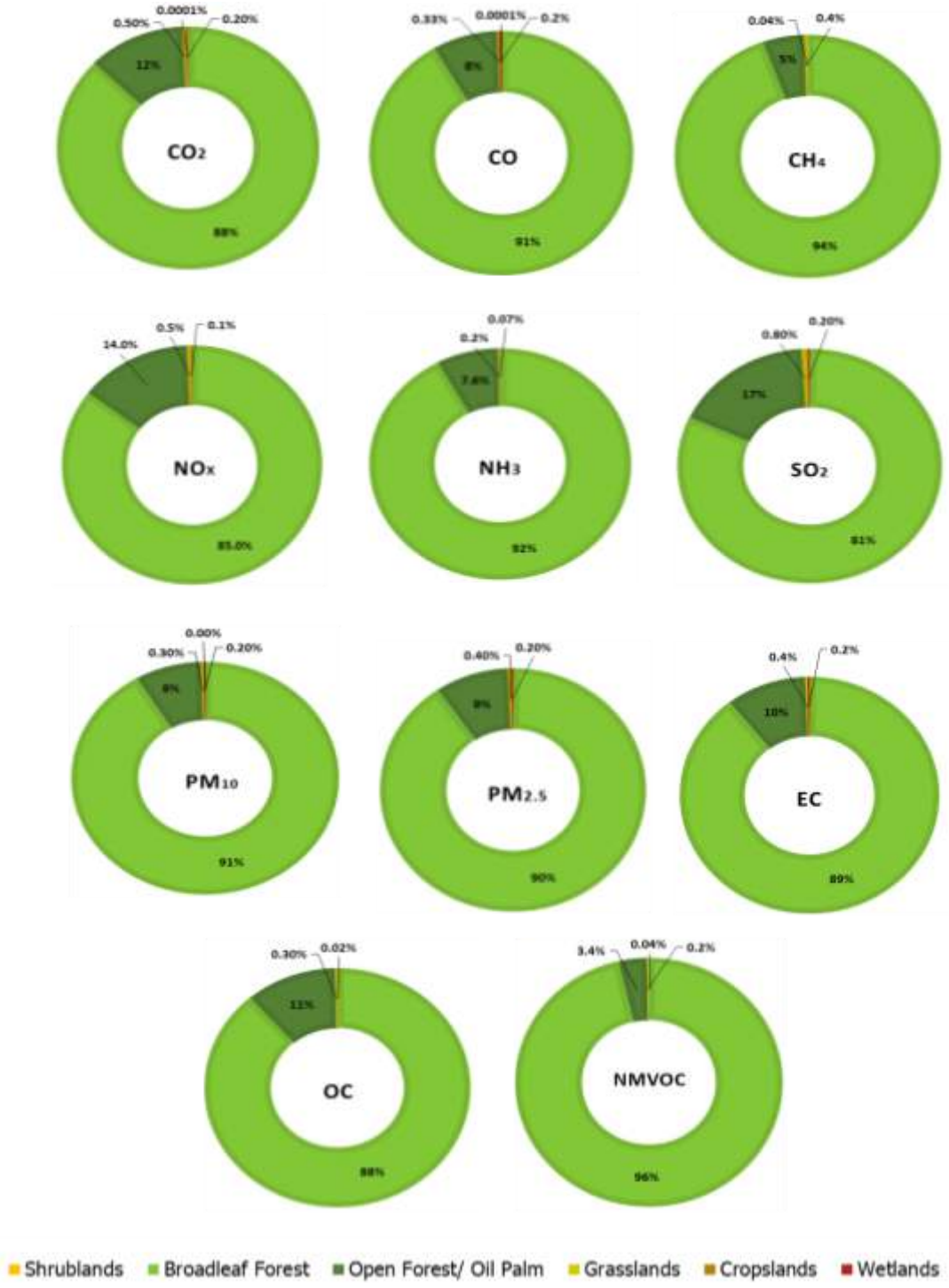

Figure 3.2.15: Contribution of Different Land Cover Type to Annual Biomass Burning Emissions in Borneo in 2013

Over decades, broadleaf forest burning in Borneo, typically in Kalimantan, was often linked to land clearing and deforestation for crop cultivation and to fulfil timber demand (Jua´rez-Orozco et al., 2017; Purnomo et al. 2017; Adrianto et al., 2019). Indonesia's high deforestation rate increases rainforest's vulnerability to fires (Van Der Werf, 2014). The burning of forests poses significant threats to the environment and destroys the important sink for atmospheric carbon dioxide when burned (Varner et al., 2015; Wehmas, 2018; Roland et al., 2019). The recurrence of fires in tropical broadleaf forests can modify the microclimatic conditions and plant composition, thereby creating positive feedback to the fire regime (Wehmas, 2018). The positive changes in fire regimes and forest structure potentially released the stored carbon dioxide of yearlong, resulting in a high emission load of pollutants (Wehmas, 2018; Adrianto et al., 2020), typically CO_2 and CO as observed in this study.

Likewise, the emission result from open forest/oil palm burning can be attributed to agricultural practices to boost soil fertility (Alam et al., 2015; Jua´rez-Orozco et al., 2017). Burned biomass or residues serve as potential nutrient sources for the soil. Therefore, fires were widely used to burn oil palm waste, either for expanding the new plantation area or circulating the nutrients (Adrianto et al., 2019,2020). However, the value of the emission factor of oil palm trees needed to be studied. In this case, the emission factors are under-represented from the surface reflectance from the remote sensing technique. Wetland burning contributed significantly to a range of nearly 0% to 0.4% of biomass emission, even with the smallest area burned (3.26 km^2).

As compared to cropland, with the greater burned area than wetland but negligible emission from all species. The significance of this emission was supported by Shi and Yamaguchi (2014), who reported the emission from wetland burning in SEA from 2001-2010 contributed to a range of 8-24% of emission but with only 7% of total burned area. Like this study, the smallest burned area was detected with significant biomass burned and emission load. Various studies (Shi and Yamaguchi, 2014; Adrianto et al., 2020) claimed that wetland has a relatively higher density of biomass than forest on average; however, the emission and biomass consumption resulting from the underground biomass burning was not considered in this study.

d) Spatial Variations of Biomass Burning Emission

Overall, the average annual biomass burning emissions of all species across South Asean is concentrated more in Sumatra and Borneo. Though the emission magnitude is similar in gridded information, CO_2 is taken as a focus as it is the main pollutants and have significant different grid information particularly over Borneo region (Figure 3.2.16). In the extend, the most dominant

emission species, CO_2 was notably spotted in Kalimantan (South Kalimantan and West Kalimantan) (Figure 3.2.17a and 3.2.17b respectively) are discussed. As mentioned, these areas were found to have more intense fire activity, resulting in increased emission density. The emission spots in South Kalimantan were mainly concentrated in the open forest/oil palm region, and a minor proportion was also found in West Kalimantan. While in East Malaysia, the emissions mostly originated from Sarawak and relatively low in Sabah, while no emissions were detected from Brunei. As reported by several studies (Chang and Song, 2010; Lamsal et al., 2012; Shi and Yamaguchi, 2014; Ponette-Gonzalez et al., 2016), fires in Indonesia are mainly used for deforestation and agriculture practices (Adrianto et al., 2020 and reference therein).

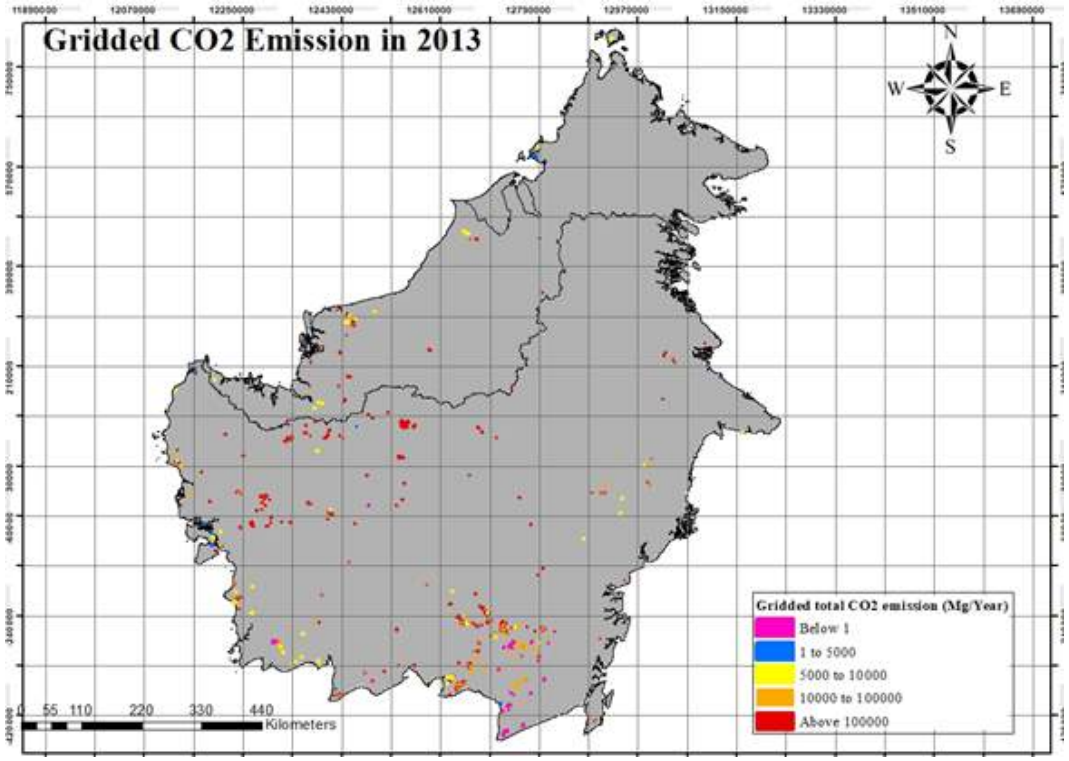

Figure 3.2.16: Gridded Distribution of CO_2 Emissions of Borneo in 2013

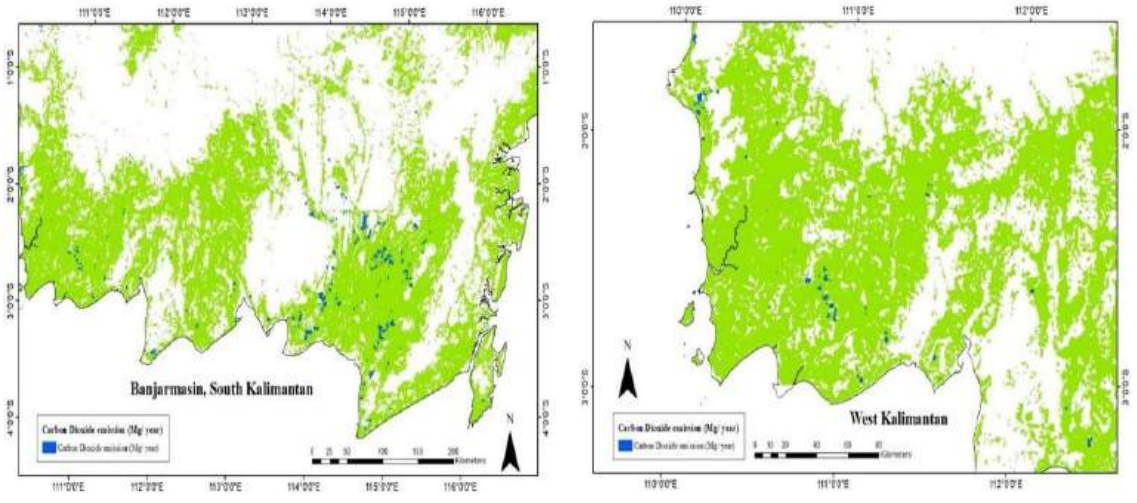

(a) (b)

Figure 3.2.17: CO_2 emission results from open forest/oil palm burning in (a) South and (b) West Kalimantan

In this case, biomass emission in this region mostly from land cultivation and residue burning to facilitate planting (Field et al., 2008; Shi and Yamaguchi, 2014), which normally occurred in Kalimantan and Sumatra over the years (Field et al., 2009; Yin, 2020). However, results obtained in this study revealed that broadleaf forest burning was the largest emission source in 2013. More details information for other emission species are shown in Appendix 3.2.5C and Appendix 3.2.5D. The emission result from broadleaf burning was not concentrated in certain regions; instead, it scattered across the study area and showed the most extensive coverage area in Borneo. There is less to be argued since evidence suggests that fire regimes in Sumatra and Kalimantan are changing; large severe fires can occur following brief dry spells and during non-ENSO years (Pittman et al*.,* 2013, Gaveau et al*.,* 2014; Ponette-González et al., 2016).

3.3 Biogenic Emission in Southeast Asia

Anthropogenic and biogenic sources volatile organic compounds (VOCs) are crucial in the tropospheric chemistry. Anthropogenic VOCs (AVOCs) including benzene, toluene, ethylbenzene, and xylene isomers (BTEX) are dominant in the urban atmosphere while biogenic VOCs (BVOCs) such as isoprene and monoterpene are released by plant and vegetation (Carlsen et al., 2018). BVOC emitted from vegetation are widely recognized for their importance in atmospheric chemistry and climate (Arneth et al., 2008). Their significance in the climate system arises from the large quantity emitted annually and from their fast reactivity with tropospheric oxidants (Atkinson, 2000).

It was estimated that the global isoprene emission in the early 90s was between the range of 454 Tg yr^{-1} to 601 Tg yr^{-1} (see Arneth et al., 2008 and reference therein). terrestrial plant and vegetation are thought to be the main source of atmospheric isoprene which contributed to more than 90% of the global isoprene (Guenther et al., 2006). Minor sources of isoprene include microbes, animals (including humans) and aquatic organisms (Wagner et al., 1999). Both isoprene and monoterpene oxidation products are important precursors for photochemical O_3 production when NOx levels are high (von Schneidemesser et al., 2015; Fitzky et al., 2019). O_3 is a potent GHG with an anthropogenic radiative forcing that is equivalent with CH_4 (Forster et al., 2007).

BVOCs thus recognised as an important precursor of O_3 and known as secondary organic aerosol (SOA) formation (Hauglustaine et al., 2004; Claeys et al., 2004). The transformation of BVOCs to SOA through the gas-to-particle partitioning and forming cloud condensation nuclei (Carslaw et al., 2010)) consequently affecting earth's radiation budget as it scatters the incoming solar radiation (Haywood and Boucher, 2000). Prior studies of (Griffin et al., 1999) has demonstrated that

less volatile BVOC species especially isoprene, monoterpene and sesquiterpenes can exquisitely produce oxidized compound that eventually transform into SOA.

Though BVOCs are important in regulating growth and reproduction of plants, while resisting from environmental stress, and to prevent harm from animals and insects (Klinger et al., 2002; Lun et al., 2020). However, depending of plant species, much of BVOCs emission are controlled by the environmental factors such as humidity (Caser et al., 2019; Saunier et al 2017), temperature (Jiang et al., 2018; Wang et al., 2021), solar radiation (Meeningen et al., 2017). Thus, biogenic emission is liable to climate and vegetation distribution change (Lathiere et al., 2005). With the warming of the planet, the future biogenic emission is remained uncertain and challenging to be estimated.

3.3.1 Biogenic Emissions Under Climate Change Scenarios

3.3.1.1 RCP4.5 Scenario

The projected isoprene emissions in SEA under RCP4.5 for 2013, 2030, 2050, 2070 and 2100 are summarized in Table 3.3.1. Figure 3.3.1 and 3.3.2, In the scenario mentioned, the projected isoprene emissions in January are found at 8.08 tons/hr in 2013, 8.29 tons/hr in 2030, 8.65 tons/hr in 2050, 8.69 tons/hr in 2070 and 9.46 tons/hr in 2100, respectively. Besides, the results show increment in isoprene emissions at 0.21 tons/hr (2.60%), 0.57 tons/hr (7.05%) and 0.61 tons/hr (7.55%) during mid-century (2030, 2050, 2070), and 1.38 tons/hr (17.08%) during the end of century (2100). Hence, the results reveal the emissions rate of isoprene in SEA region are projected in increasing trend from 2013 to 2100 during January.

Indonesia has recorded the highest isoprene emissions within the projected years (in January at 8.08 to 8.95 tons/hr, continued with Malaysia and Brunei at 7.13 to 7.93 tons/hr, Thailand at 3.92 to 6.57 tons/hr, Cambodia at 3.25 to 5.47 tons/hr, Philippines at 3.79 to 4.88 tons/hr, Vietnam at 2.69 to 4.31 tons/hr, Laos at 2.10 to 5.01 tons/hr, Myanmar at 1.73 to 3.35 tons/hr, and Singapore at 1.47 to 3.08 tons/hr, respectively (Appendix 3.3.1A). Furthermore, Malaysia and Indonesia are the main oil palm producers in SEA (Uning et al., 2020) with isoprene emissions of five times greater than primary tropical forest landscapes (Hewitt et al., 2009). Thus, the projected results reveal the emissions of isoprene in Malaysia and Indonesia are significantly higher than other countries within SEA region.

Table 3.3.1: Total Isoprene emissions in Southeast Asia under RCP4.5.

Year	Month	Isoprene Emissions (tons/hr)	Changes (tons/hr)	Percentage in Increment (%)
2013	**January**	8.08	-	-
	July	7.56	-	-
2030	**January**	8.29	0.21	2.60
	July	7.72	0.16	2.12

2050	**January**	8.65	0.57	7.05
	July	8.21	0.65	8.60
2070	**January**	8.69	0.61	7.55
	July	7.94	0.38	5.03
2100	**January**	9.46	1.38	17.08
	July	8.57	1.01	13.36

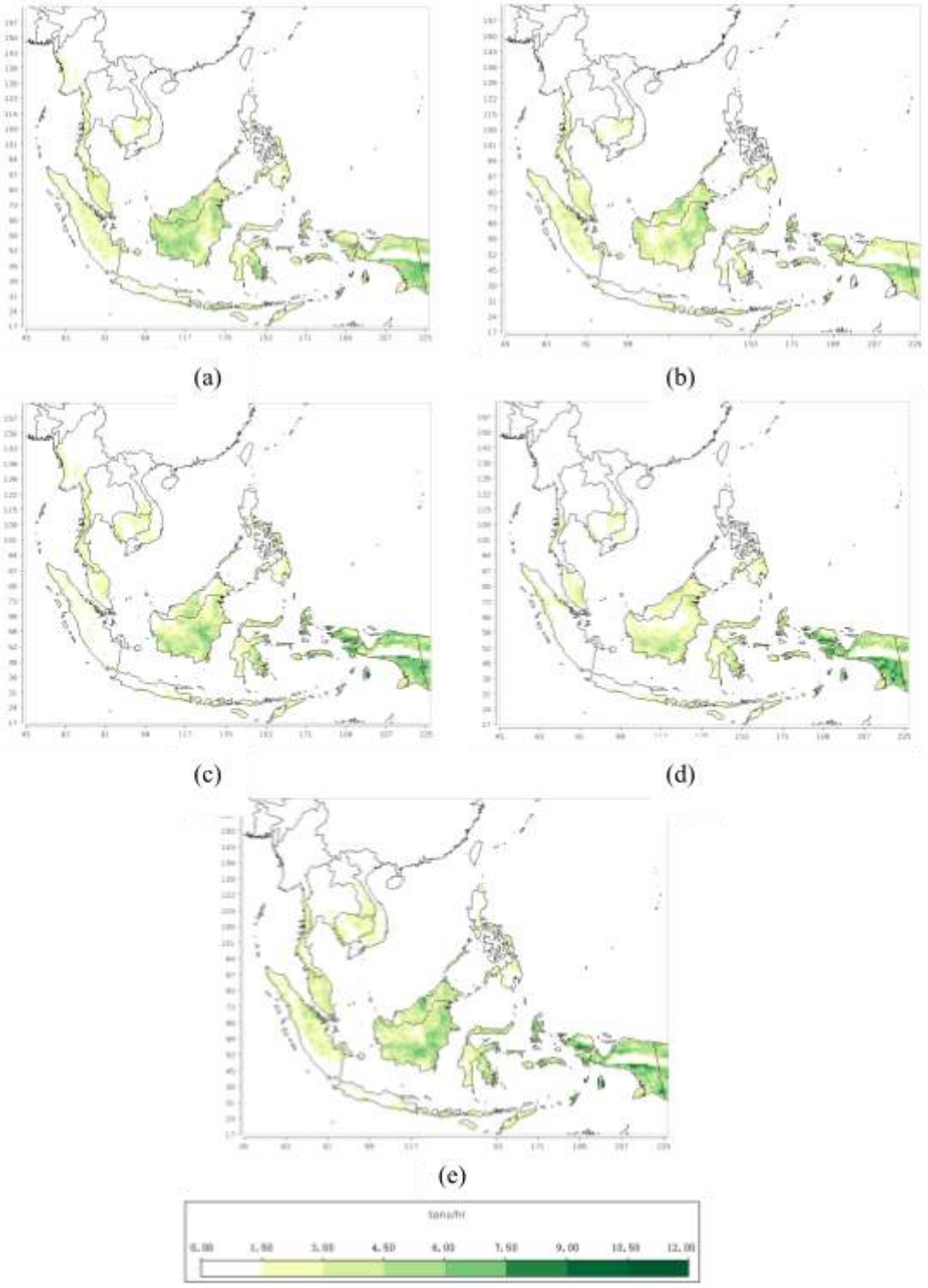

Figure 3.3.1: Total isoprene emissions for January in (a) 2013, (b) 2030, (c) 2050, (d) 2070 and (e) 2100 under RCP4.5 scenario.

As shown in Figure 3.2.1, the projected simulation in January shows the higher isoprene emitter are within Borneo, Sulawesi and Papua Island while the lowest emitters are within the mainland of SEA, such as Myanmar, Laos and Vietnam, which may be due to the lowest temperature that could inhibits the emission of isoprene (Oku et al., 2014; Mutanda et al., 2016). However, during the end of century, Papua Island can be observed with the highest isoprene emissions among the region, and both Sumatra and West Malaysia show an increment in emission of isoprene. The finding in West Malaysia is similar with Hamid et al. (2019).

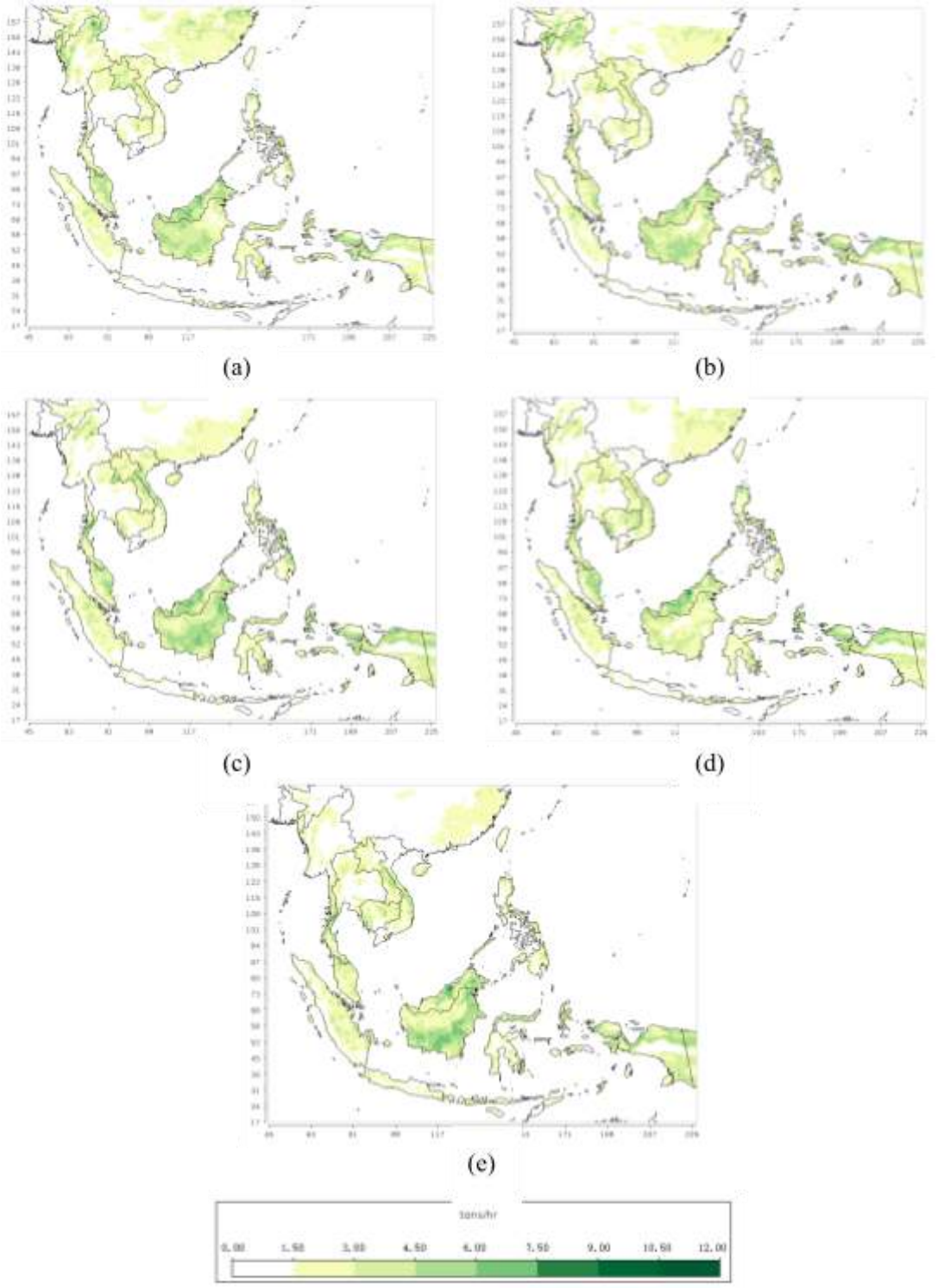

Figure 3.3.2: Total isoprene emissions for July in (a) 2013, (b) 2030, (c) 2050, (d) 2070 and (e) 2100 under RCP4.5 scenario.

In July (figure 3.3.2), the highest isoprene emission is 8.57 tons/hr in 2100, and continued by 8.21 tons/hr in 2050, 7.94 tons/hr in 2070, 7.72 tons/hr in 2030 and 7.56 tons/hr in 2013 respectively. In comparison with the baseline (2013), the total isoprene emissions increased by 0.16 tons/hr (2.12%), 0.65 tons/hr (8.60%), 0.38 tons/hr (5.03%) and 1.01 tons/hr (13.36%) in 2030, 2050, 2070 and 2100. The emissions were increasing through the year of 2030, 2050 but decreasing in 2070, however, the emission rate increase much more in 2100. Similar to the projected temperature in, the temperature trend over SEA in July is also decreasing during 2070 hence it supports that the isoprene emissions are influenced by the changing of temperature.

Furthermore, mainland SEA in July shows an increment of isoprene emissions within the projected years (2013, 2030, 2050, 2070, 2100) at 5.97 to 8.39 tons/hr in Vietnam, 4.63 to 8.39 tons/hr in Laos, 5.86 to 7.18 tons/hr in Thailand, 4.10 to 7.11 tons/hr in Cambodia, and 3.11 to 5.77 in Myanmar, by comparing to January. However, Malaysia and Brunei reveal the highest emission of isoprene at 5.95 to 8.50 tons/hr during July, while Indonesia was the second highest among the countries at 6.96 to 7.64 tons/hr, then continued by Philippines at 5.93 to 7.93 tons/hr, and the lowest is in Singapore at 1.43 to 3.47 tons/hr. A study by Seco et al. (2015) supports that broadleaved mixed forest (which largely found in tropical region) was observed with a relative high isoprene emission during the July.

The projected simulation in July shows a lower isoprene emission rate compares to January. In 2013, Papua Island was the largest isoprene emitter, while Borneo Island are predicted the highest isoprene emitter during 2050 and 2100 as well. Obviously, SEA mainland shows an increment of isoprene emissions in July compared to January, as the temperature in July are higher within the region. It may be caused by the drought stress which decline plant's photosynthesis rate, stomata conductance and transpiration rate (De Swaef and Steppe, 2010; Zhou et al., 2014), that results plant undergo stress, then enhance isoprene emissions to overcome the stress (Jiang et al., 2018). Nevertheless, Jawa Indonesia remains lower emission of isoprene in both January and July, while Sulawesi Indonesia shows higher isoprene emissions in January than July.

3.3.1.2 RCP6.0 Scenario

In RCP6.0 scenario, the projected isoprene emissions are expected higher than RCP4.5 scenario, as the RCP6.0 is a medium range of emission scenario. Based on projected results Table 3.3.2, the highest value of isoprene emissions in January is projected at 10.48 tons/hr in 2100, and continued by 8.92 tons/hr in 2070, 8.65 tons/hr in 2030, 8.59 tons/hr in 2050 and 8.37 tons/hr in 2013 respectively. Also, the increment of isoprene emission in SEA was recorded as 0.28 tons/hr (3.35%), 0.22 tons/hr (2.63%), 0.55 tons/hr (6.57%), 2.11 tons/hr (25.21%) in 2030, 2050, 2070 and 2100. During the end of century, the total emission of isoprene was predicted at the highest rate among the years, hence, it suggests that more secondary organic aerosols will be produced through the chemistry reactions with the emissions in the atmosphere (Hallquist et al., 2009).

Among the SEA countries, Indonesia is the top emitter of isoprene emission in January with an average emission from 8.61 to 15.86 tons/hr within 2013, 2030, 2050, 2070 and 2100. While Malaysia and Brunei are the second highest emitter after Indonesia with an emission range of 1.41 to 8.37 tons/hr. Besides, the other countries have an average of isoprene emissions not more than 6.31 tons/hr – Philippines (4.02 to 4.96 tons/hr), Thailand (0.22 to 6.31 tons/hr), Cambodia (0.33 to 5.53 tons/hr), Vietnam (0.34 to 5.19 tons/hr), Laos (0.23 to 5.19 tons/hr), Singapore (0.35 to 2.45 tons/hr) and Myanmar (0 to 2.85 tons/hr) (Appendix 3.3.1B). Hence, the projected results show that mainland of SEA and Singapore has a lower emission, as the predicted temperature in mainland SEA were lower in January and Singapore is a small Island which has a limited vegetation area.

The projected simulations in January in the current scenario (Figure 3.3.3) show a higher emission of isoprene at the region of Borneo, Sulawesi, and Papua Island among all. Similar with RCP4.5 scenario, the mainland SEA and Indonesia (Sumatra, Java, Timor-Leste) region has the lowest emission rate in January. Several studies suggest that isoprene emissions could be inhibited either by increasing CO_2 (long-term) or decreasing isoprene synthase activities (Monson et al., 2007; Possell and Hewitt, 2011). By the end of century, the isoprene emissions in Borneo, Sulawesi and Papua Island are observed with the highest rate which indicates that these regions may be strongly influent by the environmental factors, which may suffer a huge O_3 production due the higher isoprene emission.

Meanwhile, the isoprene emissions in July (Figure 3.3.4) for the year of 2013, 2030, 2050, 2070 and 2100 were in increasing trend by 7.08 tons/hr, 7.74 tons/hr, 8.00 tons/hr, 8.63 tons/hr and 9.28 tons/hr respectively. Moreover, the increment in July was higher as compared to January with 0.66 tons/hr (9.32%) in 2030, 0.92 tons/hr (12.99%) in 2050, 1.55 tons/hr (21.89%) in 2070 and 2.20 tons/hr (31.07%) in 2100. Similar to RCP4.5, the isoprene emissions under RCP6.0 in January are much higher than the emission rate in July. Therefore, the projected results suggest that the temperature range in January is most affecting to the appearance of isoprene emission in SEA region compared to July.

Table 3.3.2: Total Isoprene emissions in Southeast Asia under RCP6.0.

Year	Month	Isoprene Emissions (tons/hr)	Changes (tons/hr)	Percentage in Increment (%)
2013	**January**	8.37	-	-
	July	7.08	-	-
2030	**January**	8.65	0.28	3.35
	July	7.74	0.66	9.32
2050	**January**	8.59	0.22	2.63
	July	8.00	0.92	12.99
2070	**January**	8.92	0.55	6.57
	July	8.63	1.55	21.89
2100	**January**	10.48	2.11	25.21
	July	9.28	2.20	31.07

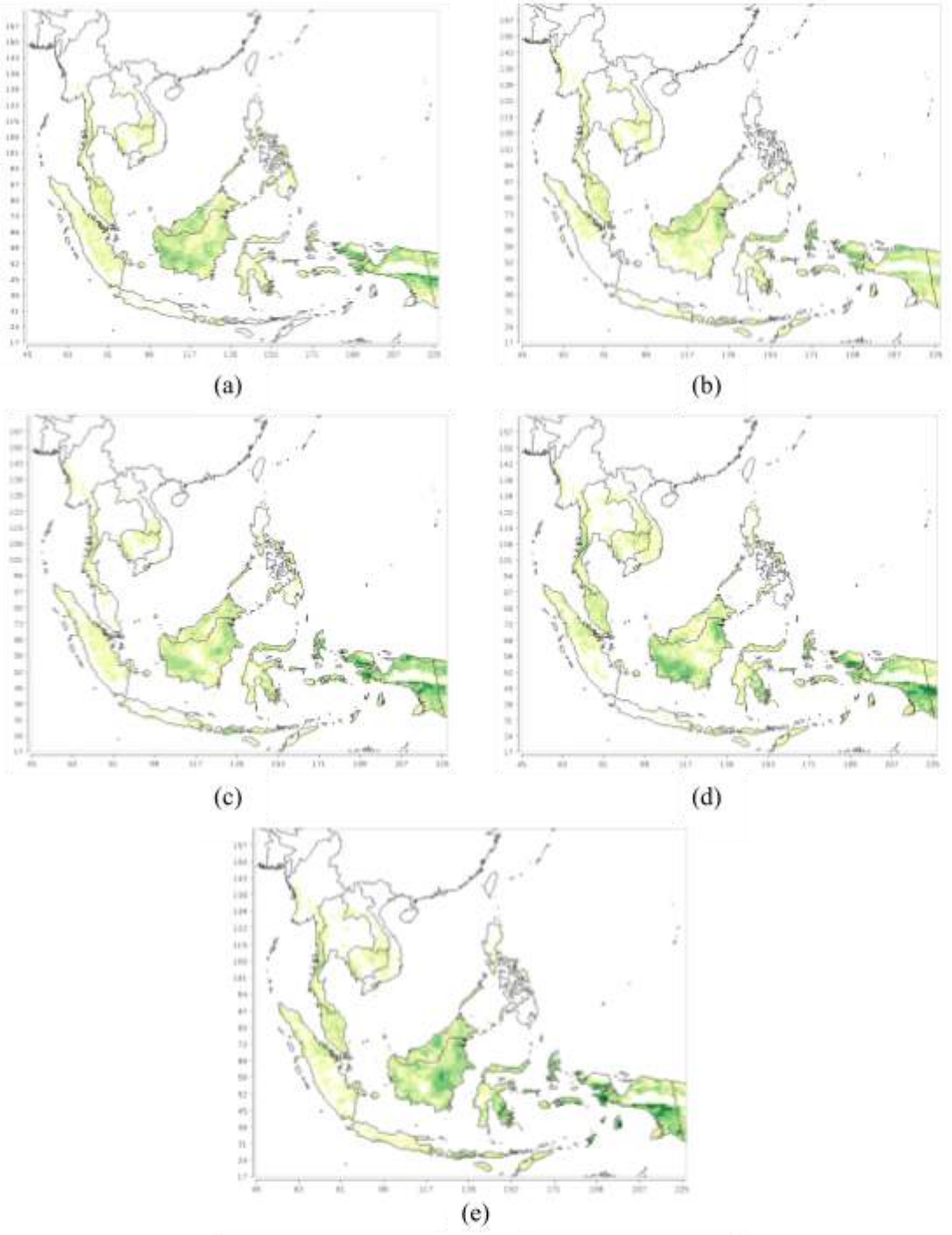

Figure 3.3.3: Total isoprene emissions for January in (a) 2013, (b) 2030, (c) 2050, (d) 2070 and (e) 2100 under RCP6.0 scenario.

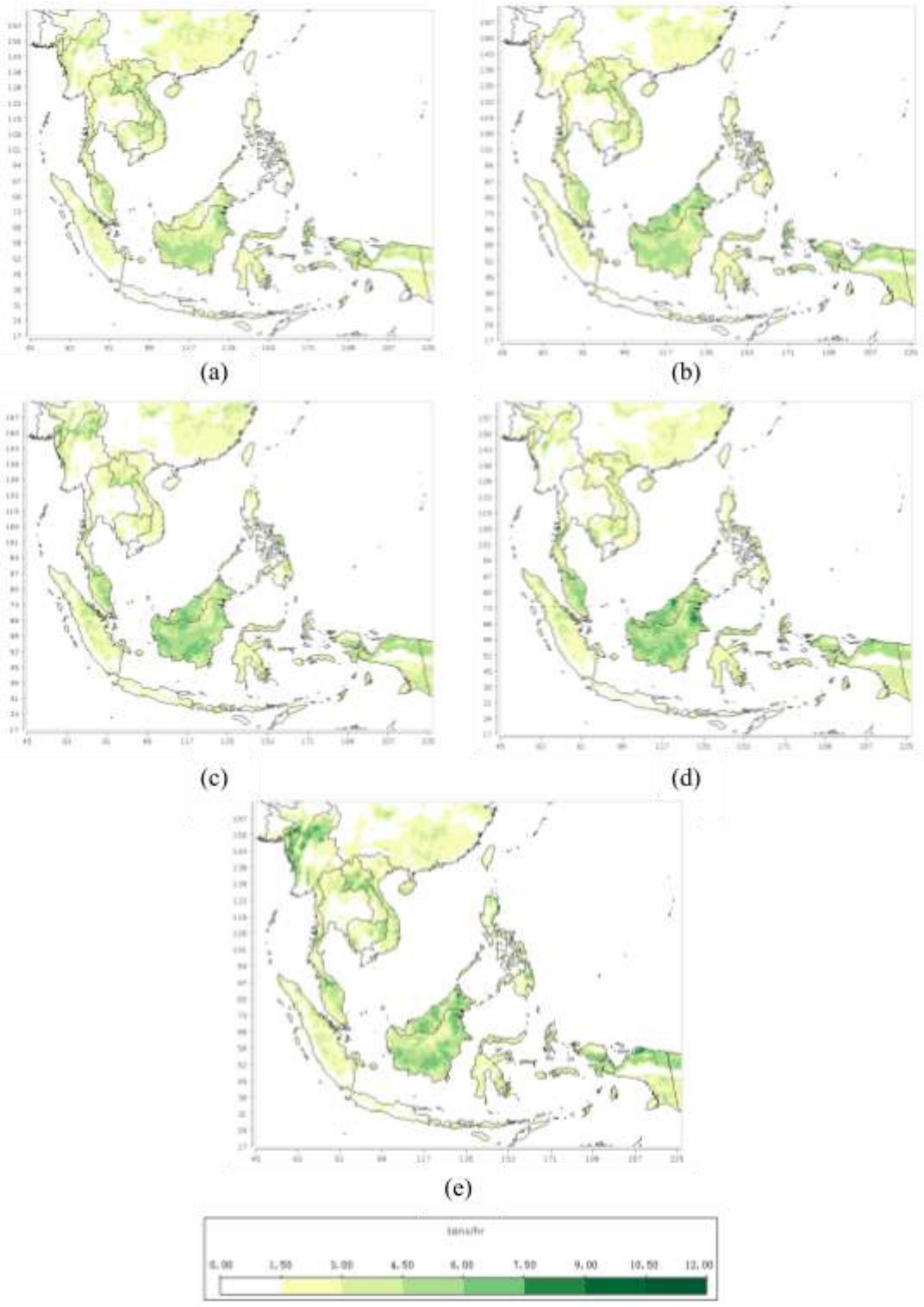

Figure 3.3.4: Total isoprene emissions for July in (a) 2013, (b) 2030, (c) 2050, (d) 2070 and (e) 2100 under RCP6.0 scenario.

Moreover, the top isoprene emitter in SEA is within Malaysia and Brunei with the highest emission rate which is up to 10.77 tons/hr in July by the end of century. While Indonesia shows the second highest isoprene emitter (similar with RCP4.5 – July) with a highest emission in 2100 at 9.74 tons/hr. Compared to January, Thailand indicates an increment of isoprene emission in July with a highest rate at 7.87 tons/hr, then followed by Philippines at 7.56 tons/hr, Myanmar at 7.18, Cambodia at 7.14 tons/hr, Vietnam at 6.39 tons/hr, Laos at 5.91 tons/hr, and Singapore at 3.82 tons/hr. Studies support that the total isoprene emissions was found higher in tropical and sub-tropical zones, due to the higher temperature and light flux that stimulate high leaf emission rates (Alves et al., 2014; Chang et al. 2014; Jardine et al., 2014, 2016).

As depicted in Figure 3.3.4, the projected simulation of isoprene emissions in July reveals a higher appearance of isoprene emissions in the whole SEA region than January, which has the lowest emissions in mainland SEA, particularly in Myanmar. Obviously, besides Borneo Island, the model projected higher rate of isoprene emitted in Mainland SEA – Myanmar, Laos, Cambodia, and Vietnam in July, especially during the end of century. Hence, it may be caused by the high O_3 concentration that influence the synthesis and emissions of terpenoids (Yang et al., 2021), thus, plant emits more isoprene emission due to their defence mechanisms to protect itself (Harrison et al., 2013; Li and Xie 2014; Hantson et al. 2017).

3.3.5.3 RCP8.5 Scenario

The RCP8.5 scenario is classified by increasing greenhouse gas emissions over time and represents scenarios in the literature that result in high levels of greenhouse gas concentration (Riahi et al., 2008). Under RCP8.5 scenario, the total isoprene emissions are projected with increasing trend in both January and July. The highest value of isoprene emissions in January is found at 12.41 tons/hr in 2100, then 11.24 tons/hr in 2070, 8.82 tons/hr in 2050, 8.27 tons/hr in 2030 and 7.86 tons/hr in 2013. Refer to Table 3.3.3, the future projection of total isoprene emissions as relative to baseline period was recorded as 0.41 tons/hr (5.22%), 0.96 tons/hr (12.21%), 3.38 tons/hr (43%), 4.55 tons/hr (57.89%) in 2030, 2050, 2070 and 2100 respectively.

Table 3.3.3: Total Isoprene emissions in Southeast Asia under RCP8.5.

Year	Month	Isoprene Emissions (tons/hr)	Changes (tons/hr)	Percentage in Increment (%)
2013	**January**	7.86	-	-

	July	7.80	-	-
2030	**January**	8.27	0.41	5.22
	July	7.87	0.07	0.90
2050	**January**	8.82	0.96	12.21
	July	8.34	0.54	6.92
2070	**January**	11.24	3.38	43.00
	July	9.05	1.25	16.03
2100	**January**	12.41	4.55	57.89
	July	10.15	2.35	30.13

Under the projected simulation, Indonesia shows the highest emitter of isoprene with increasing trend in January at 7.76 tons/hr (2013), 8.59 tons/hr (2030), 8.66 tons/hr (2050), 10.70 tons/hr (2070) and 15.35 tons/hr (2100). Besides, Malaysia and Brunei were estimated the second highest isoprene emitter among SEA region with an emission range at 5.95 to 8.834 tons/hr (Brunei) and 6.86 to 8.83 tons/hr (Malaysia) throughout the projected years. While the rest reveals a decreasing trend during the end of century by projected an emission at 5.26 tons/hr in Philippines, 4.52 tons/hr in Thailand, 3.37 tons/hr in Cambodia, 3.02 tons/hr in Vietnam, 2.98 tons/hr in Laos, 1.72 tons/hr in Myanmar, and 0.97 tons/hr in Singapore (Appendix 3.3.1AC).

Furthermore, Figure 3.3.5 reveals that Papua Island has the highest amount of isoprene emissions in January in the period of 2013, 2030, 2050, 2070 and 2100. While Borneo Island was at the second highest isoprene emitter throughout the projected years and notable during 2030 and 2100, except in 2070 which suggest a decrement of isoprene emission. Sulawesi Indonesia can be observed with a medium rate of isoprene emission after Borneo and Papua Island, especially during the of the century. On the other hand, mainland of SEA (including Thailand, Myanmar, Laos, Vietnam, and Cambodia) suggests lesser amount of isoprene emissions but higher in 2100. Also, both Java Indonesia and Philippines show a lower emission of isoprene during January.

Moreover, the projected isoprene emissions in July (figure 3.3.6) for the year of 2013, 2030, 2050, 2070 and 2100 were 7.80 tons/hr, 7.87 tons/hr, 8.34 tons/hr, 9.05 tons/hr and 10.15 tons/hr, respectively. However, the increment of isoprene emissions in July is smaller than January in this scenario, with 0.07 tons/hr (0.90%) in 2030, 0.54 tons/hr (6.92%) in 2050, 1.25 tons/hr (16.03%) in 2070 and 2.35 tons/hr (30.13%) in 2100. Compared to January, the isoprene emissions in SEA region during July is projected with a lower emission, and most notable in 2070 and 2100 by the changes of 2.19 tons/hr (2070) and 2.26 tons/hr (2100).

Although the emissions of isoprene in SEA region during July were lower than January, however, Indonesia shows a large increment during the end of century with a total amount of 17.92 tons/hr, which has the highest emission record than January. Nevertheless, Malaysia, Brunei, Philippines, Thailand, and Myanmar were projected with 11.87, 11.06, 8.64, 8.95, 7.60 tons/hr by the

end of century, and thus reveal a higher emission in July compared to January. Also, Vietnam, Laos and Cambodia are projected a higher isoprene in July during the year of 2070 at 8.79, 8.95, 8.40 tons/hr but then decrease by the end of century. Similarly, Singapore is projected the least isoprene emission within SEA region and suggests a decreasing trend at total emission of 1.05 tons/hr in 2100.

Projected isoprene simulation in July (Figure 3.3.6) depicts a continuous trend of increasing isoprene emission from 2013 to 2100. Obviously, the highest rate of the isoprene emissions was emitted from Borneo and Papua Island and most notable during the end of century. Besides, mainland SEA such as Thailand, Myanmar, Laos, Vietnam and Cambodia suggest an increasing trend during the projected years, except in 2030 – Cambodia shows a lower appearance of isoprene emissions through the year. In addition, West Malaysia and Sumatra Indonesia were also notable with higher isoprene emission in July and increase in emission rate throughout the projected years.

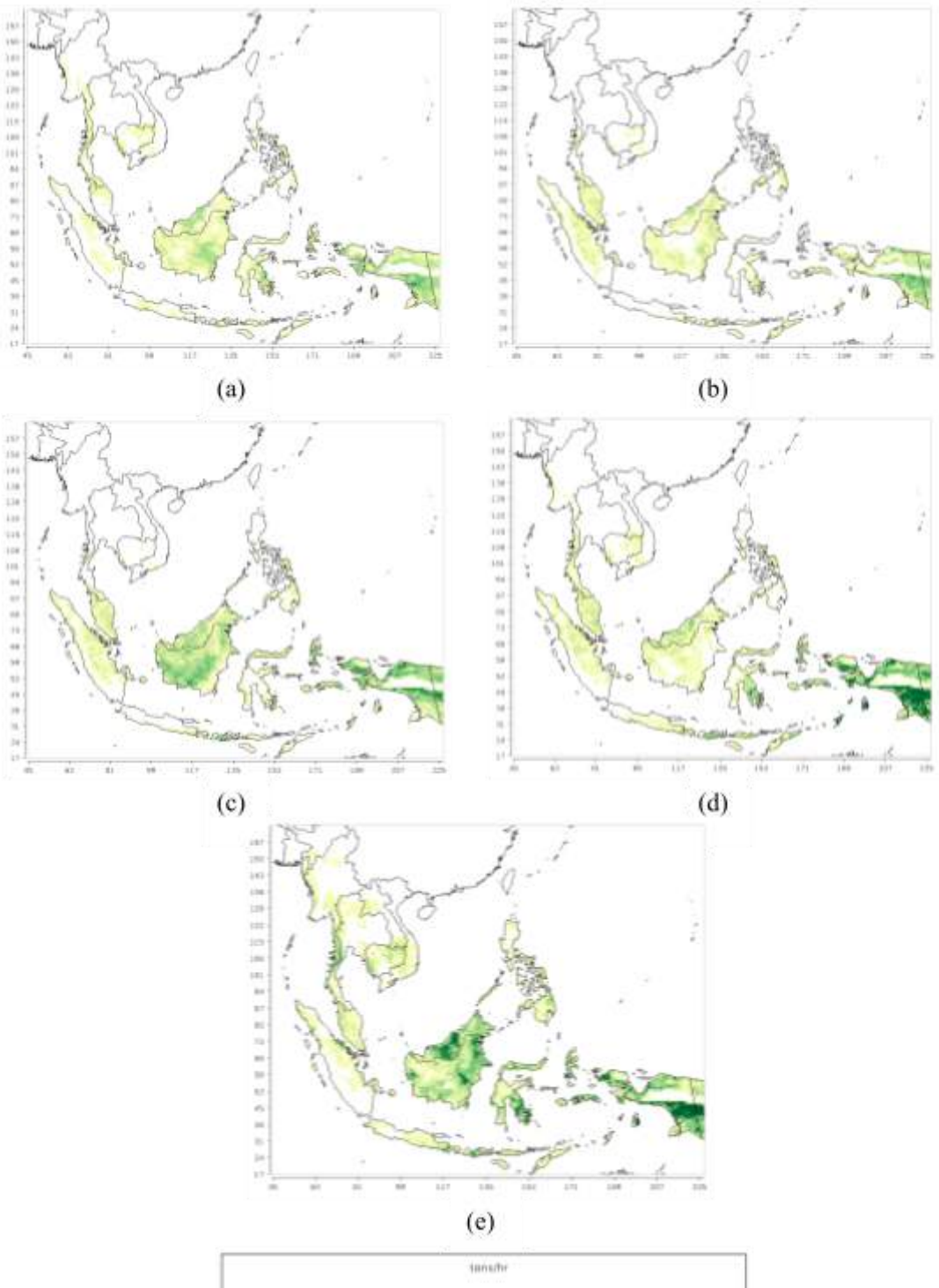

Figure 3.3.5: Total isoprene emissions for January in (a) 2013, (b)8. 2030, (c) 2050, (d) 2070 and (e) 2100 under RCP scenario

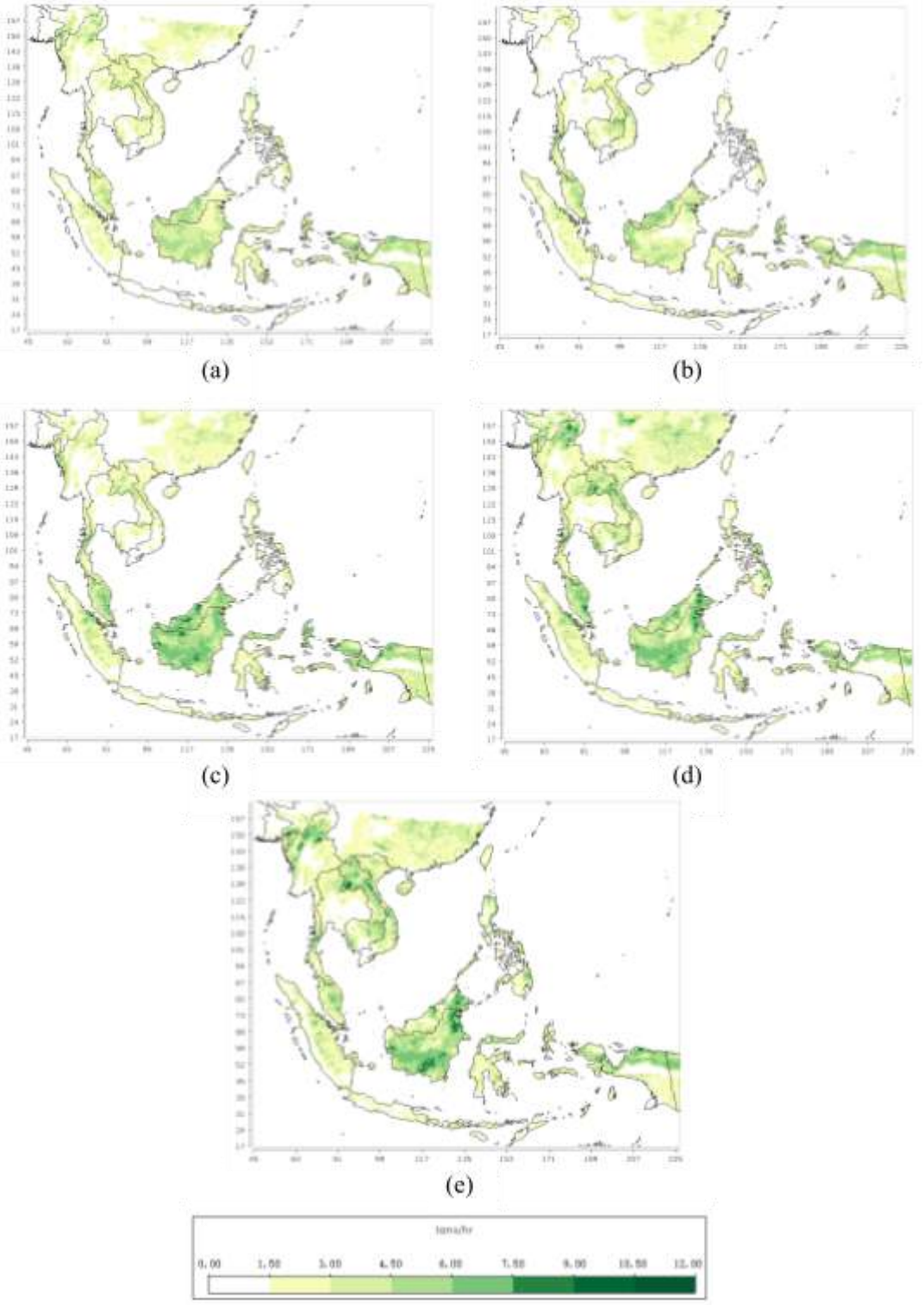

Figure 3.3.6: Total isoprene emissions for July in (a) 2013, (b) 2030, (c) 2050, (d) 2070 and (e) 2100 under RCP8.5 scenario

Overall, the projected isoprene emissions in January are higher compared to July due to the vegetation – plant species (Meeningen et al., 2016) and various climatic conditions (Jiang et al., 2018), including ambient ozone, water stress, CO_2 concentration and drought, especially temperature and light (Pacifico et al., 2009; Hu, 2015). Besides, Mainland SEA were predicted with lower temperature range in January which may inhibits the emission of isoprene at temperature below 10 to 20 °C (Oku et al., 2014; Mutanda et al., 2016). Also, SEA considered as tropical region that consists one of the largest tropical forests (Kanakidou et al., 2005) which release isoprene emission from the 20% of the tropical species (Loreto and Fineschi, 2015).

3.3.2 Biogenic Emission Hot-Spot Areas

Most studies revealed that isoprene emission rates are controlled by the environmental factors (Grote and Biinemets, 2008; Niinemets et al., 2010; Guenther et al., 2012; Monson et al., 2012; Jiang et al., 2018), which highly vulnerable to temperature (Monson et al., 2012; Pacifico et al., 2012; Unger et al., 2013; Grote et al., 2014; Holopainen et al., 2018; Feng et al., 2019). To further investigate the regulation mechanism of isoprene emission under climate change (temperature), different correlations among isoprene emission and temperature in January and July during 2013 and 2100 were observed and analysed under RCP4.5 and 8.5 scenarios. To get the efficiency of the relationship between temperature and isoprene, three areas have been selected within Southeast Asia region – Borneo Island, Papua Island and the region of West Malaysia and Sumatra, Indonesia (Figure 3.3.7).

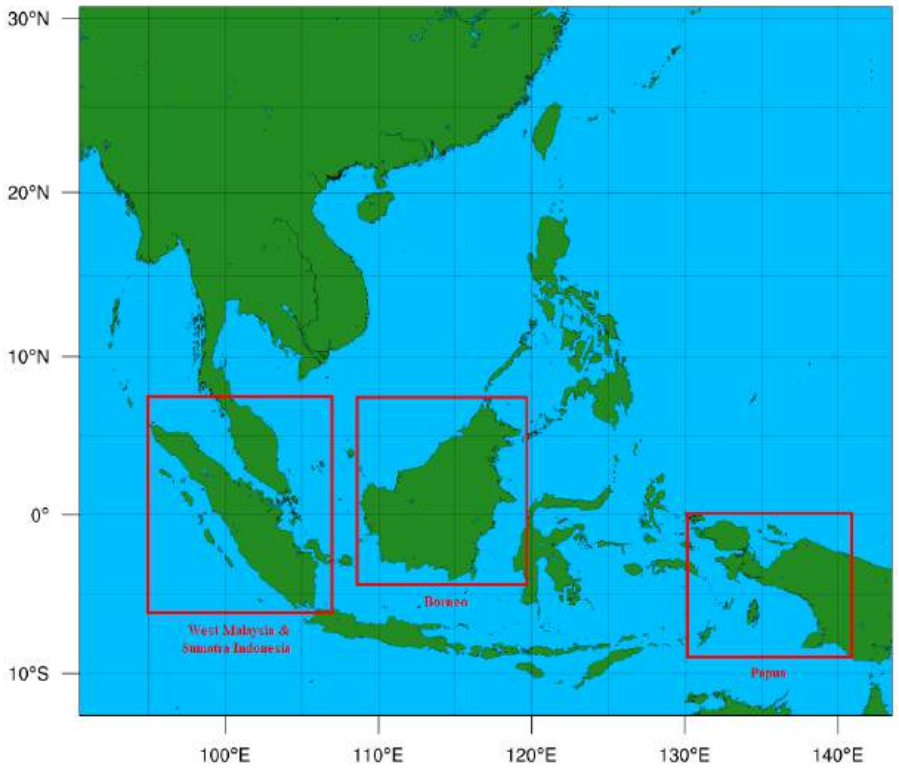

Figure 3.3.7: Three selected areas (Borneo, Papua, and West Malaysia & Sumatra Indonesia) within Southeast Asia Region.

3.3.2.1 Borneo Island

Based on the projected simulations (section 3.1 and 3.3), Borneo Island was found to have a higher value of both temperature and isoprene. As expected, the emission of isoprene in Borneo Island was found to be highly correlated with temperature at r value of 0.763 in January and 0.867 in July during the year of 2013, and r value of 0.715 in January and 0.648 in July during the end of century under RCP4.5 scenario, respectively (Table 3.3.4). Both 2013 and 2100 also indicates that the most favourable conditions for isoprene emission appear to be in the temperature range of 27.42 to 28.86℃ and 28.48 to 29.74 ℃ in January; and 27.96 to 29.86 ℃ and 29.12 to 30.43 ℃ in July. Besides, the rate of isoprene emissions was found at 5.49 to 7.88 tons/hr in January and 5.59 to 8.52 tons/hr in July during 2013 and 2100 within this region.

In RCP8.5 scenario, the correlation between isoprene emission and temperature in Borneo Island is also show a good relationship at r value of 0.712 and 0.895 in January and July during 2013, where the emission of isoprene can be found at the temperature range of 27.57 to 28.81 ℃ in January and 28.09 to 30.21 ℃ in July, respectively. However, there is a moderate correlation at r value of 0.460 in January, but a strong correlation at r value of 0.825 in July during the end of century. The isoprene emission can be observed at the range of temperature between 29.35 and 31.31 ℃ in January, 30.44 and 32.17 ℃ in July. The emission rate of isoprene in the year of 2013 and 2100 were found between 5 to 10.59 tons/hr in January and 5.26 to 11.77 tons/hr.

Table 3.3.4: Correlation Coefficient between Surface Temperature and Isoprene Emission in Borneo, Papua Island, and West Malaysia and Sumatra Indonesia during 2013 (baseline) and 2100 (end of century) under RCP4.5 and 8.5 scenarios

Scenarios	**Area**	**Correlation Coefficient**			
		2013		**2100**	
		Jan	**Jul**	**Jan**	**Jul**
RCP45	Borneo Island	0.763	0.876	0.715	0.648
	Papua Island	0.754	0.662	0.816	0.853
	West Malaysia & Sumatra Indonesia	0.813	0.711	0.451	0.739

RCP85	Borneo Island	0.712	0.895	0.460	0.825
	Papua Island	0.615	0.797	0.831	0.690
	West Malaysia & Sumatra Indonesia	0.282	0.948	0.270	0.195

RCP4.5 scenario shows a strong relationship between isoprene and temperature in Borneo Island at r value above 0.6, where the isoprene emission was highly dependent on temperature with optimum range between 20 to 40℃ (Guenther et al., 2012; Egigu et al., 2014; Huang et al., 2018). Compared to RCP4.5 scenario, the temperature and isoprene emission analyzed in Borneo Island were much higher under RCP8.5 scenario due to the high assumption of RCP8.5 in future emission (Riahi et al., 2008). Besides, a finding of Mishra and Sinha (2020) reveals a strong correlation of isoprene emission and temperature during the monsoon and summer seasons in India. Also, Mishra and Sinha (2020) support that the preferred condition for biogenic emissions to be appear during temperature range below 40℃ and soil moisture was limited.

In addition, Borneo Island is the largest oil palm's production (Gaveau et al., 2016), where the oil palm emits greater amount compared to tropical forest landscapes (Hewit et al., 2009), and it is predicted to be increase in the future due to the high demand of palm oil (Corley, 2009; Malins, 2017). Hence, this explained that higher rate of isoprene emission in Borneo Island may be due to the larger area of oil palm's plantation. Moreover, since Borneo Island is located in tropical area, the isoprene emissions can be largely found within the Borneo Island, as the emission are higher in tropical habitats (Exton et al., 2015).

3.3.2.2 Papua Island

Papua Island is one of the top isoprene emitters among the Southeast Asia region beside Borneo Island, which can be observed from the projected simulations. In RCP4.5 scenario, the projected isoprene emission found to be highly correlated with temperature at r value of 0.754 and 0.662 in January and July during 2013, while much higher during 2100 at r value of 0.816 in January and 0.853 in July, respectively (Table 3.3.4). Hence, the temperature range between 27.10 to 28.48℃ and 25.56 to 26.74℃ are spotted with the presence of isoprene emissions for both January and July during 2013 at the emissions rate from 5.24 to 8.92 tons/hr. At the end of century, isoprene emissions rate between 6.09 to 11.52 tons/hr are spotted at the range of temperature at 27.53 to 29.66 ℃ in January and 26.94 to 27.77 ℃ in July.

In RCP8.5 scenario, both year of 2013 and 2100 show a good correlation between isoprene emission and temperature at the value r above 0.5, which are 0.615 (2013) and 0.831 (2100) during January while 0.797 (2013) and 0.690 (2100) during July, respectively. The isoprene emissions are likely to appears in temperature between 27.10 to 28.05 ℃ in January and 26.13 to 27.24 ℃ in July

with an emission rate between 5.90 to 8.55 tons/hr but less likely to appears at the temperature above 27.24℃ during the year of 2013. While the isoprene emission rate at 7.45 to 15.77 tons/hr can be observed at the temperature range between 30.25 to 31.65 ℃ in January and 27.72 to 29.14 ℃ in July during 2100.

Both RCP4.5 and 8.5 scenarios show a satisfactory correlation between isoprene emission and temperature with value r above 0.6 during 2013 and 2100. Compared to Borneo Island, Papua Island has the highest rate of isoprene emission that reached 15.77 tons/hr in January 2100 under RCP8.5 scenario. Besides, Guenther et al. (1995) and Pugh et al. (2013) also support the product of isoprene is increasing exponentially with temperature as it is driven by light and temperature. In general, isoprene emissions are produced in the photosynthesis process and controlled by temperature and hours of light presence (Dani et al., 2017), and study by Hrebien et al. (2021) also reveals a higher temperature and increased of hours of light are the main factors affecting the production of isoprene in the tropics.

3.3.2.3 West Malaysia and Sumatra Indonesia

The region of West Malaysia and Sumatra Indonesia can be observed in the projected simulations with a moderate isoprene emission rate, but higher emission rate during certain year especially in July. Under RCP4.5 scenario, the correlation of isoprene and temperature in the year of 2013 shows a positive relationship with r value of 0.813 in January and 0.711 in July (Table 3.3.4). While in the year of 2100, the relationship between isoprene and temperature shows a moderate correlation with r value of 0.451 in January, but a good correlation at r of 0.739 in July. Hence, it reveals a moderate dependent of isoprene emission to temperature in January but higher in July. The emissions rate of isoprene within this region was at the range from 3.12 – 7.11 tons/hr, with the range of temperature at 26.34 to 29.17 ℃ in January and 28.20 to 30.22℃ in July during both year of 2013 and 2100.

In RCP8.5 scenario, the projected isoprene found to be weak correlated with temperature at r value of 0.282 in January, but very high correlated at r value of 0.948 in July during 2013. The temperature range between 27.03 to 28.02℃ and 28.45 to 29.79℃ are spotted with the presence of isoprene emissions at 3.76 to 7.03 tons/hr for both January and July during 2013. However, at the end of the century, both January and July show a weak correlation between isoprene emission and temperature with r values of 0.270 and 0.195. The emissions of isoprene were observed during the temperature between 28.37 to 30.30℃ in January and 30.27 to 31.41℃ in July during 2100, with the emission rate from 5.26 to 9.16 tons/hr. Hence, this indicates that the isoprene emissions are not influenced by the changing of temperature within this region during the end of the century.

The heating effect is likely to suppress the effect of higher CO2 concentrations as the temperatures rise in the future (Tingey et al., 2007; Lahr et al., 2015) and could lead to the increase emissions of BVOCs in urban areas (Norton et al., 2015). However, some studies revealed that

increasing of CO2 could lead to the declining of isoprene emission (Sharkey and Monson, 2014; Monson et al., 2016; Rasulov et al., 2018; Lantz et al., 2019). Also, Potosnak et al. (2014) found that a high CO2 concentration could reduce isoprene emissions by increasing leaf temperature at 20-35℃.

3.4 Climate Change Impact on Air Quality in Southeast Asia

3.4.1 CMAQ Model Evaluation

For performance evaluation of the coupled model, the results from the baseline scenarios were evaluated against the measurements for the same period at the respective sites. The air concentrations were maximum daily average 1-hour surface ozone (Max 1-hr O_3). Both hourly average CO and NOx were also considered as they were the precursors of O_3. For this analysis, the comparison between observed and measured values focused on a period of January and July during the year 2013. Due to the limitation of data availability in Southeast Asia, and air quality evaluation was made based on the daily surface observation dataset in Malaysia. The simulation for air quality based on RCP baseline scenarios was also being compared with the reanalysis dataset. In general, the model performance was carried out based on 4 separated ways as shown below:

a. CMAQ_RCP85 and observation (DOE)

b. CMAQ_RCP85and CMAQ_NCEP

c. CMAQ_RCP45 and observation (DOE)

d. MAQ_RCP45 and CMAQ_NCEP

3.4.1.1 Evaluation of CMAQ_RCP85

Table 3.4.1 shows the seasonal statistical performance of CMAQ, induced by WRF_RCP8.5 meteorological data and MIC_Asia emission inventory during January and July 2013. In January, the projection of maximum 1-hour average ozone over the 5 cities compares well with observation data, with NMB and Fa2 around 28.0% and 1.2 value respectively. However, a slightly overestimated was found during the July season with a bias of 38.3% and Fa2 of 1.3 value. As shown in Table 3.4.2, 24-h average CO was highly overestimated in January period with values value recorded as -69.1% (NMB) and 0.3 (Fa2). Meanwhile, the projection of 24-hour average NOx during January also underestimated of -92.3% (NMB) and 0.076 (Fa2) as relative to observe dataset. In July, underestimation was slightly lower with NMB and Fa2 around -86.7% and 0.13 value respectively.

Table 3.4.1: Statistical Performance between CMAQ_RCP8.5 and observation for surface ozone (O_3), carbon monoxide (CO), and oxides of nitrogen (NO_x)

Variable	Projection	DOE	NMB	FB	NMSE	Fa2
January						

Max 1-h O_3 (ppb)	50.5	39.4	28.0	0.24	0.062	1.2
Hourly average NO_x (ppb)	1.22	15.8	-92.3	-1.71	11.0	0.076
Hourly average CO (ppb)	142.4	461.1	-69.1	-1.05	1.5	0.30
July						
Max 1-h O_3 (ppb)	52.7	38.1	38.3	0.32	0.10	1.3
Hourly average NO_x (ppb)	2.0	15.0	-86.7	-1.5	5.6	0.13
Hourly average CO (ppb)	151.5	489.6	-69.0	-1.05	1.5	0.30

NMB: Normalized Mean Bias, FB: Fractional Bias, NMSE: Normalized Mean Square Error, Fa2: Factor of Two.

The NMB for maximum daily average 1-hour O_3 mixing ratio between CMAQ_RCP8.5 and CMAQ_NCEP was 10.9% and 11.6% during January and July respectively (Table 3.4.2). The model performed with slightly over-estimation and 1.1 value of Fa2 for both periods. The monthly variation and spatial distribution of the average simulated max 1-h ozone by CMAQ_RCP8.5 were comparable agree to the NCEP reanalysis dataset (Figure 3.4.1). Both models have projected that the average surface O_3 mixing ratio in July was higher compared to January. Meanwhile, a higher O_3 was observed over Malaysian Peninsula than Malaysian Borneo. The CMAQ model projections were overestimated over NCEP reanalysis data across most of the domain in January (Figure 3.4.2). In July, the max 1-h ozone was found overestimated over the north Malaysian Peninsula but highly underestimated over the south.

The overestimation of O_3 might be caused by the overestimation and underestimation of O_3 precursor in the model chemistry. Similar overestimations of other primary emitted species of NO_x and CO have been seen in the study of Apel et al., (2015). A part of this, is due to the WRF model's tendency to underestimate overnight mixing in urban areas (Appel et al., 2013), as either the PBL heights are too low and the minimum eddy diffusivity is too small, resulting in an over estimation of pollutants near the surface and high model biases. Diurnal variations of precursor with the present of photochemical activity are important as it dominate the process of production and emission of precursor continuous throughout the day and night (Appel et al., 2013; Apel et al., 2015). As such, those elements would tend to cause overestimation during projecting O_3 due to bias mixing in the model (Querol et al., 2017).

Table 3.4.2: Statistical Performance between CMAQ_RCP8.5 and NCEP for surface O_3, CO, NO_x, OH, HO_2, and HNO_3 with CMAQ_NCEP

Variable	Projection	CMAQ_NCEP	NMB	FB	NMSE	Fa2
January						
Max 1-h O_3 (ppb)	47.8	42.8	11.6	0.11	0.012	1.1
Hourly average NO_x (ppb)	0.53	0.52	1.9	0.019	0.00036	1.0

Hourly average CO (ppb)	125	102.7	21.7	0.19	0.038	1.2
Hourly average OH (ppm)	0.059	0.053	11.3	0.10	0.011	1.1
Hourly average HNO_3 (ppb)	0.47	0.25	88.0	0.61	0.42	1.8
July						
Max 1-h O_3 (ppb)	43.4	39.1	10.9	0.10	0.010	1.1
Hourly average NO_x (ppb)	0.59	0.6	-1.6	-0.016	0.00028	0.98
Hourly average CO (ppb)	112.4	96.1	16.9	0.15	0.024	1.1
Hourly average OH (ppm)	0.044	0.035	25.7	0.22	0.052	1.2
Hourly average HNO_3 (ppb)	0.36	0.37	-2.7	-0.027	0.00075	0.97

NMB: Normalized Mean Bias, FB: Fractional Bias, NMSE: Normalized Mean Square Error, Fa2: Factor of Two.

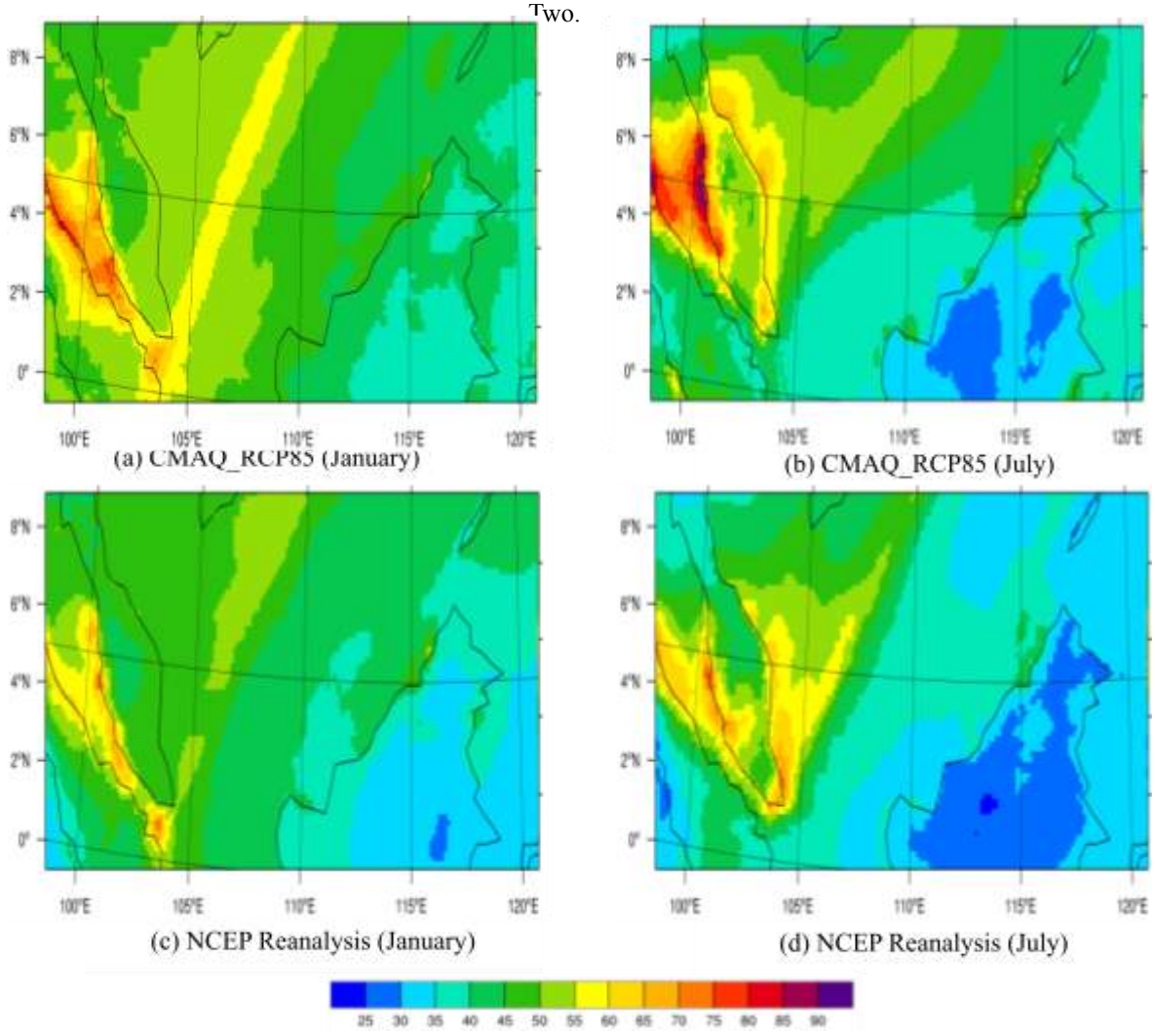

Figure 3.4.1: M1-hour daily average 1-hour surface ozone (ppb) for (a)-(b) January and July in CMAQ_RCP8.5 simulation and CMAQ_NCEP for (c)-(d) January and July by 2013.

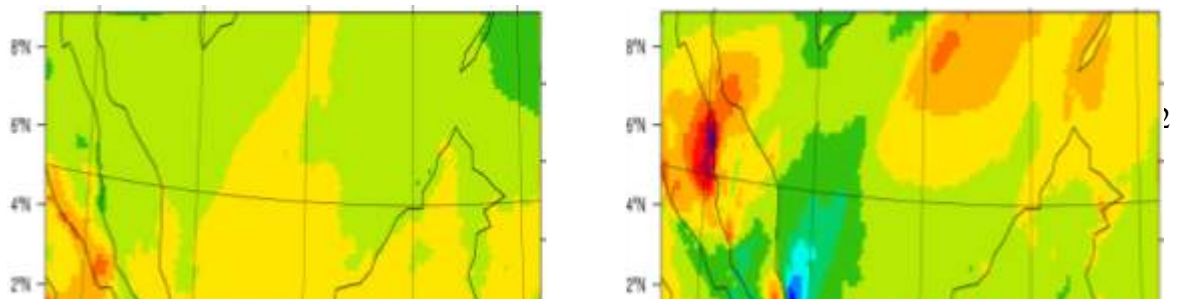

Figure 3.4.2: Changes of Maximum daily average 1-hour surface O_3 (pbb) between CMAQ_RCP8.5 and CMAQ_NCEP for January (a) and July (b) in 2013

Figure 3.4.3 shows the simulated of 1 hour average NO_x for CMAQ_RCP8.5 compared to CMAQ_NCEP. The NMB was 1.9% and -1.6% during January and July period respectively showing a very close estimation between both datasets (Table 3.4.2). Moreover, the Fa2 for both seasons was nearly 1.0 value. Meanwhile, both datasets indicated that the NO_x mixing ratio was high over certain areas of the Malaysian Peninsula and the South China Sea for both seasons. As shown in Figure 3.4.4, CMAQ_RCP8.5 agreed well with CMAQ_NCEP across most of the research domain except the small part of the southern Malaysian Peninsula underestimation was found (Figure 3.4.4).

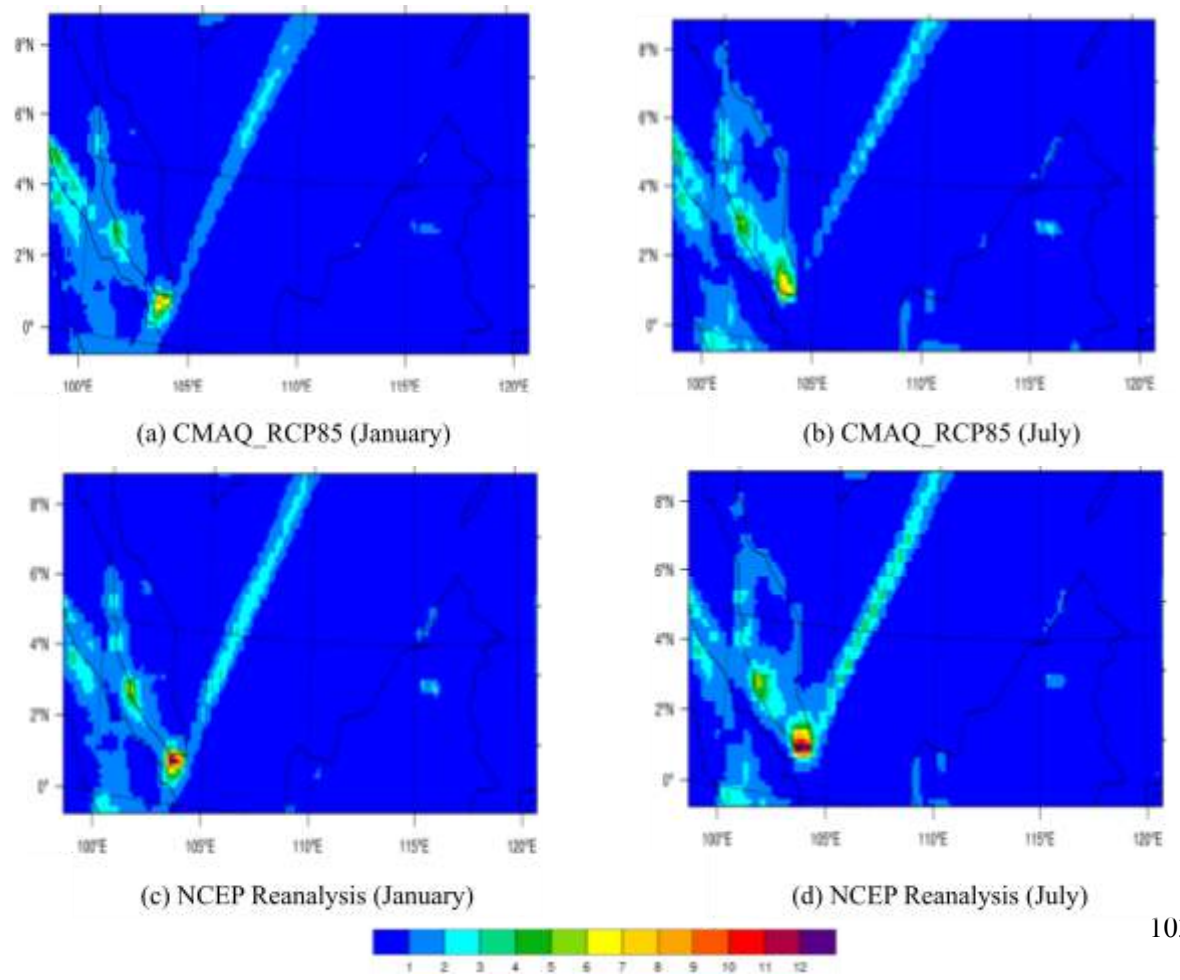

Figure 3.4.3: Hourly average of NO_x (ppb) for (a)-(b) January and July in CMAQ_RCP8.5 simulation and CMAQ_NCEP for (c)-(d) January and July by 2013.

The simulation of CMAQ_RCP8.5 and CMAQ_NCEP of hourly average carbon monoxide (CO) over the country are shown in Figure 3.4.5 The CO mixing ratio bias was relatively small by 21.7% in January and 16.9% in July. The small values of NMSE indicate performance CMAQ_RCP8.5 simulation. Meanwhile, the nearly 1.0 value of Fa2 shows an almost ideal model in projecting the CO mixing ratio. Figure 3.4.5 shows that the CO mixing ratio was higher over the west coast of the Malaysian Peninsula as compared to the other region for both seasons. The CMAQ_RCP8.5 overestimated CMAQ_NCEP by 22.3ppb (January) and 16.3ppb (July) as shown in Figure 3.4.6. The CO mixing ratio was largely overestimated by CMAQ_RCP8.5 over the northern part of the Malaysian Peninsula (> 80ppb), under-predicted across the southern region (< -20ppb) in July.

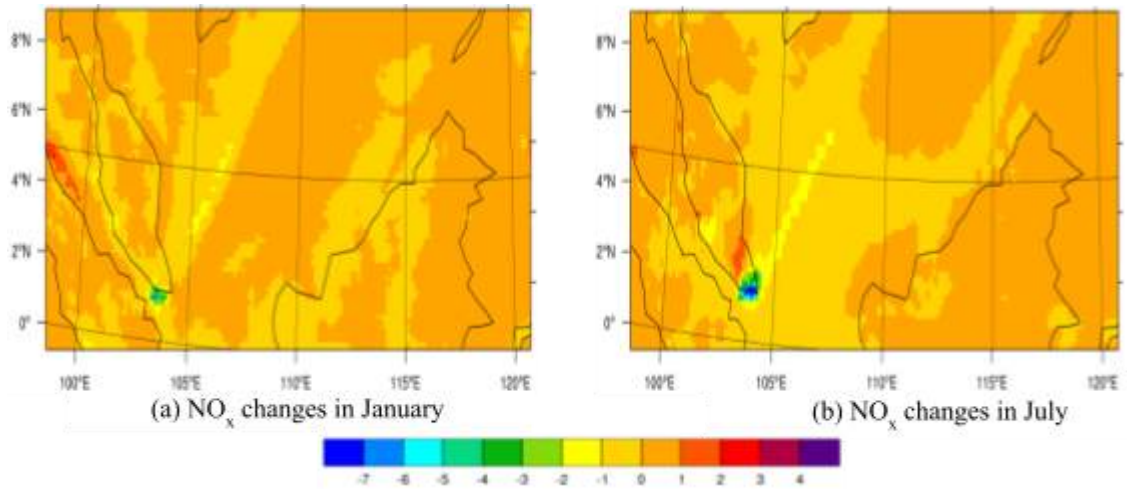

Figure 3.4.4: Hourly average changes of NO_x (ppb) between CMAQ_RCP8.5 and CMAQ_NCEP for January (a) and July (b) in 2013.

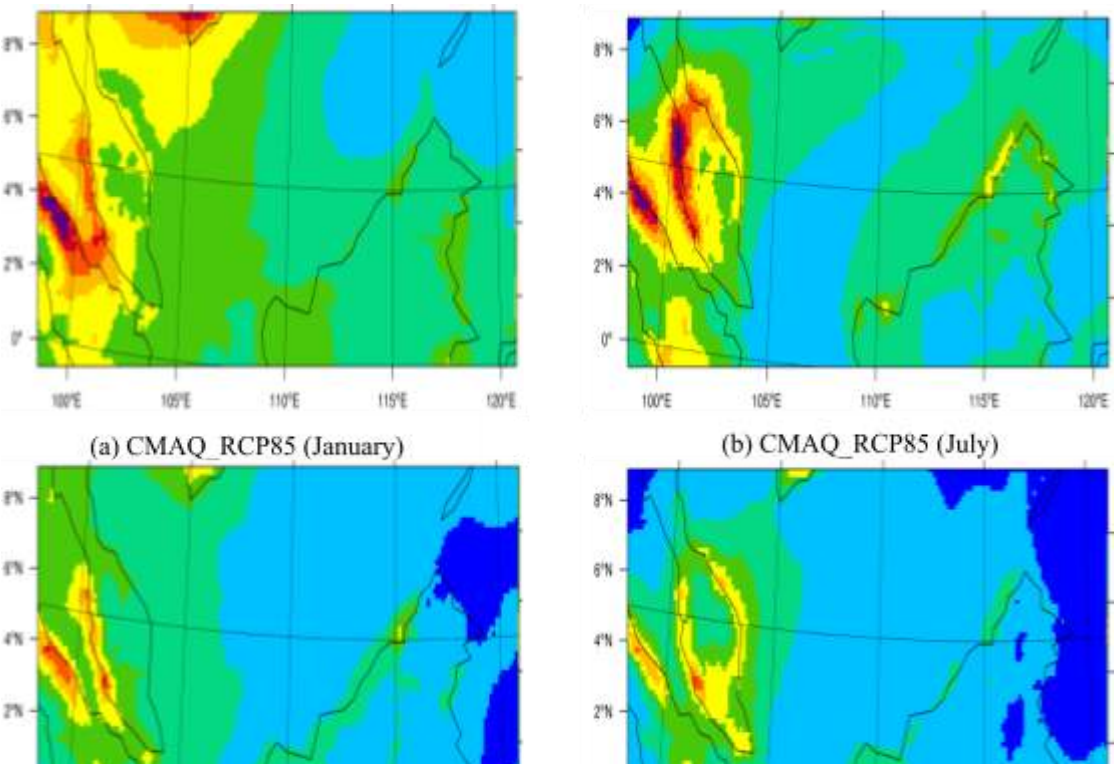

(a) CMAQ_RCP85 (January)

(b) CMAQ_RCP85 (July)

Figure 3.4.5: Hourly average of CO (ppb) for (a)-(b) January and July in CMAQ_RCP8.5 simulation and CMAQ_NCEP for (c)-(d) January and July by 2013.

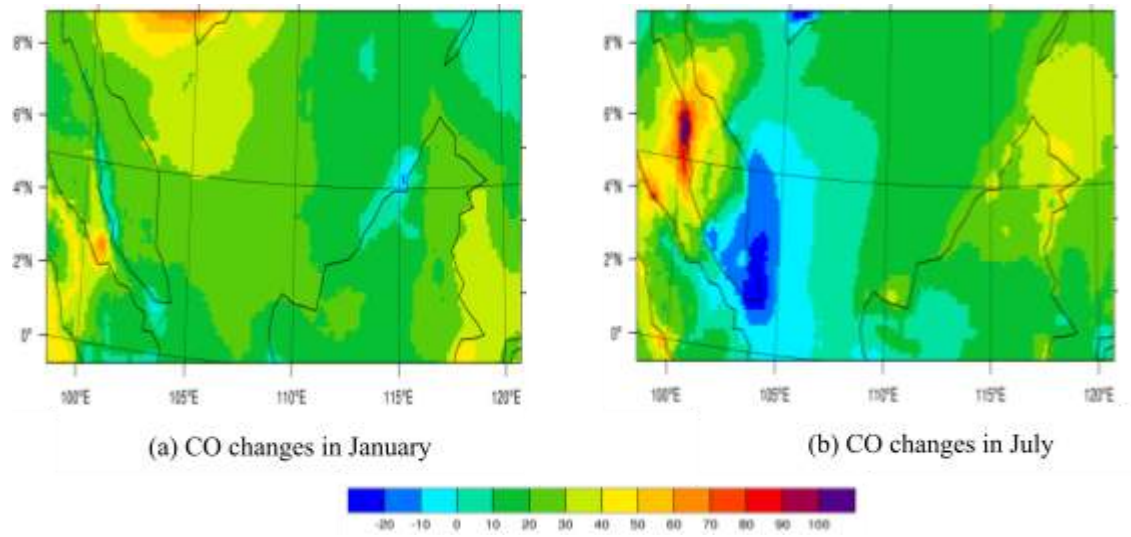

(a) CO changes in January

(b) CO changes in July

Figure 3.4.6: Hourly average changes of CO (ppb) between CMAQ_RCP8.5 and CMAQ_NCEP for January (a) and July (b) in 2013.

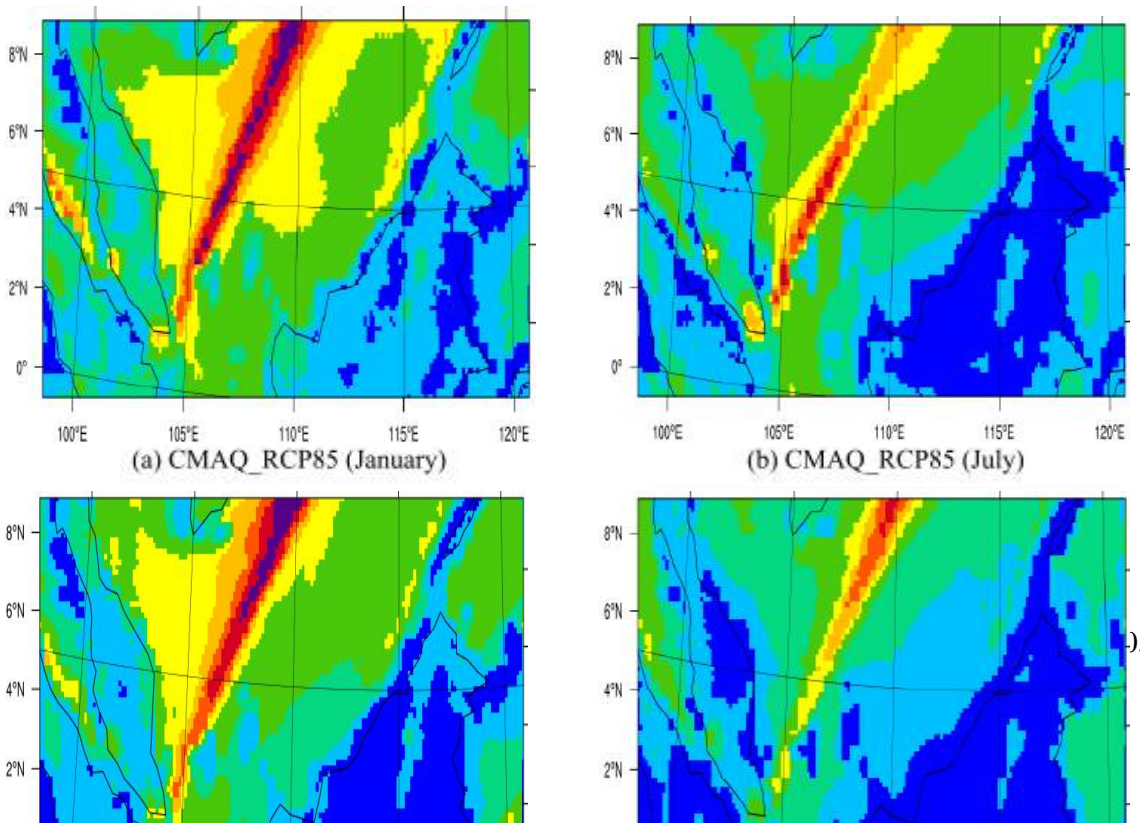

(a) CMAQ_RCP85 (January)

(b) CMAQ_RCP85 (July)

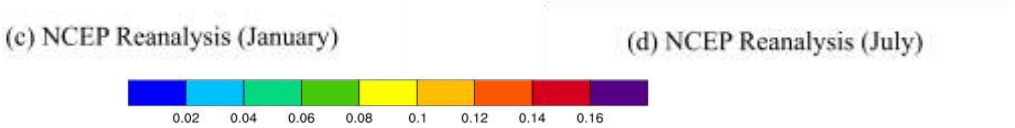

Figure 3.4.7: Hourly average of OH (ppm) for (a)-(b) January and July in CMAQ_RCP8.5 simulation and CMAQ_NCEP for (c)-(d) January and July by 2013.

The NMB of OH mixing ratio between both was overestimated by 11.3% and 25.7% in January and July respectively (Figure 3.4.7). The Fa2 between CMAQ_RCP8.5 and CMAQ_NCEP were relatively ideal by 1.1 during January and 1.2 during July. Both the WRF_RCP85 and NCEP reanalysis data suggested that the OH mixing ratio is highly distributed over the South China Sea. Based on Figure 3.4.8, the CMAQ_RCP8.5 simulated well with CMAQ_NCEP over most of the research domain in January. In July, high overestimation was found over a certain area of the South China Sea.

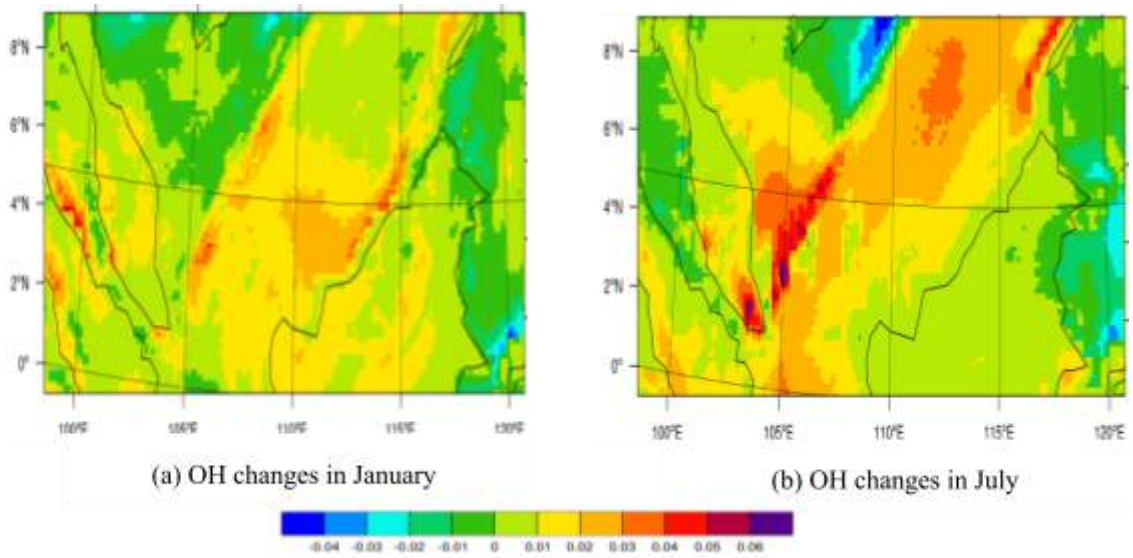

Figure 3.4.8: Hourly average changes of OH (ppm) between CMAQ_RCP8.5 and CMAQ_NCEP for January (a) and July (b) in 2013.

The projection of CMAQ_RCP8.5 and CMAQ_NCEP of hourly average HNO_3 over the country are shown in Figure 3.4.9. The HNO_3 mixing ratio bias was very high by 88% in January and relatively smaller by -2.7% in July. The Fa2 showed a value of 1.8 indicating a high estimation in January and a low estimation in July. The results show that the HNO_3 mixing ratio was higher over the

Malacca Straits and the South China Sea as compared to the other region for both seasons. During January, the CMAQ_RCP8.5 overestimated CMAQ_NCEP over the whole domain as shown in Figure 3.4.10. Meanwhile, the HNO_3 mixing ratio was overestimated by CMAQ_RCP8.the 5 over the northern part of the Malaysian Peninsula (> 0.8 underestimated across the southern region (< -1.2ppb) in Ju

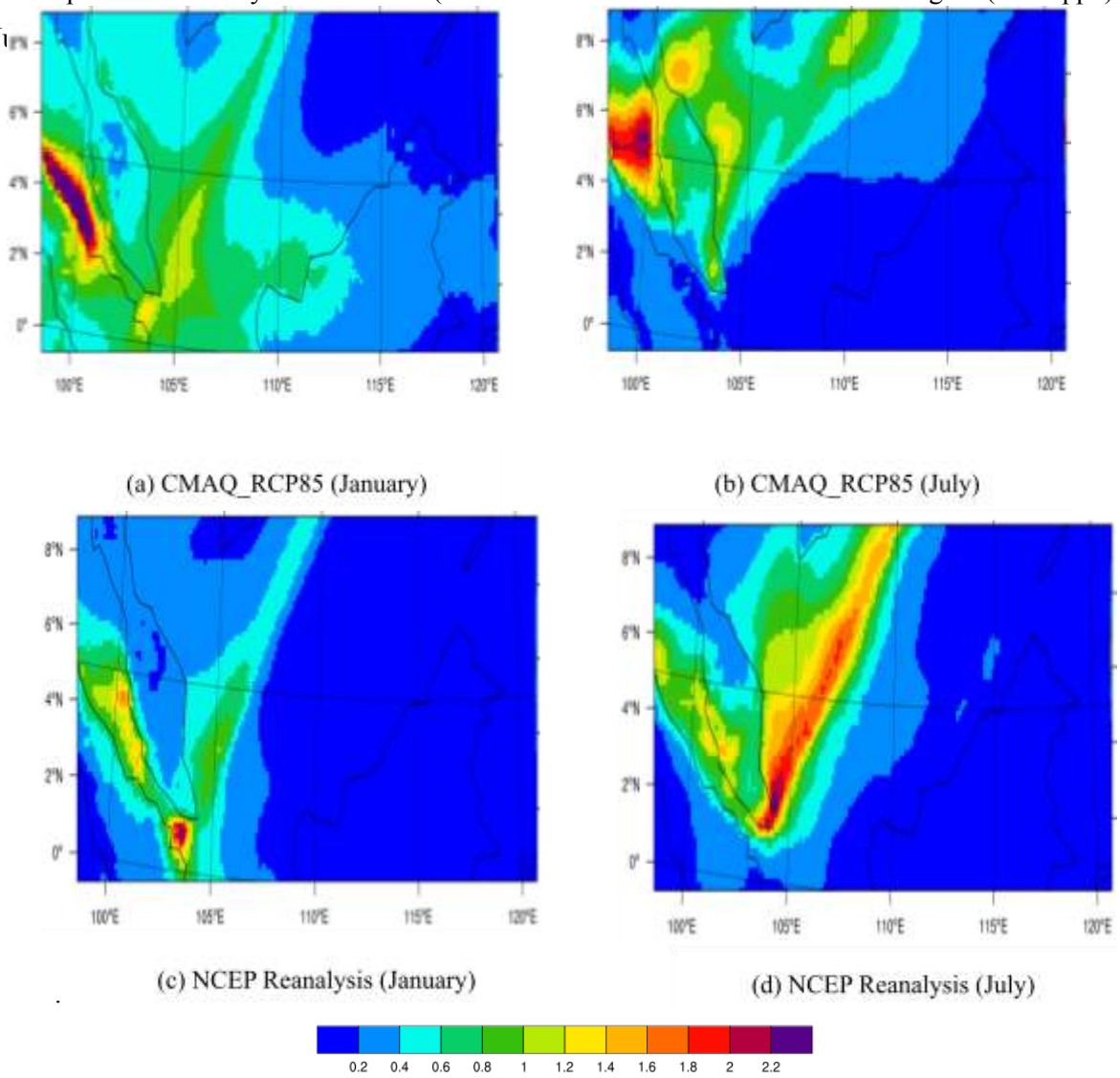

Figure 3.4.9: Hourly average changes of HNO_3 (ppb) between CMAQ_RCP8.5 and CMAQ_NCEP for January (a) and July (b) in 2013.

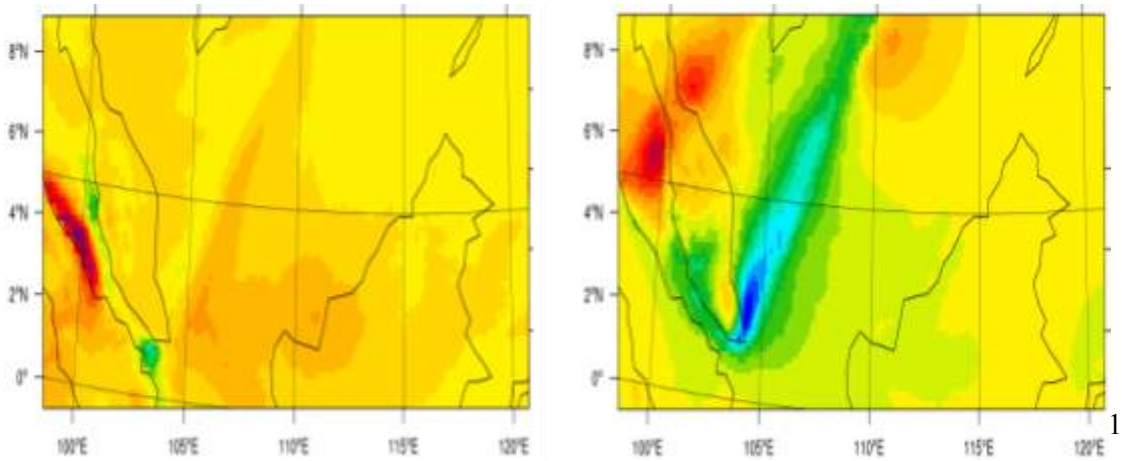

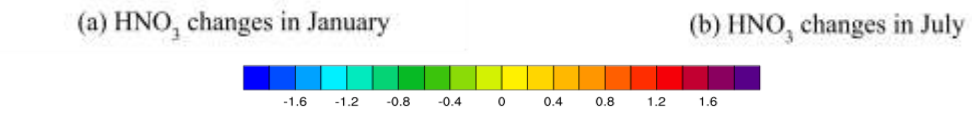

Figure 3.4.10: Hourly average changes of HNO_3 (ppb) between CMAQ_RCP8.5 and CMAQ_NCEP for January (a) and July (b) in 2013.

Uncertainties occur between the model output and observation in the present study ozone projection can be largely due to the uncertainties in the emission precursors especially the underestimation of CO and NO_x ($NO+NO_2$) and imprecision of meteorological variables as mentioned by Dentenel et al, (2006), Wang and Zhang (2012) and Ashley et al. (2015). The underestimation of CMAQ_RCP8.5 in projecting observed CO can be caused by overestimation in CO dry deposition, where more CO in the atmosphere falls back to the earth's surface. As shown in the chemical reaction of R1 and R2, the underestimation of NO can be the main reason for underestimation of NO_x.

$$RO_2 + NO \rightarrow RO + NO_2 \quad \text{(R1)}$$

$$HO_2 + NO \rightarrow OH + NO_2 \quad \text{(R2)}$$

Besides the emission factor, the overestimation of the modelled ozone can also be related to the uncertainty of RCM in simulating the surface temperature and solar radiation. In Section 3.1 (Climate Change), the WRF_RCP8.5 slightly underestimated the observed surface temperature (at least over the whole Malaysia region). The underestimation of surface temperature may be associated with the underestimation of modelled short-wave radiation from the sun. This is because the low surface temperature causes more cooling, and this happened when the earth's surface receives less radiation. As shown in R3, the destruction of surface ozone in the troposphere happened when the sunlight splits the ozone into molecule oxygen and atomic oxygen again. Therefore, more ozone can be created with less exposure to solar radiation.

$$O_3 + h\nu \rightarrow O_2 + O(^1D) \quad \text{(R3)}$$

Generally, the performance between the model output and reanalysis data for ozone, CO, and NO_x was much better than the performance between the modelled and observed. Since the reanalysis data was processed through the same version of the CMAQ model, with the same WRF output data and emission inventory as CMAQ_RCP8.5, the uncertainty of inherent model physics and chemistry can be eliminated. Meanwhile, such good agreement between CMAQ_RCP8.5 and CMAQ_NCEP for ozone simulation was related to the good agreement of both datasets in simulating CO and NO_x, with

the range of bias between -1.6% to 21.7%, since both pollutants are the precursors of the ozone (Drechsler, 2004; Steiner et al., 2006; Ahrens, 2013).

Besides the reasons of emission and meteorological effect, lack of seasonal cycle in anthropogenic emission or consideration of the stratospheric influx of O_3 might cause the overestimation of O_3 (Stevenson et al., 2006), which was not simulated in the study. In addition, the coarse resolution of the model in 15km × 15km might not be sufficient to simulate the meteorological phenomena and chemical composition (Ashley et al., 2015). Some limitations existed in the present study that leads to the uncertainties. Land use, land cover, vegetation, and emission inventory were kept constant throughout the whole research. Meanwhile, model biases could also be due to the model exclusion on the emission of dust and lightning NO_x. Other limitations such as the limited length the of simulation, applying a single RCM and air quality model, and also the use of the offline coupled model (Ashley et al., 2015), was also noted.

3.4.1.2 Evaluation of CMAQ_RCP45

The seasonal statistical performance of CMAQ, induced by WRF_RCP4.5 meteorological data and emission inventory during winter and summer 2013 is shown in Table 3.4.3. The simulation of maximum 1-hour average ozone during the winter season projected well with observation data by 38.0% (NMB) and 1.3 value (Fa2). In the summertime, a slightly higher maximum daily average of 1 hour of over-projection was observed by 41.6% as compared to the winter season. The model suggested that the ozone precursors such as CO and NO_x appeared to be underestimated relative to monitoring data. For instance, the hourly average CO under-projected the observed data by -69.1% (NMB) and 0.30 value (Fa2) in the winter seasons. The model also underestimated the NO_x by -91.5% (NMB) and 0.084 value (Fa2) for the season mentioned. In the summer season, the simulation showed under projection as compared with observed data, but with lower magnitude than the bias in the winter season.

Table 3.4.3: Statistical Performance between CMAQ_RCP4.5 and observation for surface ozone (O_3), carbon monoxide (CO), and oxides of nitrogen (NO_x)

Variable	Projection	DOE	NMB	FB	NMSE	Fa2
January						
Max 1-h O_3 (ppb)	46.2	39.4	17.2	0.15	0.025	1.1
Hourly average NO_x (ppb)	1.3	15.8	-91.8	-1.7	10.2	0.082
Hourly average CO (ppb)	131.3	461.1	-71.5	-1.1	1.8	0.28
July						
Max 1-h O_3 (ppb)	54.0	38.1	41.6	0.34	0.12	1.4

Hourly average NO_x (ppb)	2.3	15.0	-84.0	-1.4	4.6	0.15
Hourly average CO (ppb)	152.7	489.6	-62.3	-0.93	1.5	0.37

NMB: Normalized Mean Bias, FB: Fractional Bias, NMSE: Normalized Mean Square Error, Fa2:Factor of Two.

The model projection between the CMAQ_RCP4.5 and CMAQ_NCEP simulation is shown in Table 3.4.4. The maximum daily average 1-hour ozone mixing ratio between CMAQ_RCP4.5 and CMAQ_NCEP was small by -0.93% and 12.0% during January and July respectively. The performance of the model was good by slightly under-estimation by 0.99 value of Fa2 for January and over-estimation by 1.1 value for July. The seasonal variation and spatial distribution of the average simulated max 1-h ozone by CMAQ_RCP4.5 were similar to the NCEP reanalysis dataset (Figure 3.4.11). The surface ozone mixing ratio in July was higher compared to the surface ozone in January. In general, the ozone mixing ratio over Malaysian Borneo was lower than the ozone over Malaysian Peninsula. The simulation performed well with CMAQ_NCEP in January except for overestimation distributed over a certain area of Malacca Straits. In July, high over projection was found over the upper part of Malacca Straits and the larger part of the South China Sea (Figure 3.4.12).

Table 3.4.4 Statistical Performance between CMAQ_RCP4.5 and NCEP for surface O_3, CO, NO_x, OH, HO_2, and HNO_3 with CMAQ_NCEP

Variable	**Projection**	**CMAQ_NCEP**	**NMB**	**FB**	**NMSE**	**Fa2**
January						
Max 1-h O_3 (ppb)	42.4	42.8	-0.93	-0.0093	0.000008	0.99
Hourly average NO_x (ppb)	0.57	0.52	9.6	0.091	0.0084	1.0
Hourly average CO (ppb)	118.6	102.7	15.4	0.14	0.020	1.1
Hourly average OH (ppm)	0.05	0.053	-5.6	-0.058	0.0033	0.94
Hourly average HNO_3 (ppb)	0.28	0.25	12	0.11	0.012	1.1
July						
Max 1-h O_3 (ppb)	43.8	39.1	12.0	0.11	0.012	1.1
Hourly average NO_x (ppb)	0.65	0.6	8.3	0.08	0.0064	1.0
Hourly average CO (ppb)	109.8	96.1	14.2	0.13	0.017	1.1
Hourly average OH (ppm)	0.043	0.035	22.8	0.20	0.042	1.2
Hourly average HNO_3 (ppb)	0.35	0.37	-5.4	-0.055	0.0031	0.94

NMB: Normalized Mean Bias, FB: Fractional Bias, NMSE: Normalized Mean Square Error, Fa2:Factor of Two.

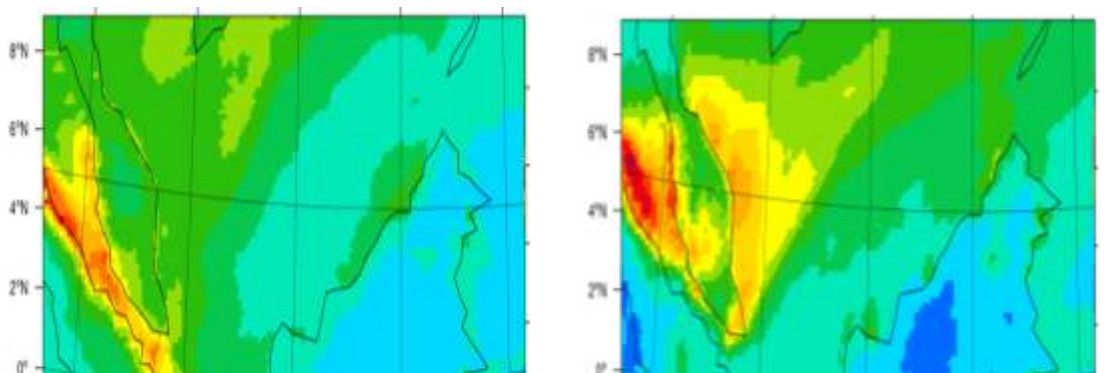

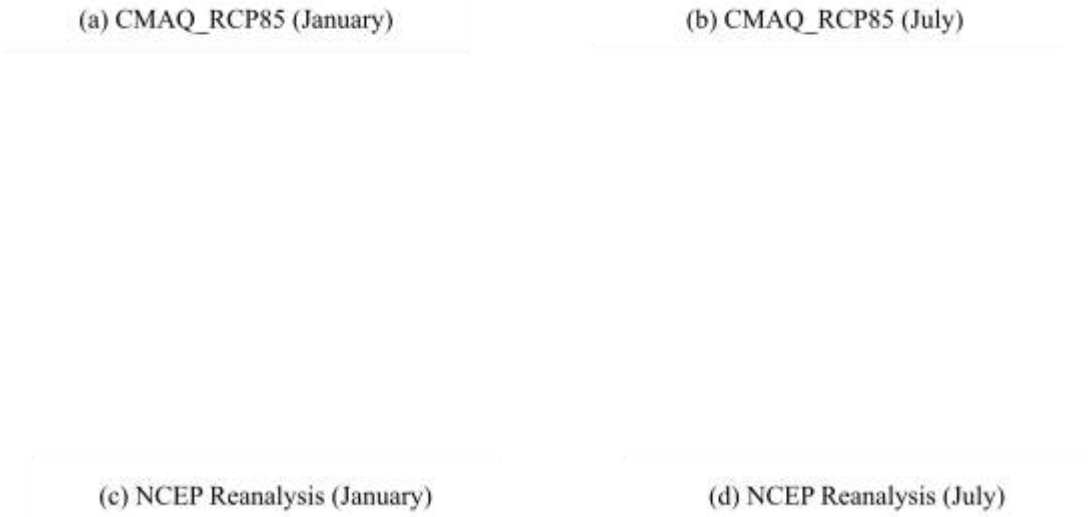

Figure 3.4.11**:** M1-hour daily average 1-hour O_3 (ppb) for (a)-(b) January and July in CMAQ_RCP4.5 simulation and CMAQ_NCEP for (c)-(d) January and July by 2013.

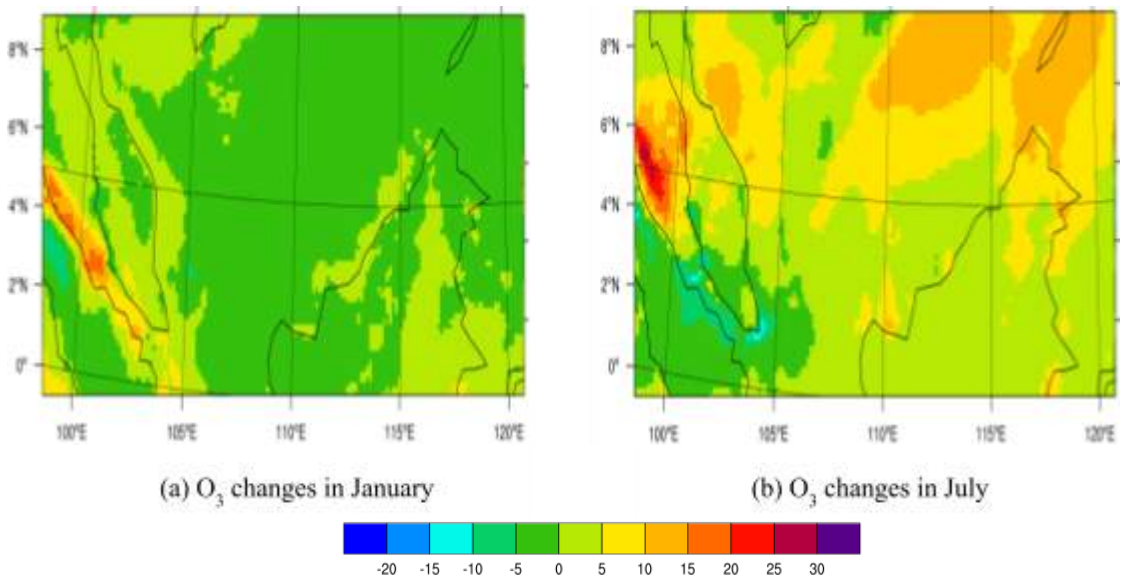

Figure 3.4.12: Hourly average changes of O_3 (ppb) between CMAQ_RCP4.5 and CMAQ_NCEP for January (a) and July (b) in 2013.

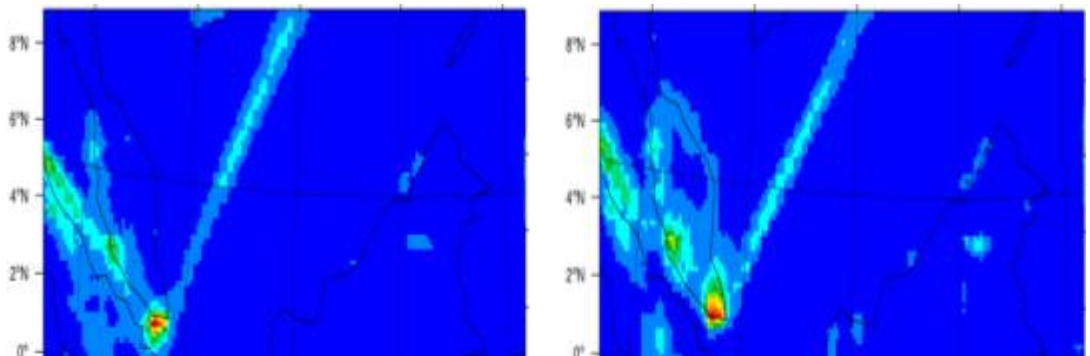

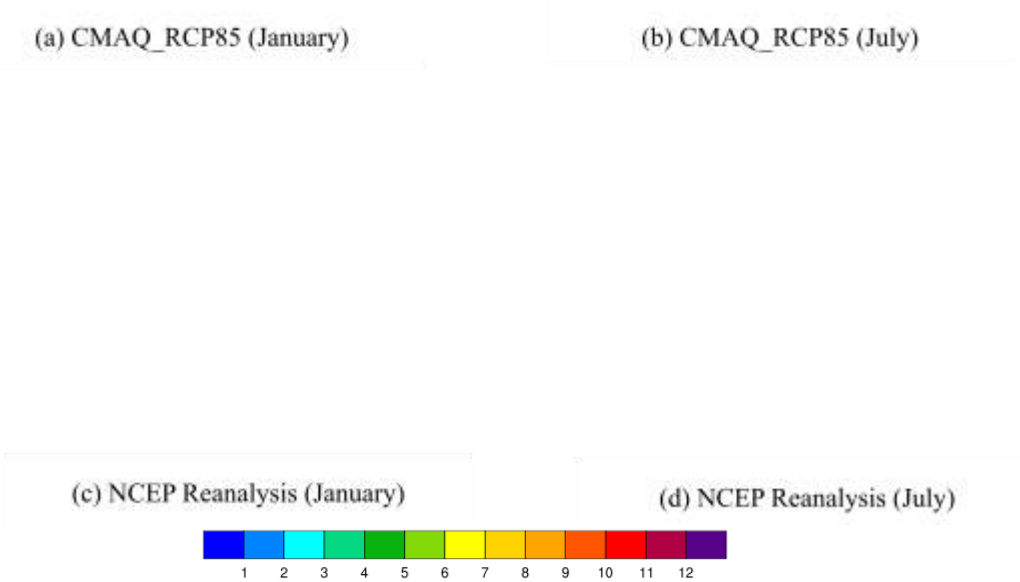

Figure 3.4.13: Hourly average of NO_x (ppb) for (a)-(b) January and July in CMAQ_RCP4.5 simulation and CMAQ_NCEP for (c)-(d) January and July by 2013.

The projected 24 hours average NO_x for CMAQ_RCP4.5 compared to CMAQ_NCEP is shown in Figure 3.4.13. The NMB was between 8.3% and 9.6%, and a nearly 0 value for Fa2. In addition, both datasets suggest that the NO_x mixing ratio during both seasons was high over certain areas of the Malaysian Peninsula and the South China Sea. The simulation of CMAQ_RCP4.5 agreed well with CMAQ_NCEP across the research domain except a small part of the southern Malaysian Peninsula in July of 2013, with a small bias of between -1ppb and 1ppb was observed (Figure 3.4.14).

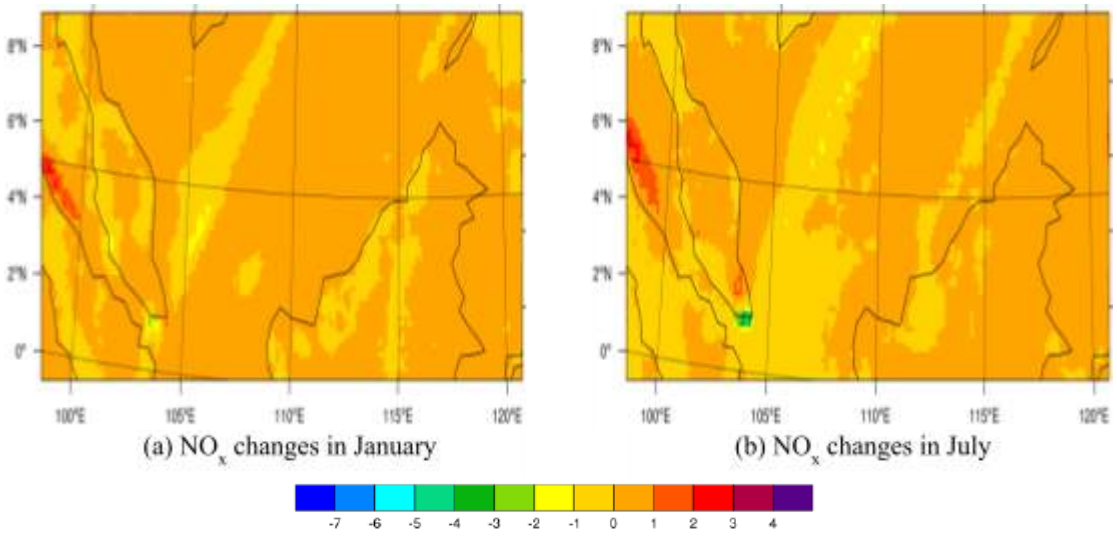

Figure 3.4.14: Hourly average changes of NOx (ppb) between CMAQ_RCP4.5 and CMAQ_NCEP for January (a) and July (b) in 2013.

The simulation of CMAQ_RCP4.5 and CMAQ_NCEP of hourly average carbon monoxide over the region are shown in Figure 3.4.15. In general, the NMB of CO mixing ratios were small around 15.4% in January and 14.2% in July. The nearly 1.0 value of Fa2 shows an almost ideal model in projecting the CO mixing ratio. The CO mixing ratio was higher over the west coast of the Malaysian Peninsula as compared to other regions for both seasons. The CO mixing ratio was largely under-predicted by CMAQ_RCP4.5 over the western part of the Malaysian Peninsula (< -20ppb) during the winter season (Figure 3.4.16). During the summer monsoon, a similar magnitude of underestimation was found over the southern part of the Malaysian Peninsula.

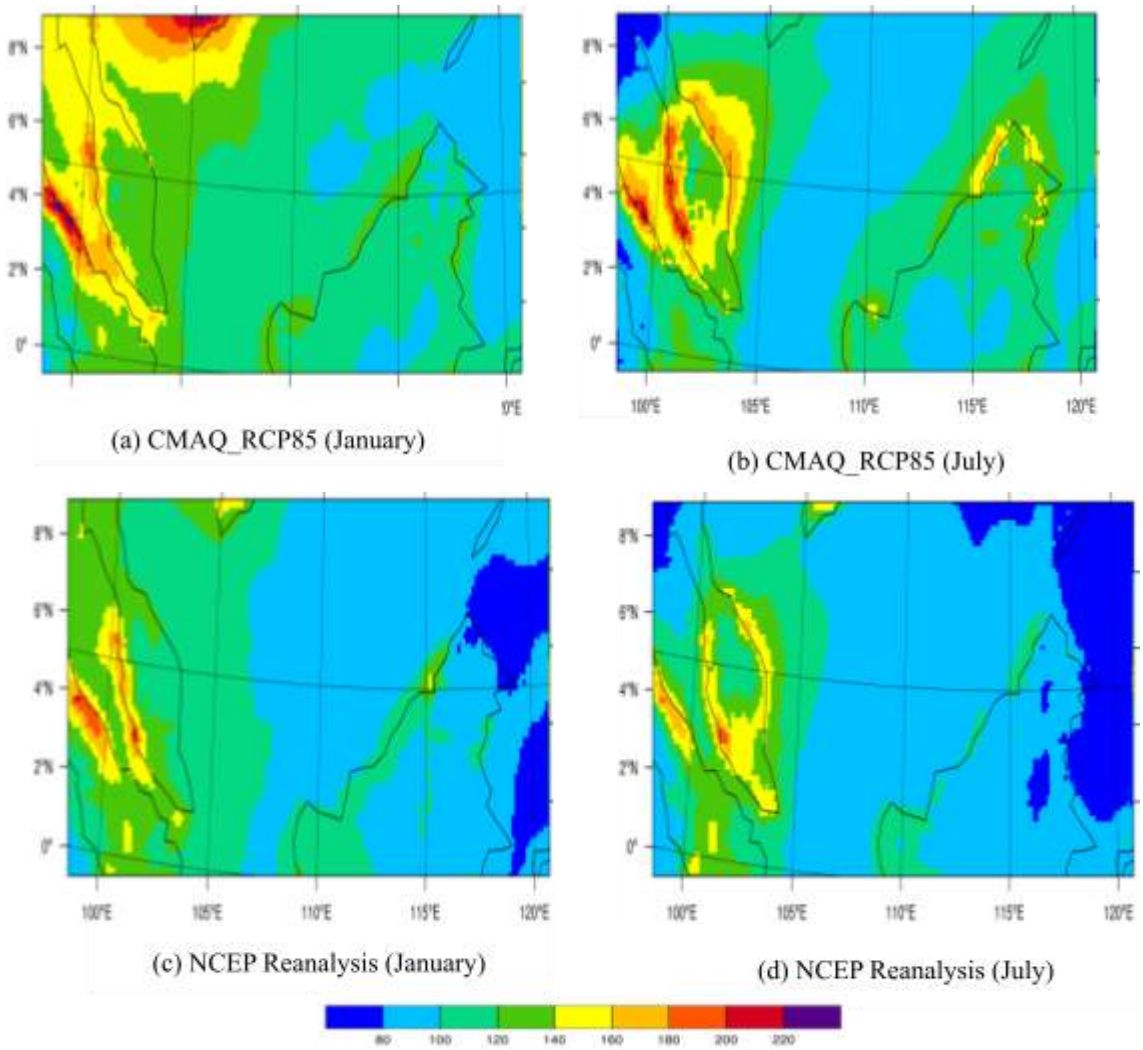

Figure 3.4.15: Hourly average of CO (ppb) for (a)-(b) January and July in CMAQ_RCP4.5 simulation and CMAQ_NCEP for (c)-(d) January and July by 2013.

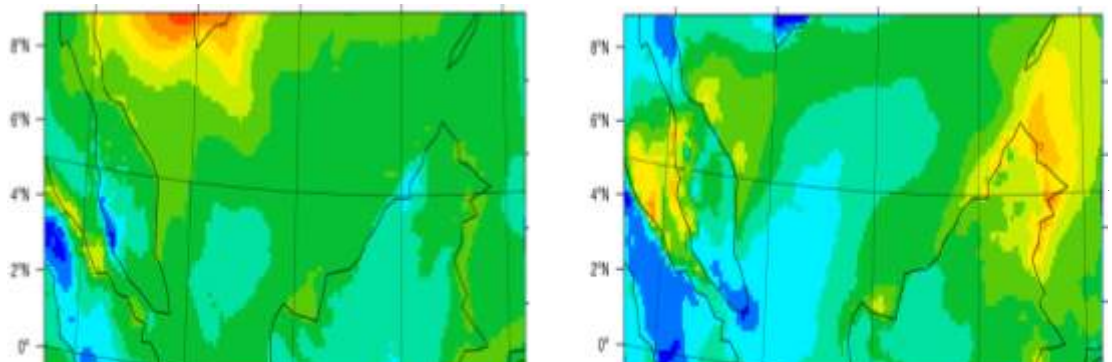

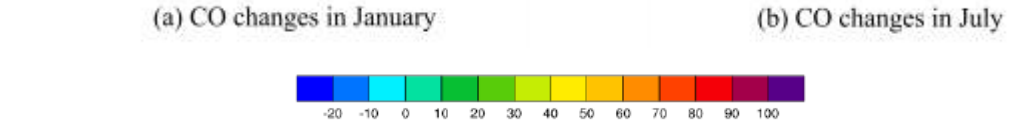

Figure 3.4.16: Hourly average changes of CO (ppb) between CMAQ_RCP4.5 and CMAQ_NCEP for January (a) and July (b) in 2013.

For the hourly average OH mixing ratio, the NMB between CMAQ_RCP45 and CMAQ_NCEP was -5.6% in January and 22.8% in July (Figure 3.4.17). Meanwhile, the Fa2 values were relatively small of 0.94 and 1.2 during January and July respectively. Both CMAQ_RCP4.5 and NCEP reanalysis data suggested that OH mixing ratios were highly distributed over the South China Sea. Figure 3.4.18 shows that the CMAQ_RCP4.5 simulated well with CMAQ_NCEP over most of the research domain in January, with a bias of between -0.01ppm and 0.01ppm. High overestimation was found over certain areas of the South China Sea in July 2013.

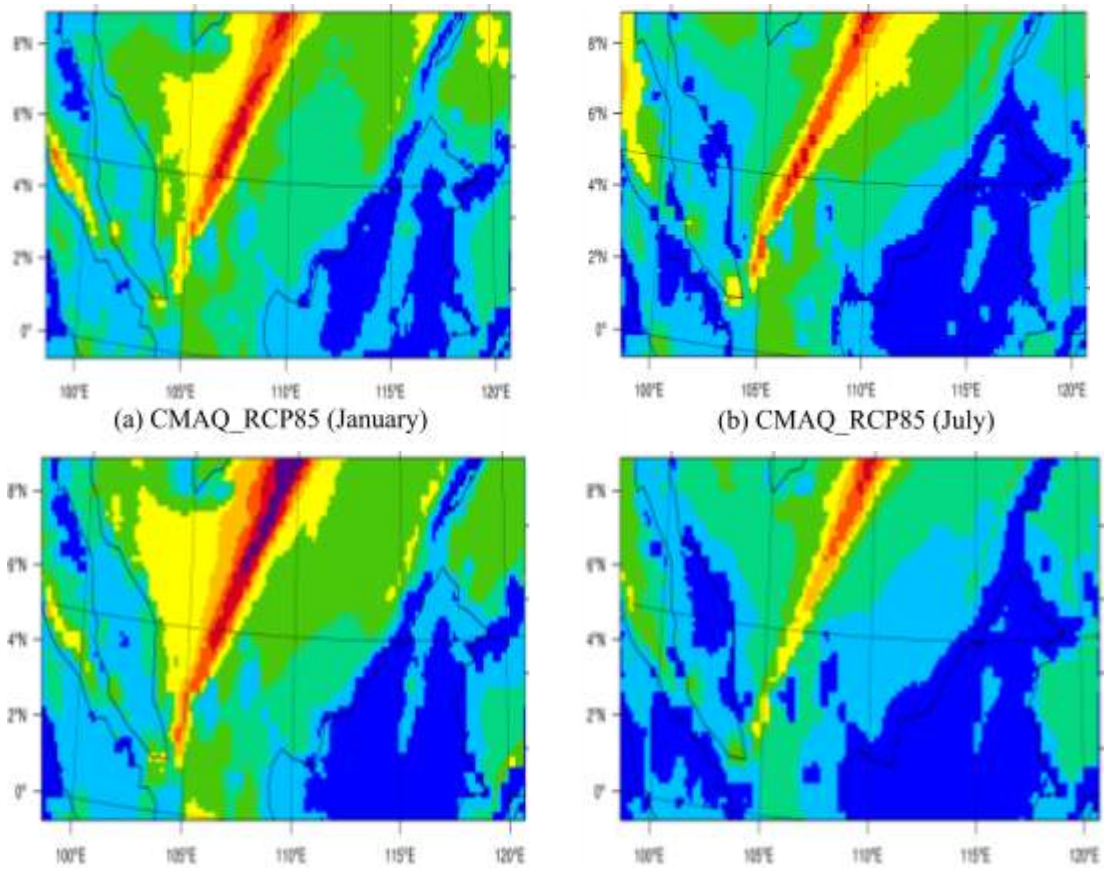

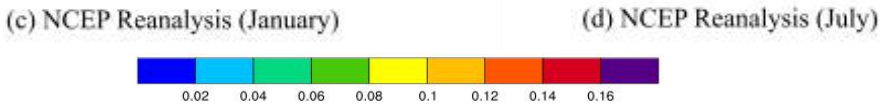

Figure 3.4.17: Hourly average changes of OH (ppm) between CMAQ_RCP4.5 and CMAQ_NCEP for January (a) and July (b) in 2013.

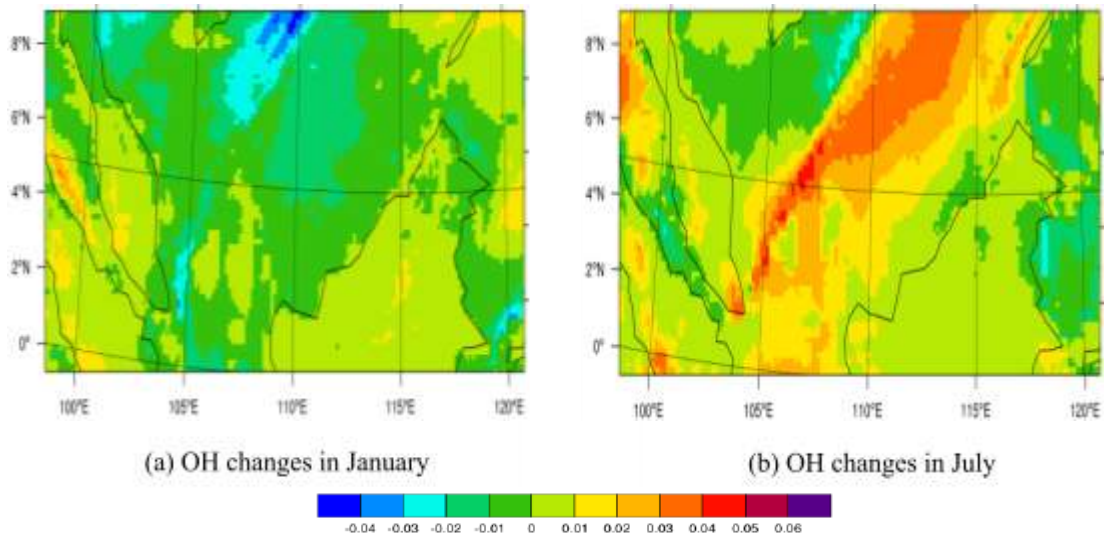

Figure 3.4.18: Hourly average changes of OH (ppm) between CMAQ_RCP4.5 and CMAQ_NCEP for January (a) and July (b) in 2013.

The simulation of CMAQ_RCP4.5 and CMAQ_NCEP of hourly average HNO_3 over the region is shown in Figure 3.4.19. The model has simulated well the HNO_3 mixing ratio with NMB of about 12% and -5.4% in January and July respectively. The Fa2 shows values of 1.1 (January) and 0.94 (July), indicating a good projection by the model. During both seasons, the HNO_3 mixing ratios were higher over the Malacca Straits and the South China Sea as compared to the other regions. The CMAQ_RCP45 overestimated CMAQ_NCEP over most domains especially over the Malacca Straits is shown in Figure 3.4.20. Meanwhile, underestimation was found over certain parts of the South China Sea with the highest magnitude in July.

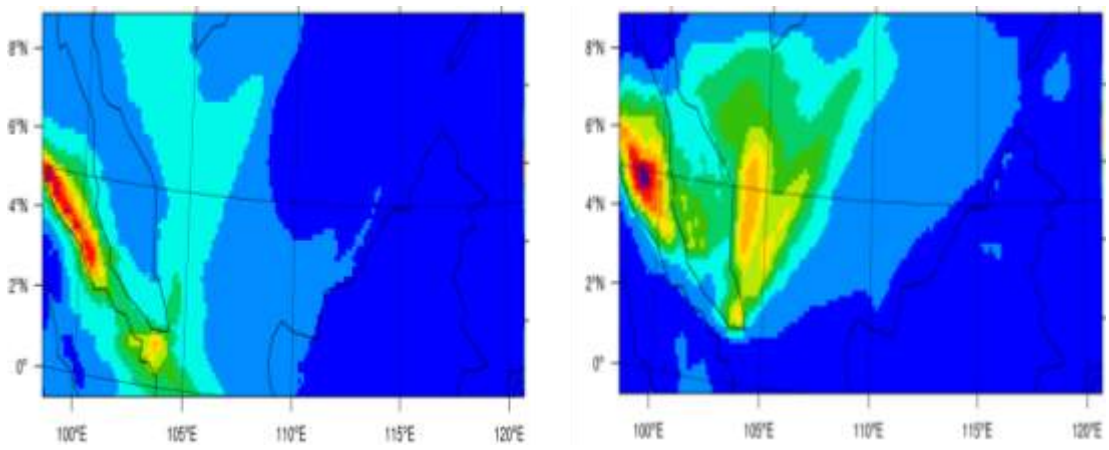

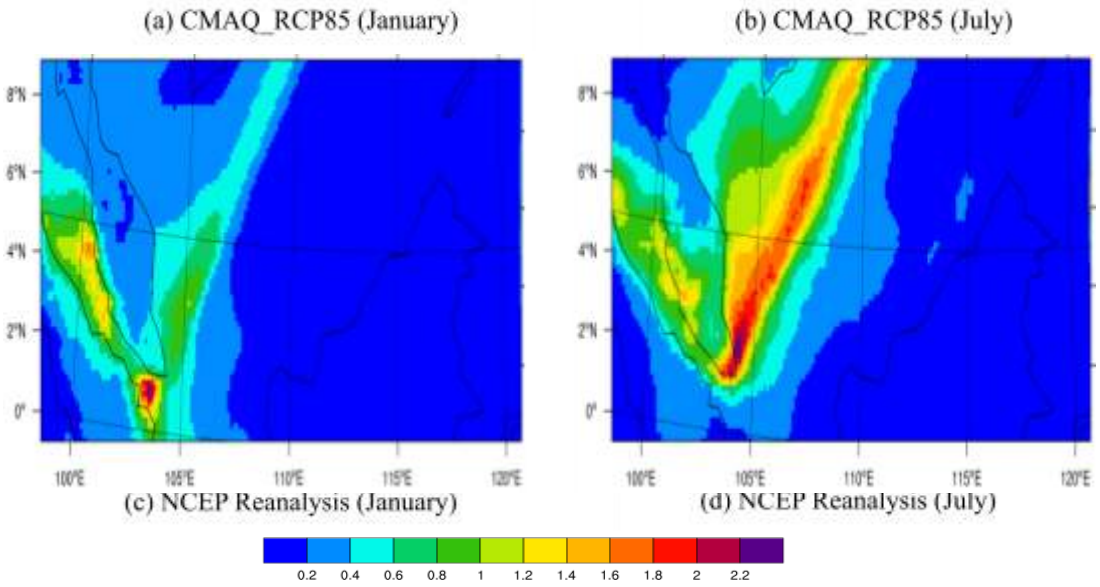

Figure 3.4.19: Hourly average of HNO_3 (ppb) for (a)-(b) January and July in CMAQ_RCP4.5 simulation and CMAQ_NCEP for (c)-(d) January and July by 2013.

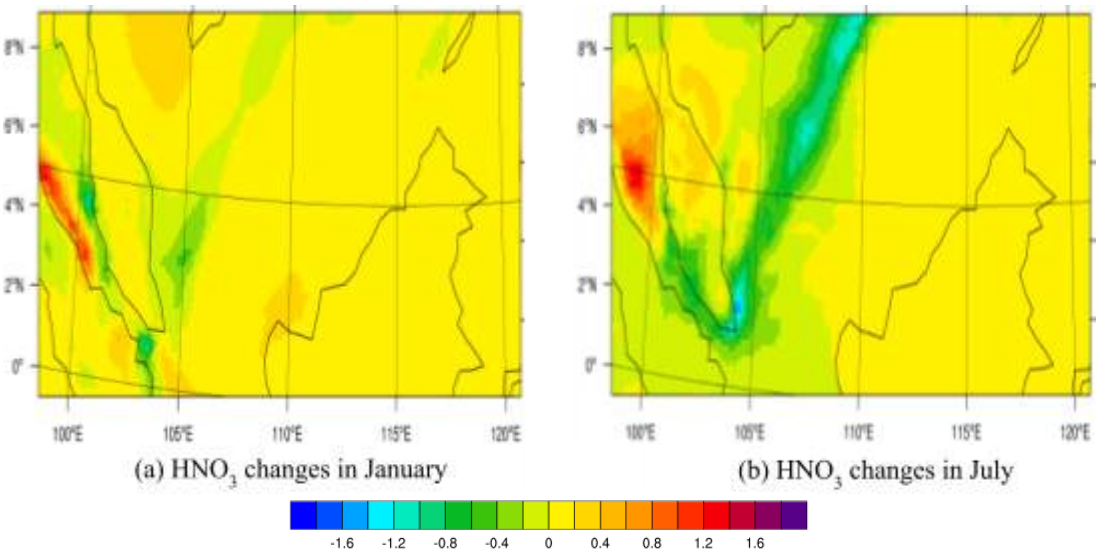

Figure 3.4.20: Hourly average changes of HNO_3 (ppm) between CMAQ_RCP4.5 and CMAQ_NCEP for January (a) and July (b) in 2013.

In general, the evaluation performance results for the ozone mixing ratio during the current year between observed DOE and CMAQ_4.5 ozone were similar as with CMAQ_RCP8.5 ozone. Both datasets suggested an underestimation of the ozone precursors such as CO and NO_x. However, the almost perfect performance of CMAQ_4.5 in ozone projection by -0.93% could be due to good agreement of RCM in temperature and precipitation projection, with NMB of 0.91% and 5% respectively. A stable behaviour of the climate model could lead towards a stable performance of the air quality model.

This analysis has revealed a complicated spatiotemporal pattern of forecasting O_3 concentrations across the study area. The complex pattern arises from the model sensitivity to input uncertainty, which demonstrating that the most efficient technique for boosting prediction accuracy varies substantially depending on time and location. Although more accurate climate simulation may enhance background O_3 predictions; however, during O_3 pollution episode especially in metropolitan areas, this will have little influence, thus improved precursor emissions and response rate data will be of more useful (Querol et al., 2017). Photolysis processes are among the most significant; therefore, effective modelling of solar radiation and cloud cover will also aid in improving projections.

3.4.2 Climate Change Impact on Regional Air Quality

3.4.2.1 Maximum Daily 1-hour Average Ozone

This section projected the concentration of maximum 1-hour average ozone mixing ratio over the Malaysian region, with 2013 as a baseline year, 2050 as the mid-century, and 2100 as the end-century. Figure 3.4.21 shows the box-and-whisper plot of the maximum average 1-hour surface ozone in the Malaysia region for the year of 2013, 2050, and 2100 simulations. The concentration of surface O_3 in 2013 (48.1 ppb) has a slightly higher median than the O_3 in 2050 (47.1 ppb) during January (Figure 3.4.21(a)) under the RCP8.5 scenario. Meanwhile, a similar inter-quartile range of 42-52 ppb in both simulations indicates the consistency of the dataset itself. In 2100, the median ozone concentration was slightly lower than the ozone concentration in 2013, with 46.5 ppb, and consists of a lower inter-quartile range by 43.3-51.4 ppb show more consistent data than the O_3in 2013 and 2050. In July, the median of surface O_3under RCP8.5 for both 2013 and 2050 was similar with a value of around 41 ppb. However, a low value of median was found in 2100 by 35.8 ppb as relative to 2013.

As shown in Figure 3.4.21€, the median O_3 mixing ratio during the January period was similar in 2013 (40.6 ppb) and 2050 (40.8 ppb) respectively under the RCP4.5 scenario. In 2100, the simulation produced a higher median by 44.1 ppb as compared to 2013 and 2050. This indicated that 50% of grid cells have a future O_3 ozone concentration above 44.1 ppb, whereas 50% of grid cells in the present year were above 40.6 ppb. During the July period, 41.9 ppb of median O_3 concentration was found in July of 2013 under the RCP45 scenario (Figure 3.4.21(d)). Meanwhile, the O_3 mixing

ratio was lower in 2050 and 2100 by 37.2 ppb and 30.8 ppb respectively. The inter-quartile range in a future year was much narrower as compared to the present period (36.7-49 ppb), with 33.3-41.2 ppb (the year 2050) and 28.5-35.0 ppb (2100) respectively. This means that the data of future simulation was less varied.

A comparison between the cumulative distribution function of the maximum daily average 1-hour over the Malaysian region in 2013, 2050, and 2100 simulations respectively as shown in Figure 3.4.21(e)-(h). It is noted that the distributions are close between each other in January under the RCP8.5 scenario (Figure 3.4.21(e)). The result suggests that the O_3 mixing ratio is not significantly different between the present and future simulations for this particular month. In July, significant surface O_3 reduction above 5ppb is seen over the whole Malaysia domain above the 20th percentile for 2100 and 2013 simulations under RCP8.5 (Figure 3.4.21(f)). Meanwhile, the surface O_3 reduction was statistically significant at most of the CDF in July of 2100 under the RCP4.5 scenario. In 2050, the O_3 decreased more than 5ppb only at 50 percentiles in July.

Under the RCP8.5, the mean simulated maximum 1-hour average O_3 mixing ratio was 47.7 ppb in 2050 and 47.5 ppb in 2100 for January (Table 3.4.5). Relative to the baseline period, the maximum 1-hour average ozone mixing ratio decreased about 0.42 ppb (1.0%) and 0.68 ppb (1.4%) in the year 2050 and 2100 respectively under the RCP8.5 scenario (Table 3.4.6). Figure 3.4.22 shows the spatial distribution of the maximum O_3 mixing ratio under the RCP8.5 scenario. In general, the O_3 mixing ratio was higher across the Malaysian Peninsula as compared to the Malaysian Borneo. A higher value of O_3 mixing ratio with more than 70 ppb was observed over the Malacca Straits, west coast of the Malaysian Peninsula, certain areas of the South China Sea, and coastal area of the northern Malaysian Borneo.

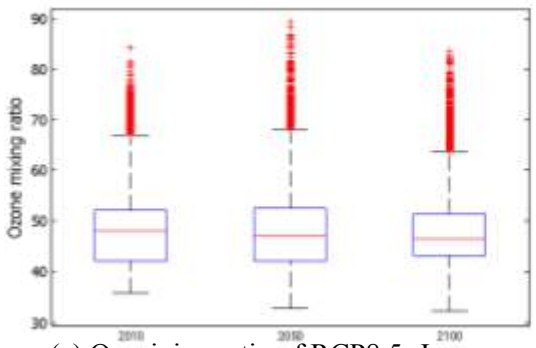

(a) O_3 mixing ratio of RCP8.5: January

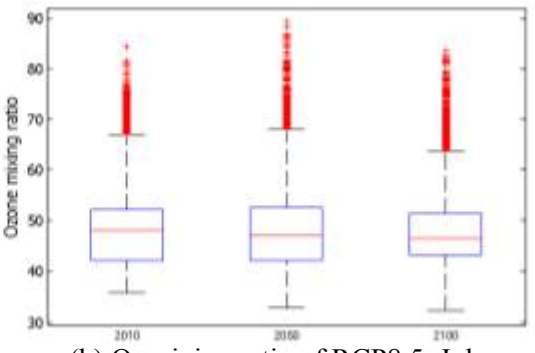

(b) O_3 mixing ratio of RCP8.5: July

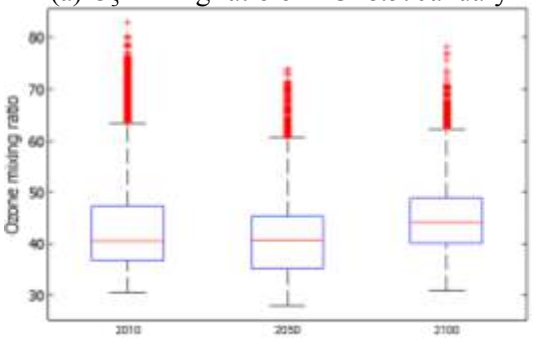

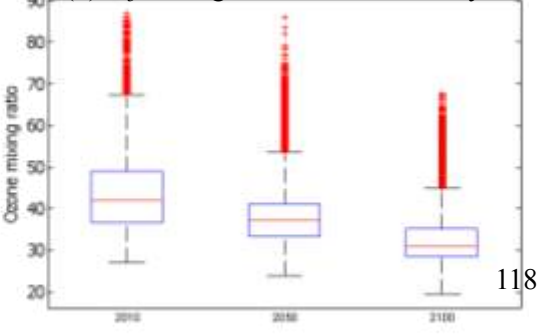

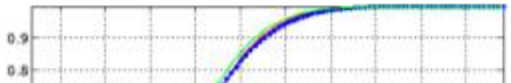

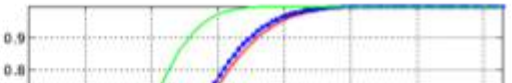

(c) O_3 mixing ratio of RCP4.5: January

(d) O_3 mixing ratio of RCP4.5: July

(e) O_3 distribution RCP8.5: January

(f) O_3 distribution RCP8.5: July

(g) O_3 distribution RCP4.5: January

(h) O_3 distribution RCP4.5: July

Figure 3.4.21: Box and whisker plots of the maximum daily average 1-hour O_3 mixing ratio (pbb) for 2013(1st box), 2050(2nd box), and 2100(3rd box) under RCP8.5 scenario (a)-(b) and under RCP4.5 scenario (c)-(d). The cumulative distribution function of the maximum daily average 1-hour ozone mixing ratio (pbb)for 2013(red line), 2050(blue dot line), and 2100(green dash line) under RCP8.5 scenario (e)-(f) and under RCP4.5 scenario (g)-(h). The left panel indicates the January period and the right panel as the July period.

During the July, the maximum 1-hour average O_3 mixing ratio was lower as compared to the mixing ratio during January under the RCP8.5 scenario (Figure 3.4.22). The simulated O_3 mixing ratios were 43.1 ppb and 36.9 ppb in 2050 and 2100 respectively. Similarly, in January, the ozone mixing ratio was higher across the Malaysian Peninsula as compared to the Malaysian Borneo, with the highest mean value over the west coast of the Malaysian Peninsula (>70 ppb) in July.

Meanwhile, the O_3 mixing ratio reduced to about 0.39 ppb (0.9%) in 2050, which was similar to in January, but highly reduced in 2100 by about -6.6 ppb (-15.2%). In July of the mid-century, most of the land area experienced an increase in ozone mixing ratio, with the largest O_3 increase of more than 10.0ppb over the sea area of the southern Malaysian Peninsula. However, the northern part of the Malaysian Peninsula was found to undergo a large decrease in O_3 mixing ratio with a concentration of less than 10.0ppb. In 2100, the ozone mixing ratio decreased over the whole research domain with the

largest decrease over the northern part of the Malaysian Peninsula and the South China Sea. High increases in precipitation can be related to the O_3 increment since rainfall plays an important role in wet deposition over this region.

Under RCP4.5 scenario, the January period simulated maximum 1-hour average O_3 mixing ratio was lower compared to the mean value under the RCP8.5 scenario, which was recorded at 0.9 ppb in 2050 and 44.3 ppb in 2100 (Table 3.4.5). Similar to the RCP8.5 scenario in January, there is a higher concentration of O_3 mixing ratio over the Malaysian Peninsula than the Malaysian Borneo (Figure 3.4.23). Under the RCP4.5, the ozone mixing ratio decreased by 1.6 ppb (3.8%) in 2050 but increased by 1.9 ppb (4.5%) in 2100. In 2050, the O_3 mixing ratio decreased over the whole Malaysia domain with the largest decrease over the Malacca Straits, the southern part of the Malaysia Peninsula, and the sea area around during January period. However, the O_3 mixing ratio across the region decreased with a lower concentration in 2100.

In January, the simulated maximum 1-hour average O_3 mixing ratio was lesser than the O_3 concentration during July period, with 38.4ppb in 2050 and 32.4 ppb in 2100 (Table 3.4.5, Figure 3.4.23). A higher concentrations O_3 mixing ratio was observed over the Malaysian Peninsula than the Malaysian Borneo. Relative to the baseline period, the mean ozone was highly decreased by 5.4 ppb (12.3%) and 11.3 ppb (25.8%) in 2050 and 2100 respectively. Figure 3.4.22 shows that the O_3 decreased across the whole research domain in both 2050 and 2100. In 2050, there was an exceptional over the southern part of the Malacca Straits, where the ozone concentration was increased (>10ppb) as compared to the baseline period. The O_3 mixing ratio decreased with more than -10ppb along the area above 2°N latitude.

The control of air quality is necessary to protect human health and the environment. Hence, the Department of Environment (DOE) Malaysia has set up the recommended Malaysian Ambient Air Quality Guidelines (MAAQG) as minimum requirements for outdoor air quality (DOE, 2011). Based on the MAAQG (DOE, 2012), the standard of hourly average ozone was 100 ppb. Table 3.4.5 shows the hourly average O_3mixing ratio during the present and future periods. Kuala Lumpur and Ipoh at the Malaysian Peninsula were categorised as urban areas, while Kapit and Danum are representing the rural area at Malaysian Borneo.

Table 3.4.5: Ozone (Max 1 hour) mixing ratio (ppb) in Kuala Lumpur (Urban), Ipoh (Urban), Kapit (Rural), and Danum Valley (Rural) under RCP8.5 and RCP4.5 scenarios.

Period	**RCP85(ppb)**			**RCP45(ppb)**		
	2013	**2050**	**2100**	**2013**	**2050**	**2100**
Kuala Lumpur (Urban)						
January	52.9	53.2	54.3	51.0	43.7	47.2
July	59.8	63.3	53.5	65.4	53.9	51.7
Ipoh (Urban)						

January	50.7	48.0	51.7	46.6	41.0	46.3
July	60.4	53.0	43.5	55.5	42.4	43.4
Kapit (Rural)						
January	40.9	37.1	37.5	33.3	28.3	33.5
July	26.3	27.4	22.6	27.2	24.8	21.7
Danum Valley (Rural)						
January	44.1	45.0	46.8	38.5	37.1	41.3
July	39.9	39.4	32.0	39.1	34.8	28.4

Table 3.4.5 also shows that the hourly average O_3 mixing ratio for the present and future periods in Kuala Lumpur was between 47.2 ppb and 65.4 ppb. Meanwhile, Ipoh was slightly lower than Kuala Lumpur with an average of 41.0 ppb and 60.4 ppb. The O_3 concentrations in rural areas (Kapit and Danum Valley) were lower than the ozone mixing ratio in the urban area, with the range of between 22.6 ppb and 40.9 ppb and 28.4 ppb - 46.8 ppb respectively. Higher emission of O_3 precursors such as CO and NO_x due to various economic activities leads to higher O_3 production (Steiner et al., 2006; Sentian, 2013; Ahrens, 2009). However, the O_3 concentration in all areas was below the MAAQG for both present and future periods under both climate scenarios.

Overall, a small decrease of maximum 1-h O_3mixing ratio was found for the RCP8.5 scenario, a but large decrease for RCP4.5 scenario except for the January of 2100. The minor decrease of O_3 under RCP8.5 as compared to RCP4.5 can be due to the doubling of CH_4 and increased stratospheric influx of O_3. Most of the models projected that the global future O_3 ozone will increase under the RCP8.5 scenario (Gao et al., 2013; Young et al., 2013; Kim et al., 2015). For example, the global ensemble mean surface O_3 in 2030 (2100) as relative to 2000 were 7% (18 %) for RCP8.5 and -2% (−7 %) for RCP4.5 (Young et al., 2013). Kim et al. (2015) showed that the future O_3 during the 2050s increased by 10 ppbv for RCP8.5 and decreased within the range of 4 - 10 ppbv under the RCP4.5 scenario.

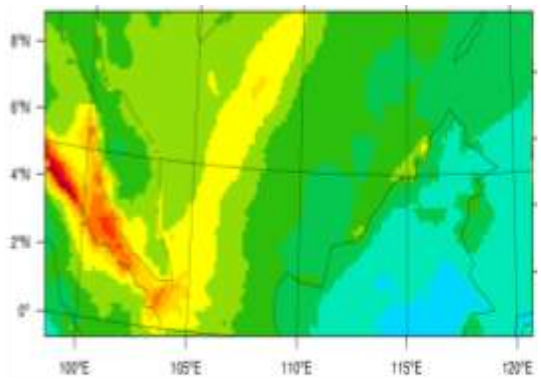

(a) O_3 concentration RCP8.5: January 2050

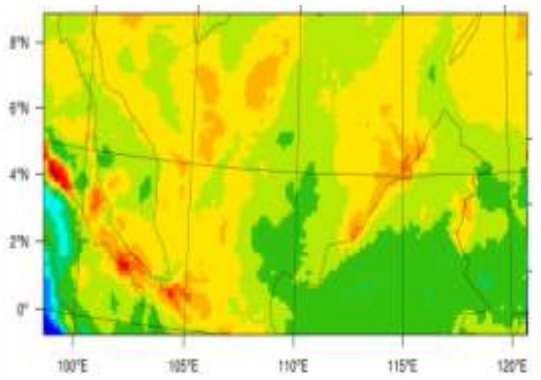

(b) O_3 RCP8.5 January changes of (2050 – 2013)

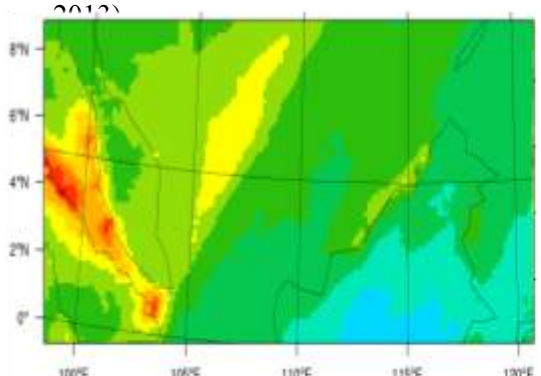

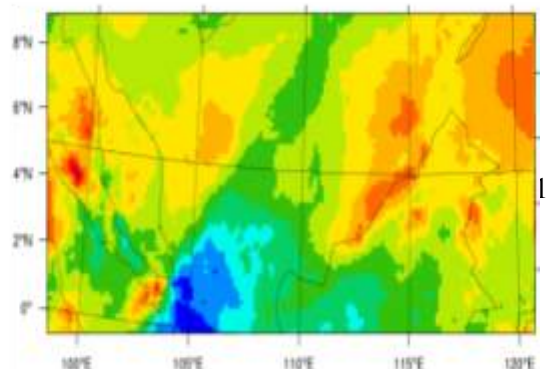

(c) O_3 concentration RCP8.5: January 2100

(d) O_3 RCP8.5 January changes of (2100 – 2013)

(e) O_3 concentration RCP8.5: July 2050

(f) O_3 RCP8.5 July changes of (2050 – 2013)

(g) O_3 concentration RCP8.5: July 2050

(h) O_3 RCP8.5 July changes of (2050 – 2013)

Figure 3.4.22: Projected surface O_3 under RCP8.5: (a),(c),(e),(g) maximum daily average 1-hour O_3 and (b),(d),(f),(h) changes of maximum average 1-hour O_3

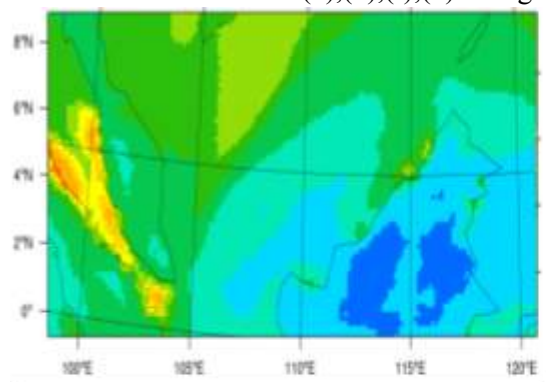

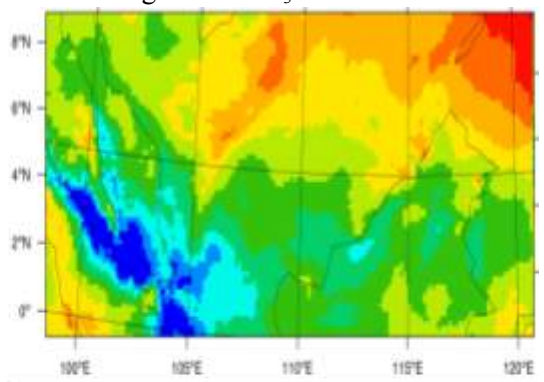

(a) O_3 concentration RCP4.5: January 2050

(b) O_3 RCP4.5 January changes of (2050 –

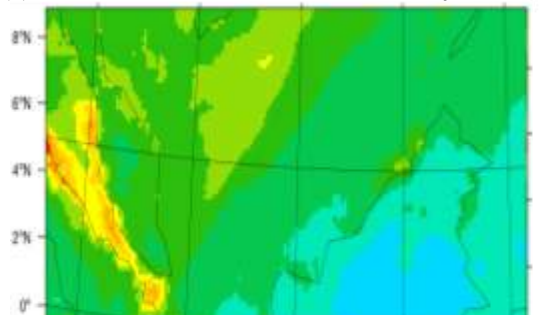

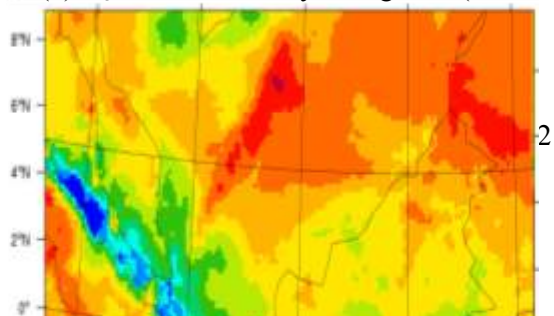

(c) O_3 concentration RCP4.5: January 2100

(d) O_3 RCP4.5 January changes of (2100 – 2013)

(e) O_3 concentration RCP4.5: July 2050

(f) O_3 RCP4.5 July changes of (2050 – 2013)

(g) O_3 concentration RCP4.5: July 2050

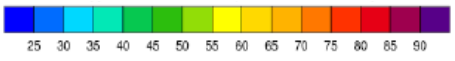

(h) O_3 RCP4.5 July changes of (2050 – 2013)

Figure 3.4.23: Projected surface O_3 under RCP4.5: (a),(c),(e),(g) maximum daily average 1-hour O_3 and (b),(d),(f),(h) changes of maximum average 1-hour O_3

The dynamical downscaling projection in Malaysia by WRF-CMQ under RCP8.5 scenario was somehow coherent with the downscaling result of Pfister et al., 2014 and in Malaysia by CiTTyCAT box model (Sentian et al., 2015; Yat and Sentian, 2015). In 2050, the 5th-95th percentile range decreased to 27-55ppb as relative to 31-79 ppb in the present period for RCP 8.5. This indicated that the significant reduction of future surface O_3 exceeds the positive feedback of global ozone increment. In Malaysia, the model suggested that the future surface ozone mixing ratio reduced by 20-50% in remote areas and 2-5% in suburban areas, and high variability changes in the urban area.

In general, the reduction of O_3 mixing ratio for future period under both RCP8.5 and RCP4.5 scenarios can be related to the climate change effect and the changes of precursors. The primary precursor that leads to surface O_3 reduction is OH (Zeng et al., 2008). The simulated future OH largely increased at the end of this century by 30% (January) and 113.6% (July) for RCP8.5, 26% (January), and 23.2% (July) for RCP4.5. The present result was consistent with Wang and Jacab (1998), which suggested that 63% of surface O_3 increases was related to a 9% decrease of OH. In other words, O_3 reduction can be linked with OH increment (Voulgarakis et al., 2013; Kim et al., 2015).

Table 3.4.6: Maximum daily average 1-hour ozone mixing ratio (ppb) under RCP8.5 and RCP4.5 scenarios.

Variables	**RCP8.5 (ppb)**			**Changes (ppb)**	
	2013	2050	2100	2050 - 2013	2100 - 2013
January	48.2	47.7	47.5	-0.42 (-1.0%)	-0.68 (-1.4%)
July	43.5	43.1	36.9	-0.39 (-0.9%)	-6.6 (-15.2%)
Variables	**RCP4.5 (ppb)**			**Changes (ppb)**	
	2013	2050	2100	2050 - 2013	2100 - 2013
January	42.4	40.9	44.3	-1.6 (-3.8%)	1.9 (4.5%)
July	43.8	38.4	32.4	-5.4 (-12.3%)	-11.3 (-25.8%)

The NO_x mixing ratio variations are also one of the factors that caused the O_3 changes (Kawase et al., 2011; Langner et al., 2012). The model suggested an increase of simulated NO_x in 2050 but a decrease at the period of 2100 under the RCP8.5 scenario. As a result, a minor increase of future NO_x might cause a small percentage of O_3 formation, but the decrease of NO_x somehow leads to a larger degree of O_3 reduction. The effect of NO_x on O_3 ozone concentration has been discussed by Stevenson et al. (2006), who mentioned that a low NO_x environment with high-water vapor content responsible for lower O_3 mixing ratio. However, the increase of radioactive forcing caused by GHGs concentration could cause the projection of O_3 distribution to be varied (Kawase et al., 2011). Moreover, the effect of NO_x reduction by 10-20% was not large enough in triggering the O_3 reduction (Steiner et al., 2006). As a result, it was believed that a high portion of atmospheric moisture was the prime cause.

The ozone variations were also related to HNO_3. The modelling results from Racherla and Adams (2008) and Kim et al. (2015) suggested that the increase of HNO_3 concentrations in the future period was due to the increase of NO_2/NO_x ratio, therefore increasing the O_3 mixing ratio. In the present study, a similar situation happened in 2050 over a certain area of the South China Sea. Meanwhile, the modelling output was opposite with the research mentioned especially at end of this century, where the surface O_3 mixing ratio generally reduced over most of the Malaysia region that

probably due to the reduction of HNO_3 concentration. In general, the mean future HNO_3 concentration reduced with a maximum -52.7% and minimum -7.5% as shown in the later section below.

However, an exceptional happened where future O_3 largely increased by 4.5% (1.9 ppb) during January 2100 as relative to 2013 under RCP4.5, while the other period showed the O_3 reduction. An increase of Max 1-h and 8-h O_3 mixing ratio can be due to a high percentage of precipitation reduction with 40% (see Climate Change Section). A similar finding was found over western Europe (Meleux et al., 2007) and the United States (Chen et al., 2009) decrease of precipitation up to a maximum of 110% caused near-surface average (peak) O_3 increase to 10-16 % (25%) over the western part of Europe. In the United States, the simulated change of precipitation with -0.1mm leads to the O_3 increment by 25% (January period) and 17% (July period) (Chen et al., 2009).

3.4.2.2 Nitrogen Oxide (NO_x)

The median NO_x concentration does not change significantly (Figure 3.4.24(a) - (d)) due to a large value of outliers within the dataset and the inter quartile range for all simulations was not obvious. Under the RCP8.5, the median NO_x mixing ratio by January increased in 2050 (0.36 ppb) but decreased in 2100 (0.32 ppb). A similar trend was also found in July. Meanwhile, the median value in January under RCP4.5 was lower in 2050 (0.30 ppb) and 2100 (0.28 ppb) as compared to 2013 (0.37 ppb). In July, the trend was similar with January but with a higher magnitude. For RCP8.5, the CDF shows that there were no significant changes in NO_x between 2013 and 2100 simulations in January. Significant decrement was found at 80 percentiles between 2013 and 2050 simulation. In July, the change was not obvious between 2013 and 2100 but showed less significant decrement for 2050 simulation. Hence, the change for NO_x in the future period was found to be not significant under the RCP4.5 scenario.

Figure 3.4.25 and Table 3.4.7 showed the projection of the concentration of hourly average NO_x over the Malaysian region of about 0.60ppb in 2050 and 0.53ppb in 2100. The high NO_x concentration was distributed across the west coast and southern part of the Malaysian Peninsula throughout the whole future period and high emission were expected as the result of marine transport activity. The NO_x mixing ratio increased by 0.065 ppb (12.3%) in 2050 but reduced 2100 by 0.005ppb (0.9%) relative to 2013. In 2050, there was a clear increase of NO_x mixing ratio with more than 1 ppb over the southern part the of Malaysian Peninsula and middle part of the South China Sea as relative to the baseline period under the RCP8.5 scenario in 2100 but was lower than in 2050.

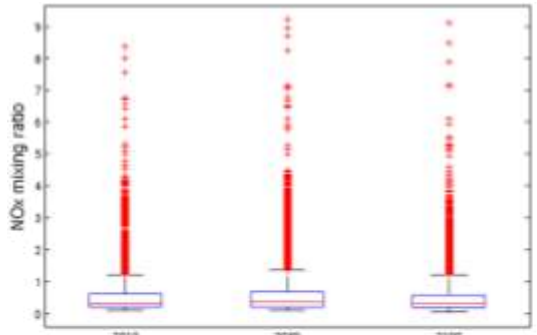

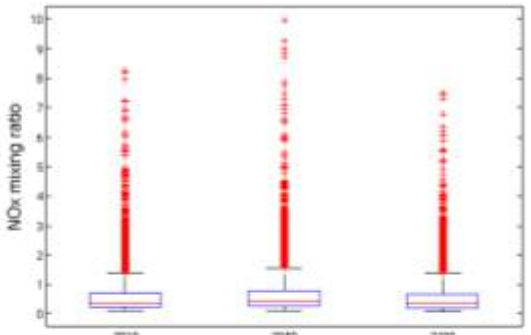

(a) NO_x mixing ratio of RCP8.5: January

(b) NO_x mixing ratio of RCP8.5: July

(c) NO_x mixing ratio of RCP4.5: January

(d) NO_x mixing ratio of RCP4.5: July

(e) NO_x distribution RCP8.5: January

(f) NO_x distribution RCP8.5: July

(g) NO_x distribution RCP4.5: January

(h) NO_x distribution RCP4.5: July

Figure 3.4.24: Box and whisker plots of the maximum hourly average NO_x mixing ratio (pbb) for 2013(1st box), 2050(2nd box), and 2100(3rd box) under RCP8.5 scenario (a)-(b) and under RCP4.5 scenario (c)-(d). The cumulative distribution function of the hourly average NO_x mixing ratio (pbb) for 2013(red line), 2050(blue dot line), and 2100(green dash line) under RCP8.5 scenario (e)-(f) and under RCP4.5 scenario (g)-(h). The left panel indicates the January period and the right panel as the July period.

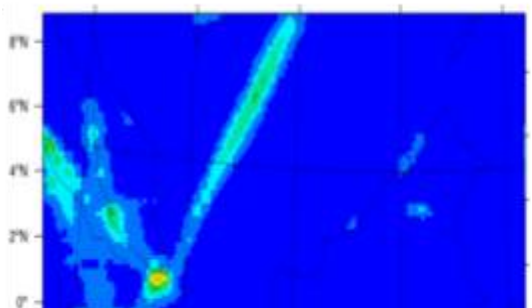

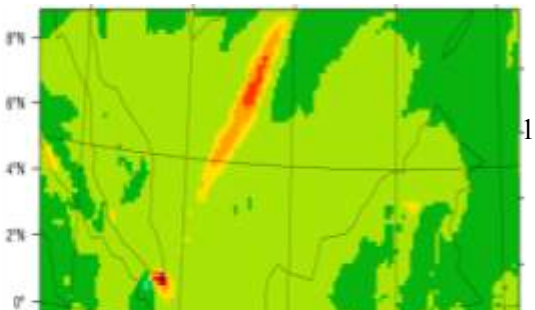

(a) NO_x concentration RCP 8.5: January 2050 (b) NO_x RCP8.5 January changes of (2050 – 2013)

(c) NO_x concentration RCP8 .5: January 2100 (d) NO_x RCP8.5 January changes of (2100 – 2013)

(e) NO_x concentration RCP8.5: July 2050 (f) NO_x RCP8.5 July changes of (2050 – 2013)

(g) NO_x concentration RCP8.5: July 2100 (h) NO_x RCP8.5 July changes of (2100 – 2013)

Figure 3.4.25: Projected NO_x under RCP8.5: (a),(c),(e),(g) average 1-hour NO_x and (b),(d),(f),(h) changes of NO_x

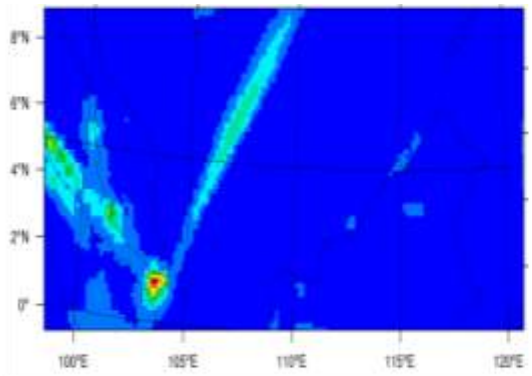

(a) NO_x concentration RCP 4.5: January 2050

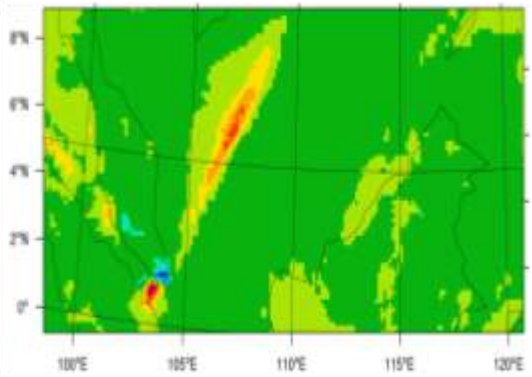

(b) NO_x RCP4.5 January changes of (2050 – 20

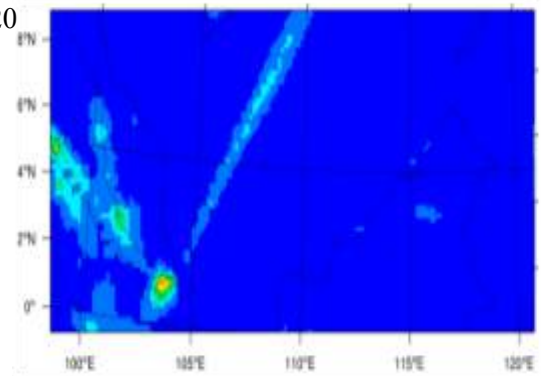

(c) NO_x concentration RCP4.5: January 2100

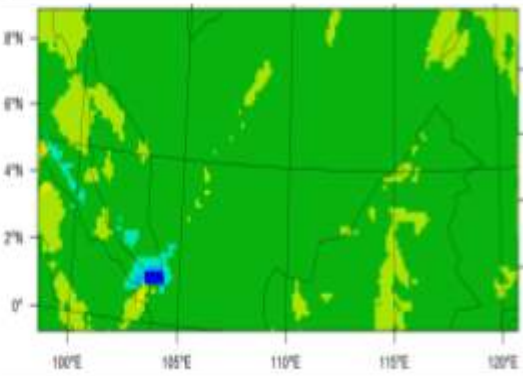

(d) NO_x RCP4.5 January changes of (2100 – 20

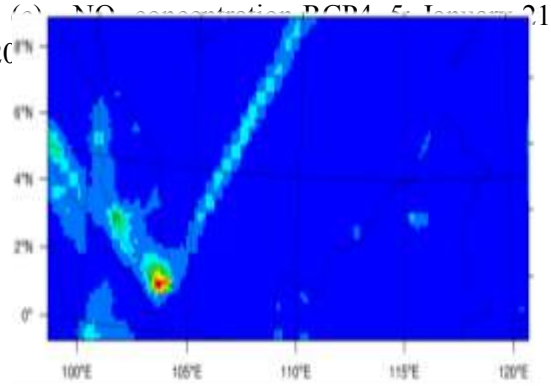

(e) NO_x concentration RCP 8.5: July 2100

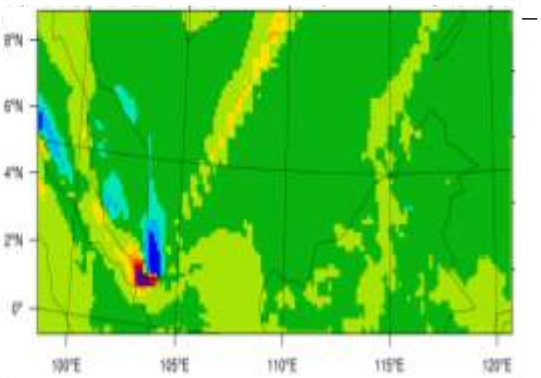

(f) NO_x RCP 8.5 July changes of (2100 – 2013)

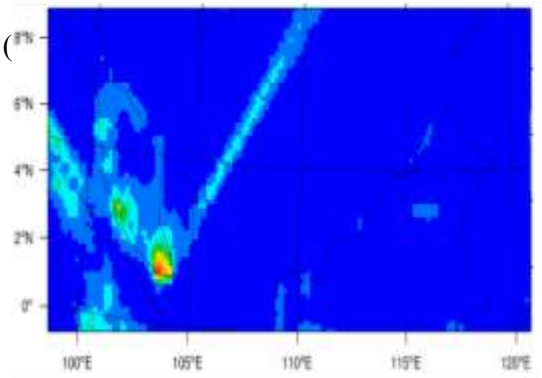

(g) NO_x concentration RCP 4.5: July 2100

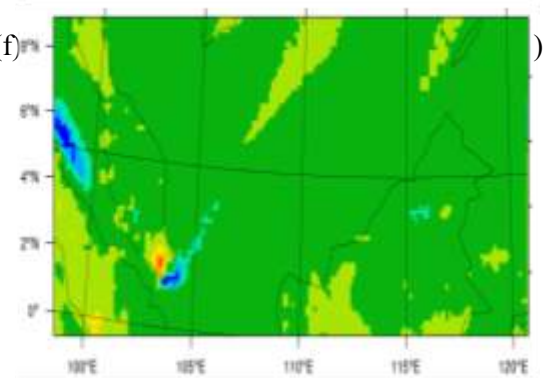

(h) NO_x RCP 4.5 July changes of (2100 – 2013)

Figure 3.4.26: Projected NO_x under RCP4.5: (a),(c),(e),(g) average 1-hour NO_x and (b),(d),(f),(h) changes of NO_x

Table 3.4.7**:** Nitrogen oxides (NO_x) mixing ratio (ppb) under RCP8.5 and RCP4.5 scenarios

Variables	**RCP8.5 (ppb)**			**Changes (ppb)**	
	2013	2050	2100	2050 - 2013	2100 - 2013
January	0.53	0.60	0.53	0.065 (12.3%)	-0.005 (-0.9%)
July	0.60	0.68	0.55	0.080(13.3%)	-0.046 (-7.7%)
Variables	**RCP4.5 (ppb)**			**Changes (ppb)**	
	2013	2050	2100	2050 - 2013	2100 - 2013
January	0.57	0.54	0.48	-0.031 (-5.4%)	-0.093 (-16.3%)
July	0.65	0.59	0.56	-0.054 (-8.3%)	-0.087 (-13.4%)

During the July, the simulated NO_x mixing ratio was higher as compared to the mixing ratio during the January under the RCP8.5 scenario (0.68 in 2050, 0.55 in 2100) (Figure 3.4.24). Similar to in January, the high NO_x concentration was observed across the west coast and southern part of the Malaysian Peninsula, and the respective region towards the northeast of the sea area. The hourly average NO_x concentration increased by 0.080 ppb (13.3%) in 2050 but reduced 2100 by about 0.046 ppb (7.7%) as relative to 2013 under the RCP8.5 scenario. The NO_x mixing ratio in 2050 increased by more than 1ppb over the southern part of the Malaysian Peninsula and middle part of the South China Sea relative to the baseline period under the RCP8.5 scenario. In 2100, such a high increment was not found.

During January of RCP4.5 scenario, the simulated hourly average NO_x mixing ratio was around 0.54 ppb in 2050 and 0.48ppb in 2100 (Figure 3.4.26). Under the RCP4.5 scenario, the NO_x mixing ratio decreased by 0.031 ppb (5.4%) in 2050 and 0.093 ppb (16.3%) in 2100. In 2050, the NO_x mixing ratio highly increased over the middle part of the South China Sea but decreased over a small part of the southern Malaysian Peninsula. However, the NO_x mixing ratio across the southern part of the West Malaysian (Peninsula) decreased with a concentration of less than 1.5 ppb in 2100. While during July, the simulated hourly average NO_x mixing ratio was 0.59ppb in 2050 and 0.56ppb in 2100. As relative to the baseline period, the mean mixing ratio of NO_x decreased by 0.054 ppb (8.3%) and 0.087ppb (13.4%) in 2050 and 2100 respectively. Less concentration of NO_x mixing ratio was found over the southern part of Malaysian, with a high concentration around the certain region in both 2050 and 2100.

3.4.2.3 Hydroxyl Radical (OH)

The box plot in Figure 3.4.27 (a-d) shows that the median of OH mixing ratio under RCP8.5 was lower in 2050 (0.052 ppm) but higher in 2100 (0.066 ppm) as relative to 2013 (0.058 ppm) under the RCP8.5 scenario in January. In July, both 2013 and 2050 have the identical median OH mixing ratio

of 0.040 ppm but increase on 2100. While under the RCP4.5 scenario, the median OH was high over 2050 and even higher in 2100 simulation, with 0.049 ppm and 0.063 ppm respectively (Table 3.4.8). The 2100 simulation has the highest inter-quartile range by 0.035-0.084 ppm. Based on CDF from Figure 3.4.27 (e) - 6.8(h), 95 percentiles of OH mixing ratio under RCP8.5 scenario was below 0.11 ppm (2013, 2050) and 0.13 ppm (2100) during the January period. However, on July, the OH increased around 0.01 ppm in 2100 yet no significant change was found between 2050 and 2013. A change of OH mixing ratio at 95 percentiles under RCP4.5 with 0.03 ppm in January and 0.02 ppm in July was also observed.

Table 3.4.8: Hydroxyl radical (OH) mixing ratio (ppb) under RCP8.5 and RCP4.5 scenarios.

Variables	**RCP8.5 (ppb)**			**Changes (ppb)**	
	2013	2050	2100	2050 - 2013	2100 - 2013
January	0.060	0.053	0.060	-0.0065 (-10.8%)	0.018 (30%)
July	0.044	0.043	0.048	-0.0010 (-2.3%)	0.051 (113.6%)
Variables	**RCP4.5 (ppb)**			**Changes (ppb)**	
	2013	2050	2100	2050 - 2013	2100 - 2013
January	0.050	0.051	0.063	0.000082 (0.16%)	0.013 (26%)
July	0.043	0.045	0.053	0.0014 (3.3%)	0.010 (23.2%)

Figure 3.4.28 shows the spatial distribution of hourly average OH over the Malaysian region under the RCP8.5 scenario. During the January period, the hourly average of OH observed to be around 0.053 ppm in 2050 and 0.060 ppm in 2100. In general, a low level of OH concentration was distributed over the land area compared to the sea area and was believed caused by ship transportation activity. As relative to the baseline period, the OH mixing ratio reduced by -0.007 ppm in 2050 but increased by 0.018 ppm in 2100 during the January. During July period, the OH concentration was slightly lower than January and reduced by -0.001 ppm in 2050 but highly increased in 2100 by 0.051 ppm.

Under RCP4.5 ss relative to the baseline period, the OH concentration increased by 0.001 ppm and 0.013 ppm in 2050 and 2100 respectively. Whereas in July, the increment are 0.001 ppm and 0.010 ppm. The OH concentration in 2050 was higher than OH in 2100 over the South China Sea. in 2050 and 2100 respectively. In general, the high degree of OH increment can be related to future changes of meteorological parameters especially water vapor (Brasseur et al., 1998; Johnson et al. 2001; Zeng and Pyle, 2003; Murazaki and Hess, 2006; Stevenson et al., 2006; Latif et al., 2012). This process is achieved through the removal of the O (^{1}D) molecules based on O (^{1}D) + $H_2O \rightarrow 2OH$ and photolysis, and finally leads to the high formation of OH.

On the other hand, the increase of OH production can exert potential impact in oxidative capacity. As shown in Wyche et al., (2021) under the hydrocarbon-limited O_3 production regime, where total NO_x decreased proportionally greater than total non-methane hydrocarbons, which led to

an increase in total hydroxyl, peroxy and organic peroxy radicals. As shown in the whisker plot the OH mixing ration increase at both RCPs over the 90 percentiles. Additionally, this leaves an expectation that the model has overestimated the OH concentration as the result of complex or unresolved boundary layer condition. As mentioned in studies of (Monks, 2005; Lelieveld et al., 2016) that the perturbations to local boundary layer air led to a shift in (OH) concentrations.

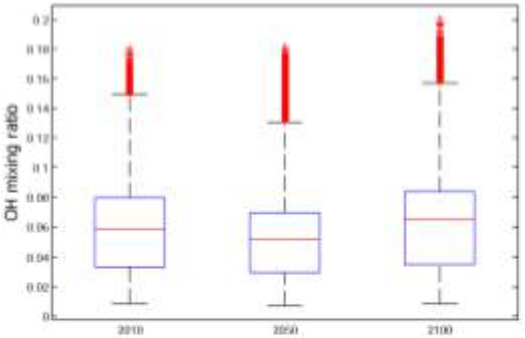

(a) OH mixing ratio of RCP8.5: January

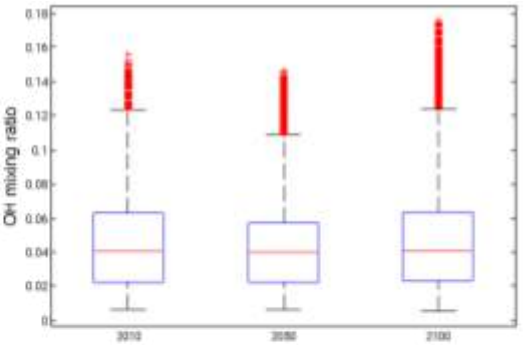

(b) OH mixing ratio of RCP8.5: July

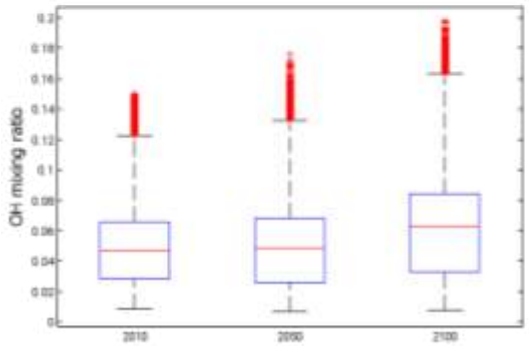

(c) OH mixing ratio of RCP4.5: January

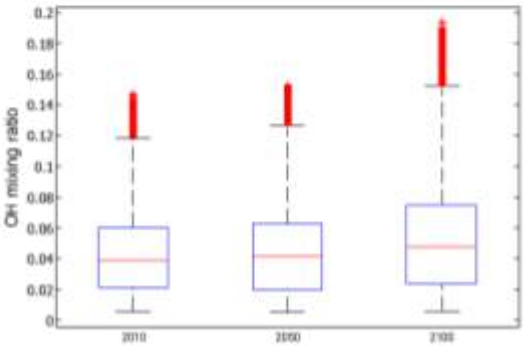

(d) OH mixing ratio of RCP4.5: July

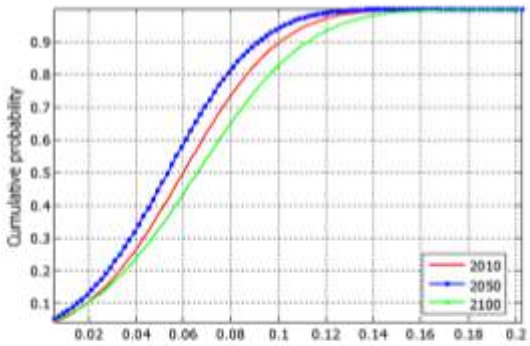

(e) OH distribution RCP8.5: January

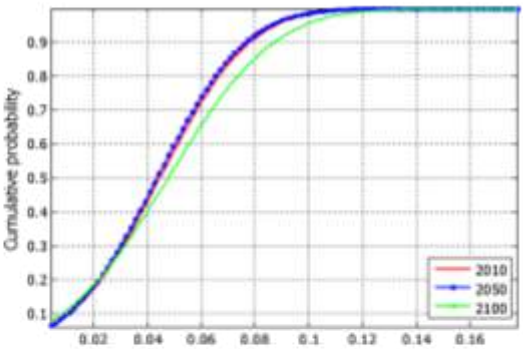

(f) OH distribution RCP8.5: July

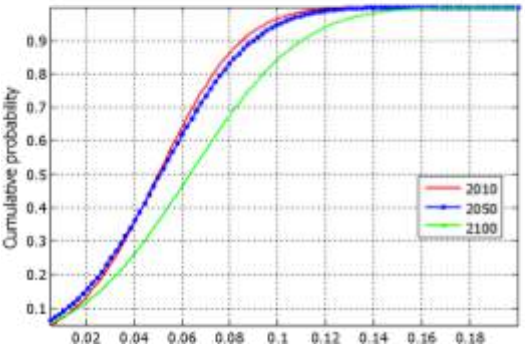

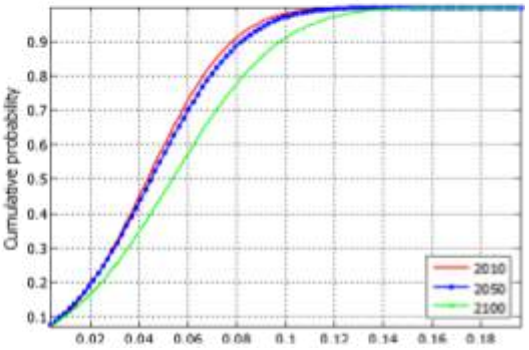

(g) OH distribution RCP4.5: January (h) OH distribution RCP4.5: July

Figure 3.4.27: Box and whisker plots of the maximum hourly average OH mixing ratio (ppm) for 2013(1st box), 2050(2nd box), and 2100(3rd box) under RCP8.5 scenario (a)-(b) and under RCP4.5 scenario (c)-(d). The cumulative distribution function of the hourly average OH mixing ratio (ppm) for 2013(red line), 2050(blue dot line), and 2100(green dash line) under RCP8.5 scenario (e)-(f) and under RCP4.5 scenario (g)-(h). The left panel indicates the January period and the right panel as the July period.

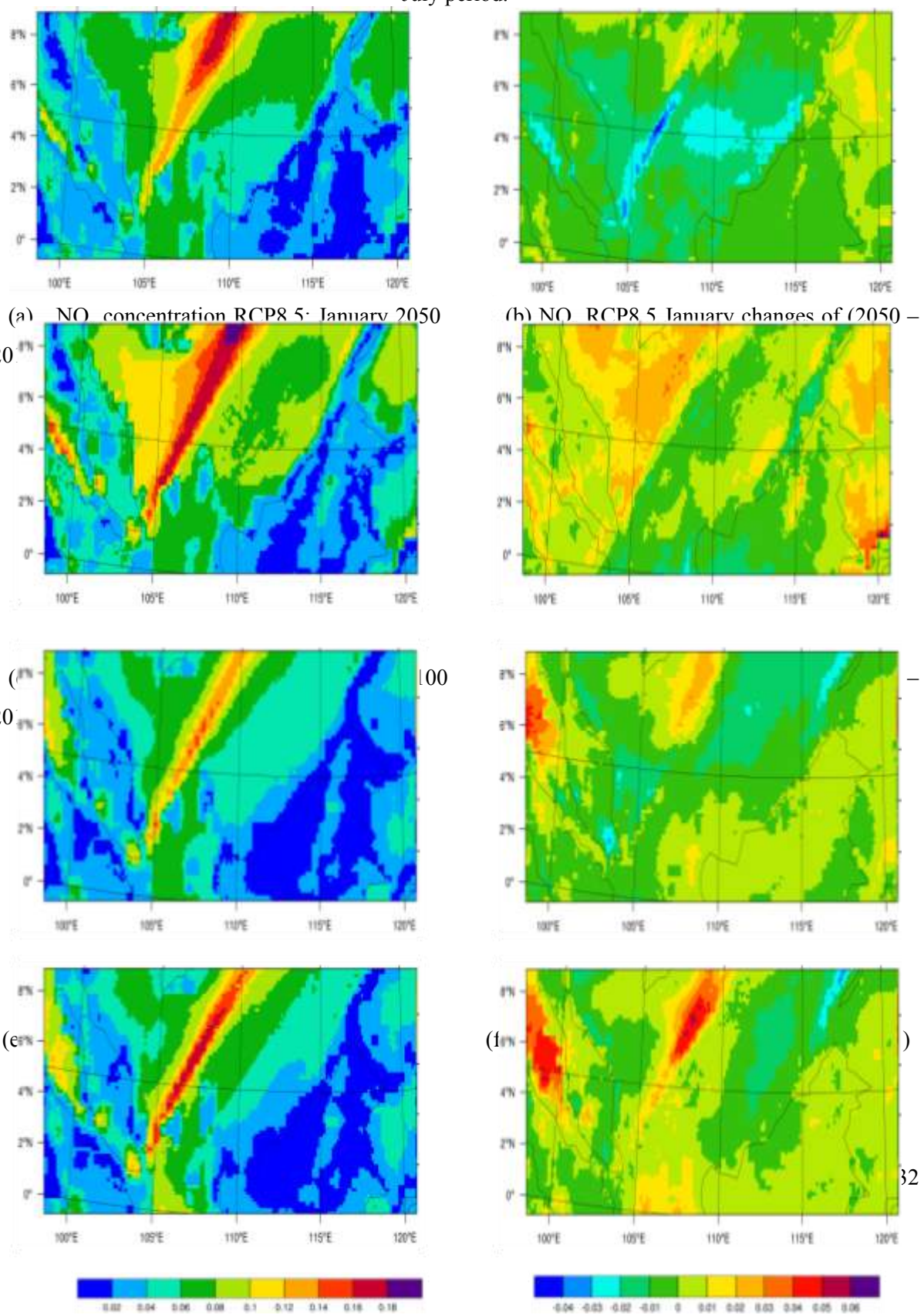

(a) NO concentration RCP8.5: January 2050 (b) NO RCP8.5 January changes of (2050 –

20

(

20

(e) (f)

32

(g) NO_x concentration RCP8.5: July 2100 (h) NO_x RCP8.5 July changes of (2100 – 2013)

Figure 3.4.28: Projected OH under RCP8.5: (a),(c),(e),(g) hourly average and (b),(d),(f),(h) average changes of OH

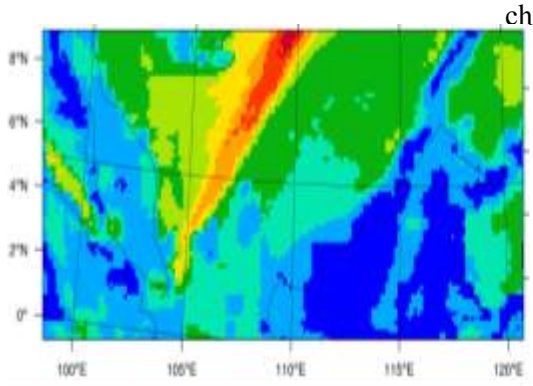

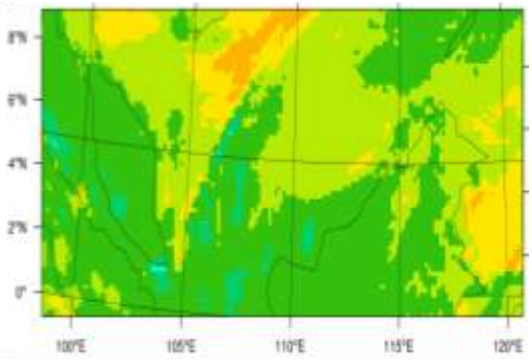

(a) NO_x concentration RCP 4.5: January 2050 (b) NO_x RCP4.5 January changes of (2050 – 2

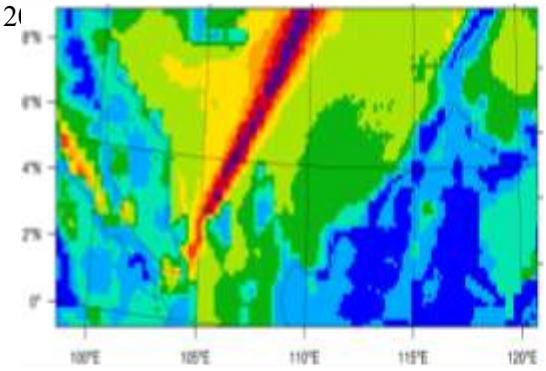

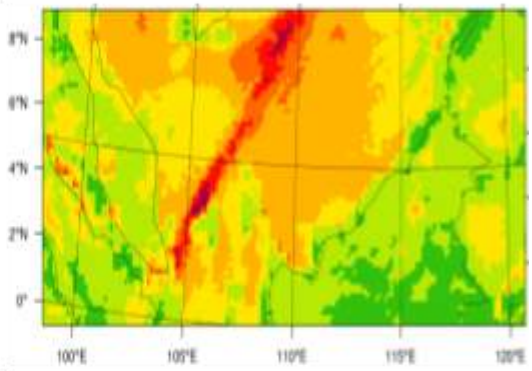

2100 00 – 2

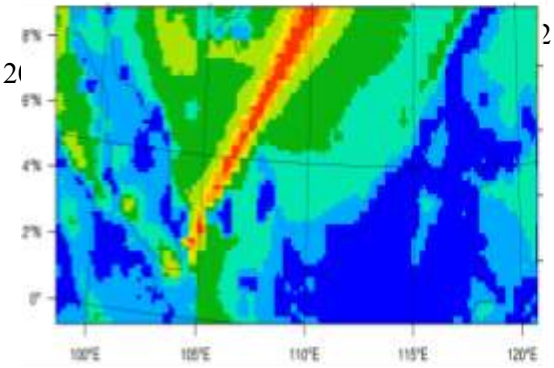

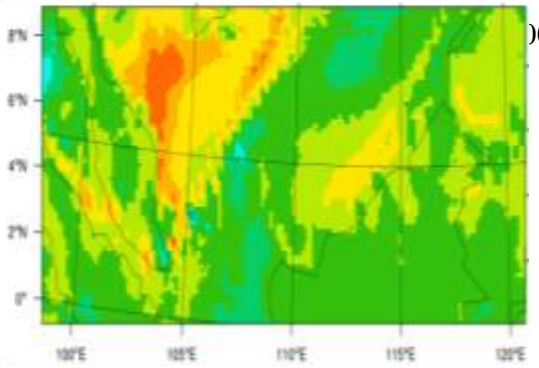

13)

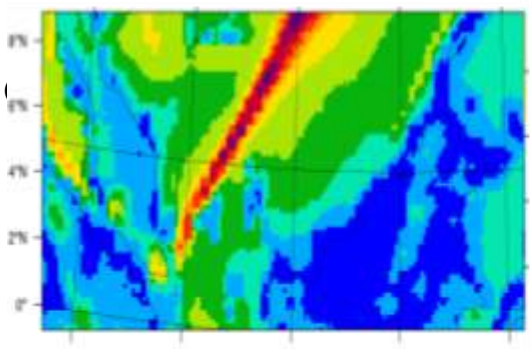

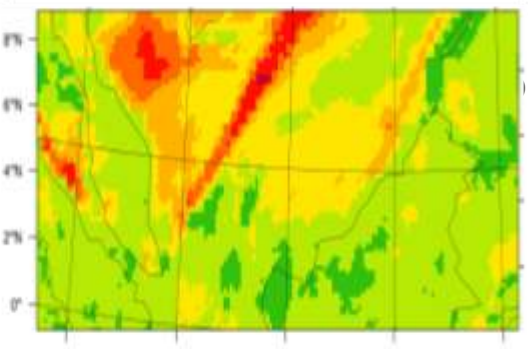

133

(g) NO_x concentration RCP4.5: July 2100 (h) NO_x RCP4.5 July changes of (2100 – 2013)

Figure 3.4.29: Projected OH under RCP4.5: (a),(c),(e),(g) hourly average and (b),(d),(f),(h) average changes of OH

There is to be argued that there was also a concomitant shift in average ambient O_3 concentrations owing to the change in oxidative capacity and perturbation of local boundary layer. The model simulation suggests that the environment that experienced increase of surface O_3, the hourly average of OH species also experienced increases. However, given the complexity of atmospheric chemistry, this cannot rule out that the combined increase of OH and O_3 will increase the overall oxidative capacity. As such the scenario is somewhat complex, and attention must also be given to the wider altered trace composition and reactivity of the atmosphere that occurred during the process. Such a dramatic changes in certain air pollutants across the species emissions spectrum, over such a relatively short time interval over large area, is unprecedented.

3.4.2.4 Nitric Acid (HNO_3)

The highest hourly average HNO_3 was 0.43ppb and the value decreased in the future period by 0.24 ppb and 0.30 ppb of both January 2050 and 2100 under RCP8.5 (Figure 3.4.30). In July, highest HNO_3 was found in 2050 but lowest in 2100. It is also noted that the inter quartile range in the July of 2100 is the lowest compared to the other simulation. While, under the RCP4.5 scenario, the highest median of HNO_3 was in 2013 with 0.22ppb, but lowest in the 2050 with 0.10ppb during January simulation. While in July, the median HNO_3 concentration got lower toward the end of this century. The decrease of HNO_3 was statistically significant at 95 percentiles for the 2050 and 2100 simulations by 0.25ppb in January. In July, the change was significant at 95 percentiles by 0.50ppb under RCP8.5 for the 2100 simulation. Under RCP4.5, the significant change was identical for both future simulations in both January and July.

Table 3.4.9 and Figure 3.4.31 indicate the spatial distribution of the hourly average of HNO_3 in the Malaysian region under the RCP8.5 scenario, with 0.39 ppb in 2050 and 0.17 ppb in 2100 during the January period. High concentration of HNO_3 distributed over Malacca Straits and the

middle of South China Sea in both period of 2050 and 2100. The HNO_3 under the RCP8.5 scenario decreased by -0.12ppb during mid-century and -0.11ppb over the end of century of January period. The HNO_3 increased over most of the research domain except the middle of the South China Sea, a with higher magnitude in 2050 compared to 2100. In July, the HNO_3 mixing ratio recorded was 0.39 ppb in 2050 and 0.17 ppb in 2100 under the RCP8.5 scenario over the Malaysian region. A small HNO_3 increment was found in 2050 by 0.026 ppb but decreased by -0.19ppb at the end of century. The results suggest that the concentration of HNO_3 was spread but concentrated over the middle of the South China Sea in 2050. Meanwhile, the simulation result indicates that HNO_3 decreased across the whole research domain in the period of July 2100.

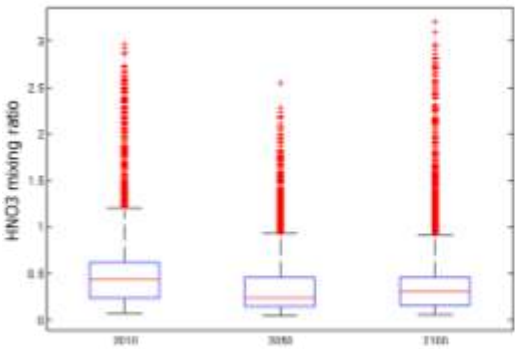

(a) HNO_3 mixing ratio of RCP8.5: January

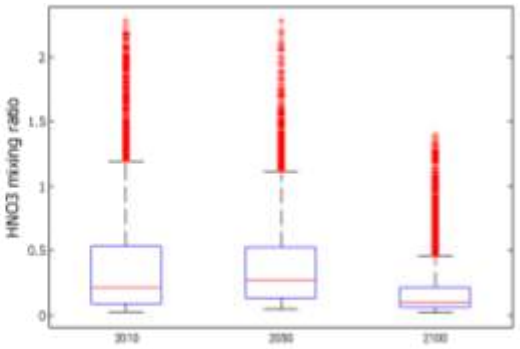

(b) HNO_3 mixing ratio of RCP8.5: July

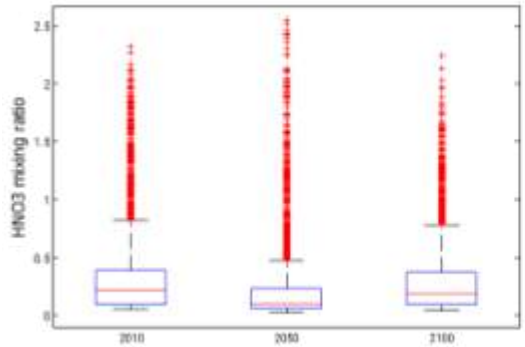

(c) HNO_3 mixing ratio of RCP4.5: January

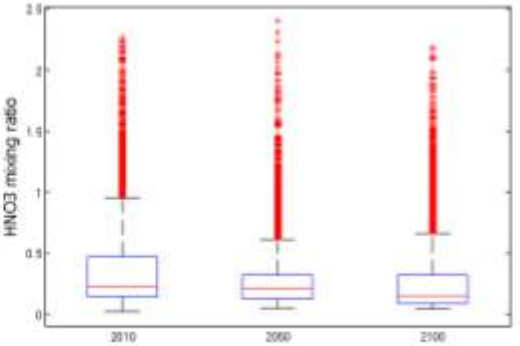

(d) HNO_3 mixing ratio of RCP4.5: July

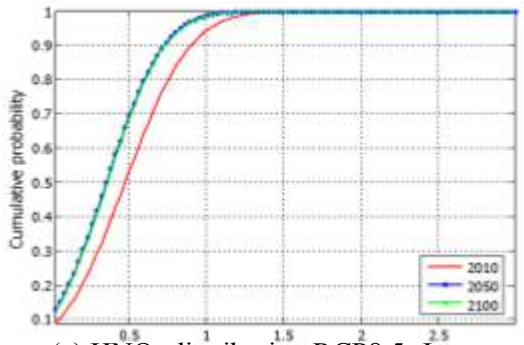

(e) HNO_3 distribution RCP8.5: January

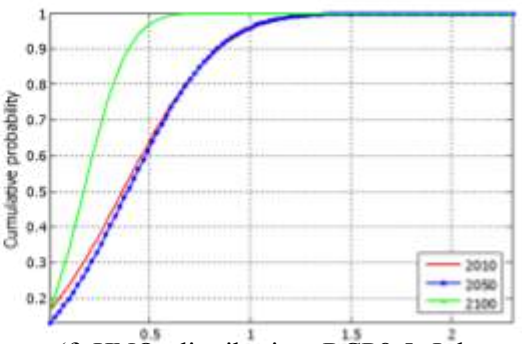

(f) HNO_3 distribution RCP8.5: July

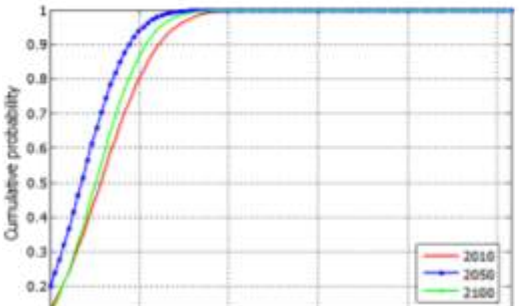

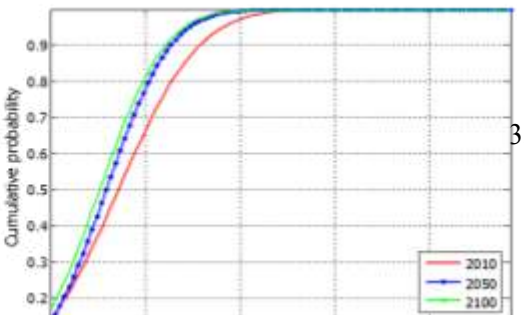

(g) HNO_3 distribution RCP4.5: January (h) HNO_3 distribution RCP4.5: July

Figure 3.4.30: Box and whisker plots of the maximum hourly average HNO_3 mixing ratio (ppm) for 2013(1st box), 2050(2nd box), and 2100(3rd box) under RCP8.5 scenario (a)-(b) and under RCP4.5 scenario (c)-(d). The cumulative distribution function of the hourly average HNO_3 mixing ratio (ppm) for 2013(red line), 2050(blue dot line), and 2100(green dash line) under RCP8.5 scenario (e)-(f) and under RCP4.5 scenario (g)-(h). The left panel indicates the January period and the right panel as the July period.

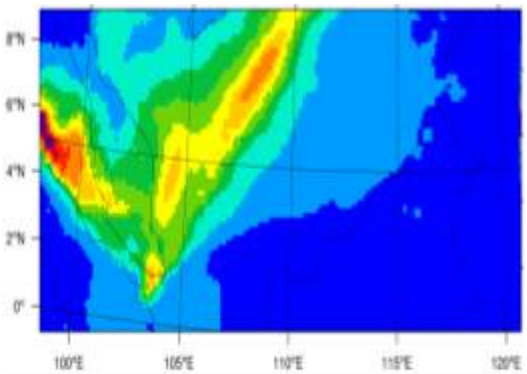

(a) HNO_3concentration RCP8.5: January 2050

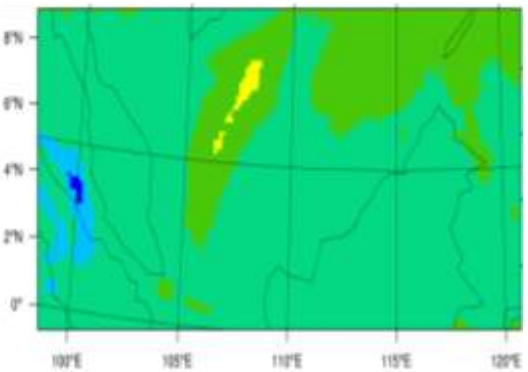

(b) HNO_3 RCP8.5 January changes of (2050 – 2013)

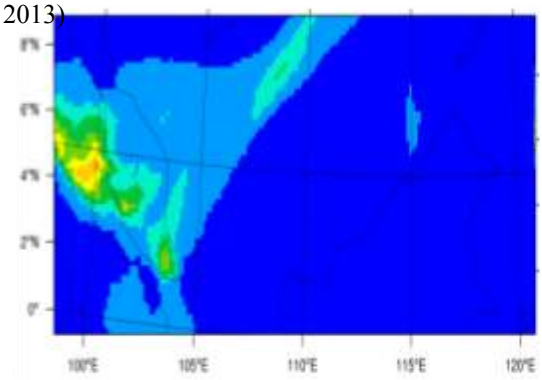

(c) HNO_3 concentration RCP8 .5: January 2100

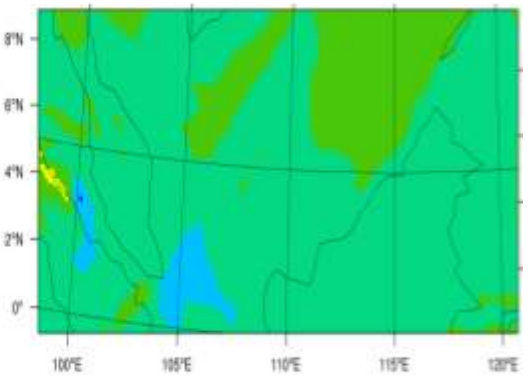

(d) HNO_3 RCP8.5 January changes of (2100 – 2013)

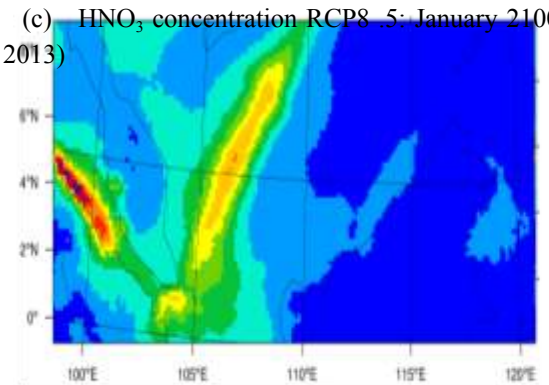

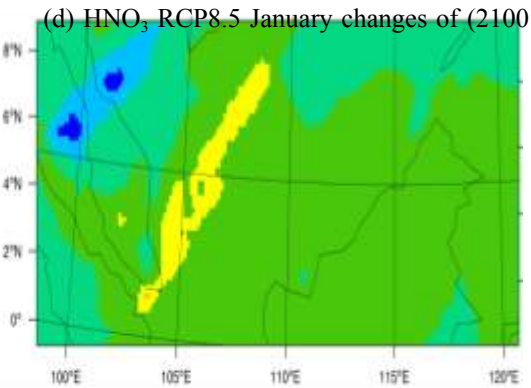

(e) HNO_3 concentration RCP8.5: July 2050 (f) HNO_3 RCP8.5 July changes of (2050 – 2013)

(g) HNO_3 concentration RCP8.5: July 2100 (h) HNO_3 RCP8.5 July changes of (2100 – 2013)

Figure 3.4.31: Projected HNO_3 under RCP8.5: (a),(c),(e),(g) hourly average and (b),(d),(f),(h) average changes of HNO_3

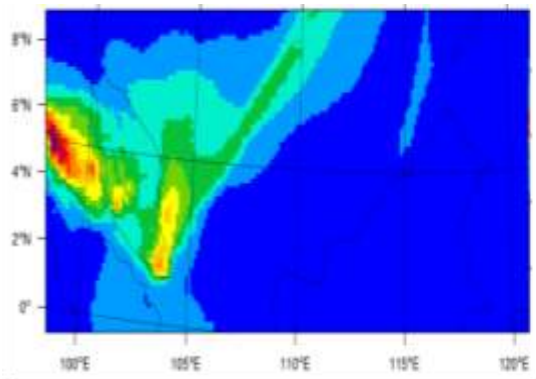

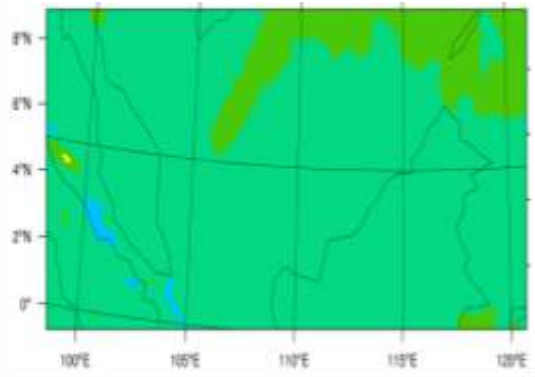

(a) HNO_3concentration RCP4.5: January 2050 (b) HNO_3 RCP4.5 January changes of (2050 – 2

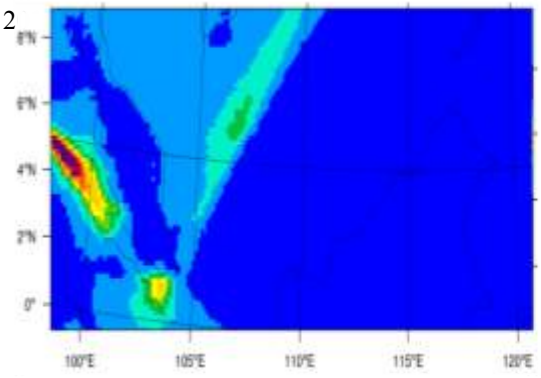

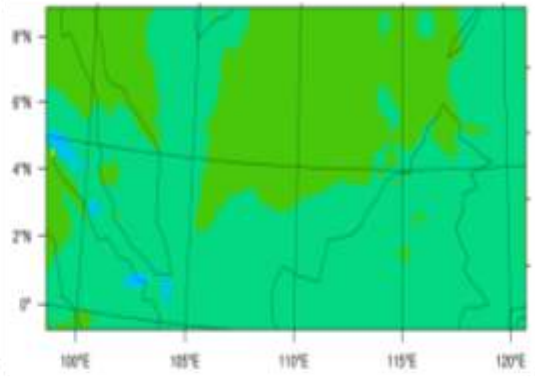

00 (d) HNO_3 RCP4.5 January changes of (2100 – 2

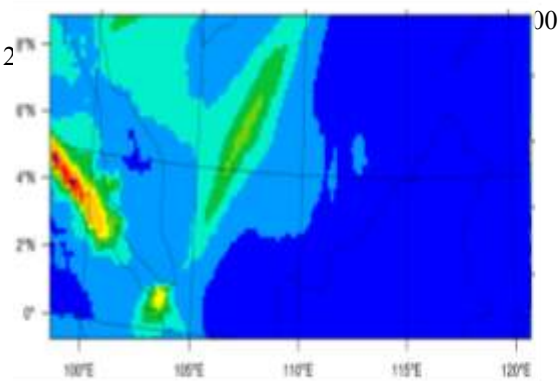

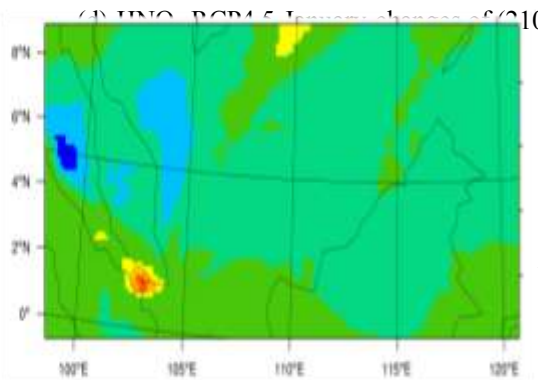

(e) HNO_3 concentration RCP4.5: July 2050 (f) HNO_3 RCP4.5 July changes of (2050 – 2013)

(g) HNO_3 concentration RCP4.5: July 2100 (h) HNO_3 RCP4.5 July changes of (2100 – 2013)

Figure 3.4.32: Projected HNO_3 under RCP4.5: (a),(c),(e),(g) hourly average and (b),(d),(f),(h) average changes of HNO_3

Table 3.4.9: Nitric Acid (HNO_3) mixing ratio (ppb) under RCP8.5 and RCP4.5 scenarios

Variables	**RCP8.5 (ppb)**			**Changes (ppb)**	
	2013	2050	2100	2050-2013	2100-2013
January	0.47	0.35	0.36	-0.12 (-25.5%)	-0.11 (-23.4%)
July	0.36	0.39	0.17	0.026 (7.2%)	-0.19 (-52.7%)
Variables	**RCP4.5 (ppb)**			**Changes (ppb)**	
	2013	2050	2100	2050-2013	2100-2013
January	0.28	0.18	0.26	-0.11 (-39.3%)	-0.063 (-22.5%)
July	0.36	0.29	0.26	-0.027 (-7.5%)	-0.097 (-26.9%)

Under the RCP4.5 scenario, the simulation of HNO_3 mixing ratio was lower than the mixing ratio under the RCP8.5 scenario, with 0.18ppb in 2050 and 0.26ppb in 2100 during the January period (Figure 3.4.32). similarly, a high concentration of HNO_3 was found on Malacca Straits and the middle of the South China Sea. Meanwhile, the HNO_3 decreased by -0.11ppb in mid-century and -0.063 ppb over the end of century as relative to the baseline period. In 2050, most of the research domain experienced a reduction in the HNO_3 mixing ratio as compared to the baseline period. However, in 2100 a slight increase of HNO_3 was observed over the northern part of the Malaysian Peninsula, Malaysian Borneo, and to the extent region of the South China Sea.

During July, the average concentration of HNO_3 was 0.29 ppb and 0.26 ppb in 2050 and 2100 respectively. A high mixing ratio of HNO_3 was distributed over the Malacca Straits, southern

Malaysian Peninsula, and middle of South China Sea for both years. A small decrease in HNO_3 was observed with -0.027ppb and -0.097ppb during mid-century and end of century. Though, in 2050, the HNO_3 increased significantly over a small part of the south Malaysian Peninsula and part of Malacca Straits. Moreover, the HNO_3 during July of 2100 decreased over a large part of the research domain relative to the baseline scenario.

The HNO_3 variations can be related to O_3 changes. The increase of HNO_3 concentrations in 2050 under both RCP8.5 and RCP4.5 scenarios, a certain part of the China Sea was due to the increase NO_x ratio driven by an increase of O_3 mixing ratio. Meanwhile, at the end of this century, the surface ozone mixing ratio generally reduced over most of the Malaysia region that probably due to the reduction of HNO_3 concentration. In general, the mean future HNO_3 concentration reduced the maximum of -52.7% and the minimum of -7.5%.

3.4.2.5 Carbon Monoxides (CO)

The box plot CO mixing ration Figure 3.4.33 below showed that the highest median hourly average CO was higher in the 2013 simulation with 121.1 ppb during January under the RCP8.5 scenario. The median CO mixing ratio got lower at 2050 (with 114.4 ppb) and 2100 (with 103.6 ppb) simulations. In July, the median CO mixing ratio follow the same pattern as in January with the median value getting lower toward the end of this century (from 174.3 ppb down to 158.1 ppb at the mid of century and 141.4 ppb at the end of century). Under the RCP4.5 scenario, the median of CO concentration decreased at the middle of century but increase toward the end of century with CO concentration from 180.3 ppb into 151.7 ppb and increase to 161.3 ppb during January, and from 167.4 ppb into 138.1 and increase to 146.8 ppb during July respectively as compared to the present simulation.

Table 3.4.10: CO mixing ratio (ppb) under RCP8.5 and RCP4.5 scenarios

Variables	**RCP8.5 (ppb)**			**Changes (ppb)**	
	2013	2050	2100	2050-2013	2100-2013
January	125.0	122.1	110.3	-2.9 (-2.3%)	-14.7 (-11.8%)
July	112.4	108.6	96.9	-3.9 (-3.5%)	-15.5 (-13.8%)
Variables	**RCP4.5 (ppb)**			**Changes (ppb)**	
	2013	2050	2100	2050-2013	2100-2013
January	118.6	100.3	100.4	-18.3 (-15.4%)	-18.2 (-15.3%)
July	109.9	92.6	97.8	-17.3 (-15.7%)	-12.0 (-10.9%)

A comparison between the cumulative distribution function of the CO concentration over the Malaysia region in 2013, 2050, and 2100 simulations respectively as shown in Figure 3.4.33 (e-h). The distributions are close between each other in January under RCP8.5 scenario between 2013 and 2050 simulations, showed the insignificantly change between both simulations. Meanwhile, a statistically significant change was observed at 95 percentiles between 2013 and 2100 with CO

concentration around 15 ppb in January. In July, the change was significant at 95 percentiles with changes more than 30 ppb under RCP8.5 for the 2100 simulation, and 10 ppb for 2050 simulation.

The average CO mixing ratio was 122.1 ppb in 2050 and 110.3 ppb in 2100 under the RCP8.5 scenario during January. The CO distributed across the west coast of the Malaysian Peninsula, Malacca Straits, north and eastern part of Malaysian Borneo in 2050 as depicted under Figure 3.4.34, however the trend of concentration decreases at the end of century (with decrement by -2.9 ppb to -14.7 ppb relative to baseline scenario). Though CO increment with more than 20ppb was obvious across most of the Malaysian Peninsula and the northern part of Malaysian Borneo in 2050 most likely as the result of increases in energy consumption was worthy to be highlighted.

During July, a low value of CO mixing ratio was observed over the Malaysian region with 108.6 ppb in 2050 and 96.9 ppb in 2100 under the RCP8.5 scenario. In general, the CO decreased by -3.9 ppb in mid-century and -15.5 ppb at the end of century. As relative to the baseline period, the CO concentration highly increased over the southern area and east sea area of the Malaysia Peninsula in the year 2050. While in 2100, most of the study domain experienced the CO reduction especially north Malaysia Peninsula.

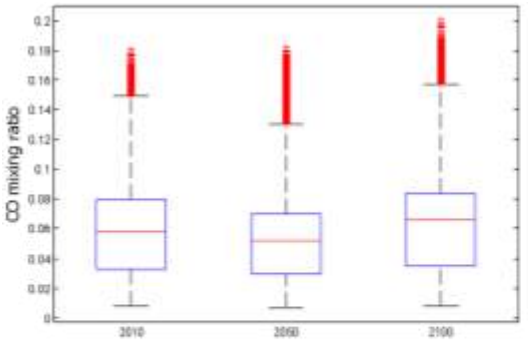

(a) CO mixing ratio of RCP8.5: January

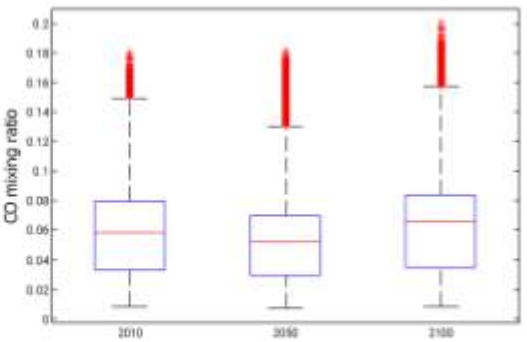

(b) CO mixing ratio of RCP8.5: July

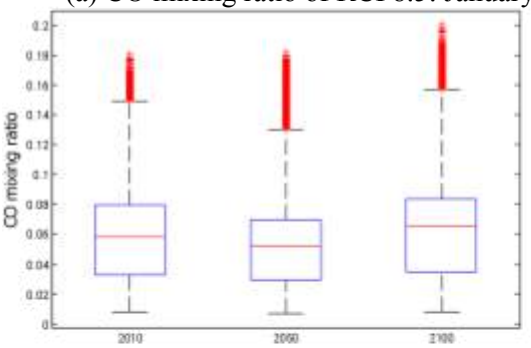

(c) CO mixing ratio of RCP4.5: January

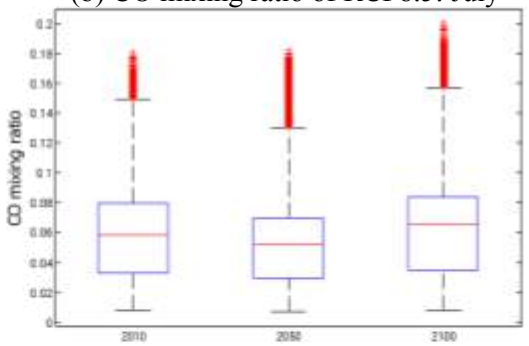

(d) CO mixing ratio of RCP4.5: July

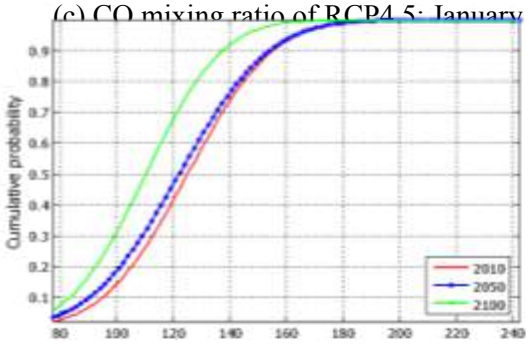

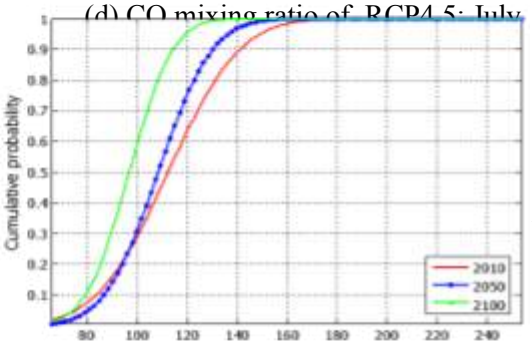

(e) CO distribution RCP8.5: January

(f) CO distribution RCP8.5: July

(g) CO distribution RCP4.5: January

(h) CO distribution RCP4.5: July

Figure 3.4.33: Box and whisker plots of the maximum hourly average CO mixing ratio (ppm) for 2013(1st box), 2050(2nd box), and 2100(3rd box) under RCP8.5 scenario (a)-(b) and under RCP4.5 scenario (c)-(d). The cumulative distribution function of the hourly average CO mixing ratio (ppm) for 2013(red line), 2050(blue dot line), and 2100(green dash line) under RCP8.5 scenario (e)-(f) and under RCP4.5 scenario (g)-(h). The left panel indicates the January period and the right panel as the July period.

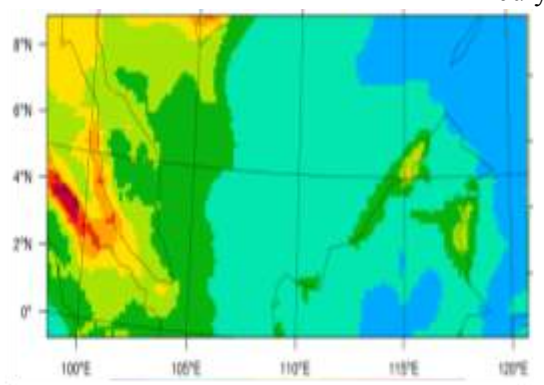

(a) CO concentration RCP8.5: January

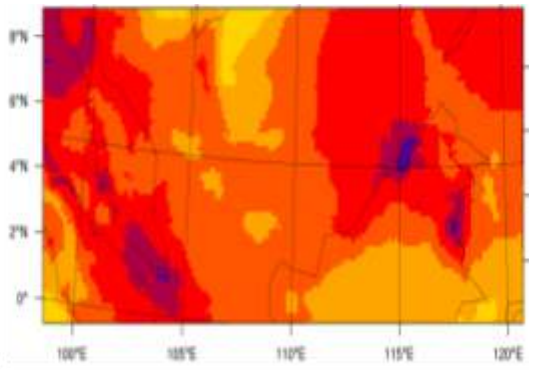

(b) CO RCP8.5 January changes of (2050 – 2013)

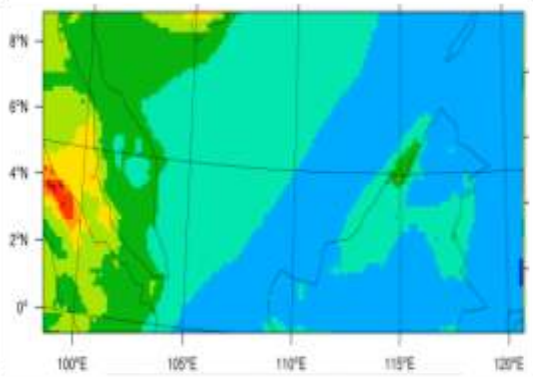

(c) CO concentration RCP8 .5: January 2100

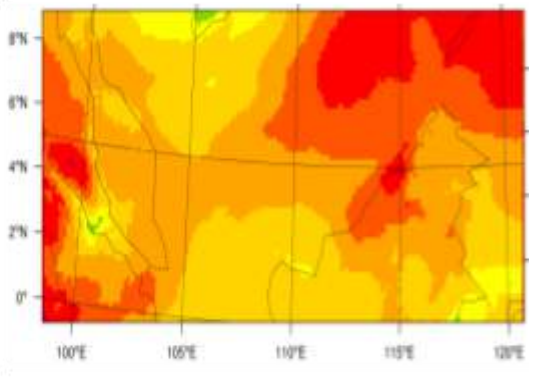

(d) CO RCP8.5 January changes of (2100 – 2013)

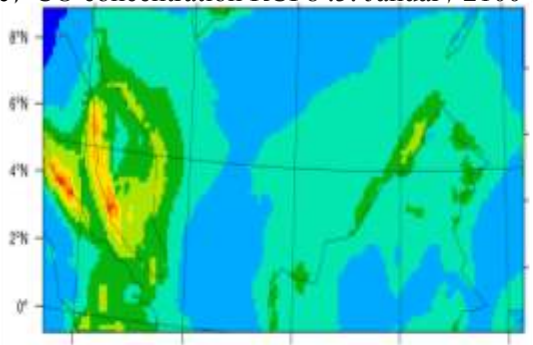

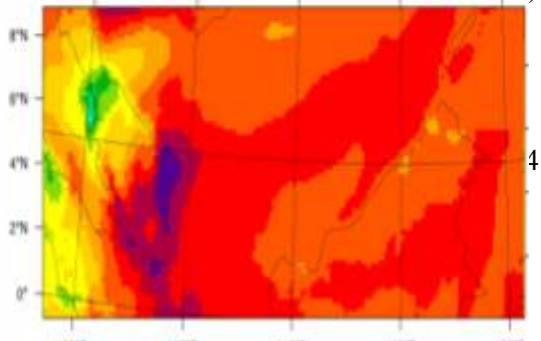

(e) CO concentration RCP8.5: July 2050 (f) CO RCP8.5 July changes of (2050 – 2013)

(g) CO concentration RCP8.5: July 2100 (h) CO RCP8.5 July changes of (2100 – 2013)

Figure 3.4.34: Projected CO under RCP8.5: (a),(c),(e),(g) hourly average and (b),(d),(f),(h) average changes of CO

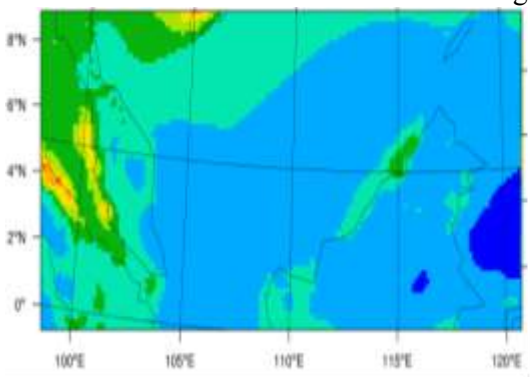
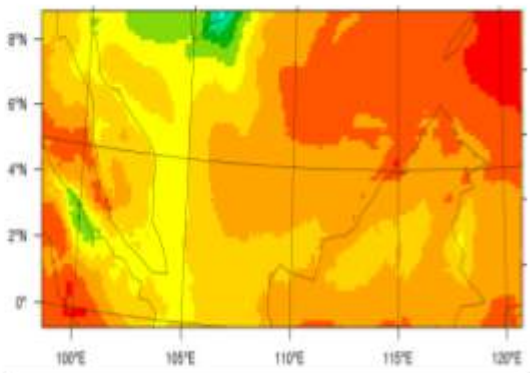

(a) CO concentration RCP4.5: January 2050 (b) CO RCP4.5 January changes of (2050 – 2013)

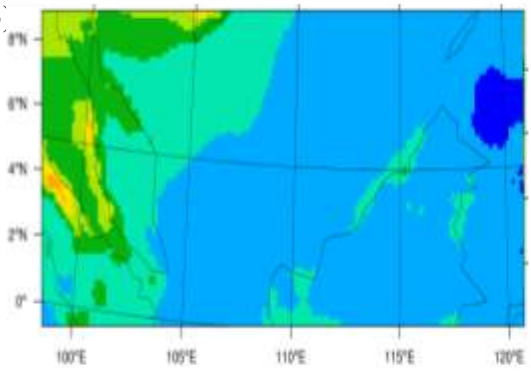
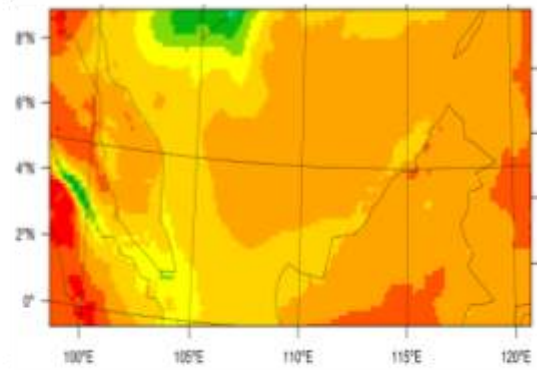

(c) – 2013)

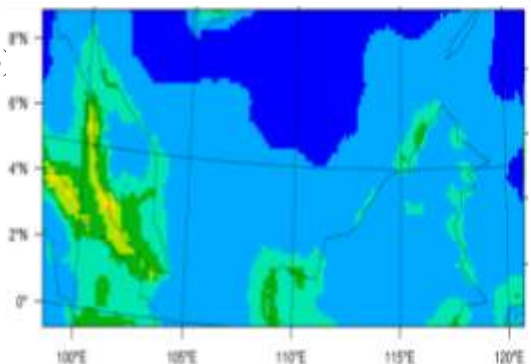
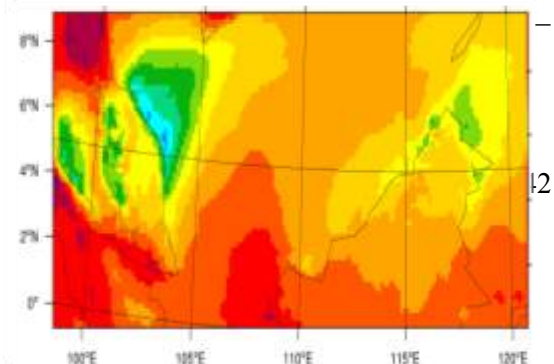

(e) CO concentration RCP4.5: July 2050

(f) CO_3 RCP4.5 July changes of (2050 – 2013)

(g) CO concentration RCP4.5: July 2100

(h) CO RCP4.5 July changes of (2100 – 2013)

Figure 3.4.35: Projected CO under RCP4.5: (a),(c),(e),(g) hourly average and (b),(d),(f),(h) average changes of CO

Under the RCP4.5 scenario, the hourly average CO mixing ratio was around 100 ppb for both future periods in January (Figure 3.4.35). In both scenarios, the CO was highly distributed over Malacca Straits. Overall, the hourly average CO reduced by around -18ppb for both periods of 2050 and 2100. The reduction seems to be equally distributed over the whole research domain. During July, the CO concentration was lower than the CO during the January season, with 92.6ppb in 2050 and 97.8ppb in 2100. The CO reduced by -17.3ppb and -12.0ppb in 2050 and 2100 respectively. Obviously, high intensity of CO decrement was observed over a sea area of north Malaysian Peninsula and north Malaysian Borneo during July 2050 under the RCP4.5 scenario. In 2100, a similar trend of decrement was found but with a smaller region than in 2050.

4 Conclusion

4.1 Climate Change Projection over SEA

The regional climate simulations over the SEA region were performed for the future period year of 2030, 2050, 2070, and 2100, relative to the present period in 2013. These simulations were focused on January and July by the application of regional climate modelling of WRF focusing on three climate scenarios which are RCP4.5, RCP6.0, and RCP8.5, and was developed based on the IPCC fifth

assessment report as input models. The projected simulation by WRF model, the surface temperature at present-day was estimated at the range between 22.88℃, 22.41℃ and 23.29℃ for January period, while 26.66℃, 26.46℃ and 26.63℃ for July period under RCP4.5, RCP6.0 and RCP8.5 respectively. The WRF simulation under all RCP scenarios well-agree with DOE and NCEP in simulating the surface temperature with bias less than 10% (-6.88% and 2.49%).

Overall, the whole SEA region is expected to experience warmer surface temperature coming toward the mid of century with temperature increment between 0.66℃ to 1.64℃ (2.63% to 7.33%) during January, and between 0.74℃ to 0.99℃ (2.89% to 3.72%) during July as relative to the baseline condition. At the end of the century, it was expected that the whole region will experience higher temperature increment between 0.82℃ to 2.11℃ (3.58% to 9.05%) in January, and 0.93℃ and 2.50℃ (3.49% to 9.37%) in July respectively. RCP6.0 projection shows the highest increment at the mid of century between 3.55% to 7.33%. While RCP8.5 depicts the highest temperature increment towards the end of the century over 9.05% to 9.37% for the whole domain.

The regional total precipitation simulations over the SEA region for RCP4.5, RCP6.0, and RCP8.5 both for present-day and future days were highly varied. The total precipitations for the baseline period over the whole domain are, 0.92 inches/day, 3.14 inches/day, and 5.49 inches/day for the January period under the respective RCPs. Whereas in July, the simulated total precipitation is, 8.80 inches/day, 8.50 inches/day, and 131.59 inches/day for the July period under RCP4.5, RCP6.0, and RCP8.5 respectively. Towards the mid of century, all three RCPs in climate simulation agrees that the whole region will experience an increase of rainfall ranging from 1.58 to 102.53 inches/day (0.50% to 18.67%) during the January period, and between 6.48 to 118.04 inches/day (0.05% to 13.88%) for July.

At the end of the century, the simulation of RCP4.5 and RCP6.0 agreed that this region will experience a higher rate of precipitation with a projected increment of 89.10 and 49.57 inches/day (15.78%-96.84%) for January, while 96.93 and 123.39 inches/day (11.00% to 14.50%) during July of 2100. Though, under RCP8.5 the projected total precipitation increases by 58.26 inches/day (10.61%) during January but decrement by 81.94 inches/day (-0.64%) during July of 2100. The projected precipitation change under the RCPs is not parallel with the surface temperature increment in this study and might be caused by the unresolved parametrization, boundary condition, and complex topographic of SEA region as after-mentioned.

Under RCP4.5 climate simulation, 40% of the study domain will experience temperature increment higher than 1.5℃ towards the mid of century especially in January while the projected changes are less significant during July. Coming toward the end of the century, 60% of the domain experienced temperature increments higher than 2.0℃ in January and 30% in July. Most of the temperature changes are pronounced over the MSEA region of Myanmar, Thailand, Cambodia, and Laos with a temperature change of 2.86℃ to 4.71℃, and -5.19℃ to 2.61℃ for mid and end of a

century respectively. This temperature change brings a shift in precipitation from 0.62% to 168.62% in MSEA and -0.36% to 31.85% over the insular region over the mid of century. At the end of the century, the MSEA region is expected to have a lower surface temperature but more frequent flood with projected precipitation changes of 7.06% to 447.12%, and between 18.79% to 224.75% over the insular region.

There is a significant temperature increment under RCP6.0 with over 70% of the SEA region will experience 1.5℃ temperature increment during January 60% in July of mid-century. While 80% of the region will experience over 2.0℃ temperature increment for both periods toward the end of the century. Despite the noticeable change in surface temperature, the projected total precipitation over the mid-century - 0.99% to 90.44% during January and, between 7.05% to 72.23% during July. While at the end of the century, the projected total precipitation is between -5.13% to 51.77% during January and, between 8.22% to 35.17% during July. The most vulnerable region under this scenario is Myanmar, Thailand, Cambodia, and the Philippines with recorded surface temperature change of 3.04℃ to 12.69℃ and total precipitation change of 78.23 inches/day to 203.58 inches/day.

Under RCP8.5 climate simulation, 50% of the study domain will experience temperature increment higher than 1.5℃ towards the mid of century, especially in January 30% during July. Coming toward the end of the century, less than 30% of the domain experienced temperature increments higher than 2.0℃ in January and less than 20% in July. Most of the total precipitation changes are pronounced in the insular region with 15.74% to 40.41% precipitation increment during January, and 3.66% to 9.18% in July of mid and end of a century respectively. Despite a less significant warming trend compared to RCP6.0, Thailand and Cambodia still recorded the highest temperature increment of 4.18℃ and 3.25℃ while Indonesia and the Philippines recorded higher total precipitation increment of 26.49 inches/day and 30.87 inches/day.

4.2 Biomass Emission Inventory of SEA

Biomass burning as open or partly open burning of organic compounds is a common practice in the SEA region which is used to boost agricultural production. BB has been receiving increasing attention over the decades due to the associated global, regional, and local impacts on air quality, public health, and climate. Extensive fire activity in Southeast Asia (SEA) is claimed as one of the major sources of global BB emissions and the available emission inventories were too general to represent the BB emission in this region. Hence, this study was to develop emission inventories from biomass burning based on land cover types in SEA during the ENSO-neutral year of 2013. Remote sensing data and Geographical Information System (GIS) techniques were the primary tools in this study and employed MODIS products of MCD64A1 and MCD12Q1 to access as well evaluate the land cover distribution and total burnt area.

This research comprised of monthly BB temporal distribution with a spatial resolution spaced at 500m x 500m. The mainland cover types in MSEA are evergreen forests and croplands, and the total burned area in 2013 was 77332.18 km^2, mainly contributed by savannas and croplands. While in Indonesia and Malaysia, the mainland covers are open forest/oil palm. Wetland, grassland, and shrublands. Borneo Island was mainly covered with broadleaf forest followed by open forest/oil palm which consists of up to 71.3% and 23% of total land cover as presented. The central part of Borneo, where large areas were unexplored and thus covered with thick and dense forested areas. While in Kalimantan, the finding showed that the broadleaf forest had the greatest coverage area, which accounted for 371055.75 km^2 from the total area.

Over 71091.11 km^2 area is burnt in 2013 with Myanmar set the largest burnt area consist of 27103.04 km^2 and followed by 23562.69 km^2. The combined of these regions exceeded half of the total burnt area over the SEA region, while the least burnt area found in Malaysia recorded 70.62 km^2 of total burnt area. Nevertheless, the highest land cover burnt during 2013 is Savannas in Cambodia, Shrublands in Laos, Deciduous in Myanmar, Croplands in Thailand and Vietnam, Broadleaf in Malaysia, and Wetland in Indonesia (which comprised of 53.44%, 38.76%, 23.49%, 48.83% and 78.68%, 45.56% and 53.43% from their total burnt area respectively).

Upon investigation, the total BB annual emission over this region, as much as 64391.02 Gg/yr of dry BB compound burnt and release into the atmosphere. From that, over 90% are released from BB activity detected in the MSEA region, thus the contribution of BB from Malaysia and Indonesia is less significant over this year. In MSEA, most of BB activity is pronounced during January to April with dry BB (with total emission ranging from 21.62% - 36.78% from the total emission). In addition, it is estimated that over 103,913.49 Gg of CO_2 and 6,538.29 Gg of CO are released to the atmosphere over the same period, which comprised 97% and 98% of the total emission.

This study rules out that most of the CO_2 and CO emissions which arise from BB activity have largely happened over Myanmar which contributed more than half of the gaseous pollutant, and it is also observed that most of the BB happened in deciduous and mixed forests. Whereas in Malaysia and Indonesia, the estimated CO_2 and CO that release into the atmosphere are only 5201.98 and 254.38 Gg of (less than 5% from the overall pollutant emission) and mostly contributed by evergreen forest and shrublands. This carries the expectation that BB in Indonesia are not primarily causing the regional transboundary pollution over the whole region of SEA, yet BB activity in MSEA has caused more air pollution issue.

4.3 Biogenic Emission Projection over SEA

MEGAN model is used to investigate the net emission of isoprene emission from terrestrial of SEA region. The input data of climate data and land cover data used in this study are obtained from WRF Model using the same climate scenarios and time slice. While the global land cover data used in this

study is adopted from the study of Ooi, *et al*., (2020). The projected isoprene emissions under RCP45 in January are found at 8.08 tons/hr in 2013, 8.29 tons/hr in 2030, 8.65 tons/hr in 2050, 8.69 tons/hr in 2070, and 9.46 tons/hr in 2100, respectively. Whereas in July period, projected isoprene emissions are 7.56 tons/hr in 2013, 7.72 tons/hr in 2030, 8.21 tons/hr in 2050, 7.94 tons/hr in 2070 and 8.57 tons/hr in 2100, respectively.

Indonesia recorded the highest isoprene emissions, reaching up from 8.29 to 8.95 tons/hr in January of mid and at the end of the century. This is followed by Malaysia at 7.13 to 7.93 tons/hr. Furthermore, as Malaysia and Indonesia are the main oil palm producers in SEA it was expected that isoprene emissions over this region are much more apparent than the rest. Indeed, as mentioned in Section 3.3, oil palm tree emits isoprene at a rate of five-time greater than the average rainforest tree. Therefore, this study rules out that both Malaysia and Indonesia are the main sources of biogenic partly caused by the large landcover conversion to palm oil plantations over the respective region.

Under RCP6.0, the projected isoprene emission in January is higher than RCP4.5 with 8.37 tons/hr in 2013, 8.65 tons/hr in 2030, 8.59 tons/hr in 2050, 8.92 tons/hr in 2070, and 10.48 tons/hr in 2100. While in July period, the projected isoprene emissions are 7.80 tons/hr in 2013, 7.74 tons/hr in 2030, 8.00 tons/hr in 2050, 8.63 tons/hr in 2070, and 9.28 tons/hr in 2100. However, under this RCP6.0 scenario, Indonesia was recorded as the highest isoprene emitter reaching up to 9.41 and 9.72 tons/hr during the mid and end of the century. Whereas in Malaysia, the projected emissions under this RCP6.0 are lower during the mid-century but higher at the end of the century from what has been observed under RCP4.5 with 7.11 and 8.37 tons/hr respectively.

The highest projected emission of isoprene was found in the RCP8.5 scenario with the value of 7.86 tons/hr, 8.27 tons/hr, 8.82 tons/hr, 11.24 tons/hr, and 12.41 tons/hr for the January period of 2013, 2030, 2050, 2070 and 2100 respectively. In July, the projected isoprene emissions are comparatively lower with 7.80 tons/hr, 7.87 tons/hr, 8.34 tons/hr, 9.05 tons/h,r, and 10.15 tons/hr following the same year respectively. Similarly, under this RCP, both Indonesia and Malaysia are the main source of isoprene emission, with estimated emissions of 8.66 – 17.92 tons/hr and 6.38 – 11.87 tons/hr during mid and end of a century respectively.

Thus, this study highlighted that most of the increment of isoprene emission was observed in January though the overall surface temperature for this region is lower than in July. However, the findings are parallel to the climate simulation as much of the temperature changes observed in the January period rather than July. Therefore, it carries the expectation that the higher the rate of temperature change, the higher the biogenic change. And detailed investigation of temperature and isoprene over the Malaysia and Indonesia region also suggests that there is indeed a correlation between temperature and isoprene changes over this region with a coefficient value ranging between 0.2 to 0.8.

Nonetheless, not all RCPs showed a high correlation between temperature and isoprene emission, thus leaving an impression that temperature indeed strongly can modulated biogenic emission but is not always prominent. The future fate of isoprene emission over the SEA region can be largely modulated by changing climate and land cover distribution. Yet, this cannot rule out the overall estimation of biogenic emission as other factors including soil moisture, humidity, and solar radiation are included upon this investigation.

4.4 Air Quality Projection

The regional climate simulations only cover the Malaysia region and were performed for the future three-time slice of 2013 (baseline), 2050 (mid-century), and 2100 (end of the century), which also focused on January and July by the application of WRF regional climate modelling. However, the investigation only covers two climate scenarios which are RCP4.5 and RCP8.5 respectively. The projected surface O_3 during the baseline period 50.5 and 52.7 ppb under RCP8.5 of January and July respectively. While under RCP4.5, the projected surface O_3 is 46.2 and 54.0 ppb following the same period. This simulation was higher than the observed value with 28.0% - 38.3% NMB under RCP8.5 and from 38.0% -41.6% NMB under RCP4.5 for January and July respectively. The overall Fa2 was between 1.2 and 1.3 which indicates an overestimation of simulation.

The overestimation of O_3 is caused by the high underestimation of O_3 precursor in the model chemistry. Similar overestimations of other primary emitted species of NO_x and CO have been seen in this study. This is due to the model's tendency to underestimate overnight mixing in urban areas which is caused by unresolved PBL heights during WRF simulation resulting in an overestimation of pollutants near the surface and high CMAQ model biases. Diurnal changes in O_3 precursor with the presence of photochemical activity and PBL height control are significant because they always take part in the generation and emission of these precursors. However, this investigation cannot rule out either the insufficient mixing in the mode solely responsible for the overall estimation.

5 Future Direction

This project has provided a great opportunity for future research. In fact, this project has a lot more to accomplished, which has not been explored in detail during the duration of this project. During the final research workshop and meeting, research team members have suggested a few points, which may shape the future direction of this research and regional collaboration. These includes:

a) Future collaboration in research to be continued especially related to climate change vulnerability and adaptation, climate impacts, regional emissions inventory (anthropogenic emissions)

b) Co-funding/grant matching to fund research in the region
c) Organising conference/Seminar together
d) Publication of research outputs (articles publications
e) Staff/students ex-change among institutions
f) Visiting scholar programme among institutions

References

1. Adrianto, H.A., Spracklen, D.V., & Arnold, S.R. (2019). Relationship between fire and forest cover loss in Riau Province, Indonesia Between 2001 and 2012. *Forests*. 10: 889.
2. Adrianto, H.A., Spracklen, D.V., Arnold, S.R., Sitanggang, I.S., & Syaufina, L. (2020). Forest and land fires are mainly associated with deforestation in Riau Province, Indonesia. *Remote Sensing*. 12: 3.
3. Afrin, S., Gupta, A., Farjad, B., Ahmed, M., Achari, G., & Hassan, Q.K. (2019). Development of Land-Use/Land-Cover Maps Using Landsat-8 and MODIS Data, and Their Integration for Hydro-Ecological Applications. *Sensors*. **19**(22): 4891.
4. Ahrens, C.D. (2013). *Meteorology Today: An introduction to weather climate and the environment* (10th edition). Cengage Learning.
5. Akagi, S.K., Yokelson, R.J., Wiedinmyer, C., Alvarado, M.J., Reid, J.S., Karl, T. & Wennberg, P.O. (2011). Emission factors for open and domestic biomass burning for use in atmospheric models. *Atmospheric Chemistry and Physics*. **11**(9): 4039–4072.
6. Alam, A.F., Er, A.C. & Begum, H. (2015). Malaysian oil palm industry: Prospect and problem. *Journal of Food Agriculture & Environment. 13:* 143-148.
7. Alexander, L.V. (2016). Global observed long-term changes in temperature and precipitation extremes: A review of progress and limitations in IPCC assessments and beyond. *Weather and Climate Extremes.* 11: 4-16.
8. Alves, E.G., Harley, P., Gonçalves, J.F.D.C., Moura, C.E.D.S., & Jardine, K. (2014). Effects of light and temperature on isoprene emission at different leaf developmental stages of Eschweilera coriacea in central Amazon. *Acta Amazonica*. 44(**1**): 9-18.
9. Apel, E.C., Hornbook, R.S., Hills, A.J., Blake, N.J., Barth, M.C., Weinheimer, A., Cantrell, C., Rutledge, S.A., Basarab, B., Crawford, J., Diskin, G., Homeyer, C.R., Campos, T., Flocke, F., Fried, A., Blake, D.R., Brune, W,m Pollack, I., Peicshl, J., Ryerson, T., Wenbberg, P.O., Crounse, D.J., Wisthaler, A., Mikoviny, T., Huey, G., Heikes, B., O'Sollivan, D.O. & Reimer, D.D (2015). Upper tropospheric ozone production from lighting NO_x- impacted convection: smoke ingestion case study from the DC3 campaign. *Journal of Geophysical Research: Atmosphere*. 120(**6**): 2505-2523.
10. Appel, K.W., Pouliot, G.A., Simon, H., Sarwar, G., Pye, H.O.T., Napelenok, S.L., Akhtar, F. & Roselle, S.J. (2013). Evaluation of dust and trace metal estimates from the Community Multiscale Air Quality (CMAQ) model version 5.0. *Geoscience Model Deviation*. 6: 883–899.
11. Arneth, A., Monson, R.K., Schurgers, G., Niiemets, U. & Palmer, P.I. (2008). Why are estimates of global terrestrial isoprene emission so similar (and why is this not so for monoterpenes)? *Atmospheric Chemistry & Physics*. 8: 4605-4620.
12. Atkinson, R. (2000). Atmospheric chemistry of VOCs and NOx. *Atmospheric Environment*. 34: 2063–2101.
13. Bai, J.H., & Baker, B. (2004). Study on the affecting factors of isoprene emission at grassland. *Chinese Journal of Atmospheric Sciences*. 28(**5**): 783-794.
14. Birch, C.E., Webster, S., Peatman, S.C., Parker, D.J., Matthews, A.J., Li, Y. & Hassim, M.E.E. (2016). Scale interactions between the MJO and the Western Maritime Continent. *Journal of Climate.* 29: 2471–2492.
15. Booth, A. (2018). *Southeast Asian Agricultural Growth: 1930–2010*: *Agricultural Development in the World Periphery*. In Pinilla, V. & Willebald, H. (*eds*). Palgrave Macmillan, Cham. Pp, 235–255.
16. Bravo-Oviedo ´.A., Alberdi-Asensio, I., Anton, C.,Barbati, A., Barreiro, S., Brang, P., Corona,

P.M., Drossler, L., et al. (2013). *Mixed Forest Definition for COST Action FP1206*. Scientific Report. Madri, Spain.
17. Brasseur, G., Kiehl, J.T., Muller, J.F., Schneider, T., Gramier, C., Tie, X. & Hauglustaine, D. (1998). Past and future changes in global tropospheric ozone: Impact on radiative forcing. *Geophysical Research Letter.* 24: 3807– 3810.
18. Bruni Zani, N., Lonati, G., Mead, M.I., Latif, M.T., & Crippa, P. (2020). Long-term satellite-based estimates of air quality and premature mortality in Equatorial Asia through deep neural networks. *Environment Research Letters*. 15: 104088.
19. Carlsen, L., Bruggemann, R. & Kenessov, B. (2018). Use of partial order in environmental pollution studies demonstrated by urban BTEX air pollution in 20 major cities worldwide. *Science of the Total Environment*. 610–611: 234–243.
20. Caser, M., Chitarra, W., D'Angiolillo, F., Perrone, I., Demasi, S., Lovisolo, C. & Scariot, V. (2019). Drought stress adaptation modulates plant secondary metabolite production in Salvia dolomitica Codd. *Industrial crops and products*. 129: 85-96.
21. Carlson, K.M., Curran, L.M., Ratnasari, D., Pittman, A.M., Soares-Filho, B.S., Asner, G.P. & Rodrigues, H.O. (2012). Committed carbon emissions, deforestation, and community land conversion from oil palm plantation expansion in West Kalimantan, Indonesia. *Proceedings of the National Academy of Sciences*. 109(**19**): 7559–7564.
22. Chang, C-P., Wang, Z., McBride, J., & Liu, C. (2005). Annual Cycle of Southeast Asia—Maritime Continent Rainfall and the Asymmetric Monsoon Transition. *Journal of Climate*. 18(**2**): 287-301.
23. Chang, D. & Song, Y. (2010). Estimates of biomass burning emissions in tropical Asia based on satellite-derived data. *Atmospheric Chemistry and Physics*. 10(**5**): 2335–2351.
24. Chang, C. C., Wang, J. L., Lung, S. C. C., Chang, C. Y., Lee, P. J., Chew, C., Liao, W.C., Chen, W.N. & Ou-Yang, C. F. (2014). Seasonal characteristics of biogenic and anthropogenic isoprene in tropical–subtropical urban environments. *Atmospheric Environment*. 99: 298-308.
25. Chen, J, Avise, J., Lamb, B., Salath, E., Mass, C., Guenther, A., Wiedinmyer, C., Lamarque, J.F., O'Neill, S., McKenzie, D. & Larkin, D. (2009). The effects of global changes upon regional ozone pollution in the United States. *Atmospheric Chemistry and Physics.* 9: 1125–1141.
26. Chen, Y. & Zhai, P.M. (2017). Revisiting summertime hot extremes in China during 1961-2015: overlooked compound extremes and significant changes. *Geophysical Research Letters.* 44: 5096-5103.
27. Cherubini, F., Peters, G.P., Berntsen, T., Strømman, A.H., & Hertwich, E. (2011). CO2 emissions from biomass combustion for bioenergy: Atmospheric decay and contribution to global warming. *GCB Bioenergy*. 3(**5**): 413–426.
28. Christensen, J.H., Kanikicharla, K.K., Aldrian, E., An, S.I., Albuquerque Cavalcanti, I.F., de Castro, M., Dong, W., Goswami, P., Hall, A., Kanyanga, J.K., Kitoh, A., Kossin, J., Lau, N. C., Renwick, J., Stephenson, D.B., Xie, S.P., Zhou, T., Abraham, L., Ambrizzi, T & Zou, L. (2013). Climate phenomena and their relevance for future regional climate change. *In Climate Change 2013 the Physical Science Basis: Working Group I Contribution to the Fifth Assessment Report of the Intergovernmental Panel on Climate Change* (Vol. 9781107057999, Cambridge University Press. pp. 1217-1308.
29. Claeys, M., Wang, W., Ion, A. C., Kourtchev, I., Gelencsér, A., & Maenhaut, W. (2004). Formation of secondary organic aerosols from isoprene and its gas-phase oxidation products through reaction with hydrogen peroxide. *Atmospheric Environment*. 38(**25**): 4093-4098.
30. Clarke, L., Edmonds, J., Jacoby, H. Pitcher, H., Reilly, J. & Richels, R. (2007). *Scenarios of Greenhouse Gas Emissions and Atmospheric Concentrations. Sub-report 2.1A of Synthesis and*

Assessment Product 2.1 by the U.S. Climate Change Science Program and the Subcommittee on Global Change Research. Department of Energy. Office of Biological & Environmental Research, Washington, 7 DC., USA. pp. 154.
31. Corley, R.H.V. (2009). How much palm oil do we need? *Environmental Science & Policy*. 12**(2)**: 134-139.
32. Dai, S., Ren, Y., Zuo, S., Lai, C., Li, J., Xie, S., & Chen, B. (2020). Investigating the Uncertainties Propagation Analysis of CO2 Emissions Gridded Maps at the Urban Scale: A Case Study of Jinjiang City, China. *Remote Sensing*. 12(**23**): 3932.
33. Dani, K.G.S., Benavides, A.M.S., Michelozzi, M., Peluso, G., Torzillo, G. & Loreto, F. (2017). Relationship between isoprene emission and photosynthesis in diatoms, and its implications for global marine isoprene estimates. *Marine Chemistry*. 189:17−24.
34. De Swaef, T., & Steppe, K. (2010). Linking stem diameter variations to sap flow, turgor and water potential in tomato. *Functional Plant Biology*. 37(**5**): 429-438.
35. Dentener, F., Stevenson, D., Ellingsen, K., van Noije, T., Schultz, M., Amann, M., Atherton, C., Bell, N., Bergmann, D., Bey, I., Bouwman, L., Butler, T., Cofala, J., Collins, B., Drevet, J., Doherty, R., Eickhout, B., Eskes, H., Fiore, A., Gauss, M., Hauglustaine, D., Horowitz, L., Isaksen, I., Josse, B., Lawrence, M., Krol, M., Lamarque, J.F., Montanaro, V., Müller, J.F., Peuch, V.H., Pitari, G., Pyle, J., Rast, S., Rodriguez, J., Sanderson, M., Savage, N.H., Shindell, D., Strahan, S., Szopa, S., Sudo, K., Van Dingenen, R., Wild, O., Zeng, G.. (2006). The global atmospheric environment for the next generation. *Environmental Science and Technology.* 40:3586-3594.
36. Dimri, A.P., Kumar, D., Choudhary, A. & Maharana, P. (2018). Future changes over the Himalayas: Maximum and minimum temperature. *Global and Planetary Change*. 162: 212-234.
37. Dodla V.B., Desamsetti, S. & Yerramilli, A. (2011). A comparison of HWRF, ARW and NMM models in Hurricane Katrina (2005) simulation. *International Journal of Environmental Research and Public Health*. 8: 2447-2467.
38. Donat, M.G., Lowry, A.L., Alexander, L.V., O'Gorman, P.A. & Maher, N. (2016). More extreme precipitation in the world's dry and wet regions. *Nature Climate Change.* 6: 508–513.
39. Donat, M.G., Angélil, O. & Ukkola, A. M. (2019). Intensification of precipitation extremes in the world's humid and water-limited regions. *Environmental Research Letter*. 14: 065003.
40. Dong, Z., Wang, L., Sun, Y., Hu, T., Limsakul, A., Singhruck, P., & Pimonsree, S. (2021). Heatwaves in Southeast Asia and their changes in a warmer world. *Earth's Future*. *9*(**7**): e2021EF001992.
41. Drechsler, D.M., Garcia, C., Mehadi, A., Nystrom, M., Propper, R., Rake, D., Takemoto, B., VanCuren, T., Webber, W., Ostro, B., Dodge, D. and Lipsett, M. (2004). *Review of the California Ambient Air Quality Standard For Ozone*. Environmental Protection Agency. California.
42. Dreiss, L. M. & Volin, J. C. (2014). *Forests: Temperate Evergreen and Deciduous*. In Wang, Y. (*Eds*). CRC Press. Pp. 214–223.
43. Dunn, R.J H., Alexander, L.V., Donat, M.G., Zhang, X., Bador, M., Herold, N., Lippmann, T., Allan, R., Aguilar, E., Barry, A.A., Brunet, M., Caesar, J., Chagnaud, G., Cheng, V., Cinco, T., Durre, I., de Guzman, R., Htay, T.M., Wan Ibadullah, W.M. & Yussof, M.N.A. (2020). Development of an Updated Global Land In Situ-Based Data Set of Temperature and Precipitation Extremes: HadEX3. *Journal of Geophysical Research: Atmospheres*. 125(**16**): e2019JD032263.
44. Egigu, M.C., Ibrahim, M.A., Riikonen, J., Yahya, A., Holopainen, T., Julkunen-Tiitto, R., & Holopainen, J. K. (2014). Effects of rising temperature on secondary compounds of Yeheb (Cordeauxia edulis Hemsley). *American Journal of Plant Sciences*. 5: 517-527.

45. Engling, G., He, J., Betha, R. & Balasubramanian, R. (2014). Assessing the regional impact of Indonesian biomass burning emissions based on organic molecular tracers and chemical mass balance modelling. *Atmospheric Chemistry and Physics.* 14(**15**): 8043–8054.
46. Erlat, E. & Türkeş, M. (2016). Dates of frost onset, frost end and the frost-free season in Turkey: Trends, variability and links to the North Atlantic and Arctic Oscillation indices, 1950-2013. *Climate Research.* 69: 155-176.
47. Exton, D.A., McGenity, T.J., Steinke, M., Smith, D.J., & Suggett, D.J. (2015). Uncovering the volatile nature of tropical coastal marine ecosystems in a changing world. *Global change biology*. 21(**4**): 1383-1394.
48. Feng, Z., Yuan, X., Fares, S., Loreto, F., Li, P., Hoshika, Y., & Paoletti, E. (2019). Isoprene is more affected by climate drivers than monoterpenes: A meta‐analytic review on plant isoprenoid emissions. *Plant, cell & environment*. 42(**6**): 1939-1949.
49. Flato, G., Marotzke, J., Abiodun, B., Braconnot, P., Chou, S.C., Collins, W., Cox, P., Driouech, F., Emori, S., Eyring, V., Forest, C., Gleckler, P., Guilyardi, E., Jakob, C., Kattsov, V., Reason, C. & Rummukainen, M. (2013). In Stocker, T.F., Qin, D., Plattner, G.-K., Tignor, M., Allen, S.K., Doschung, J., Nauels, A., Xia, Y., Bex, V., & Midgley, P.M. (Eds) Evaluation of climate models. *In Climate Change 2013: The Physical Science Basis. Contribution of Working Group I to the Fifth Assessment Report of the Intergovernmental Panel on Climate Change*. Cambridge University Press, pp. 741-882.
50. Field, R.D. & Shen, S.S.P. (2008). Predictability of carbon emissions from biomass burning in Indonesia from 1997 to 2006. *Journal of Geophysical Research: Biogeosciences.* 113: G4000694.
51. Field, R.D., van der Werf, G.R. & Shen S.S. (2009). Human amplification of drought-induced biomass burning in Indonesia since 1960. *Natural Geoscience.* 2: 185–188.
52. Fitzky, A.C., Sandén, H., Karl, T., Fares, S., Calfapietra, C., Grote, R., Saunier, A. & Rewald, B. (2019). The interplay between ozone and urban vegetation—BVOC emissions, ozone deposition, and tree ecophysiology. *Frontiers in Forests and Global Change*. 2: 50.
53. Flynn, C.M. & Mauritsen, T. (2020). On the climate sensitivity and historical warming evolution in recent coupled model ensembles. *Atmospheric Chemistry and Physics.* 20: 7829-7842.
54. Forster, P., Ramaswamy, V., Artaxo, P., Berntsen, T., Betts, R., Fahey, D. W., Haywood, J., Lean, J., Lowe, D. C., et al. (2007). Changes in atmospheric constituents and radiative forcing, in: Climate Change 2007: *The Physical Science Basis, contribution of Working Group I to the Fourth Assesment Report of the Intergovernmental Panel on Climate Change*. In Solomon, S., Qin, D., Manning, M., Chen, Z., Marquis, M., Averyt, K. B., Tignor, M., and Miller, H. L. (Eds). Cambridge University Press, Cambridge, UK.
55. Fujino, J., Nair, R., Kainuma, M., Masui, T. & Matsuoka, Y. (2006). Multi-gas mitigation analysis on stabilization scenarios using AIM global model: Multigas Mitigation and Climate Policy. *The Energy Journal*. 3: 343-354.
56. Gao, Y., Fu, J.S., Drake, J.B., Lamarque, J.F. and Liu, Y. (2013). The impact of emission and climate change on ozone in the United States under representative concentration pathways (RCPs). *Atmospheric Chemistry and Physics.* 13: 9607–9621.
57. Gaveau, D.L., Sheil, D., Salim, M.A., Arjasakusuma, S., Ancrenaz, M., Pacheco, P., & Meijaard, E. (2016). Rapid conversions and avoided deforestation: examining four decades of industrial plantation expansion in Borneo. *Scientific reports*. 6(**1**): 1-13.
58. Gaveau, D.L.A *et al.,* (2014). Major atmospheric emissions from peat fires in Southeast Asia during non-drought years: evidence form the 2013 Sumatran fires *Science Report.* 4: 6112.

59. Ge, F., Zhu, S., Peng, T., Sielamm, F., Fraedrich, K., Zhi, X., Liu, X., Tang, W. & Ji, L. (2019). Risk of precipitation extremes over Southeast Asia: does 1.5℃ or 2.0℃ global warming make a difference? *Environmental Research*. 14: 44015.
60. Ge, F., Zhu, S., Luo, H., Zhi, X., & Wang, H. (2021). Future changes in precipitation extremes over Southeast Asia: Insights from CMIP6 multi-model ensemble. *Environmental Research Letters.* 16: 024013.
61. Geron, C., Owen, S., Guenther, A., Greenberg, J., Rasmussen, R., Bai, J. H., Li, Q.J. & Baker, B. (2006). Volatile organic compounds from vegetation in southern Yunnan Province, China: Emission rates and some potential regional implications. *Atmospheric Environment*. 40(**10**): 1759-1773.
62. Givnish, T.J. (2002). Adaptive significance of Evergreen vs. Deciduous Leaves: Solving the triple paradox. *Silva Fennica*. 36(**3**): 703-743.
63. Golaz, J.-C., Caldwell, P.M., Van Roekel, L.P., Petersen, M.R., Tang, Q., Wolfe, J. D., et al. (2019). The DOE E3SM coupled model version 1: Overview and evaluation at standard resolution. *Journal of Advances in Modelling Earth Systems.* 11: 2089-2129.
64. Griffin, R.J., Cocker, D.R., Seinfeld, J.H., & Dabdub, D. (1999). Estimate of global atmospheric organic aerosol from oxidation of biogenic hydrocarbons. *Geophysical research letters.* 26(**17**): 2721-2724.
65. Guenther, A., Hewitt, C. N., Erickson, D., Fall, R., Geron, C., Graedel, T., Harley, P., Klinger, L., Lerdau, M., McKay, W.A. & Pierce, T. (1995). A global model of natural volatile organic compound emissions. *Journal of Geophysical Research: Atmospheres*. 100(**D5**): 8873-8892
66. Guenther, A., Karl, T., Harley, P., Wiedinmyer, C., Palmer, P.I. & Geron, C. (2006). Estimates of global terrestrial isoprene emission using MEGAN (model of emissions of gases and aerosols from nature. *Atmospheric Chemistry and Physics.* 6(**11**): 3181-3210.
67. Guenther, A.B., Jiang, X., Heald, C.L., Sakulyanontvittaya, T., Duhl, T., Emmons, L.K., & Wang, X. (2012). The Model of Emissions of Gases and Aerosols from Nature version 2.1 (MEGAN2. 1): an extended and updated framework for modeling biogenic emissions. *Geoscientific Model Development*. 5(**6**): 1471-1492.
68. Gupta, M.K., Sharif, M. & Shulka, S.S. (2021). Spatio-temporal analysis of temperature projections based on representative concentration pathways for Sutlej River Basin, India. *Cogent Engineering*. 8: 1933683.
69. Gunarso, P., Hartoyo, M.E., Agus, Fahmuddin. & Killeen, T.J. (2013). *Oil palm and land use change in Indonesia, Malaysia and Papua New Guinea.* Reports from the technical panels of the 2nd greenhouse gas working group of the Roundtable Sustainable Palm Oil (RSPO). Pp: 29-63.
70. Hallquist, M., Wenger, J. C., Baltensperger, U., Rudich, Y., Simpson, D., Claeys, M., Dommen, J., Donahue, N.M., George, C., Goldstein, A.H. & Hamilton, J.F. (2009). The formation, properties and impact of secondary organic aerosol: current and emerging issues. *Atmospheric chemistry and physics*. 9(**14**): 5155-5236.
71. Hamid, H. A., Hazman, M. H. M., Nadzir, M. S. M., Uning, R., Latif, M. T., & Kannan, N. (2019). Anthropogenic and biogenic volatile organic compounds and ozone formation potential in ambient air of Kuala Lumpur, Malaysia. In IOP Conference Series: *Earth and Environmental Science.* 228: 12001.
72. Hantson, S., Knorr, W., Schurgers, G., Pugh, T. A., & Arneth, A. (2017). Global isoprene and monoterpene emissions under changing climate, vegetation, CO2 and land use. *Atmospheric Environment*, *155*: 35-45.

73. Harrison, S.P., Morfopoulos, C., Dani, K.S., Prentice, I.C., Arneth, A., Atwell, B.J., Barkley, M.P., Leishman, M.R., Loreto, F., Medlyn, B.E. & Niinemets, Ü. (2013). Volatile isoprenoid emissions from plastid to planet. *New Phytologist*. 197(**1**): 49-57.
74. Hauglustaine, D.A., Hourdin, F., Jourdain, L., Filiberti, M.A., Walters, S., Lamarque, J.F., & Holland, E.A. (2004). Composition and Chemistry-D04314. Interactive chemistry in the Laboratoire de M6t6orologie Dynamique general circulation model: Description and background tropospheric chemistry evaluation. *Journal of Geophysical Research-Atmospheres*. 109(4).
75. Haywood, J. & Boucher, O. (2000). Estimates of the direct and indirect radiative forcing due to tropospheric aerosols: A review. *Reviews of geophysics*. 38(**4**): 513-543.
76. Held, I.M. & Soden, B.J. (2006) Robust responses of the hydrological cycle to global warming *Journal of Climate*. 19: 5686–5699.
77. Hewitt, C.N., MacKenzie, A.R., Di Carlo, P., Di Marco, C.F., Dorsey, J.R., Evans, M., et al. (2009). Nitrogen management is essential to prevent tropical oil palm plantations from causing ground-level ozone pollution. *Proceedings of the National Academy of Sciences of the United States of America*. 106(**44**): 18447–18451.
78. Hidayat, R & Kizu, S. (2010) Influence of the Madden–Julian Oscillation on Indonesian rainfall variability in austral summer. *International Journal of Climatology*. 30: 1816–1825.
79. Hijioka, Y., Matsuoka, Y., Nishimoto, H., Masui, M. & Kainuma, M. (2008). Global GHG emissions scenarios under GHG concentration stabilization targets. *Journal of Global Environmental Engineering*. 13: 97-108.
80. Hijioka. Y., Lasco. R., Surjan A. & Pereira, J. (2014). *Asia. In: Climate change 2014: impacts, adaptation, and vulnerability. Part B Regional aspects. Contribution of working group II to the Fifth Assessment Report of the IPCC*. Cambridge University Press, Cambridge.
81. Hirota, M., Holmgren, M., Van Nes, E. H., & Scheffer, M. (2011). Global Resilience of Tropical Forest and Savanna to Critical Transitions. *Science*. 334(**6053**): 232–235. https://doi.org/10.1126/science.1210657.
82. Holopainen, J.K., Virjamo, V., Ghimire, R.P., Blande, J.D., Julkunen-Tiitto, R., & Kivimäenpää, M. (2018). Climate change effects on secondary compounds of forest trees in the northern hemisphere. *Frontiers in plant science*. 9: 1445.
83. Hrebien, V., Deschaseaux, E. & Eyre, B.D. (2021). Isoprene fluxes from warm temperate and tropical seagrass communities. *Marine ecology progress series*. 676: 1-17.
84. Hu, L., Millet, D.B., Baasandorj, M., Griffis, T.J., Turner, P., Helmig, D., Curtis, A.J. & Hueber, J. (2015). Isoprene emissions and impacts over an ecological transition region in the US Upper Midwest inferred from tall tower measurements. *Journal of Geophysical Research*: *Atmospheres*. 120(**8**): 3553-3571.
85. Huang, W., Wang, S., Yen, M., Lin, N., & Promchote, P. (2016). Interannual variation of springtime biomass burning in Indochina: Regional differences, associated atmospheric dynamical changes, and downwind impacts. *Journal of Geophysical Research. Atmospheres*. 121(**17**): 10016–10028.
86. Huang, J., Hartmann, H., Hellén, H., Wisthaler, A., Perreca, E., Weinhold, A., Rücker, A., van Dam, N.M., Gershenzon, J., Trumbore, S. & Behrendt, T. (2018). New perspectives on CO2, temperature, and light effects on BVOC emissions using online measurements by PTR-MS and cavity ring-down spectroscopy. *Environmental science & technology*. 52(**23**): 13811-13823.
87. Huang, L., Lin, W., Li, F., Wang, Y., & Jiang, B. (2019). Climate Impacts of the Biomass Burning in Indochina on Atmospheric Conditions over Southern China. *Aerosol and Air Quality Research*. 9(**12**): 2707–2720.
88. Hungerford, R. D., Harrington, M. G., Frandsen, W. H., Ryan, K. C., & Niehoff, G. J. (1990).

Influence of fire on factors that affect site productivity. *Proceedings - Management and Productivity of Western-Montane Forest Soils*, 10–12.
89. Hurrell, J.W., Holland, M.M., Gent, P.R., Ghan, S., Kay, J.E., Kushner, P.J., Lamarque, J.F., Large, W.G., Lawrence, D.M., Lindsay, K., Lipscomb, W.H., Long, M.C., Mahowald, N., Marsh, D.R., Neale, R.B., Rasch, P., Vavrus, S., Vertenstein, M., Bader, D., Collins, W.D., Hack, J.J., Kiehl, J.T. & Marshall, S. (2013). The Community Earth System Model: A framework for collaborative research. *Bulletin of the American Meteorological Society.* 94: 1339-1360.
90. Imada, Y., Maeda, S., Watanabe, M., Shiogama, H., Mizuta, R., Ishii, M. & Kimoto, M. (2017). Recent Enhanced Seasonal Temperature Contrast in Japan from Large Ensemble High-Resolution Climate Simulations. *Atmosphere.* 8(**3**): 57.
91. IPCC (Intergovernmental Panel on Climate Change). (2001). *Climate change 2001: the scientific basis – contribution of Working Group I to the third Assessment Report of the Intergovernmental Panel on Climate Change*. Cambridge University Press, Cambridge.
92. IPCC, (2013). Climate change 2013: The physical science basis. *Contribution of Working Group I to the Fifth Assessment Report of the Intergovernmental Panel on Climate Change*. Cambridge University Press, Cambridge, UK and New York, NY.
93. IPCC, (2014). Climate Change 2014. *Contribution of Working Groups I, II and III to the Fifth Assessment Report of the Intergovernmental Panel on Climate Change*. In Hiegh-Guldberg, O., Sharina, A.H., Bindi, M., Liverman, D., singh, C., Warren, R., Zhou, G. (eds.). Geneva, Switzerland. Pp: 238-267.
94. IPCC, (2018). Global warming of 1.5°C. *An IPCC Special Report on the impacts of global warming of 1.5°C above pre-industrial levels and related global greenhouse gas emission pathways, in the context of strengthening the global response to the threat of climate change, sustainable development, and efforts to eradicate poverty* [Masson-Delmotte, V., Zhai, P., Pörtner, H.O., Roberts, D., Skea, J., Shukla, P.R., Pirani, A., Moufouma-Okia, W., Péan, C., Pidcock, R., Connors, S., Matthews, J.B.R., Chen, Y., Zhou, X., Gomis, M.I., Lonnoy, E., Maycock, T., Tignor, M. & Waterfield, T. (eds.) Cambridge University Press, Cambridge.
95. IPCC, (2021). *Climate Change 2021: The Physical Science Basis. Contribution of Working Group I to the Sixth Assessment Report of the Intergovernmental Panel on Climate Change* [Masson-Delmotte, V., P. Zhai, A. Pirani, S.L. Connors, C. Péan, S. Berger, N. Caud, Y. Chen, L. Goldfarb, M.I. Gomis, M. Huang, K. Leitzell, E. Lonnoy, J.B.R. Matthews, T.K. Maycock, T. Waterfield, O. Yelekçi, R. Yu, & B. Zhou (eds.). Cambridge University Press. Cambridge.
96. Jardine, K.J., Jardine, A.B., Souza, V.F., Carneiro, V., Ceron, J.V., Gimenez, B.O., Soares, C.P., Durgante, F.M., Higuchi, N., Manzi, A.O. & Gonçalves, J.F. (2016). Methanol and isoprene emissions from the fast growing tropical pioneer species Vismia guianensis (Aubl.) Pers. (Hypericaceae) in the central Amazon Forest. *Atmospheric Chemistry and Physics*. 16(**10**): 6441-6452.
97. Jardine, K., Chambers, J., Alves, E.G., Teixeira, A., Garcia, S., Holm, J., Higuchi, N., Manzi, A., Abrell, L., Fuentes, J.D. & Nielsen, L.K. (2014). Dynamic balancing of isoprene carbon sources reflects photosynthetic and photorespiratory responses to temperature stress. *Plant physiology*. 166(**4**): 2051-2064.
98. Jayachandran, S. (2009). Air quality and early-life mortality evidence from Indonesia's wildfires. *Journal of Human Resources*. 44: 916–954.
99. Jiang, X., Guenther, A., Potosnak, M., Geron, C., Seco, R., Karl, T., Kim, S., Gu, L. & Pallardy, S. (2018). Isoprene emission response to drought and the impact on global atmospheric chemistry. *Atmospheric Environment*. 183: 69-83.

100. Johnson, C.E., Stevenson, D.S., Collins, W.J. & Derwent, R.G. (2001). Role of climate feedback on methane and ozone studies with a coupled ocean-atmosphere-chemistry model. *Geophysical Research Letter.* 28: 1723–1726.

101. Juárez-Orozco, S. M., Siebe, C. & Fernández Fernández, D. (2017). Causes and Effects of Forest Fires in Tropical Rainforests: A Bibliometric Approach. *Tropical Conservation Science.* 10: 194008291773720.

102. Kanakidou, M., Seinfeld, J. H., Pandis, S. N., Barnes, I., Dentener, F. J., Facchini, M. C., Dingenen, R.V., Ervens, B., Nenes, A.N.C.J.S.E., Nielsen, C.J. & Swietlicki, E. (2005). Organic aerosol and global climate modelling: a review. *Atmospheric Chemistry and Physics*. 5(**4**): 1053-1123.

103. Kang, S., Im, E-S. & Eltahir, E.A.B. (2019). Future climate change enhances rainfall seasonality in a regional model of western Maritime Continent. *Climate Dynamics*. 52: 747–764.

104. Karl, M., Brauers, T., Dorn, H.P., Holland, F., Komenda, M., Poppe, D., Rohrer, F., Rupp, L., Schaub, A. & Wahner, A. (2004). Kinetic Study of the OH‐isoprene and O3‐isoprene reaction in the atmosphere simulation chamber, SAPHIR. *Geophysical research letters*. 31(**5**).

105. Kaul, H. & Sopan, I. (2012). Land use land cover classification and change detection using high resolution temporal satellite data. *The Journal of Environment*. 1: 146–162.

106. Kawase, H., Nagashima, T., Sudo, K. &Nozawa, T. (2011). Future changes in tropospheric ozone under Representative Concentration Pathways (RCPs). *Geophysical Research Letter.* 38: L05801.

107. Kim, M.J., Park, R.J, Ho, C.H, Woo, J.H., Choi, K.C, Song, C.K. & Lee, J.B. (2015). Future ozone and oxidants change under the RCP scenarios. *Atmospheric Environment.* 101**:**103-115.

108. Kim, D., Kim, H. & Lee, M-I. (2017). Why does the MJO detour the Maritime Continent during austral summer? *Geophysical Research Letter*. 44: 2579–2587.

109. Kim Oanh, N.T., Permadi, D.A., Hopke, P.K., Smith, K.R., Dong, N.P. & Dang, A.N. (2018). Annual emissions of air toxics emitted from crop residue open burning in Southeast Asia over the period of 2010–2015. *Atmospheric Environment.* 187: 163–173.

110. Klinger, L.F., Li, Q.J., Guenther, A.B., Greenberg, J.P., Baker, B. & Bai, J.H. (2002). Assessment of volatile organic compound emissions from ecosystems of China. *Journal of Geophysical Research: Atmospheres*. 107(D21): ACH-16.

111. Knutti, R. & Sedlacek, J. (2013). Robustness and uncertainties in the new CMIP5 climate model projections. *Natural Climate Change.* 3: 369-373.

112. Knutti, R., Masson, D. & Gettelman, A. (2013). Climate model genealogy: Generation CMIP5 and how we got there. *Geophysical Research Letter.* 40: 1194-1199.

113. Kripalani, R.H., & Kulkarni, A. (1997). Climatic impact of El Nino/La Nina on the Indian monsoon: A new perspective. *Weather.* 52(**2**): 39-46.

114. Lahr, E.C., Schade, G.W., Crossett, C.C., & Watson, M.R. (2015). Photosynthesis and isoprene emission from trees along an urban–rural gradient in Texas. *Global Change Biology*. 21(**11**): 4221-4236.

115. Lamsal, S., Rizzo, D.M. & Meentemeyer, R.K. (2012). Spatial variation and prediction of forest biomass in a heterogeneous landscape. *Journal of Forestry Research.* 23**(1**): 13–22

116. Langner, A. & Siegert, F. (2009). Spatiotemporal fire occurrence in Borneo over a period of 10 years. *Global Change Biology.* 15(**1**): 48–62.

117. Langner, J., Engardt, M. & Andersson, C. (2012). European summer surface ozone 1990–2100. *Atmospheric Chemistry and Physics Discussion.* 12: 7705–7726.

118. Langston, J.D., Riggs, R.A., Sururi, Y., Sunderland, T. & Munawir, M. (2017). Estate crops more attractive than community forests in West Kalimantan. *Indonesia. Land* 6: 12.

119. Lathiere, J., Huglustaine, D.A., Noblet-Ducoudre, N., Krinner, G. & Folberth, G.A. 2005. Past and future changes in biogenic volatile organic compound emission simulated with a global dynamic vegetation model. *Geophysical Research Letter*. 32: L20818.

120. Latif, M.T., Lim, S.H. & Juneng, L. (2012). Variations of surface ozone concentration across the Klang Valley, Malaysia. *Atmospheric Environment.* 61: 434-445.

121. Lasslop, G. & Kloster, S. (2015). Impact of fuel variability on wildfire emission estimates. *Atmospheric Environment.* 121: 93–102.

122. Lantz, A.T., Allman, J., Weraduwage, S.M., & Sharkey, T.D. (2019). Isoprene: New insights into the control of emission and mediation of stress tolerance by gene expression. *Plant, Cell & Environment.* 42(**10**): 2808-2826.

123. Lelieveld, J., Gromov, S., Pozzer, A. & Taraborrelli, D. (2016). Global tropospheric hydroxyl distribution, budget and reactivity. *Atmospheric Chemistry & Physics*. 16: 12477–12493.

124. Lehmann, C.E.R., Anderson, T.M., Sankaran, M., Higgins, S.I., Archibald, S., Hoffmann, W.A., Hanan, N.P., Williams, R.J., Fensham, R.J., Felfili, J., Hutley, L.B., Ratnam, J., San Jose, J., Montes, R., Franklin, D., Russell-Smith, J., Ryan, C.M., Durigan, G., Hiernaux, P., & Haidar, R. (2014). Savanna Vegetation-Fire-Climate Relationships Differ Among Continents. *Science*. 34 (**6170**): 548–552.

125. Li, L.Y., & Xie, S.D. (2014). Historical variations of biogenic volatile organic compound emission inventories in China, 1981–2003. *Atmospheric environment*. 95: 185-196.

126. Liu, L. & Mishchenko, M. (2018). Scattering and Radiative Properties of Morphologically Complex Carbonaceous Aerosols: A Systematic Modeling Study. *Remote Sensing.* 10(**10**): 1634.

127. Liu, Mingliang & Rajagopalan, Kirti & Chung, Serena & Jiang, X. & Harrison, John & Nergui, Tsengel & Guenther, Alex & Miller, C. & Reyes, Julian & Tague, Christina & Choate, J. & Salathé, Eric & Stockle, Claudio & Adam, J. (2014). What is the importance of climate model bias when projecting the impacts of climate change on land surface processes? *Biogeosciences*. 112601.

128. Loo, Y. Y., Billa, L., & Singh, A. (2015). Effect of climate change on seasonal monsoon in Asia and its impact on the variability of monsoon rainfall in Southeast Asia. *Geoscience Frontiers,* 6(**6**): 817-823.

129. Loreto, F. & Fineschi, S. (2015). Reconciling functions and evolution of isoprene emission in higher plants. *New Phytologist*. 206(**2**): 578-582.

130. Lu, L., Kuenzer, C., Guo, H., Li, Q., Long, T., & Li, X. (2014). A Novel Land Cover Classification Map Based on a MODIS Time-Series in Xinjiang, China. *Remote Sensing.* 6(**4**): 3387–3408.

131. Lun, X., Lin, Y., Chai, F., Fan, C,m Li, H. & Liu, J. (2020). Reviews of emission of biogenic volatile organic compounds (BVOCs) in Asia. *Journal of Environmental Sciences.* 95: 266-277.

132. Manomaiphiboon. K., Octaviani. M., Torsri. K. & Towprayoon, S. (2013). Projected changes in means and extremes of temperature and precipitation over Thailand under three future emissions scenarios. *Climate Research*. 58: 97–115.

133. Marengo, J. A., Jones, R., Alves, L. M., & Valverde, M. C. (2009). Future change of temperature and precipitation extremes in South America as derived from the PRECIS regional

climate modeling system. International Journal of Climatology: *A Journal of the Royal Meteorological Society*. 29(**15**): 2241-2255.

134. Marengo, J.A., Liebmann, B., Grimm, A.M., Misra, V., Silva Dias, P.L., Cavalcanti, I.F.A., Carvalho, L.M.V., Berbery, E.H., Ambrizzi, T., Vera, C.S., Saulo, A.C., Nogues-Paegle, J., Zipser, E., Seth, A. and Alves, L.M. (2012). Recent developments on the South American monsoon system. *International. Journal of Climatology*, 32: 1-21.

135. Masui, T., Matsumoto, K., Hijioka, Y., Kinoshita, T., Nozawa,T., Ishiwatari,S., Kato, E., Shukla, P. R., Yamagata, Y. & Kainuma, M. (2011). An emission pathway for stabilization at 6 Wm-2 radiative forcing. *Climate Change.* 109: 59-76.

136. Meleux, F., Solmon, F. & Giorgi, F. (2007). Increase in Summer Europe Ozone Amounts due to Climate Change. *Atmospheric Environment.* 41: 7577-7587.

137. Meeningen, Y.V., Schurgers, G., Rinnan, R., & Holst, T. (2016). BVOC emissions from English oak (Quercus robur) and European beech (Fagus sylvatica) along a latitudinal gradient. *Biogeosciences*. 13(**21**): 6067-6080.

138. Meeningen, Y.V., Schurgers, G., Rinnan, R., & Holst, T. (2017). Isoprenoid emission response to changing light conditions of English oak, European beech and Norway spruce. *Biogeosciences*. 14(**18**): 4045-4060.

139. Miettinen, J., Stibig, H.-J., & Achard, F. (2014). Remote sensing of forest degradation in Southeast Asia—Aiming for a regional view through 5–30 m satellite data. *Global Ecology and Conservation*. ***2***: 24–36.

140. Mishra, A.K., & Sinha, V. (2020). Emission drivers and variability of ambient isoprene, formaldehyde and acetaldehyde in north-west India during monsoon season. *Environmental Pollution*. 267: 115538.

141. MMD (Malaysian Meteorological Department), (2013). *Monsoon*. Online Retrieved February 17, 2020 from:http://www.met.gov.my/index.php?option=com_content&task=view&id=69&Itemid=160&lang=english

142. Monks, P.S. (2005). Gas-phase radical chemistry in the troposphere. Chemistry Society Review. 34: 376–395.

143. Monson, R. K., Trahan, N., Rosenstiel, T. N., Veres, P., Moore, D., Wilkinson, M., Norby, R.J., Volder, A., Tjoelker, M.G., Briske, D.D. & Karnosky, D.F. (2007). Isoprene emission from terrestrial ecosystems in response to global change: minding the gap between models and observations. *Philosophical Transactions of the Royal Society A: Mathematical, Physical and Engineering Sciences*. 365(**1856**): 1677-1695.

144. Monson, R.K., Grote, R., Niinemets, Ü., & Schnitzler, J.P. (2012). Modeling the isoprene emission rate from leaves. *New Phytologist*. 195(**3**): 541-559.

145. Moran, J., NaSuwan, C., & Poocharoen, O.-O. (2019). The haze problem in northern Thailand and policies to combat it: A review. *Environmental Science & Policy*. 97, 1–15.

146. Murazaki, K. & Hess, P. (2006). How does climate change contribute to surface ozone change over the United States? *Journal of Geophysical Research.* 111: D05301.

147. Mutanda, I., Inafuku, M., Saitoh, S., Iwasaki, H., Fukuta, M., Watanabe, K., & Oku, H. (2016). Temperature controls on the basal emission rate of isoprene in a tropical tree Ficus

septica: exploring molecular regulatory mechanisms. *Plant, cell & environment*. 39(**10**): 2260-2275.

148. Nazarenko, L., Schmidt, G. A., Miller, R. L., Tausnev, N., Kelley, M., Ruedy, R., Russell, G. et al.,. (2015). Future climate change under RCP emission scenarios with GISS ModelE2. *Journal of Advances in Modelling Earth Systems*. 7: 244-267.
149. NCEP (National Centers for Environmental Prediction/National Weather Service/NOAA/U.S. Department of Commerce, 1994: updated monthly. (2015). NCEP/NCAR Global Reanalysis Products, 1948-continuing. Research Data Archive at the National Center for Atmospheric Research, Computational and Information Systems Laboratory. https://rda.ucar.edu/datasets/ds090.0/. Accessed 05 May 2015
150. Ngo-Duc, T., Kieu, C., Thatcher, M., Nguyen-Le, D. & Phan-Van, T. (2014). Climate projections for Vietnam based on regional climate models. *Climate Research*. 60: 199–213.
151. Nguyen, G.T.H., Shimadera, H., Uranishi, K., Matsuo, T. & Kondo, A. (2019). Numerical assessment of PM2.5 and O3 air quality in continental Southeast Asia: Impact of potential future climate change. *Atmospheric Environment*. 215: 116901.
152. Norris, J., Chen, G. & Neelin, J.D. (2019). Thermodynamic versus dynamic controls on extreme precipitation in a warming climate from the community earth system model large ensemble. *Journal of Climate*. 32: 1025–1045.
153. Oda, T., Bun, R., Kinakh, V., Topylko, P., Halushchak, M., Marland, G., Lauvaux, T., Jonas, M., Maksyutov, S., Nahorski, Z., Lesiv, M., Danylo, O., & Horabik-Pyzel, J. (2019). Errors and uncertainties in a gridded carbon dioxide emissions inventory. *Mitigation and Adaptation Strategies for Global Change*. 24(**6**): 1007–1050.
154. Ojha, S. & Kumar, A. (2010). A Pilot Study to Develop Forecasting Models for Predicting Hourly Ozone Concentration near Cincinnati, Ohio. *Advances in Environmental Research*, Vol. 8. Nova Science Publishers.
155. Ohja, N., Merlin, O., Amazirh, A., Quaadi, N., Rivalland, V., Jarlan, L., Er-Rake, S. & Escorihuela, M.J. (2021). A calibration/Disaggregation Coupling Scheme for retrieving soil moisture at high spatio-temporal resolution: synergy between SMAP passive microwave, MODIS/Landsat Optical/Thermal and Sentinel-1 radar data. *Sensor*. 21: 7406.
156. Oku, H., Inafuku, M., Takamine, T., Nagamine, M., Saitoh, S., & Fukuta, M. (2014). Temperature threshold of isoprene emission from tropical trees, Ficus virgata and Ficus septica. *Chemosphere*. 95: 268-273.
157. Ooi, M.C.G., Harris, N.R., Bolas, C., Bran, S.H., Macatangay, R.C., Chan, A., Teh, YA., Jaafar, W.S.W.M., Yusup, Y., Latif, M.T. & Khan, M.F. (2020). Driving Factors for Isoprene-Surface Ozone and Carbon Dioxide Chemistry Over an Oil Palm plantation in Malaysia.
158. Overland, J. E., Ballinger, T. J., Cohen, J., Francis, J. A., Hanna, E., Jaiser, R., Kim, B.M., Kim, S.J., Ukita, J., Vihma, T., Wang, M. & Zhang, X. (2021). How do intermittency and simultaneous processes obfuscate the Arctic influence on midlatitude winter extreme weather events?. *Environmental Research Letters*. 16(**4**): 043002
159. Palmer, T.N. & Stevens, B. (2019). The scientific challenge of understanding and estimating climate change. *Proceedings of the National Academy of Sciences of the United States of America.* 116: 24390-24395.
160. Pacifico, F., Harrison, S.P., Jones, C.D., & Sitch, S. (2009). Isoprene emissions and climate. *Atmospheric Environment*. 43(**39**): 6121-6135.
161. Penrod, A., Zhang, Y., Wang, K., Wu, S. Y., & Leung, L. R. (2014). Impacts of future climate and emission changes on US air quality. *Atmospheric Environment*. 89: 533-547.

162. Pfister, G.G., Walters, S., Lamarque, J.F., Fast, J., Barth, M.C., Wong, J., Done, J., Holland, G. & Bruyère., C.L. (2014). *Journal of Geophysical Research: Atmospheres.* 119: 5559–5582.

163. Pittman, A.M., Carlson, K.M., Curran, L.M. & Ponette-González, A. (2013) NASA satellite data used to study the impact of oil palm expansion across Indonesian Borneo *Earth Obervations*. 25: 12–15.

164. Ponette-González, A.G., Curran, L.M., Pittman, A.M., Carlson, K.M., Steel, B.G., Ratnasary, D., Mujiman, C.W. Kathleen C.W. (2016). Biomass burning dirves atmospheric nutrient redistribution within forested peatlands in Borneo. *Environmental Research Letter*. 11: 085003.

165. Possell, M., & Hewitt, C.N. (2011). Isoprene emissions from plants are mediated by atmospheric CO2 concentrations. *Global Change Biology*. 17(**4**): 1595-1610.

166. Potosnak, M. J., LeStourgeon, L. & Nunez, O. (2014). Increasing leaf temperature reduces the suppression of isoprene emission by elevated CO2 concentration. *Science of the Total Environment*. 481: 352-359.

167. Pugh, T.A.M., Ashworth, K., Wild, O., & Hewitt, C.N. (2013). Effects of the spatial resolution of climate data on estimates of biogenic isoprene emissions. *Atmospheric Environment.* 70: 1-6.

168. Purnomo, H., Okarda, B., Dermawan, A., Ilham, Q.P., Pacheco, P., Nurfatriani, F. & Suhendang, E. (2020). Reconciling oil palm economic development and environmental conservation in Indonesia: A value chain dynamic approach. *Forest Policy and Economics.* 111: 102089.

169. Querol, X., Gangoiti, G., Mantilla, E., Alastuey, A., Minguillón, M. C., Amato, F., Reche, C., Viana, M., et al. (2017). Phenomenology of high-ozone episodes in NE Spain. *Atmospheric Chemistry & Physics*. 17: 2817–2838.

170. Qian, C., Zhang, X., & Li, Z. (2019). Linear Trends in Temperature Extremes in China, with an Emphasis on Non-gaussian and Serially Dependent Characteristics. *Climate Dynamics. 53*(**1**): 533–550.

171. Racherla, P.N. & Adams, P.J. (2008). The Response of Surface Ozone to Climate Change over the Eastern United States. *Atmospheric Chemistry and Physics.* 8:871-885.

172. Raghavan, S.V., Vu, M.T. & Liong, S.Y. (2017). Ensemble climate projections of mean and extreme rainfall over Vietnam. *Global Planet Change*. 148: 96–104.

173. Rahman, S.R.A., Ismail, S.N.S., Raml, M.F., Latif, M.T., Abidin, E.Z., & Praveena, S.M. (2015). The assessment of ambient air pollution trend in Klang Valley, Malaysia. *World Environment. 5*(**1**): 1-11.

174. Rahimi, M. & Hejabi, S. (2018) Spatial and Temporal Analysis of Trends in Extreme Temperature Indices in Iran over the Period 1960-2014. *International Journal of Climatology.* 38: 272-282.

175. Rahimi-Moghaddam, Sajjad & Kambouzia, Jafar & Deihimfard, Reza. (2018). Adaptation strategies to lessen negative impact of climate change on grain maize under hot climatic conditions: A model-based assessment. *Agricultural and Forest Meteorology.* 253: 1-14.

176. Randerson, J.T., Chen, Y., Van der Werf, G.R., Rogers, B. M. & Morton, D.C. (2012). Global burned area and biomass burning emissions from small fires. *Journal of Geophysical Research: Biogeosciences.* 117: G04012.

177. Rao, S. & Riahi, K. (2006). The role of non-CO2 greenhouse gases in climate change mitigation: Long-term scenarios for the 21st century: Multigas mitigation and climate policy. *The Energy Journal*. 3: 177-200.
178. Rasulov, B., Talts, E., Bichele, I., & Niinemets, Ü. (2018). Evidence that isoprene emission is not limited by cytosolic metabolites. Exogenous malate does not invert the reverse sensitivity of isoprene emission to high [CO2]. *Plant physiology*. 176(**2**): 1573-1586.
179. Ratnam, J., Tomlinson, K.W., Rasquinha, D.N., & Sankaran, M. (2016). Savannahs of Asia: antiquity, biogeography, and an uncertain future. *Philosophical Transactions of the Royal Society B: Biological Sciences*. 371(**1703**): 20150305.
180. Reddington, C.L., Conibear, L., Robinson, S., Knote, C., Arnold, S.R. & Spracklen, D.V. (2021). Air pollution from forest and vegetation forest in Southeast Asea disproportionately impact the poor. *Geohealth*. 5(**9**): 2021GH000418.
181. Riahi, K., Gruebler, A. & Nakicenovic, N. 2007. Scenarios of long-term socio-economic and environmental development under climate stabilization. *Technological Forecasting and Social Change*. 74(**7**): 887-935.
182. Riahi, R.S., Runci, P., Stouffer, R., van Vuuren, D., Weyant, J., Wilbanks, T., van Ypersele, J.P. & Zurek, M. (2008). Towards New Scenarios for Analysis of Emissions, Climate Change, Impacts, and Response Strategies. *Intergovernmental Panel on Climate Change*, *Geneva*, p. 132.
183. Riahi, K., Rao, S., Krey, V., Cho, C., Chirkov, V., Fischer, G., kindermann, G. & Nakicenovic, N. (2011). RCP8.5 – A scenario of comparatively high greenhouse gas emissions. *Climatic Change*. 109: 33-57.
184. Rife, D.L., Pinto, J.O., Monaghan, A.J., Davis, C.A. & Hannan, J.R. (2014). NCAR global climate four-dimensional data assimilation (CFDDA) hourly 40 km reanalysis. Research of Data architecture, National Center, Atmospheric Research, Computational and Information Systems Laboratory Dataset. Online, http://dx.doi.org/10.5065/D6M32STK. Accessed 20 Apr 2015.
185. Robertson, A.W., Moron, V., Qian, J.H., Chang, C.P., Tangang, F., Aldrian, E., Koh, T.Y. and Liew, J., (2011). The maritime continent monsoon. *In The global monsoon system: research and forecast*. pp. 85-98.
186. Roland, C.A., Schmidt, J.H., Winder, S.G., Stehn, S.E. & Nicklen, E.F. (2019). Regional variation in interior Alaskan boreal forests is driven by fire disturbance, topography, and climate. *Ecological Monographs*. 89(3): E01369.
187. Roy, P. S., & Roy, A. (2010). Land use and land cover change in India: A remote sensing & GIS prespective. *Journal of the Indian Institute of Science*. **90**: 389–502.
188. Saunier, A., Ormeño, E., Boissard, C., Wortham, H., Temime-Roussel, B., Lecareux, C., Armengaud, A & Fernandez, C. (2017). Effect of mid-term drought on Quercus pubescens BVOCs' emission seasonality and their dependency on light and/or temperature. *Atmospheric Chemistry and Physics*. 17(**12**): 7555-7566.
189. Seco, R., Karl, T., Guenther, A., Hosman, K. P., Pallardy, S. G., Gu, L., Geron, C., Harley, P. & Kim, S. (2015). Ecosystem‐scale volatile organic compound fluxes during an extreme drought in a broadleaf temperate forest of the Missouri Ozarks (central USA). *Global change biology*. 21(**10**): 3657-3674.
190. Sentian, J., MacKenzie, R. A., & Hewitt, C. N. (2009). *Regional Climate Change Modelling in Southeast Asia: Technical report No. 3/7*. Lancaster Environmental Centre. University of Lancaster.
191. Sentian, J., Yat, A.C.N & Chong, L. Z. W. (2015). Tropospheric Ozone Response on Climate Change in Malaysia. *Advanced Science Letters*. 21(**2**):165-168.

192. Serreze, M.C. (2010). Understanding recent climate change. *Conservation Biology*. 24(**1**): 10-17.
193. Serreze, M.C., & Barry, R.G. (2011). Processes and impacts of Arctic amplification: A research synthesis. *Global and planetary change.* 77(**1-2**): 85-96.
194. Sharkey, T.D., & Monson, R.K. (2014). The future of isoprene emission from leaves, canopies and landscapes. *Plant, Cell & Environment*. 37(**8**): 1727-1740.
195. Shepherd, T. (2014). Atmospheric circulation as a source of uncertainty in climate change projections. *Nature Geoscience.* 7: 703-708.
196. Shi, Y., & Yamaguchi, Y. (2014). A high-resolution and multi-year emissions inventory for biomass burning in Southeast Asia during 2001–2010. *Atmospheric Environment*. 98. 8–16.
197. Sirignano, C., Riccio, A., Chianese, E., Ni, H., Zenker, K., D'Onofrio, A., Meijer, H.A.J., & Dusek, U. (2019). High Contribution of Biomass Combustion to PM2.5 in the City Centre of Naples (Italy). *Atmosphere*. 10(**8**): 451.
198. Smith, S.J. & Wigley, T.M.L. (2006). Multi-Gas Forcing Stabilization with the MiniCAM. *The Energy Journal*. 3: 373-391.
199. Spessa, A., Weber, U., Langner, A., Siegert, F. & Heil, A. (2009). Fire in the vegetation and peatlands of Borneo, 1997-2007: Patterns, Drivers and Emissions. *Geophysical Research Abstracts.* **11**: 8247.
200. Staver, A.C., Archibald, S., & Levin, S.A. (2011). The Global Extent and Determinants of Savanna and Forest as Alternative Biome States. *Science*. 334(**6053**): 230–232.
201. Steiner, A.L., Tonse, S., Cohen, R.C., Goldstein, A.H. &Harley, R.A. (2006). Influence of Future Climate and Emissions on Regional Air Quality in California. *Journal of Geophysical Research*. 11:D18303, doi:1029/2005JD006935.
202. Stevenson, D.S., Dentener, F.J., Schultz, M.G., Ellingsen, K., van Noije, T.P.C., Wild, O., et al. (2006). Multimodel ensemble simulations of present-day and near-future tropospheric ozone. *Journal of Geophysical Research.* 111: D08301.
203. Stroud, C., Makar, P., Karl, T., Guenther, A., Geron, C., Turnipseed, A., Nemitz, E., Baker, B., Potosnak, M. & Fuentes, J.D. (2005). Role of canopy‐scale photochemistry in modifying biogenic‐atmosphere exchange of reactive terpene species: Results from the CELTIC field study. *Journal of Geophysical Research: Atmospheres*. 110(D17).
204. Tangang, F., Chung, J-X., Juneng, L., Salimun, E., Ngai, S.T., Jamaluddin, A.F., Mohd, M.S.F., Cruz, F., Narisma, G., Santisirisomboon, J., Ngo-Duc, T., Tan., P.V., Singhruck, P., Gunawan, D., Aldrian, E., Sopaheluwakan, A., Grigory, N., Remedio, A.R.C., Sein, D.V., Griggs, D.H., McGregor, J.L., Yang, H., Sasaki, H. & Kumar, P. (2020). Projected future changes in rainfall in Southeast Asia based on CORDEX SEA multi model simulation. *Climate Dynamics*. 55: 1247-1267.
205. Tarigan, S.D., Sunarti, S. & Widyaliza, S. (2015). Expansion of Oil Palm Plantations and Forest Cover Changes in Bungo and Merangin Districts, Jambi Province, Indonesia. *Procedia Environmental Sciences.* 24: 199–205.
206. Tarigan, S., Merten, J., Röll, A., Guillaume, T., Meijide, A., Agusta, H., Dislich, C., Dittrich, C., Faust, H., Gunawan, D., Hein, J., Hendrayanto, Knohl, A., Kuzyakov, Y., Wiegand, K. & Hölscher, D. (2016). Water scarcity and oil palm expansion: social views and environmental processes. *Ecology Society.* 21(**2**): 5.
207. Taylor, K.E., Stouffer, R.J., & Meehl, G.A. (2012). An overview of CMIP5 and the experiment design bull. *American Meteorological Society.* 93: 485-498.
208. Tharwat, A. (2021). Classification Assessment Methods. *Applied Computing and Informatics*. 17: 168-192.

209. Thirumalai, K., DiNezio, P.N., Okumura, Y. & Deser, C. (2017). Extreme temperatures in Southeast Asia caused by El Nino and worsened by global warming. *Nature communication.* 8: 15531.
210. Thomson, A. M., Calvin, K. V., Smith, S. J., Kyle, G. P., Volke, A., Patel, P., Delgado-Arias, S., Bond-Lamberty, B., Wise, M. A., Clarke, L. E. & Edmond, J. A. (2011). RCP4.5: A pathway for stabilization of radiative forcing by 2100. *Climate Change.* 109: 77-94.
211. Tingey, D.T., Lee, E.H., Phillips, D.L., Rygiewicz, P.T., Waschmann, R.S., Johnson, M.G., & Olszyk, D.M. (2007). Elevated CO2 and temperature alter net ecosystem C exchange in a young Douglas fir mesocosm experiment. *Plant, cell & environment*. 30(**11**): 1400-1410.
212. TMD (Thai Meteorological Department), (2013). *Regional mean and variability characteristics of temperature and precipitation over Thailand in 1961-2000 by a regional climate model and their evaluation, Theory.* In Torsri, K., Octaviani, M., Manomaiphiboon, K., and Towprayoon, S. (Eds). Applied Climatology. vol. 113, pp. TMD, Climate of Thailand, Thai Meteorological Department, Pp. 289-304.
213. Toh, Y.Y., Lim, S.F., & von Glasow, R. (2013). The influence of meteorological factors and biomass burning on surface ozone concentrations at Tanah Rata, Malaysia. *Atmospheric Environment*. 70: 435–446.
214. Unger, N., Harper, K., Zheng, Y., Kiang, N.Y., Aleinov, I., Arneth, A., Schurgers, G., Amelynck, C., Goldstein, A., Guenther, A. & Heinesch, B. (2013). Photosynthesis-dependent isoprene emission from leaf to planet in a global carbon-chemistry-climate model. *Atmospheric Chemistry and Physics*. 13(**20**): 10243-10269.
215. Uning, R., Latif, M. T., Othman, M., Juneng, L., Mohd Hanif, N., Nadzir, M. S. M., Abdul Maulud, K.N., Jaafar, W.S.W.M., Said, N.F.S., Ahamad, F. & Takriff, M. S. (2020). A review of Southeast Asian oil palm and Its CO2 fluxes. *Sustainability*. 12(**12**): 5077.
216. Vadrevu, K.P., Lasko, K., Giglio, L., Schroeder, W., Biswas, S., & Justice, C. (2019). *Trends in vegetation fires in South and Southeast Asian Countries*. Scientific Reports. 9: 7422.
217. Van der Werf, G.R., Randerson, J.T., Giglio, L., Collatz, G.J., Mu, M., Kasibhatla, P.S. & Van Leeuwen, T. (2010). Global fire emissions and the contribution of deforestation, savanna, forest, agricultural, and peat fires (1997–2009). *Atmospheric Chemistry and Physics*. 10(**23**): 11707–11735.
218. Van der Werf, G.R., Van Leeuwen, T.T., Hoffmann, A.A., Detmers, R.G., Rücker, G., French, N.H.F. & Trollope, W.S. (2014). Biomass burning fuel consumption rates: a field measurement database. *Biogeosciences.* 11(**24**): 7305–7329.
219. van der Linden, R., Fink, A.H., Pinto, J.G., Phan-Van, T. & Kiladis, G.N. (2016) Modulation of daily rainfall in southern Vietnam by the Madden–Julian Oscillation and convectively coupled equatorial waves. *Journal of Climate*. 29: 5801–5820.
220. Van Vuuren, D. P., Eickhout, B., Lucas, P. L. & den Elzen, M. G. J. (2006). Long-term multi-gas scenarios to stabilise radiative forcing — Exploring costs and benefits within an integrated assessment framework. Multigas mitigation and climate policy. *The Energy Journal*. 3: 201-234.
221. Van Vuuren, D., den Elzen, M., Lucas, P., Eickhout, B., Strengers, B., van Ruijven, B., Wonink, S. & van Houdt, R. (2007). Stabilizing greenhouse gas concentrations at low levels: an assessment of reduction strategies and costs. *Climatic Change*. 18(**2**): 119-159.
222. Van Vuuren, D. P., Stehfest, E., Michel G. J., Kram, T., Vliet, J. A., Deetman, S., Isaac, M., Goldewijk, K. K., Hof, A., Beltran, A. M., Oostenrijk, R. & Ruijven, B. V. (2011). RCP2.6: Exploring the possibility to keep global mean temperature increase below 2C. *Climate Change.* 109: 95-116.

223. Varner, J.M., Kane, J.M., Kreye, J.K. & Engber, E. (2015). The Flammability of Forest and Woodland Litter: a Synthesis. *Current Forestry Reports*. 1(**2**): 91–99.
224. Veldman, J.W. (2016). Clarifying the confusion: old-growth savannahs and tropical ecosystem degradation. *Philosophical Transactions of the Royal Society B.* 371(**1703**): 4978865.
225. Viera, A., & Garrett, J. (2005). Understanding Interobserver Agreement: The Kappa Statistic. *Family Medicine*. 37: 360–363.
226. Von Schneidemesser, E., Monks, P. S., Allan, J. D., Bruhwiler, L., Forster, P., Fowler, D., Lauer A, Morgan WT, Paasonen P, Righi M. & Sindelarova K. (2015). Chemistry and the linkages between air quality and climate change. *Chemical Reviews*. 115(**10**): 3856-3897.
227. Voulgarakis, A., Naik, V., Lamarque, J.F., Shindell, D.T., Young, P.J., Prather, M.J., Wild, O., et al., (2013). Analysis of present day and future OH and methane lifetime in the ACCMIP simulations. *Atmospheric Chemistry and Physics.* 13**:** 2563-2587.
228. Wagner, W., Nemecek-Marshall, M. & Fall, R. (1999). Three Distinct Phases of Isoprene Formation during Growth and Sporulation of Bacillus subtilis. *Journal of Bacteriology*. 181(**15**): 4700–4703.
229. Wang, Y. & Jacob, D.J. (1998). Anthropogenic forcing on tropospheric O3 and OH since preindustrial times. *Journal of Geophysical Research.* 103(**31**): 123 -135.
230. Wang, K. & Zhang, Y. (2012). Application evaluation, and process analysis of the US EPA's 2002 multiple-pollutant air quality modelling platform. *Atmospheric and Climate Science.* 2:254-289.
231. Wang, Y., Li, X. & Li, J. (2014). Study on the Response of Ecological Capacity to Land-Use/Cover Change in Wuhan City: A Remote Sensing and GIS Based Approach. *The Scientific World Journal*. 4*:* 794323.
232. Wang, H., Wu, Q., Guenther, A.B., Yang, X., Wang, L., Xiao, T., Li, J., Feng, J., Xu, Q. & Cheng, H. (2021). A long-term estimation of biogenic volatile organic compound (BVOC) emission in China from 2001–2016: the roles of land cover change and climate variability. *Atmospheric Chemistry and Physics*. 21(**6**): 4825-4848.
233. Wehmas, M.I. (2018). Temporal and spatial variation of broadleaf forest flammability in boreal Alaska.
234. Winkler, D.E., Kaitlin, L. & Carrell, A.A. (2019). *Response of Alpine plant communities to climate warming*. Oak Ridg, United States. Pp: 297–346.
235. Wise, M.A., Calvin, K.V., Thomson, A. M., Clarke, L.E., Bond-Lamberty, B., Sands, R.D., Smith, S.J., Janetos, A.C. & Edmonds, J.A. (2009). Implications of Limiting CO2 Concentrations for Land Use and Energy. *Science*. 324: 1183-1186.
236. World Bank, (2011). Climate Change and the World Bank Group [Book], Phase II - The Challenge of Low-Carbon Development.
237. Wu, C., Wu, D. & Yu, J.Z. (2019). Estimation and uncertainty analysis of secondary organic carbon using 1 year hourly organic elemental carbon data. *Journal of Geophysical Research: Atmospheres*.124: 2774–2795.
238. Xavier, P., Lim, See., Abdullah, M., Bala, M., Chenoli, S., Handayani, A., Marzin, C., Permana, D., Tangang, F., Williams, K., & Jeong, Y.D. (2020). Seasonal Dependence of Cold Surges and their Interaction with the Madden–Julian Oscillation over Southeast *Asia. Journal of Climate*. 33: 2467-2482.
239. Yadav, I. C. & Devi, N. L. (2018). Biomass Burning, Regional Air Quality, and Climate Change. *Reference Module in Earth Systems and Environmental Sciences*. 2: 386-391.

240. Yang, W., Cao, J., Wu, Y., Kong, F., & Li, L. (2021). Review on plant terpenoid emissions worldwide and in China. *Science of the Total Environment*. 787: 147454.
241. Yat, A.C.N & Sentian, J. (2015). Climate Change Impacts on Hydroxyl Radical (OH) from the CiTTyCAT Tropospheric Chemistry Model Simulations. *Australian Journal of Basic & Applied Science***.** 9(**32**): 327-332.
242. Yin, S. (2020). Biomass burning spatiotemporal variations over South and Southeast Asia. *Environment International*. 145: 106153.
243. Yin, Y., Ma, D. & Wu, S. (2018). Climate change risk to forests in China associated with warming. *Scientific Reports*. 8: 493.
244. Young, P.J., Archibald, A.T., Bowman, K.W., Lamarque, J.F., Naik, V., Stevenson, D.S., et al. (2013). Pre-industrial to end 21st century projections of tropospheric ozone from the Atmospheric Chemistry and Climate Model Intercomparison Project (ACCMIP). *Atmospheric Chemistry and Physics*. 13: 2063–2090.
245. Zeng, G. & Pyle, J.A. (2003). Changes in tropospheric ozone between 2000 and 2100 modeled in a chemistry-climate model. *Geophysical Research Letter.* 30(**7**): 1392.
246. Zeng, G., Pyle, J.A. & Young, P.Y. (2008). Impact of climate change on tropospheric ozone and its global budgets. *Atmospheric Chemistry and Physics.* 8**:** 369-387.
247. Zeng, Z., Piao, S., Li, L.Z.X., Zhou, L., Ciais, P., Wang, T., Li, Y., Lian, X., Wood, E. F., Friedlingstein, P., Mao, J., Estes, L.D., Myneni, R.B., Peng, S., Shi, X., Seneviratne, S.I., & Wang, Y. (2017). Climate mitigation from vegetation biophysical feedbacks during the past three decades. *Nature Climate Change.* 7(**6**): 432-436.
248. Zhou, T., Yu, R., Zhang, J., Drange, H., Cassou, C., Deser, C., Hodson, D.L.R., Sanchez-Gomez, E., Li, J., Keenlyside, X. & Okumura, Y. (2009). Why the western Pacific subtropical high has extended westward since the late 1970s. *Journal of Climate.* 22(**8)**: 2199-2215.
249. Zhou, T., Yang, X., Wang, L., Xu, J., & Zhang, X. (2014). GhTZF1 regulates drought stress responses and delays leaf senescence by inhibiting reactive oxygen species accumulation in transgenic Arabidopsis. *Plant molecular biology*. 85(**1-2**): 163-177.
250. Zhou, Y., Xing, X., Lang, J., Chen, D., Cheng, S., Wei, L., Wei, X., & Liu, C. (2017). A comprehensive biomass burning emission inventory with high spatial and temporal resolution in China. *Atmospheric Chemistry and Physics*. 17(**4**): 2839–2864.
251. Zhu, J., Xia, X., Che, H., Wang, J., Zhang, J., & Duan, Y. (2016). Study of aerosol optical properties at Kunming in southwest China and long-range transport of biomass burning aerosols from North Burma. *Atmospheric Research*. 169: 237–247.

APPENDIX

APPENDIX 3.1 PROJECTED CLIMATE CHANGE IN SEA

Appendix 3.1.1A: Projected surface temperature (^{o}C) over SEA region under RCP4.5

JANUARY					
YEAR	**2013**	**2030**	**2050**	**2070**	**2100**
Myanmar	16.24	16.32	17.12	12.46	11.05
Thailand	22.07	26.27	26.68	14.93	17.58
Cambodia	28.24	32.12	32.95	25.17	30.85
Laos	22.82	26.83	25.68	13.60	17.68
Vietnam	22.70	25.54	23.68	15.36	19.86
Malaysia	27.51	28.55	28.63	28.48	28.69
Indonesia	28.10	28.46	28.76	28.99	29.26
Philippines	26.35	27.80	27.73	27.26	27.65

JULY					
Myanmar	23.82	24.49	23.58	24.05	24.41
Thailand	26.82	29.43	27.14	28.36	29.64
Cambodia	31.08	30.81	31.31	33.74	33.82
Laos	29.01	31.54	29.18	31.69	30.98
Vietnam	30.26	31.95	29.98	32.50	30.44
Malaysia	29.06	29.23	29.47	29.70	29.82
Indonesia	27.36	28.19	28.38	28.79	29.00
Philippines	28.45	28.61	29.39	28.80	29.20

Appendix 3.1.1B: Projected surface temperature (ºC) over SEA region under RCP6.0

JANUARY					
YEAR	**2013**	**2030**	**2050**	**2070**	**2100**
Myanmar	11.72	13.45	17.16	18.05	15.61
Thailand	14.60	21.50	26.87	24.73	23.87
Cambodia	22.54	30.28	32.98	29.80	32.71
Laos	14.64	22.41	27.33	23.93	25.55
Vietnam	16.66	23.02	25.53	23.51	25.92
Malaysia	27.37	28.28	28.84	28.55	29.47
Indonesia	28.21	28.49	29.14	29.01	29.64
Philippines	26.06	27.12	27.66	27.62	28.07

JULY					
Myanmar	21.41	25.43	25.77	24.20	24.02
Thailand	25.96	30.18	28.99	25.34	25.45
Cambodia	29.79	30.81	31.17	32.44	31.73
Laos	26.98	31.81	29.67	26.64	27.80
Vietnam	27.83	31.64	30.13	28.99	30.25
Malaysia	28.76	29.53	29.58	29.99	31.50
Indonesia	27.46	28.50	28.62	29.09	29.94
Philippines	27.65	28.95	29.09	29.26	30.63

Appendix 3.1.1C: Projected surface temperature (ºC) over SEA region under RCP8.5

JANUARY					
YEAR	**2013**	**2030**	**2050**	**2070**	**2100**
Myanmar	15.27	15.21	15.04	18.01	15.49
Thailand	21.28	21.83	25.46	27.50	21.29
Cambodia	28.27	27.67	31.52	33.08	28.41
Laos	21.86	21.50	27.60	29.19	22.30
Vietnam	22.87	21.46	27.16	29.14	22.43
Malaysia	27.97	28.27	28.23	29.26	29.61
Indonesia	28.09	28.69	28.66	29.66	30.54
Philippines	27.73	27.30	27.65	28.78	29.71

JULY					
Myanmar	24.65	25.77	24.52	25.83	26.93
Thailand	28.90	28.50	25.40	30.68	30.88
Cambodia	32.28	31.08	31.33	34.74	32.48
Laos	30.97	30.24	27.65	33.27	32.00
Vietnam	31.36	30.25	29.21	33.08	32.70
Malaysia	29.72	29.46	30.67	30.27	31.47
Indonesia	28.65	28.71	29.24	29.27	29.86
Philippines	29.01	28.50	29.39	30.21	30.83

Appendix 3.1.1D: Projected total precipitation (icnhes/day) over SEA region under RCP4.5

JANUARY					
YEAR	**2013**	**2030**	**2050**	**2070**	**2100**
Myanmar	0.21	0.63	0.73	0.06	10.32
Thailand	0.10	0.22	3.63	0.01	8.86
Cambodia	0.00	0.75	0.09	0.01	5.25
Laos	0.02	0.26	2.71	0.00	7.17
Vietnam	0.01	1.28	1.44	0.00	8.09
Malaysia	0.27	164.95	8.71	8.17	69.32
Indonesia	1.93	205.74	13.44	18.68	160.47
Philippines	1.44	59.17	0.91	2.03	66.31

JULY					
Myanmar	18.86	8.34	30.60	207.88	196.61
Thailand	11.92	13.46	22.83	180.13	96.17
Cambodia	10.74	21.72	31.47	194.67	145.69
Laos	6.32	16.92	20.72	176.25	86.09
Vietnam	6.73	10.63	24.46	147.66	110.97
Malaysia	1.92	5.43	13.95	81.18	103.32
Indonesia	0.30	3.06	7.22	27.64	30.54
Philippines	11.57	1.81	17.99	251.80	229.18

Appendix 3.1.1E: Projected total precipitation (icnhes/day) over SEA region under RCP6.0

JANUARY					
YEAR	**2013**	**2030**	**2050**	**2070**	**2100**
Myanmar	0.09	8.75	0.82	0.00	4.75
Thailand	0.00	8.75	0.01	0.00	8.10
Cambodia	0.00	0.16	0.02	0.03	0.50
Laos	0.00	5.57	0.01	0.00	5.75
Vietnam	0.00	2.19	0.02	0.07	3.08
Malaysia	6.08	31.66	6.86	10.31	70.73
Indonesia	7.23	92.86	8.84	14.32	108.75
Philippines	1.51	41.19	1.70	6.59	27.58

JULY					
Myanmar	7.04	174.47	197.37	231.34	205.04
Thailand	16.23	137.93	156.45	193.98	203.67
Cambodia	20.97	306.61	370.69	202.78	406.65
Laos	21.89	162.77	176.29	178.32	250.94
Vietnam	18.85	179.16	199.64	162.08	253.86
Malaysia	9.30	102.57	133.84	52.75	154.04
Indonesia	1.58	26.61	21.05	16.80	40.26
Philippines	23.53	194.91	229.77	185.74	217.15

Appendix 3.1.1F: Projected total precipitation (icnhes/day) over SEA region under RCP8.5

JANUARY					
YEAR	**2013**	**2030**	**2050**	**2070**	**2100**
Myanmar	0.29	0.53	2.70	0.66	3.15
Thailand	2.35	0.03	4.36	2.06	0.98
Cambodia	10.10	0.02	1.62	1.94	0.09
Laos	5.13	0.001	3.22	1.74	0.13
Vietnam	2.21	0.17	3.12	0.51	0.07
Malaysia	8.04	134.77	135.67	8.03	27.20
Indonesia	9.75	268.28	160.70	8.13	88.86
Philippines	3.35	77.75	106.84	2.68	33.95

JULY					
Myanmar	197.66	242.52	176.10	215.17	37.43
Thailand	160.19	221.66	204.97	160.34	58.20
Cambodia	299.60	208.40	342.36	319.03	108.50
Laos	187.78	242.31	264.77	198.03	75.92
Vietnam	125.56	265.33	269.10	180.97	70.29
Malaysia	138.14	61.82	180.12	130.79	36.14
Indonesia	19.96	26.72	27.61	48.34	3.77
Philippines	295.67	295.91	223.13	200.10	113.45

APPENDIX 3.2. BIOMASS BURNING EMISSION IN SEA

Appendix 3.2.1A Kappa Analysis of Accuracy Assessment for Land Cover of MSEA in 2013

Classes	Evergreen Forests	Deciduous Forests	Mixed Forests	Shrub lands	Savannas	Wet-lands	Crop-lands	Others	Total	User's Accuracy	Kappa
Evergreen Forests	115	0	0	1	1	0	0	1	118	0.98	0
Deciduous Forests	0	14	0	0	0	0	0	0	14	1	0
Mixed Forests	0	0	20	0	0	0	0	0	20	1	0
Shrublands	6	0	0	57	1	1	2	2	69	0.83	0
Savannas	0	0	0	8	50	1	7	5	71	0.70	0
Wetlands	0	0	0	0	0	9	0	1	10	0.90	0
Croplands	0	0	0	7	1	0	84	5	97	0.87	0
Others	1	0	0	1	1	1	1	5	10	0.5	0
Total	122	14	20	74	54	12	94	19	409	0	0
Producer's Accuracy	0.9	1	1	0.77	0.93	0.75	0.89	0.26	0	0.87	0
Kappa	0	0	0	0	0	0	0	0	0	0	0.8320

Appendix 3.2.1B Kappa Analysis of Accuracy Assessment for Land Cover of Borneo in 2013

Classes	Broadleaf forest	Shrubland	Open forest/ oil palm	Grassland	Cropland	Wetland	Built-up	Others	Total	User's Accuracy	Kappa
Broadleaf Forest	147	4	4	0	0	1	0	2	158	0.93	0

Shrubland	0	18	0	0	2	0	0	0	20	0.90	0
Open Forest/ Oil Palm	7	1	34	2	0	0	2	0	46	0.74	0
Grassland	2	2	1	31	1	0	1	0	38	0.82	0
Cropsland	0	0	0	3	15	0	2	2	20	0.75	0
Wetland	0	0	0	0	0	15	2	2	17	0.88	0
Built-up	1	1	3	1	0	1	24	0	31	0.77	0
Others	3	0	1	1	2	0	0	18	25	0.72	0
Total	160	26	43	38	20	17	27	24	355	0	0
Producer's Accuracy	0.92	0.69	0.79	0.82	0.75	0.88	0.89	0.75	0		0
Kappa	0	0	0	0	0	0	0	0	0	0	0.8012

APPENDIX 3.2.2 TOTAL BURNED AREA

Appendix 3.2.2A Amount of Dry Biomass Burned of Cambodia in 2013

Land Cover Type	Total Burned Area (km^2)	Dry Biomass Burned (Gg/year)
Evergreen	1199.6338	2154.7823
Deciduous	4610.2765	8280.9786
Mixed	1736.6268	3119.3291
Shrublands	1755.2295	1541.9059
Savannas	12592.3093	1601.4458
Wetlands	16.7001	5.511
Croplands	1651.923	59.4692
Total	23562.699	16763.4219

Appendix 3.2.2B Amount of Dry Biomass Burned of Laos in 2013

Land Cover Type	Total Burned Area (km^2)	Dry Biomass Burned (Gg/year)
Evergreen	2654.0988	4767.2922
Deciduous	209.9428	377.0993
Mixed	182.3568	327.5492
Shrublands	2823.3835	2480.2407
Savannas	1356.7184	172.5427
Wetlands	4.0001	1.32
Croplands	52.8435	1.9024
Total	7283.3439	8127.9465

Appendix 3.2.2C Amount of Dry Biomass Burned of Myanmar in 2013

Land Cover Type	Total Burned Area (km^2)	Dry Biomass Burned (Gg/year)
Evergreen	2914.5756	5235.1608
Deciduous	6367.9944	11438.1915
Mixed	6057.9752	10881.3351
Shrublands	5385.0240	4730.5497
Savannas	3763.1883	478.5891
Wetlands	21.2373	7.0083
Croplands	2593.0503	93.3498
Total	27103.0451	32864.1843

Appendix 3.2.2D Amount of Dry Biomass Burned of Thailand in 2013

Land Cover Type	Total Burned Area (km^2)	Dry Biomass Burned (Gg/year)
Evergreen	572.4203	1028.1813
Deciduous	1120.438	2012.5307
Mixed	162.5476	291.9681
Shrublands	1293.6092	1136.3891
Savannas	1868.1799	237.5886
Wetlands	10.1186	3.3391
Croplands	4798.84	172.7582
Total	9826.1536	4882.7551

Appendix 3.2.2E Amount of Dry Biomass Burned of Vietnam in 2013

Land Cover Type	Total Burned Area (km^2)	Dry Biomass Burned (Gg/year)
Evergreen	340.5259	611.6527
Deciduous	204.081	366.5703
Mixed	6.2854	11.2898
Shrublands	389.3369	342.0185
Savannas	1078.6436	137.1781
Wetlands	17.019	5.6163
Croplands	7515.6802	270.5645
Total	9551.572	1744.8902

Appendix 3.2.2F Amount of Dry Biomass Burned of South ASEAN in 2013

Land Cover Type	Total Burned Area (km^2)		Dry Biomass Burned (Gg/year)
	Malaysia	Indonesia	
Broadleaf Forest	32.18	340.5259	618.5215
Open Forest/ Oil Palm	28.04	204.081	79.78163
Grassland	9.12	6.2854	3.55458
Cropland	-	389.3369	0.00048
Wetland	1.28	1078.6436	1.0758
Total	70.62	17.019	702.934

APPENDIX 3.2.3 TEMPORAL BB EMISSION BY LAND COVER

Appendix 3.2.3A Amount of Dry Biomass Burned of MSEA in January 2013

Land Cover Type	Total Burned Area (km^2)	Dry Biomass Burned (Gg/year)
Evergreen	270.5708	485.9994
Deciduous	3647.1368	6550.9871
Mixed	901.0622	1618.4881
Shrublands	682.2834	599.3614
Savannas	7977.9091	1014.6026
Wetlands	1.3616	0.4493
Croplands	1971.6506	70.9794
Total	15451.9745	10340.8673

Appendix 3.2.3B Amount of Dry Biomass Burned of MSEA in February 2013

Land Cover Type	Total Burned Area (km^2)	Dry Biomass Burned (Gg/year)
Evergreen	933.4247	1676.6175
Deciduous	5374.2776	9653.2774
Mixed	2491.5582	4475.3369
Shrublands	1948.8673	1712.0097
Savannas	6204.1852	789.0266
Wetlands	9.2814	3.0629
Croplands	6723.733404	242.0544
Total	23685.3278	18551.3854

Appendix 3.2.3C Amount of Dry Biomass Burned of MSEA in March 2013

Land Cover Type	Total Burned Area (km^2)	Dry Biomass Burned (Gg/year)

Evergreen	1535.5698	2758.1905
Deciduous	2696.5524	4843.5474
Mixed	3258.3523	5852.6525
Shrublands	4212.7154	3700.7189
Savannas	4105.7128	522.1502
Wetlands	23.6151	7.7930
Croplands	4740.2235	170.6480
Total	20572.7413	17855.7005

Appendix 3.2.3D Amount of Dry Biomass Burned of MSEA in April 2013

Land Cover Type	Total Burned Area (km^2)	Dry Biomass Burned (Gg/year)
Evergreen	4631.9942	8319.9881
Deciduous	714.9365	1284.1690
Mixed	1483.4228	2664.5241
Shrublands	4656.4894	4090.5583
Savannas	1460.358	185.7232
Wetlands	22.0446	7.2747
Croplands	952.3511	34.2846
Total	13921.5966	16586.5220

Appendix 3.2.3E Amount of Dry Biomass Burned of MSEA in May 2013

Land Cover Type	Total Burned Area (km^2)	Dry Biomass Burned (Gg/year)
Evergreen	233.3057	419.0637
Deciduous	4.4124	7.9255

Mixed	1.5192	2.7289
Shrublands	72.8095	63.9605
Savannas	47.1616	5.9979
Wetlands	5.9016	1.9475
Croplands	213.6284	7.6906
Total	578.7384	509.3146

Appendix 3.2.3F Amount of Dry Biomass Burned of MSEA in June 2013

Land Cover Type	Total Burned Area (km^2)	Dry Biomass Burned (Gg/year)
Evergreen	11.2844	20.2690
Deciduous	0.008374	0.01504
Mixed	0	0
Shrublands	5.7707	5.0694
Savannas	11.3601	1.4447
Wetlands	2.0699	0.6831
Croplands	109.0348	3.9253
Total	139.5283	31.4065

Appendix 3.2.3G Amount of Dry Biomass Burned of MSEA in July 2013

Land Cover Type	Total Burned Area (km^2)	Dry Biomass Burned (Gg/year)
Evergreen	7.2190	12.9668
Deciduous	0	0
Mixed	0	0
Shrublands	1.3760	1.2087
Savannas	4.5840	0.5830
Wetlands	0.3347	0.1104
Croplands	166.8189	6.0055
Total	180.3326	20.8744

Appendix 3.2.3H Amount of Dry Biomass Burned of MSEA in August 2013

Land Cover Type	Total Burned Area (km^2)	Dry Biomass Burned (Gg/year)
Evergreen	10.0904	18.1244
Deciduous	0.1498	0.2691
Mixed	0	0
Shrublands	11.8631	10.4213
Savannas	15.6180	1.9862
Wetlands	1.4212	0.4690
Croplands	129.4240	4.6593
Total	168.5665	35.9293

Appendix 3.2.3I Amount of Dry Biomass Burned of MSEA in September 2013

Land Cover Type	Total Burned Area (km^2)	Dry Biomass Burned (Gg/year)
Evergreen	0	0
Deciduous	0	0
Mixed	0	0
Shrublands	0.2791	0.2452
Savannas	3.0894	0.3929
Wetlands	0.7910	0.2610
Croplands	17.2151	0.6197
Total	21.3746	1.5188

Appendix 3.2.3J Amount of Dry Biomass Burned of MSEA in October 2013

Land Cover Type	Total Burned Area (km^2)	Dry Biomass Burned (Gg/year)
Evergreen	10.09	18.1236
Deciduous	0.03	0.05398
Mixed	0	0
Shrublands	0.2791	0.2452
Savannas	46.2526	5.8822
Wetlands	0.9755	0.3219
Croplands	202.4854	7.2895
Total	260.1126	31.91638

Appendix 3.2.3K Amount of Dry Biomass Burned of MSEA in November 2013

Land Cover Type	Total Burned Area (km^2)	Dry Biomass Burned (Gg/year)
Evergreen	18.3342	32.9320
Deciduous	9.0554	16.2652
Mixed	1.1296	2.0290
Shrublands	5.1337	4.5097

Savannas	115.7293	14.7180
Wetlands	1.1315	0.3734
Croplands	577.4329	20.7876
Total	727.9466	91.6149

Appendix 3.2.3L Amount of Dry Biomass Burned of MSEA in December 2013

Land Cover Type	Total Burned Area (km^2)	Dry Biomass Burned (Gg/year)
Evergreen	20.1168	36.1339
Deciduous	67.2771	120.8431
Mixed	9.9104	17.8011
Shrublands	35.9808	31.6078
Savannas	667.7556	84.9228
Wetlands	0.8436	0.2784
Croplands	808.3583	29.1009
Total	1610.2426	320.6880

APPENDIX 3.2.4 TEMPORAL BB EMISSION SPECIES

Appendix 3.2.4A: Typical Pollutant Emission of January 2013 (Gg/year)

Land Cover Type	CO_2	CO	CH_4	NO_x	NH_3	SO_2	PM_{10}	$PM_{2.5}$	EC	OC	NMVOC
Evergreen Forests	270.57	486.0	798.50	44.71	2.48	1.26	0.37	0.22	6.22	4.96	0.24
Deciduous Forests	10678.11	668.20	32.76	8.52	9.83	6.55	83.85	80.58	3.93	60.27	72.06
Mixed Forests	2638.13	165.09	8.092	2.10	2.43	1.62	20.72	19.91	0.97	14.89	22.66
Shrublands	1028.50	40.76	1.56	2.34	0.72	0.41	5.09	4.73	0.30	3.96	2.88
Savannas	1741.06	59.86	1.52	2.84	0.51	0.69	10.04	6.39	0.41	2.64	9.44
Wetlands	0.79	95.37	1.52	2.13	0.61	0.81	12.68	11.36	0.53	6.39	6.90
Croplands	96.07	5.40	0.20	0.21	0.10	0.028	0.45	0.35	0.045	0.14	0.70
Others	-	-	-	-	-	-	-	-	-	-	-
Total	16453.23	1520.68	844.152	62.85	16.68	11.37	133.20	123.54	12.41	93.25	114.88

Appendix 3.2.4B: Typical Pollutant Emission of February 2013 (Gg/year)

Land Cover Type	CO_2	CO	CH_4	NO_x	NH_3	SO_2	PM_{10}	$PM_{2.5}$	EC	OC	NMVOC
Evergreen Forests	2754.68	154.25	8.55	4.36	1.27	0.75	21.46	17.10	0.84	7.88	40.24
Deciduous Forests	15734.84	984.63	48.27	12.55	14.48	9.65	123.56	118.74	5.79	88.81	106.19
Mixed Forests	7294.80	456.48	22.38	5.82	6.71	4.48	57.28	55.05	2.69	41.17	62.66
Shrublands	2937.81	116.42	4.45	6.68	2.05	1.16	14.55	13.52	0.86	11.30	8.22
Savannas	1353.97	46.55	1.18	2.21	0.39	0.54	7.81	4.97	0.32	2.05	7.34
Wetlands	5.41	74.17	1.18	1.66	0.47	0.63	9.86	8.84	0.41	4.97	5.37
Croplands	327.62	18.42	0.68	0.70	0.34	0.10	1.52	1.21	0.15	0.48	2.37
Others	-	-	-	-	-	-	-	-	-	-	-
Total	30409.13	1850.92	86.69	33.98	25.71	17.31	236.04	219.43	11.06	156.66	232.39

Appendix 3.2.4C: Typical Pollutant Emission of March 2013 (Gg/year)

Land Cover Type	CO_2	CO	CH_4	NO_x	NH_3	SO_2	PM_{10}	$PM_{2.5}$	EC	OC	NMVOC
Evergreen Forests	4531.71	253.75	14.07	7.17	2.10	1.24	35.30	28.13	1.38	12.96	66.20

Deciduous Forests	7894.98	494.04	24.22	6.30	7.27	4.84	62.00	59.58	2.91	44.56	53.28
Mixed Forests	9539.82	596.97	29.26	7.61	8.78	5.85	74.91	71.99	3.51	53.84	81.94
Shrublands	6350.43	251.65	9.62	14.43	4.44	2.52	31.46	29.26	1.85	24.42	17.76
Savannas	896.01	30.81	0.78	1.46	0.26	0.356	5.17	3.29	0.21	1.36	4.86
Wetlands	13.76	49.08	0.78	1.10	0.31	0.42	6.53	5.85	0.27	3.29	3.55
Croplands	230.97	12.99	0.48	0.49	0.24	0.068	1.08	0.85	0.11	0.34	1.67
Others	-	-	-	-	-	-	-	-	-	-	-
Total	29457.68	1689.29	79.21	38.56	23.4	15.30	216.45	198.95	10.24	140.77	229.26

Appendix 3.2.4D: Typical Pollutant Emission of April 2013 (Gg/year)

Land Cover Type	**CO_2**	**CO**	**CH_4**	**NO_x**	**NH_3**	**SO_2**	**PM_{10}**	**$PM_{2.5}$**	**EC**	**OC**	**NMVOC**
Evergreen Forests	13669.74	765.44	42.43	21.63	6.32	3.74	106.50	84.86	4.16	39.10	199.68
Deciduous Forests	2093.20	130.99	6.42	1.67	1.93	1.28	16.44	15.80	0.77	11.81	14.13
Mixed Forests	4343.17	271.78	13.32	3.46	4.00	2.66	34.11	32.77	1.60	24.51	37.30

Shrublands	7019.40	278.16	10.64	15.95	4.91	2.78	34.77	32.32	2.05	27.00	19.64
Savannas	318.70	10.96	0.28	0.52	0.093	0.13	1.84	1.17	0.074	0.48	1.73
Wetlands	12.84	17.46	0.28	0.39	0.11	0.15	2.32	2.08	0.097	1.17	1.26
Croplands	46.40	2.61	0.096	0.099	0.048	0.014	0.22	0.17	0.022	0.069	0.336
Others	-	-	-	-	-	-	-	-	-	-	-
Total	27503.45	1477.40	73.47	43.72	17.41	10.75	196.2	169.17	8.77	104.14	274.08

Appendix 3.2.4E: Typical Pollutant Emission of May 2013 (Gg/year)

Land Cover Type	**CO_2**	**CO**	**CH_4**	**NO_x**	**NH_3**	**SO_2**	**PM_{10}**	**$PM_{2.5}$**	**EC**	**OC**	**NMVOC**
Evergreen Forests	688.52	38.55	2.14	1.09	0.32	0.19	5.36	4.27	0.21	1.97	10.06
Deciduous Forests	12.92	0.81	0.040	0.010	0.012	0.0079	0.10	0.097	0.0048	0.073	0.087
Mixed Forests	4.45	0.28	0.014	0.0036	0.0041	0.0027	0.035	0.036	0.0016	0.025	0.038
Shrublands	109.76	4.35	0.17	0.25	0.077	0.043	0.54	0.51	0.032	0.42	0.31
Savannas	10.29	0.35	0.0090	0.017	0.0030	0.0041	0.059	0.038	0.0024	0.016	0.056

Wetlands	3.44	0.56	0.0088	0.013	0.0036	0.0048	0.075	0.067	0.0032	0.038	0.041
Croplands	10.41	0.59	0.022	0.022	0.011	0.0031	0.048	0.038	0.0048	0.015	0.075
Others	-	-	-	-	-	-	-	-	-	-	-
Total	839.79	45.49	2.40	1.41	0.43	0.26	6.22	5.06	0.26	2.56	10.67

Appendix 3.2.4F: Typical Pollutant Emission of June 2013 (Gg/year)

Land Cover Type	**CO_2**	**CO**	**CH_4**	**NO_x**	**NH_3**	**SO_2**	**PM_{10}**	**$PM_{2.5}$**	**EC**	**OC**	**NMVOC**
Evergreen Forests	33.30	1.86	0.10	0.052	0.015	0.0091	0.26	0.21	0.010	0.095	0.49
Deciduous Forests	0.0084	0.015	0.025	0.0015	0.000075	0.00002	0.000023	0.000015	0.00019	0.00019	0.0000090
Mixed Forests	0	0	0	0	0	0	0	0	0	0	0
Shrublands	8.70	0.34	0.013	0.020	0.0061	0.0034	0.04	0.040	0.0025	0.033	0.024
Savannas	2.48	0.085	0.0022	0.0040	0.00072	0.00098	0.014	0.0091	0.00058	0.0038	0.013
Wetlands	1.21	0.14	0.0022	0.0030	0.00087	0.0012	0.018	0.016	0.00075	0.0091	0.0098
Croplands	5.31	0.30	0.011	0.011	0.0055	0.0016	0.025	0.020	0.0025	0.0079	0.038

Others	-	-	-	-	-	-	-	-	-	-	-
Total	51.01	2.74	0.15	0.092	0.028	0.016	0.36	0.30	0.017	0.15	0.57

Appendix 3.2.4G: Typical Pollutant Emission of July 2013 (Gg/year)

Land Cover Type	**CO_2**	**CO**	**CH_4**	**NO_x**	**NH_3**	**SO_2**	**PM_{10}**	**$PM_{2.5}$**	**EC**	**OC**	**NMVOC**
Evergreen Forests	21.30	1.19	0.066	0.034	0.0099	0.0058	0.17	0.13	0.0065	0.061	0.31
Deciduous Forests	0	0	0	0	0	0	0	0	0	0	0
Mixed Forests	0	0	0	0	0	0	0	0	0	0	0
Shrublands	2.07	0.082	0.0031	0.0047	0.0015	0.00082	0.010	0.0095	0.00060	0.0080	0.0058
Savannas	1.00	0.034	0.00087	0.0016	0.00029	0.00040	0.0058	0.0037	0.00023	0.0015	0.0054
Wetlands	0.19	0.055	0.00087	0.0012	0.00035	0.00047	0.0073	0.0065	0.00030	0.0037	0.0040
Croplands	8.13	0.46	0.017	0.017	0.0084	0.0024	0.038	0.030	0.0038	0.012	0.059
Others	-	-	-	-	-	-	-	-	-	-	-
Total	32.69	1.82	0.088	0.059	0.020	0.0099	0.23	0.18	0.011	0.086	0.38

Appendix 3.2.4H: Typical Pollutant Emission of August 2013 (Gg/year)

Land Cover Type	CO_2	CO	CH_4	NO_x	NH_3	SO_2	PM_{10}	$PM_{2.5}$	EC	OC	NMVOC
Evergreen Forests	29.78	1.67	0.092	0.047	0.014	0.0082	0.23	0.18	0.0091	0.085	0.43
Deciduous Forests	0.44	0.027	0.0013	0.00035	0.00040	0.00027	0.0034	0.0033	0.00016	0.0025	0.0030
Mixed Forests	0	0	0	0	0	0	0	0	0	0	0
Shrublands	17.88	0.71	0.027	0.041	0.013	0.0071	0.089	0.082	0.0052	0.069	0.050
Savannas	3.41	0.12	0.0030	0.0056	0.0010	0.0014	0.020	0.013	0.00079	0.0052	0.018
Wetlands	0.83	0.19	0.0030	0.0042	0.0012	0.0016	0.025	0.022	0.0010	0.013	0.014
Croplands	6.31	0.35	0.013	0.014	0.0065	0.0019	0.029	0.023	0.0029	0.0093	0.046
Others	-	-	-	-	-	-	-	-	-	-	-
Total	58.65	3.07	0.14	0.11	0.036	0.020	0.40	0.32	0.019	0.18	0.56

Appendix 3.2.4I: Typical Pollutant Emission of September 2013 (Gg/year)

Land Cover Type	CO_2	CO	CH_4	NO_x	NH_3	SO_2	PM_{10}	$PM_{2.5}$	EC	OC	NMVOC
Evergreen Forests	0	0	0	0	0	0	0	0	0	0	0
Deciduous Forests	0	0	0	0	0	0	0	0	0	0	0
Mixed Forests	0	0	0	0	0	0	0	0	0	0	0
Shrublands	0.42	0.017	0.00064	0.00096	0.00029	0.00017	0.0021	0.0019	0.00012	0.0016	0.0012
Savannas	0.67	0.023	0.00059	0.0011	0.00020	0.00027	0.0039	0.0025	0.00016	0.0010	0.0037
Wetlands	0.46	0.037	0.00059	0.00082	0.00024	0.00031	0.0049	0.0044	0.00020	0.0025	0.0027
Croplands	0.84	0.047	0.0017	0.0018	0.00087	0.00025	0.0039	0.0031	0.00039	0.0012	0.0061
Others	-	-	-	-	-	-	-	-	-	-	-
Total	2.39	0.12	0.0035	0.0047	0.0016	0.001	0.015	0.012	0.00087	0.0063	0.014

Appendix 3.2.4J: Typical Pollutant Emission of October 2013 (Gg/year)

Land Cover Type	CO_2	CO	CH_4	NO_x	NH_3	SO_2	PM_{10}	$PM_{2.5}$	EC	OC	NMVOC
Evergreen Forests	29.78	1.67	0.092	0.047	0.014	0.0082	0.23	0.18	0.0091	0.085	0.43
Deciduous Forests	0.088	0.0055	0.00027	0.000070	0.000080	0.000053	0.00069	0.00066	0.000032	0.00050	0.00059
Mixed Forests	0	0	0	0	0	0	0	0	0	0	0
Shrublands	0.42	0.017	0.00064	0.00096	0.00029	0.00017	0.0021	0.0019	0.00012	0.0016	0.0012
Savannas	10.09	0.35	0.0088	0.016	0.0029	0.0040	0.058	0.037	0.0024	0.015	0.055
Wetlands	0.57	0.55	0.0088	0.012	0.0035	0.0047	0.074	0.066	0.0031	0.037	0.040
Croplands	9.87	0.55	0.020	0.021	0.010	0.0029	0.046	0.036	0.0046	0.015	0.071
Others	-	-	-	-	-	-	-	-	-	-	-
Total	50.82	3.14	0.13	0.097	0.031	0.020	0.41	0.32	0.019	0.15	0.60

Appendix 3.2.4K: Typical Pollutant Emission of November 2013 (Gg/year)

Land Cover Type	CO_2	CO	CH_4	NO_x	NH_3	SO_2	PM_{10}	$PM_{2.5}$	EC	OC	NMVOC
Evergreen Forests	54.10	3.03	0.17	0.086	0.025	0.015	0.42	0.34	0.017	0.15	0.79
Deciduous Forests	26.51	1.66	0.081	0.021	0.024	0.016	0.21	0.20	0.0098	0.15	0.18
Mixed Forests	3.31	0.21	0.010	0.0026	0.0030	0.0020	0.026	0.025	0.0012	0.019	0.028
Shrublands	7.74	0.31	0.012	0.018	0.0054	0.0031	0.038	0.036	0.0023	0.030	0.022
Savannas	25.26	0.87	0.022	0.041	0.0074	0.010	0.15	0.093	0.0059	0.038	0.13
Wetlands	0.66	1.38	0.022	0.031	0.0088	0.012	0.18	0.16	0.0077	0.093	0.10
Croplands	28.14	1.58	0.058	0.060	0.029	0.0083	0.13	0.10	0.013	0.042	0.20
Others	-	-	-	-	-	-	-	-	-	-	-
Total	145.72	9.04	0.38	0.26	0.10	0.07	1.15	0.95	0.056	0.52	1.45

Appendix 3.2.4L: Typical Pollutant Emission of December 2013 (Gg/year)

Land Cover Type	CO_2	CO	CH_4	NO_x	NH_3	SO_2	PM_{10}	$PM_{2.5}$	EC	OC	NMVOC
Evergreen Forests	59.37	3.32	0.18	0.094	0.027	0.016	0.46	0.37	0.018	0.17	0.87

Deciduous Forests	196.97	12.33	0.60	0.16	0.18	0.12	1.55	1.49	0.072	1.11	1.33
Mixed Forests	29.02	1.816	0.089	0.023	0.027	0.018	0.23	0.22	0.011	0.16	0.25
Shrublands	54.24	2.15	0.082	0.12	0.038	0.021	0.27	0.25	0.016	0.21	0.15
Savannas	145.73	5.01	0.13	0.24	0.042	0.058	0.84	0.54	0.034	0.22	0.79
Wetlands	0.49	7.98	0.13	0.18	0.051	0.068	1.06	0.95	0.044	0.54	0.58
Croplands	39.39	2.21	0.081	0.084	0.041	0.012	0.18	0.15	0.018	0.058	0.29
Others	-	-	-	-	-	-	-	-	-	-	-
Total	525.21	34.82	1.29	0.90	0.41	0.31	4.59	3.97	0.21	2.47	4.26

APPENDIX 3.2.5 TEMPORAL VARIATION OF BURNED AREA

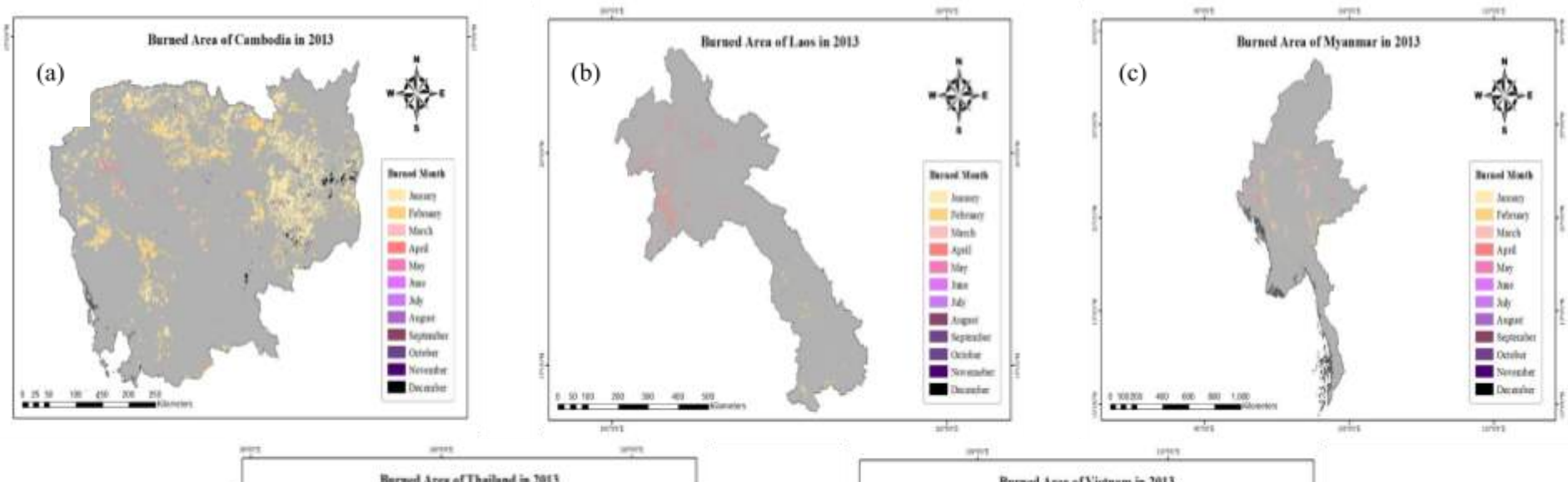

(d) (e)

Appendix 3.2.5A: Burned Area in MSEA for 2013; (a) Cambodia, (b) Laos, (c) Myanmar, (d) Thailand, (e) Vietnam

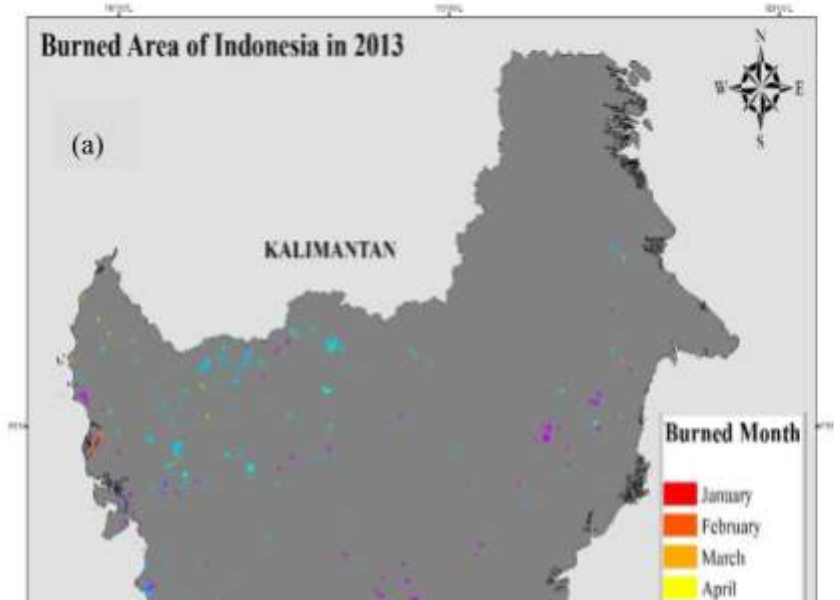

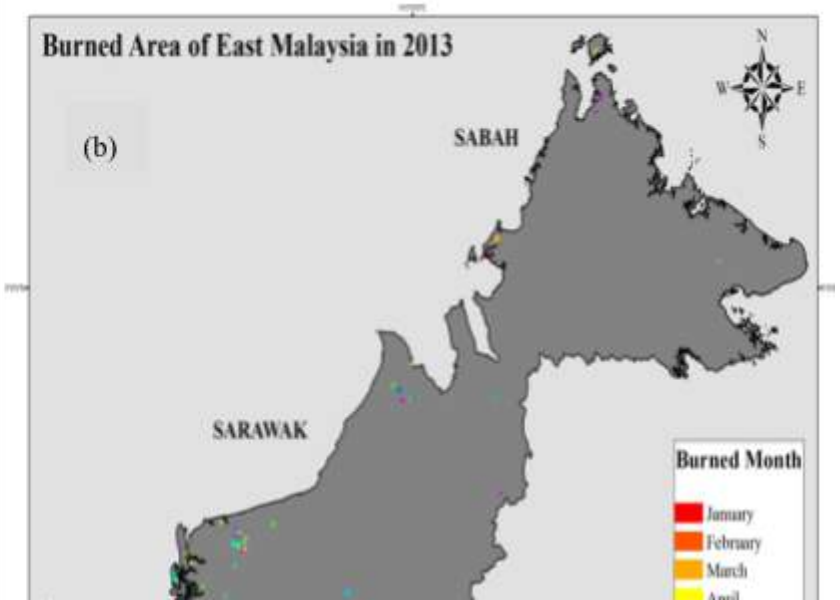

Appendix 3.2.5B: Burned Area in Borneo for 2013; (a) Kalimantan, (b) East Malaysia

APPENDIX 3.2.6 SPATIAL VARIATION OF BB EMISSION SPECIES

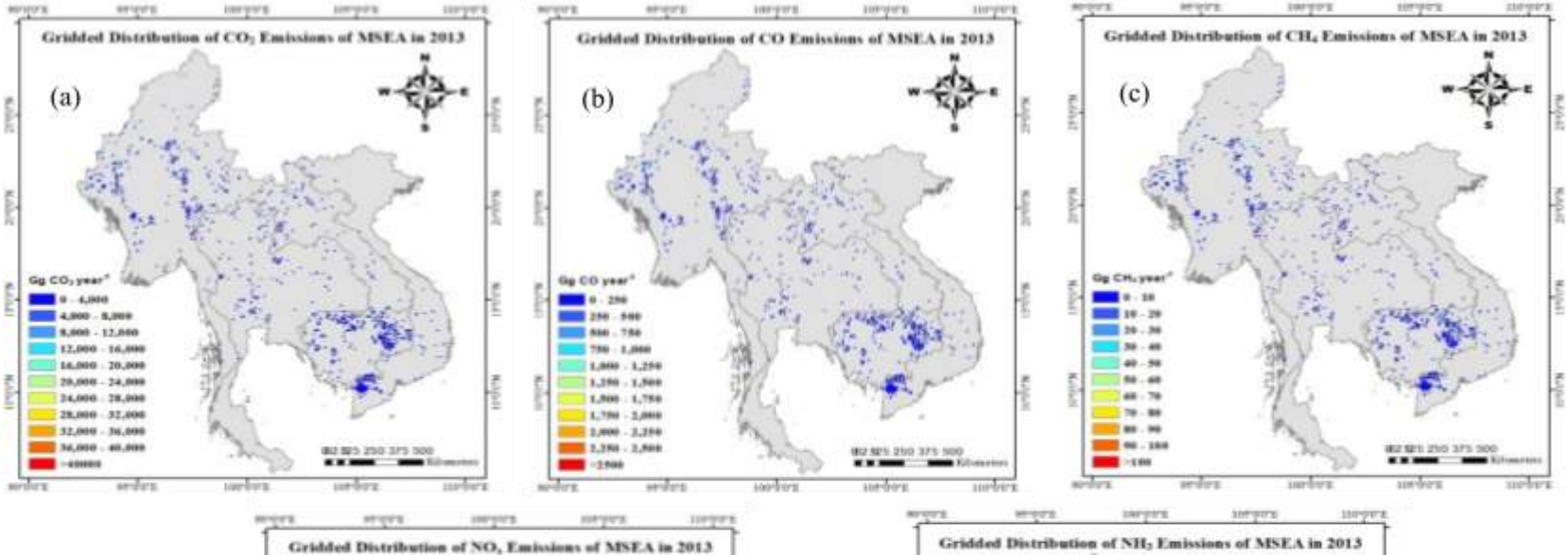

Appendix 3.2.6A: Gridded Distribution of Emissions source in MSEA for 2013; (a) CO_2, (b) CO, (c) CH_4, (d) NO_x, (e) NH_4

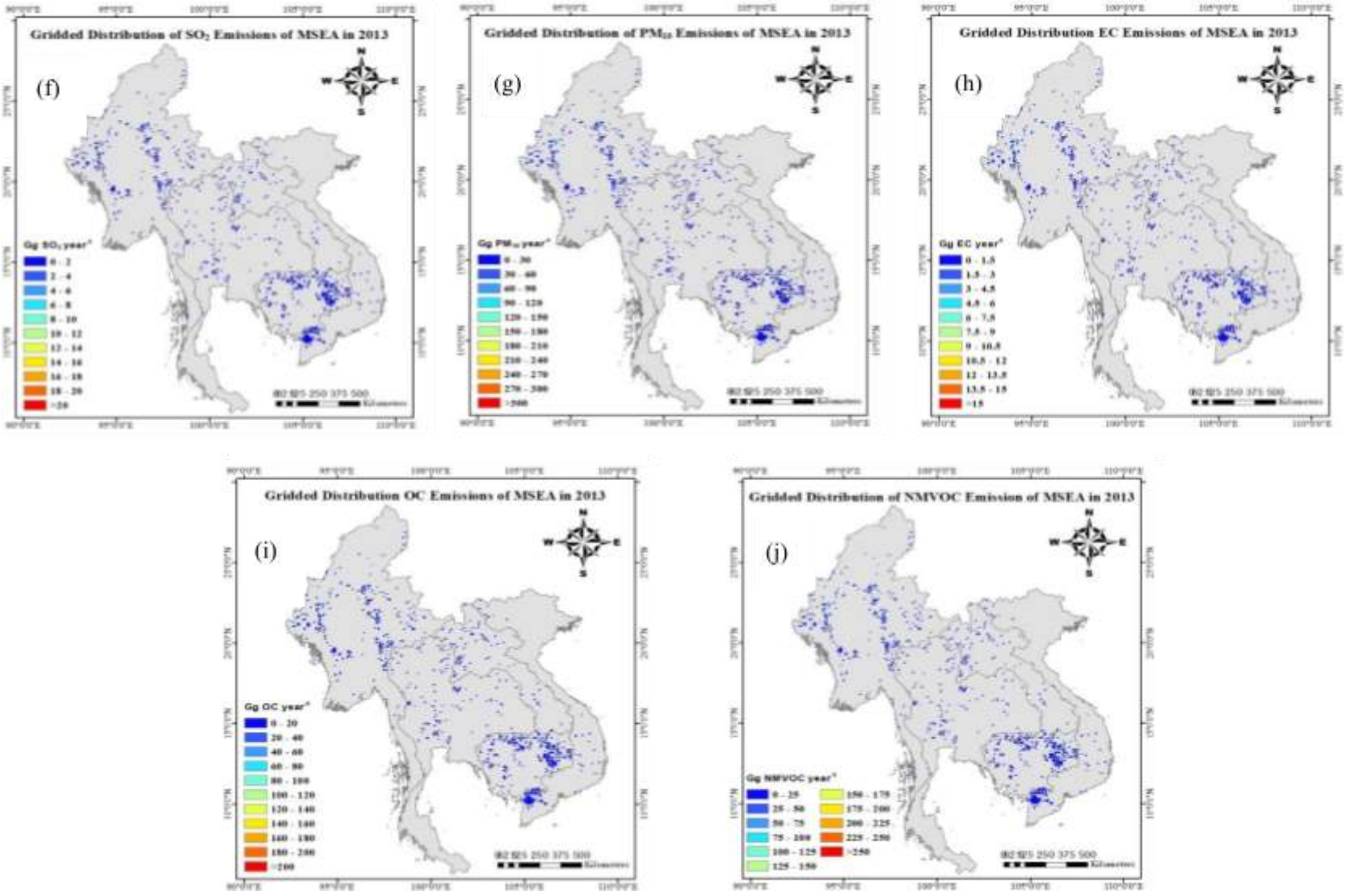

Appendix 3.2.6B: Gridded Distribution of Emissions source in MSEA for 2013; (f) SO_2, (g) PM_{10}, (h) EC, (i) OC, (j) NMVOC

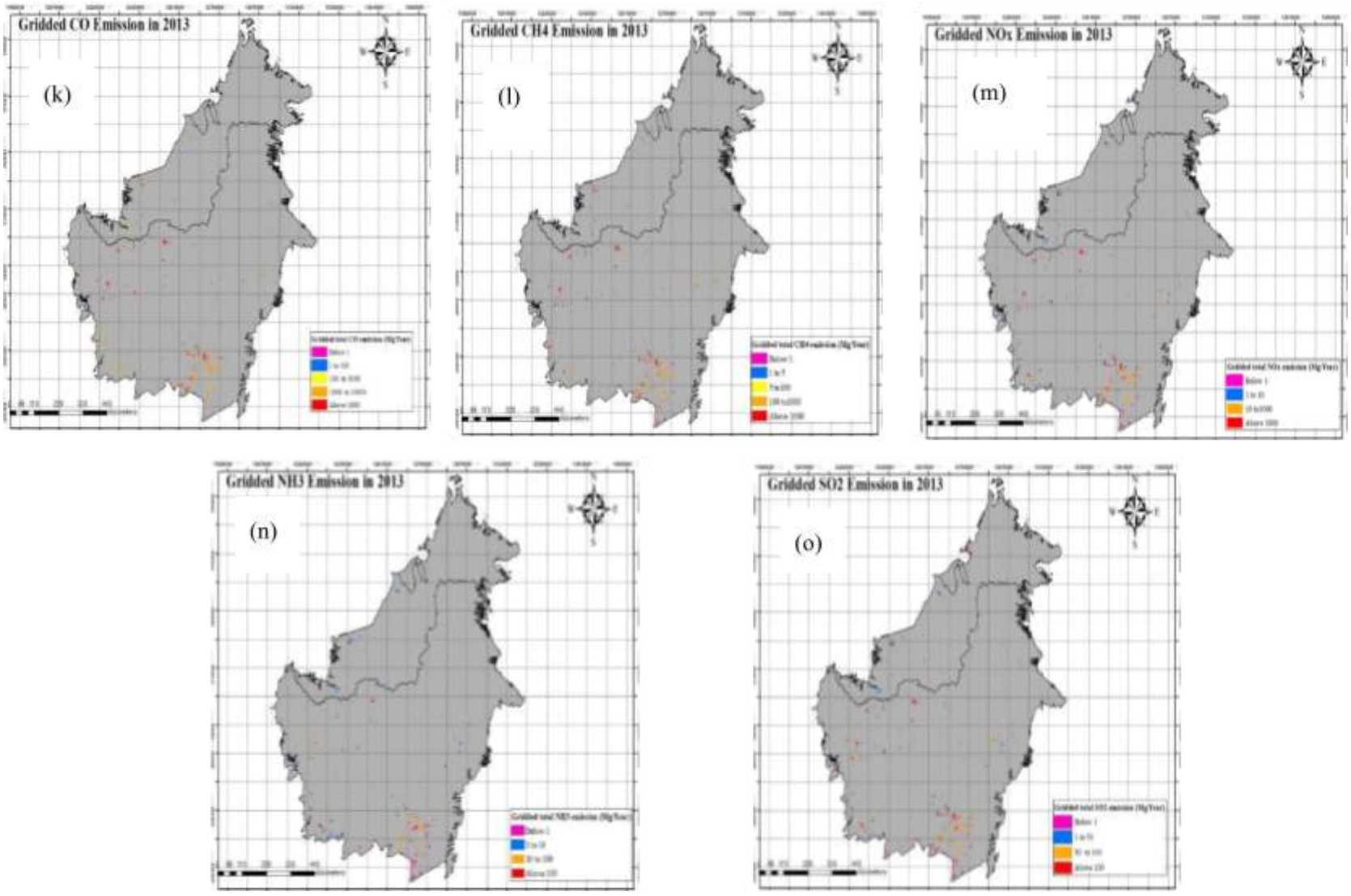

Appendix 3.2.6C: Gridded Distribution of Emissions source in Borneo for 2013; (k) CO, (i) CH_4, (m) NO_x, (n) NH_3, (o) SO_2

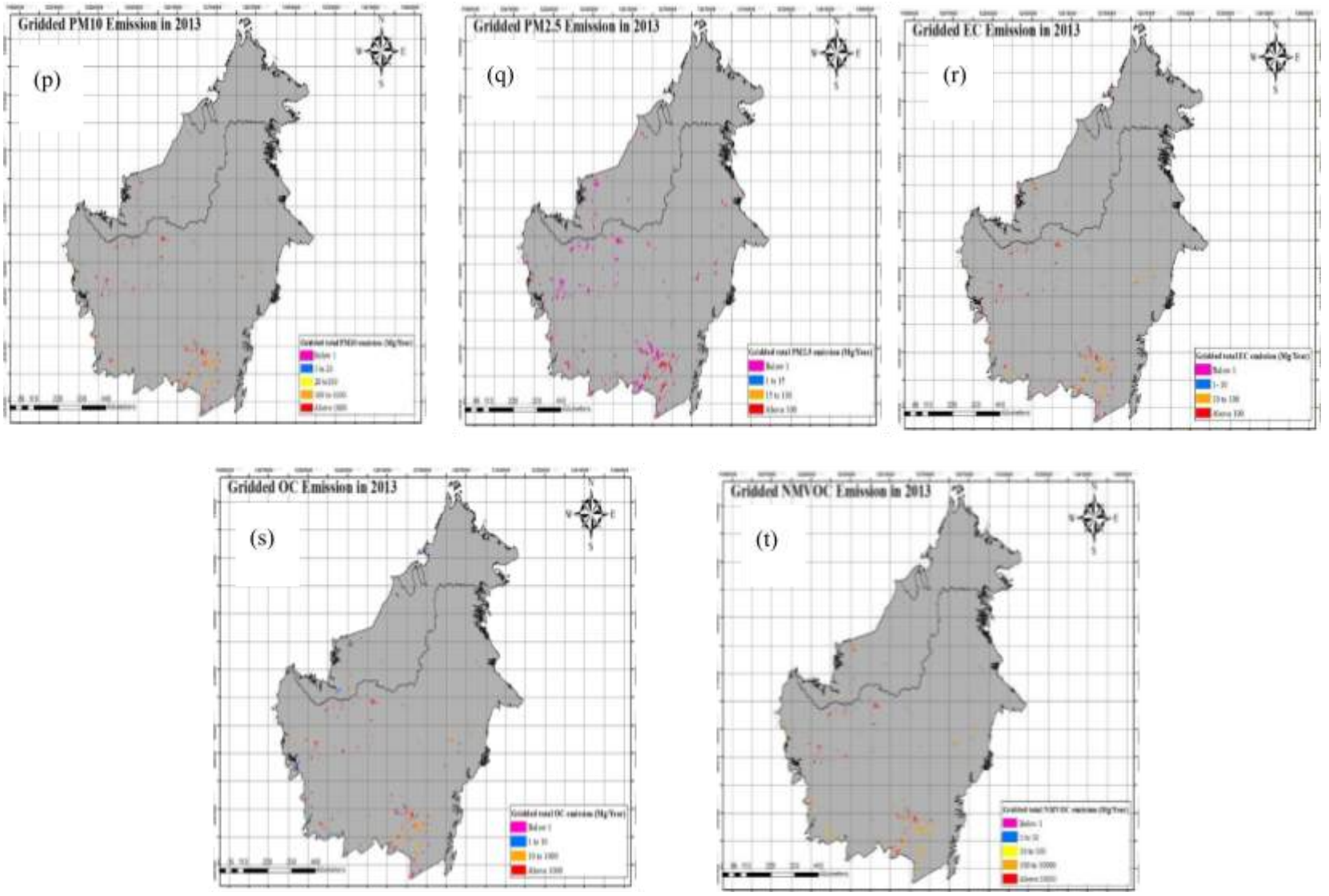

Appendix 3.2.6D: Gridded Distribution of Emissions source in Borneo for 2013; (p) PM_{10}, (q) $PM_{2.5}$, (r) EC, (s) OC, (t) NMVOC

APPENDIX 3.3 PROJECTED BIOGENIC EMISSION IN SEA

Appendix 3.3.1A: Projected isoprene emission over SEA region under RCP4.5

Isoprene Emission (tons/hr)										
Year	**2013**		**2030**		**2050**		**2070**		**2100**	
Region	**Jan**	**Jul**	**Jan**	**Jul**	**Jan**	**Jul**	**Jan**	**Jul**	**Jan**	**Jul**
Myanmar	2.10	5.14	2.89	5.77	3.35	3.11	2.24	5.76	1.73	4.48
Thailand	3.92	5.97	5.90	6.70	6.57	5.86	4.40	7.11	5.77	7.18
Cambodia	3.92	5.97	5.43	5.48	5.47	4.10	3.25	7.11	4.31	6.55
Laos	3.04	4.63	4.29	6.70	5.01	6.23	2.10	8.39	3.32	5.49
Vietnam	3.04	5.97	4.29	7.01	5.06	6.23	2.69	8.39	4.31	6.70
Malaysia	7.33	8.50	7.93	7.00	7.54	7.14	7.13	8.14	6.82	8.50
Indonesia	8.51	6.96	8.33	7.28	8.29	7.38	8.08	7.64	8.95	7.30
Philippines	3.86	5.98	4.63	6.61	4.88	7.41	4.85	5.93	3.79	6.11

Appendix 3.3.1B: Projected isoprene emission over SEA region under RCP6.0

Isoprene Emission (tons/hr)										
Year	**2013**		**2030**		**2050**		**2070**		**2100**	
Region	**Jan**	**Jul**	**Jan**	**Jul**	**Jan**	**Jul**	**Jan**	**Jul**	**Jan**	**Jul**
Myanmar	1.95	2.70	0.00	6.39	2.85	7.18	2.77	4.48	2.53	6.63
Thailand	3.77	5.65	0.22	5.69	6.31	6.39	6.02	6.94	5.53	7.87
Cambodia	3.53	4.39	0.33	4.89	5.19	6.39	5.22	6.21	5.53	7.14
Laos	2.66	4.06	0.23	5.40	5.19	5.14	3.47	5.91	4.81	5.50
Vietnam	2.67	4.31	0.34	5.40	5.19	6.39	3.88	5.93	4.97	5.50
Malaysia	6.22	6.52	4.11	8.23	7.11	6.87	6.04	7.28	8.37	10.77
Indonesia	9.13	6.52	15.86	7.34	9.41	7.38	8.61	8.33	9.72	9.74
Philippines	4.02	5.35	4.51	5.97	4.81	5.99	4.96	5.93	4.83	7.56

Appendix 3.3.1C: Projected isoprene emission over SEA region under RCP8.5

Isoprene Emission (tons/hr)										
Year	**2013**		**2030**		**2050**		**2070**		**2100**	
Region	**Jan**	**Jul**	**Jan**	**Jul**	**Jan**	**Jul**	**Jan**	**Jul**	**Jan**	**Jul**
Myanmar	2.55	5.47	2.22	1.37	2.52	6.03	3.39	6.73	1.72	7.60
Thailand	3.76	5.59	4.35	3.13	5.66	7.05	7.17	7.22	4.52	8.95
Cambodia	3.46	5.59	4.04	3.13	4.96	7.03	6.00	8.40	3.37	7.05
Laos	1.98	5.27	2.15	3.48	3.94	5.82	5.18	8.95	2.98	5.87
Vietnam	3.03	5.82	2.95	3.48	4.42	7.03	5.52	8.79	3.02	7.05
Malaysia	6.86	7.74	7.06	8.48	6.38	9.10	7.83	9.16	8.83	11.87
Indonesia	7.76	7.86	8.59	7.65	8.66	7.79	10.70	8.28	15.35	17.92
Philippines	4.25	5.92	4.21	4.44	4.53	6.69	5.42	7.25	5.26	8.64

No.	Conferences/ Symposia/ Workshops	Agenda	Date/ Venue	Participants	Organisations
1	I[st] APN Research Workshop & Meeting	Agenda: 1. APN Project Introduction 2. Regional climate change and air quality 3. Biogenic emissions and surface ozone 4. Regional climate modeling scenarios 5. Forest fire and emission inventory 6. Biomass and industries emissions 7. Urban pollution and emission inventories 8. Aerosols and long range transport 9. Airborne particulate and human health 10. Research Collaboration Meeting; *a. Research Planning* *b. Research Objectives* *c. Research Team & Responsibilities* *d. Research Funding* e. *Research Output – Publications & Conferences*	14-15 September 2017 Ranau/Kota Kinabalu, Malaysia	**Research Team:** 1. Assoc. Prof. Dr. Justin Sentian (Project Leader) 2. Assoc Prof. Dr. Carolyn Melissa Payus 3. Assoc. Prof. Dr. Mohd Shahrul Mohd Nadzir 4. Dr. Steven Kong Soon Kai 5. Assoc. Prof. Dr. Mylene G. Cayetano 6. Assoc. Prof. Dr. Nina Yulianti 7. Prof. Ir. Dr Puji Lestari 8. Dr. Narisara Thongboonchoo 9. Dr. Ronald Macatangay **Research Assistants:** 1. Franky Herman 2. Felicia Sue 3. Lam Hui Yee 4. Nurul Fazlina Osman **Workshop Participants:** 1. Kay Soo Hooi 2. Kwong Ye Leng	1. Universiti Malaysia Sabah Malaysia/jsentian@ums.edu.my 2. Universiti Malaysia Sabah, Malaysia/melpayus@ums.edu.my 3. Universiti Kebangsaan Malaysia/ shahrulnadzir@ukm.edu.my 4. National Central University, Taiwan, skong@gmail.com 5. University of The Phillipines Diliman/mbgonzaga@gmail.com 6. University of Palangkaraya, Indonesia/ nyulianti@agr.upr.ac.id 7. Institute Technology of Bandung, Indonesia/pujilest@indo.net.id 8. King Mongkut's Institute of Technology Thailand/nthongbo@gmail.com 9. NARIT, Thailand/ ronmcdo@gmail.com 1. Universiti Malaysia Sabah 2. Universiti Malaysia Sabah 3. Universiti Malaysia Sabah 4. Universiti Malaysia Sabah 1. Environmental Science Dept, UMS

				3. Voo Shen Mui	2. Environmental Science Dept, UMS
				4. Tan Eng That	3. Environmental Science Dept, UMS
				5. Lam Kwai Hiong	4. Environmental Science Dept, UMS
				6. Kueh Kiang Joo	5. Environmental Science Dept, UMS
				7. Chia Ngiik Hiong	6. Environmental Science Dept, UMS
				8. Yeap Kiew Lee	7. Environmental Science Dept, UMS
				9. Ang Ee Voon	8. Environmental Science Dept, UMS
				10. Chan Kah Yin	9. Environmental Science Dept, UMS
				11. Eileen Ho Ming Ying	10. Environmental Science Dept, UMS
				12. Ang Pei Wen	11. Environmental Science Dept, UMS
				13. Siti Mastura Bt Mat Zain	12. Environmental Science Dept, UMS
				14. Khor Shi Yun	13. Environmental Science Dept, UMS
				15. Pamela Ang Jee-Ann	14. Environmental Science Dept, UMS
				16. Jennifer Ng Phei Ling	15. Environmental Science Dept, UMS
				17. Putri Atilia Juasnatasha Juaser	16. Earth Science Dept, FSSA, UMS
				18. Priya A/P Mohan	17. Earth Science Dept, FSSA, UMS
				19. Low Suee Ling	18. Earth Science Dept, FSSA, UMS
				20. Lim Yen Mei	19. Earth Science Dept, FSSA, UMS
				21. Sucmalaa A/P Sing Hooi	20. Earth Science Dept, FSSA, UMS
				22. Lorny A/P Som	21. Earth Science Dept, FSSA, UMS
				23. Wong Pick Leh	22. Earth Science Dept, FSSA, UMS
				24. Julie Yong Fui Mee	23. Earth Science Dept, FSSA, UMS
				25. Kassthurei A/P Yogarajan	24. Forestry Dept, FIF, UMS
				26. Ung Chen Yee	25. Forestry Dept, FIF, UMS
				27. Anzella Binti Juwilin Kuin	26. Forestry Dept, FIF, UMS
				28. Asnul Hisyam Bin Mohd Ali	27. Forestry Dept, FIF, UMS
				29. Claoston Anak Nardon	28. Forestry Dept, FIF, UMS
				30. Norashidah Abdul Razak	29. Forestry Dept, FIF, UMS
				31. Noreenawati Nordin	30. Forestry Dept, FIF, UMS
				32. Salina Binti Nor Azam	31. Forestry Dept, FIF, UMS
				33. Goh Mea How	32. Forestry Dept, FIF, UMS
				34. Tan Zhong Qing	33. Forestry Dept, FIF, UMS
				35. Ong Qi Hong	34. Sabah Wetland Society
				36. Wong Yie Sing	35. Sabah Wetland Society
				37. Mohd Fitri Bin Johari	36. Sabah Wetland Society
				38. Muhammad Izhar Bin Shamsudin	37. WWF Sabah
				39. Jesson Oliver Lian Lee	38. WWF Sabah

				40. Melissa Melody Leduning 41. Saidatul Akma Nurliyana Bt Safian 42. Harry John Kuling 43. Fabio Isaac Rahul Anak Rajes 44. Fairuz Afiqah Binti Buslima 45. Chin Kah Sing 46. Vitalis Moduying 47. Susan Pudin	39. WWF Sabah 40. Department of Environment Malaysia 41. Department of Environment Malaysia 42. Department of Environment Malaysia 43. Department of Environment Malaysia 44. Environmental Protection Department 45. Environmental Protection Department 46. Environmental Protection Department 47. Environmental Protection Department
2	2nd APN Research Workshop & Meeting	Agenda: 1. Forest Fire and Southeast Asia 2. Greenhouse Gases and Landuse 3. Urban Air Quality 4. Climate Change in Southeast Asia 5. Biomass Emission and Landuse 6. Research Collaboration Meeting; *a. Research Progress Planning* *b. Research Team & Responsibilities* *c. Research Output – Publications & Conferences*	29-31 May 2018 Manila, Philippines	**Research Team:** 1. Assoc. Prof. Dr. Justin Sentian (Project Leader) 2. Assoc Prof. Dr. Carolyn Melissa Payus 3. Assoc. Prof. Dr. Mohd Shahrul Mohd Nadzir 4. Dr. Steven Kong Soon Kai 5. Assoc. Prof. Dr. Mylene G. Cayetano 6. Assoc. Prof. Dr. Nina Yulianti 7. Prof. Ir. Dr Puji Lestari 8. Dr. Narisara Thongboonchoo 9. Dr. Ronald Macatangay **Research Assistants:** 1. Franky Herman 2. Felicia Sue 3. Lam Hui Yee	1. Universiti Malaysia Sabah Malaysia/jsentian@ums.edu.my 2. Universiti Malaysia Sabah, Malaysia/melpayus@ums.edu.my 3. Universiti Kebangsaan Malaysia/ shahrulnadzir@ukm.edu.my 4. National Central University, Taiwan, skong@gmail.com 5. University of The Phillipines Diliman/mbgonzaga@gmail.com 6. University of Palangkaraya, Indonesia/ nyulianti@agr.upr.ac.id 7. Institute Technology of Bandung, Indonesia/pujilest@indo.net.id 8. King Mongkut's Institute of Technology Thailand/nthongbo@gmail.com 9. NARIT, Thailand/ ronmcdo@gmail.com 1. Universiti Malaysia Sabah 2. Universiti Malaysia Sabah

				4. Nurul Fazlina Osman **Workshop Participants:** 1. Abante Carlo 2. Abino Azyleah 3. Alosnos Elmer 4. Asilo Sonia 5. Aviso Jamie Ara 6. Baludo Marjohn 7. Banasihan Ethel Princess 8. Bantayan Nathaniel 9. Barua Leonardo 10. Bermoy Monalaine 11. Betos Christy Mae 12. Bilaro Virgil 13. Blanco Ariel 14. Camaso Eliza 15. Candare Rudolph Joshua 16. Carandang Monina 17. Castillo Alyssa Dawn 18. Del Rosario Collin 19. Dela Paz Maria Angelica 20. Diocampo Ryan 21. Guihawan Jaime 22. Gutierrez Mary Anne 23. Hilario Flaviana 24. Hilario Paul Leonard 25. Ibay Analiza 26. Ignacio Nicole 27. Lopez Toni Beth	3. Universiti Malaysia Sabah 4. Universiti Malaysia Sabah 1. Bicol University 2. Laguna Lake Development Authority 3. Philippine Rice Research Institute 4. Philippine Rice Research Institute 5. Manila Observatory 6. Institute of Environmental Science and Meteorology 7. International Rice Research Institute (IRRI) 8. UP Los Banos 9. UP Los Banos 10. Geo-SAFER Mindanao Program/Caraga State University 11. University of the Philippines Manila 12. Bicol University 13. University of the Philippines (Department of Geodetic Engineering) 14. ICCEM-CLSU 15. Center for Resource Assessment, Analytics and Emerging Technologies 16. University of the Philippines Los Banos 17. UP IESM 18. University of the Philippines Manila 19. Manila Observatory 20. UP IESM 21. UP Training Center for Applied Geodesy and Photogrammetry 22. International Rice Research Institute 23. PAG-ASA 24. UP EEEI 25. Technological University of the Philippines 26. IESM Microsat

				28. Lor Daniel 29. Losaria Paul Mabalay 30. Mary Rose Macagba 31. Sharon Feliza Ann Macagba 32. Macalalad Ernest 33. Olalia Laverne 34. Oliveros Jervie 35. Paguirigan Neale Marvin 36. Paringit Enrico 37. Paulete Honeybeth 38. Ricafort Neil 39. Rivera Roselle Leah 40. Rolloda Irjay 41. Romuge Gene Christhopher 42. San Pedro Jonah John 43. Santos Rijaldia 44. Tamondong Ayin	27. Technological University of the Philippines 28. Institute of Environmental Science and Meteorology 29. UP IESM 30. Philippine Rice Research Institute 31. University of the Philippines Los Banos 32. MAPUA UNIVERSITY 33. Sugar Regulatory Administration 34. Technological University of the Philippines 35. International Rice Research Institute (IRRI) 36. University of the Philippines 37. Laguna Lake Development Authority 38. CENRO - CITY GOV'T OF PARANAQUE 39. College of Social Work and Community Development 40. UP IESM 41. International Rice Research Institute 42. UP IESM 43. National Mapping and Resource Information Authority 44. UP Department of Geodetic Engineering
3	3rd APN Research Workshop and Meeting	Agenda: 1. Regional climate change 2. Climate Change and IPCC 3. Climate Change and Biomass Burning 4. Biogenic Emissions and Inventory 5. Biomass Emissions and Atmospheric	7-9 December 2018 Chiang Mai, Thailand	**Research Team:** 1. Assoc. Prof. Dr. Justin Sentian (Project Leader) 2. Assoc Prof. Dr. Carolyn Melissa Payus 3. Dr. Wilson Wong 4. Assoc. Prof. Dr. Mohd Shahrul Mohd Nadzir	1. Universiti Malaysia Sabah Malaysia/jsentian@ums.edu.my 2. Universiti Malaysia Sabah, Malaysia/melpayus@ums.edu.my 3. Universiti Malaysia Sabah /wilsonw@ums.edu.my 4. Universiti Kebangsaan Malaysia/ shahrulnadzir@ukm.edu.my

		Acidity 6. Short-Lived Climate Pollutants 7. Air Pollution Inventory 8. Ozone Chemistry Modelling 9. Air Pollution in Thailand 10. Application of Remote Sensing in Biomass Emission Inventory 11. Research Collaboration Meeting; *a. Research Progress Planning* *b. Research Team & Responsibilities* *c. Research Output – Publications & Conferences*		5. Dr. Steven Kong Soon Kai 6. Assoc. Prof. Dr. Mylene G. Cayetano 7. Assoc. Prof. Dr. Nina Yulianti 8. Prof. Ir. Dr Puji Lestari 9. Dr. Narisara Thongboonchoo 10. Dr. Ronald Macatangay **Research Assistants:** 1. Franky Herman 2. Vivian Kong Wan Yee 3. Vichawan Sakulsupich 4. Sherin Hassan Bran **Workshop Participants:**	5. National Central University, Taiwan, skong@gmail.com 6. University of The Phillipines Diliman/mbgonzaga@gmail.com 7. University of Palangkaraya, Indonesia/ nyulianti@agr.upr.ac.id 8. Institute Technology of Bandung, Indonesia/pujilest@indo.net.id 9. King Mongkut's Institute of Technology Thailand/nthongbo@gmail.com 10. NARIT, Thailand/ ronmcdo@gmail.com 1. Universiti Malaysia Sabah 2. Universiti Malaysia Sabah 3. NARIT, Thailand 4. NARIT, Thailand
4	I[st] APN Research Workshop	Agenda: 1. Climate Change in Southeast Asia 2. Biomass Emission Inventory 3. Biogenic Emission Inventory 4. Climate Change Impact on Regional Air Quality 5. Research Collaboration Meeting; *a. Research Progress and Final Meeting* *b. Research Future Direction* *c. Research Funding*	28-29 August Kota Kinabalu/Malaysia (Hybrid: Physical & Online))	**Research Team:** 1. Assoc. Prof. Dr. Justin Sentian (Project Leader) 2. Assoc Prof. Dr. Carolyn Melissa Payus 3. Assoc. Prof. Dr. Mohd Shahrul Mohd Nadzir 4. Dr. Steven Kong Soon Kai 5. Assoc. Prof. Dr. Mylene G. Cayetano 6. Assoc. Prof. Dr. Nina Yulianti 7. Prof. Ir. Dr Puji Lestari	1. Universiti Malaysia Sabah Malaysia/jsentian@ums.edu.my 2. Universiti Malaysia Sabah, Malaysia/melpayus@ums.edu.my 3. Universiti Kebangsaan Malaysia/ shahrulnadzir@ukm.edu.my 4. National Central University, Taiwan, skong@gmail.com 5. University of The Phillipines Diliman/mbgonzaga@gmail.com 6. University of Palangkaraya, Indonesia/ nyulianti@agr.upr.ac.id

		d. *Research Output – Publications & Conferences*		8. Dr. Narisara Thongboonchoo 9. Dr. Ronald Macatangay **Research Assistants:** 1. Franky Herman 2. Vivian Kon Wan Yee 3. Lam Hui Yee 4. Nurul Fazlina Osman 5. Nathaniel Maikol **Workshop Participants (Physical):** 1. Justin Sentian 2. Melissa Leduning 3. Dr. Vijaykumar Pattathil 4. Nathaniel Bin Maikol 5. Hartini Binti Mahidin 6. Nur Afifah Nabila Binti Masnin 7. Amelia Syahira Binti Mohd Noor 8. Maxcynable Anak Pengarah 9. Teo Yu Rou 10. Azilah Binti Boseng 11. Siti Irbah Binti Anuar 12. Nur Ain Batrishiya Binti Abd Razid 13. Nur Syamimi Syauqina Binti Yusof 14. Nuratiqah Binti Mohamad Alias 15. Nur Adibah Binti Mohd Shaiful Bahri 16. Chai Yee Theng 17. Alfred Cheam 18. Ooi Xin Yi 19. Pheeona Connie Teo 20. Maryell Irisha 21. Salwa Binti	7. Institute Technology of Bandung, Indonesia/pujilest@indo.net.id 8. King Mongkut's Institute of Technology Thailand/nthongbo@gmail.com 9. NARIT, Thailand/ ronmcdo@gmail.com 1. Universiti Malaysia Sabah 2. Universiti Malaysia Sabah 3. Universiti Malaysia Sabah 4. Universiti Malaysia Sabah 1. Universiti Malaysia Sabah 2. Universiti Malaysia Sabah 3. Universiti Malaysia Sabah 4. Universiti Malaysia Sabah 5. Universiti Malaysia Sabah 6. Universiti Malaysia Sabah 7. Universiti Malaysia Sabah 8. Universiti Malaysia Sabah 9. Universiti Malaysia Sabah 10. Universiti Malaysia Sabah 11. Universiti Malaysia Sabah 12. Universiti Malaysia Sabah 13. Universiti Malaysia Sabah 14. Universiti Malaysia Sabah 15. Universiti Malaysia Sabah 16. Universiti Malaysia Sabah 17. Universiti Malaysia Sabah 18. Universiti Malaysia Sabah 19. Universiti Malaysia Sabah 20. Universiti Malaysia Sabah 21. Universiti Malaysia Sabah

				Workshop Participants (Online):	
				1. Mahendar Chand Rajwar	India
				2. Diaby Kassamba Mohamed Lamine	Cote D'Ivoire
				3. Sanny Rathore	India
				4. Dudam Bharath Kumar	India
				5. Dr. Dhanya Kc	India
				6. Nina Yulianti	Indonesia
				7. Muhammad Abdul Basit Ahmad Tajudin	Japan
				8. Mohd Afzanizam Muda	Malaysia
				9. Wong Yiik Mee	Malaysia
				10. Franklin Berandah	Malaysia
				11. Muhammad Zahiruddin Bin Zaki	Malaysia
				12. Mohd Shahrul Mohd Nadzir	Malaysia
				13. Mohd Talib Latif	Malaysia
				14. Abdul Hakim Bin Ramli	Malaysia
				15. Hartini Mahidin	Malaysia
				16. Dr Hasifah Binti Abdul Aziz	Malaysia
				17. Royston Uning	Malaysia
				18. Juliana Jalaludin	Malaysia
				19. Fairus Bin Muhamad Darus	Namibia
				20. Anna Alfeus	Pakistan
				21. Naeem Hussain	Pakistan
				22. Fasiha Safdar	Philippines
				23. Hannah Meim	Philippines
				24. Larry Aragon	Philippines
				25. Angelo Benedict Ragunjan	Philippines
				26. Munir J. Baldomero	Philippines
				27. Jervie Oliveros	Philippines
				28. Mary Crystalline T. Araracap	Philippines
				29. Mylene Cayetano	Philippines
				30. Krishna E. Santos	Philippines
				31. Karen Apoloan	Thailand
				32. Krishna E. Santos	Thailand
				33. Worradorn Phairuang	Thailand
				34. Dr Ling Song Kai	Thailand
					Thailand

				35. Jirasak Noisapung 36. Orachorn Kamnoet 37. Panwadee Suwattiga 38. Thao Pham 39. Dr. Rer. Nat. Ronald C. Macatangay 40. Radshadaporn Janta 41. Sherin Bran 42. Vanisa 43. Anurak Chakpor 44. Songsit 45. Worradorn Phairuang 46. Angkhana Ketjalan 47. Pankaj Kumar Jha 48. Zeeba Saeed 49. Zahid Naeem Qaisrani	Thailand Thailand Thailand Thailand Thailand Thailand Thailand Thailand Thailand Thailand Thailand
5	Seminar Science and Technology, Universiti Malaysia Sabah	Agenda: 1. Biogenic Emission in Southeast Asia 2. Greenhouse Gas Emission	6-7 October 2020 Kota Kinabalu Malaysia (Online)	**Participants:** 1. Assoc. Prof. Dr. Justin Sentian (Session Chair) 2. Vivian Kong Wan Yee (Presenter) 3. John Harry Kuling (Presenter) Other Participants: - Universiti Malaysia Sabah - Etc	Universiti Malaysia Sabah Universiti Malaysia Sabah Universiti Malaysia Sabah Malaysia Thailand Indonesia Philippines etc

Funding sources outside the APN

In-Kind Support:

a) Universiti Malaysia Sabah
b) University of the Philippines Diliman
c) NARIT, Thailand
d) Department of Environment Malaysia

List of Young Scientists

1. *Franky Herman*
   He is actively involved in this project since its inception of this project. As a Research Assistant and postgraduate student at the Universiti of Malaysia Sabah, he was assigned to work on regional climate change and air quality modelling. He obtained his MSc in Environmental Science in 2019.
   Contact: +60196461643
   Email: frankypeng62@gmail.com

   "I am very thankful for allowing working with Assoc. Prof. Dr. Justin Sentian (Supervisor) in climate change and air quality modelling. Being a research assistant and at the same time a postgraduate student, I have learned to run and analyse the modelling results, which is something new to me. I also had the opportunity to meet with other participants during the meeting and workshop, which enriched my research interest and network. I hope I can involve more work like this in the future" – Franky Herman

2. *Vivian Kong*
   She is involved mainly in the research related to biogenic emission modelling in Southeast Asia. She is also a Research Assistant and postgraduate student at the Universiti of Malaysia Sabah. She has just completed her master's thesis in 2021.
   Contact: +60149693932
   Email: vvnkong96@gmail.com

   "Biogenic emission is something new to me. I'm very grateful to be part of the research team on this subject at Universiti Malaysia Sabah. My involvement in this work has widened my horizon in this field and hope to pursue my research further on this subject in the future"
   – Vivian Kong Wan Yee

3. *Harry John Kuling*
   He is involved mainly in research related to regional land-use and greenhouse gas emissions. He is also a Research Assistant and postgraduate student at the Universiti of Malaysia Sabah. He has just completed his master's thesis in 2021.
   Contact: +60109673420
   Email: harryjohnk@gmail.com

   "I only involved in a small part of the APN project, which I enjoyed especially dealing with land-use and greenhouse gas. I had the opportunity to work with a great research team which I appreciated. I hope I have the opportunity with the team again in the near future.
   – John Harry Kuling

Glossary of Terms

LIST OF UNITS

^{o}	-	Degree
^{o}C	-	Degree Celsius
cm	-	Centimetre
$g\ kg^{-1}$	-	Gram per kilogram
K	-	Kelvin
km	-	Kilometre
km^2	-	Kilometre square
m	-	Meter
m^2m^{-2}	-	Meter square per meter sqaure
m^3m^{-3}	-	Meter cube per meter cube
mg	-	Milligram
$mgC\ g^{-2}\ h^{-1}$	-	Milligram of carbon per gram square per hour
$mgm^{-2}\ h^{-1}$	-	Milligram per meter square per hour
ms^{-1}	-	Meter per second
Tg	-	Terragram
$Tg\ yr^{-1}$	-	Terragram per year
$TgC\ yr^{-1}$	-	Terragram of carbon per year
tons/hr	-	Tonnes per hour
$\mu gC\ hr^{-1}$	-	Microgram of carbon per hour
$\mu g\ g^{-1}\ h^{-1}$	-	Microgram per gram per hour
$\mu mol\ m^{-2}\ s^{-1}$	-	Micromole per meter square per second
Wm^{-2}	-	Watts per meter square

LIST OF SYMBOLS

%	-	Percentage
>	-	Greater than
<	-	Lower than
^{2}	-	Power of two, square
^{3}	-	Power of three, cube
γ_{CE}	-	Variation due to Leaf Area Index (LAI) and light, temperature, humidity and wind conditions within the canopy environment
γ_{LAI}	-	Variation of LAI compared to standard conditions of 5 m^2m^{-2}
γ_P	-	Variation of radiation
γ_{SM}	-	Variation due to soil moisture
γ_T	-	Variation of temperature
γ_{age}	-	Variation due to leaf age

LIST OF ABBREVIATIONS

AFWA	-	Department of Defense's Air Force Weather Agency
AR5	-	Fifth Assessment Report
AR6	-	Sixth Assessment Report
ARW	-	Advanced Research Model
AVOC	-	Anthropogenic Volatile Organic Compound
C_i	-	Leaf Internal concentration
CB4	-	Carbon Bond Mechanism 4
CB5	-	Carbon Bond Mechanism 5

CB6	-	Carbon Bond Mechanism 6
CESM	-	Community Earth System Model
CH_4	-	Methane
CMIP3	-	Coupled Model Intercomparison Experiment Phase 3
CMIP5	-	Coupled Model Intercomparison Experiment Phase 5
CMIP6	-	Coupled Model Intercomparison Experiment Phase 6
CO	-	Carbon Monoxide
CO_2	-	Carbon Dioxide
CORDEX	-	Coordinated Regional Climate Downscaling Experiment
DOE	-	Department of Environment
DMAPP	-	Dimethylally Pyrophosphate
ECMWF	-	European Centre for Medium-Range Weather Forecasting Nanometre
ENSO	-	El~Niño-Southern Oscillation
ESRL	-	Earth Systems Research Laboratory
FAA	-	Federal Aviation Administration
Fa2	-	Factor of Two
FB	-	Fractional Bias
GCM	-	Global Climate Model
GDAS	-	Global Dataset Assimilation Process
GHGs	-	Greenhouse gases
GLOBEIS	-	Global Biosphere Emissions and Interactions System
GSD	-	Global Systems Division
GTS	-	Global Telecommunications System
IPCC	-	Intergovernmental Panel on Climate Change
LAI	-	Leaf Area Index
IOD	-	Indian Ocean Dipole
MEP	-	Methyl Erythritol 1-Phosphate

MEGAN	-	Model of Emissions of Gases and Aerosols from Nature
MetMsia	-	Malaysia Meteorological Department
MJO	-	Madden–Julian Oscillation
MODIS	-	Moderate Resolution Imaging Spectroradiometer
MOZART	-	Model for Ozone and Related Chemical Tracers
MMM	-	Mesoscale Microscale Meteorology Division
NAO	-	North Atlantic Oscillation
NASA	-	National Aeronautics and Space Administration
NCAR	-	National Centre for Atmospheric Research
NCEP	-	National Centre of Environmental Prediction
NetCDF	-	Network Common Data Form
NMB	-	Normalized Mean Bias
NMBVOC	-	Non-methane Biogenic Volatile Organic Compound
NMM	-	Non-hydrostatic Mesoscale Model
NMSE	-	Normalised Mean Square Error
MSE	-	Mean Square Error
NO_X	-	Nitrogen Oxides
NO_2	-	Nitrogen Dioxide
NOAA	-	National Oceanographic and Atmosphere Administration
OH	-	Hydroxyl
PAN	-	Peroxyacetyl Nitrate
PAR	-	Photosynthetic Active Radiation
PBL	-	Planetary Boundary Layer
PFT	-	Plant Functional Type
$PM_{2.5}$	-	Particulate Matter (Diameter of less than 2.5 micrometers)
PPFD	-	Photosynthetic Photon Flux Density
PRECIS	-	Providing Regional Climates for Impact Studies
RCP	-	Representative Concentration Pathway

RCM	-	Regional Climate Modelling
RMSE	-	Root Mean Square Error
RO_2	-	Organic Peroxy Radical
SEA	-	Southeast Asia
SEACLID	-	Southeast Asia Regional Climate Downscaling
SOA	-	Secondary Organic Aerosol
SO_2	-	Sulphur Dioxide
SRES	-	Special Report on Emissions Scenarios
SSP	-	Shared Socioeconomic Pathway
UTC	-	Universal Time Coordinate
Ver	-	Version
VOCs	-	Volatile organic compounds
WPS	-	WRF Pre-processing System
WRF	-	Weather Research Forecast
WRF-DA	-	WRF Data Assimilation

1. Seminar Science and Technology, University Malaysia Sabah

Abstracts No.1

ISOPRENE EMISSION RESPONSES UNDER CHANGING CLIMATE AND LANDCOVER FORCINGS OVER BORNEO ISLAND

J. Sentian, V.K.W. Yee and F. Herman

Climate Change Research Group, Faculty of Science and Natural Resources, Universiti Malaysia Sabah, Sabah, Malaysia.

jsentian@ums.edu.my

***Abstract*:** Isoprene is the most active biogenic volatile organic compounds (BVOCs). It is largely produced by plants and is known to play important roles in the tropospheric chemistry, greatly influencing the tropospheric ozone budget and atmospheric oxidation capacity. This paper focuses on how climate change and landcover affect isoprene emissions in the Borneo region. Climate change scenarios (RCP4.5 and RCP8.5) were developed for the Borneo region using the Weather Research Forecasting (WRF v4.0) model. The Model Emission of Gases and Aerosol from Nature (MEGAN v2.1) was used to simulate isoprene fluxes using climate output datasets scenarios from WRF model. Both climate scenarios would lead to a warming atmosphere at the end of the century, with surface temperature increases of 2.8^{o}C (RCP4.5) and 3.1^{o}C (RCP8.5), respectively. Under the present-day vegetation landcover scenario for RCP8.5, future emission of isoprene was projected to decrease by 11% (0.39 TgC/yr). Comparatively, higher decreases of isoprene emissions were projected under moderate climate forcing (RCP4.5) by 38% (1.14 TgC/yr) under present-day vegetation landcover. This indicates that climate forcing will have a significant impact on isoprene emissions in the region. Thus, challenges in dealing with future emission of isoprene in the region are closely tied to the management of greenhouse gases emission sources, which is the main precursor of climate change.

***Keywords*:** Biogenic emission, climate change, isoprene, landcover, MEGAN model, WRF model

Abstract No.2:

THE IMPACT OF LAND-USE CHANGES ON GREENHOUSE GASES ALONG THE OIL PALM PLANTATION TO RIPARIAN BUFFER STRIPS

H.J. Kuling*[1]and J. Sentian*[1,2]

[1]Faculty of Science and Natural Resources, Universiti Malaysia Sabah, Malaysia
[2]Climate Change and Research Group, Universiti Malaysia Sabah, Malaysia
*jsentian@ums.edu.my

Abstract: The impact of land-use changes on soil greenhouse gas flux in a tropical forest, nitrous oxide (N_2O), carbon dioxide (CO_2), and methane (CH_4) are few to be understood. This study is to assess the magnitude, short-term spatial, and temporal variability in GHG of land-use change oil palm plantation and the importance of riparian strips adjacent to the oil palm as a source of N_2O and CH_4. Runoff and leaching of fertiliser and herbicides routinely used in oil palm management will accumulate in properly working riparian buffer strips, leading to raised soil nutrient, thus giving sources of GHGs. We installed measurement transects from three mature oil palm plantations (Site 1, Site 2, and Site 3) to adjacent riparian buffer areas in SAFE Projects landscape (https://www.safeproject.net), SE Sabah. From this study, we found that CH_4 emission is higher in oil palm (91.02 ± 40.18 μg m^{-2} h^{-1}) whilst N_2O and CO_2 shows higher in riparian, 88.49 ± 90.52 μg m^{-2} h^{-1} and 267.80 ± 264.38 mg m^{-2} h^{-1} respectively.